MAGNETOELASTIC COUPLING BETWEEN SURFACE ACOUSTIC WAVES AND VARIOUS TYPES OF SPIN WAVES

by

NICHOLAS HOMROCKY

A dissertation submitted in partial fulfillment of the
requirements for the degree of

DOCTOR OF PHILOSOPHY IN APPLIED AND COMPUTATIONAL PHYSICS

2026

Oakland University
Rochester, Michigan

Doctoral Advisory Committee:

Vasyl Tyberkevych, Ph.D., Chair
Eugene Surdutovich, Ph.D.
Steven Louis, Ph.D.

To everyone who helped me on this journey,

thank you all for being a part of such a grand adventure.

ACKNOWLEDGMENTS

The author wishes to express his appreciation for extensive mentorship provided by Vasyl Tyberkevych, his adviser. Thanks are due to committee members Eugene Surdutovich, Ph.D., and Steven Louis, Jr., Ph.D., for their contributions to this dissertation. Likewise, acknowledgment is extended to Andrei Slavin, Ph,D., and Cody Trevillian Ph.D., as coauthors.

Nicholas Homrocky

ABSTRACT

MAGNETOELASTIC COUPLING BETWEEN SURFACE ACOUSTIC WAVES AND VARIOUS TYPES OF SPIN WAVES

by

Nicholas Homrocky

Adviser: Vasyl Tyberkevych, Ph.D.

We theoretically investigate magnetoelastic (ME) coupling between surface acoustic waves (SAWs) and spin waves (SWs) in yttrium iron garnet (YIG)/gadolinium gallium garnet (GGG) bi-layers. Two SW types propagating in an in-plane magnetized film are considered: surface spin waves (SSWs), backward volume spin waves (BVSWs).

A general analytical expression for ME coupling is derived via interacting wavevector modes and transversal profiles. The coupling is systematically analyzed via applied magnetic fields and geometric parameters. Optimal conditions for coupling exceed both damping rates of the SAW and SWs, enabling observation of coherent coupling phenomena. The calculated spectra of the hybrid ME waves show anti-crossing gaps.

Coupling SAW-SSW vanishes for Damon-Eschbach geometry, where the magnetic film is magnetized at 90° relative to direction of wave propagation. Optimal conditions for SAW-SSW interactions occur at 45°, where SWs maintain a surface characteristic with non-reciprocal wave profiles. This non-reciprocity makes coupling highly non-reciprocal. The ratio of coupling for opposite propagating waves exceeds 5 for practically achievable parameters that can be exploited to develop non-reciprocal ME devices as isolators or filters.

Coupling SAWs-BVSWs exhibit intriguing phenomena. The waves possess dispersion curves of opposite slopes, which opens a forbidden frequency band (bandgap)

where wave propagation is entirely prohibited. This bandgap, where coupling occurs, is controllable via magnetic field either for a localized spatial region or short time interval. Spatially inhomogeneous fields, implemented via current-carrying wire atop YIG, transforms SAWs into BVSWs propagating in the opposite direction. This mechanism offers a route toward voltage-controlled SW transducers and SAW filters. Current-carrying wires create an effective potential well for hybrid ME waves, yielding ultra-narrow transmission bands for SAWs corresponding to ME eigenmodes of the well.

SAW-BVSW transduction is also achieved applying a short, spatially homogeneous magnetic field pulse. The BVSW shifts its frequency while preserving the wavevector of the incident SAW. This behavior contrasts the spatially inhomogeneous case, by frequency conservation and a shift in the wavevector. Combining spatially and temporally non-uniform configurations, operations of time reversal and frequency inversion is successfully realized opening a path forward to novel hybrid ME space-time metamaterials tailored for advanced microwave signal processing at GHz frequencies.

TABLE OF CONTENTS

LIST OF TABLES

LIST OF FIGURES

LIST OF ABBREVIATIONS

BVSW	backward volume spin wave
FM	ferromagnet
FMR	ferromagnetic resonance
GGG	gadolinium gallium garnet
IDT	inter-digital transducer
ME	magneto-elastic
SAW	surface acoustic wave
SSW	surface spin wave
SW	spin wave
YIG	yttrium iron garnet

CHAPTER ONE

INTRODUCTION

Cost of energy is always the number one factor people consider before diving deeper into any topic. Electronic circuits today are prone to joule-heating, electrostatic discharge, and have reached a limit on small sizes with transistors, transducers, and memory density [1]–[5]. A good solution to this high energy cost, with also high energy loss, is the use of spintronic devices. They have the potential to replace key components in electronic circuits today that are in high demand [6]–[11]. Spintronics is an advancing technological field developing the next generation of devices that society will need. Utilizing the magnetic properties that come with almost any material, due to the spin of electrons, we can achieve technology that uses less energy and has less heating loss [12]–[14] along with many other phenomena that can be taken advantage from magnetism. These spintronic devices are already replacing modern circuits with vital technology that will help in humanity's goal for quantum computers, and artificial intelligence [15]–[21]. Spintronics will help bridge this gap to more advanced technology.

Spintronic devices use what is called a magnon or spin wave (SW) as their signal source for carrying and/or processing information. SWs have been shown to use less energy and operate in terahertz range [22]–[26] when compared to today's devices. As a start, it is vital to know how to excite a SW. Conceptually, a magnet has atomically aligned magnetic moments. If a magnetic moment is perturbed in a certain way this will cause that magnetic moment to oscillate and will cause its neighbors to be disturbed also. Thus, creating an oscillating wave of magnetic moments known as a SW.

While SWs can be excited using an antenna, it is better suggested to couple SWs to another carrier of information. This is to create processing techniques in future devices with SWs that would not be there if the SW was alone.

Modern microwave technology utilizes many signal processing methods via various solid-state phenomena. A commonly used method is based on using acoustic waves, specifically surface acoustic waves (SAWs). These SAWs are used in practical applications such as touchscreens, signal processing for radios or TVs, sensor technology for chemical, pressure, radar, and seismic activity shown in [27]–[30]. These SAWs are excited and detected very efficiently with inter-digital transducers with a relative complicated design and passively perform advanced filtering operations [28], [30], [31]. One of the main advantages of using SAWs for signal processing in smaller devices is that SAWs have a smaller wavelength than that of electromagnetic waves and a lower speed [27], [28], [31], [32].

This begins our study on coupling between SAWs and various SWs. While magneto-elastic (ME) interactions between SAWs and SWs have been studied, for a few decades, much more can still be contributed to the field. Some theoretical work includes [33]–[37], not to mention experimental data reported by [38]–[42]. This research has shown fascinating properties of ME coupled hybrid waves and shows great potential for practical applications [32], [43]–[49].

Intensive studies with ME coupling continues with new materials and phenomena [50]. Novel ME interactions in ferromagnetic [51], [52] materials have been proposed [32], [53]. Theoretical research on ME coupling in antiferromagnets [51], [52] demonstrated the possibility of controlling antiferromagnetic order parameter via SAW-induced strain [43]. Another study by [54] proposed using SAWs for excitation and detection of antiferromagnetic SWs. One growing field of interest involves the ME coupling with quantum states via SW properties. Recent reviews and observations can be found in [55]–[58]. Other studies describe the impact of acoustic behavior on spin current manipulation [44]–[46]. Additional areas of interest include SAW-induced domain wall movement [59] and skyrmion or vortex manipulation [60]. These ME interactions between SWs and SAWs offers many openings to situations needed for devices today.

In this work, we theoretically consider ME coupling between SAWs and two cases of magnetostatic SWs. With respect to wave-propagation and in-plane magnetized film geometries, we study ME coupling of SAWs to surface spin waves (SSWs) and backward volume spin waves (BVSWs). Theoretically derived formulas are solved via numerical calculations done in a standard system of epitaxial yttrium iron garnet (YIG) placed on top of a thick gadolinium gallium garnet (GGG) substrate as a bi-layer system. Our work does include consideration of discrete dipole-exchange SW resonant modes [61] existing in the YIG layer. Although YIG and GGG are not piezoelectric materials, it is possible to excite SAWs by depositing a thin piezoelectric layer on top [62]–[65].

From our simple work, we expand into a new growing field concerning space-time meta-materials that influence waves in, as the name suggests, space and time. However, we are getting ahead of ourselves, and need to review these waves individually before exploring this new territory.

CHAPTER TWO

LITERATURE REVIEW

We begin reviewing history of all the waves considered in this work and current research that leads into our interest with ME coupling phenomena.

2.1 Acoustic Waves

Acoustic waves were first studied centuries ago and it wasn't until the early 19th century when modern day acoustics started to take form [66]–[69]. This included sounds link to frequency, resonators, architecture, etc. It was experimentally proven by [70] that sound or acoustic waves need a medium to travel. Not until further mathematical theories and the discovery of piezoelectric materials from [71], [72] lead to research exploiting these acoustic waves for modern engineering purposes. Acoustic waves are the movement of particles in a way creating properties exactly as any normal wave. These acoustic waves are best shown off as ripples on a calm water pond, vibrations of a guitar string, earthquakes, etc.

Acoustic waves move particles of a medium in different directions depending on the atomic lattice structure. Figure 2.1 provides a beautiful illustration of mechanical waves in a simple cubic structure. From Fig. 2.1, consider these grid-like boxes as space that contains one atomic particle of the cubic lattice form. The propagation of an acoustic wave distorts the space between the particles in the medium. This happens either in a compression and decompression motion or perpendicular movement to the direction of wave propagation. Wave A in Fig. 2.1, shows the spacing between particles, through expanding and contracting space, creating a sense of pressure as the acoustic wave travels through the medium. Wave B in Fig. 2.1, shows particles being displaced perpendicular to the direction of wave propagation. The particles, for wave B, in this simple case can move perpendicularly either in a left and right or up and down motion maintaining the pattern of a wave. The movement of particles in these ways are respectively named longitudinal polarized acoustic waves and shear polarized acoustic waves [73]–[75].

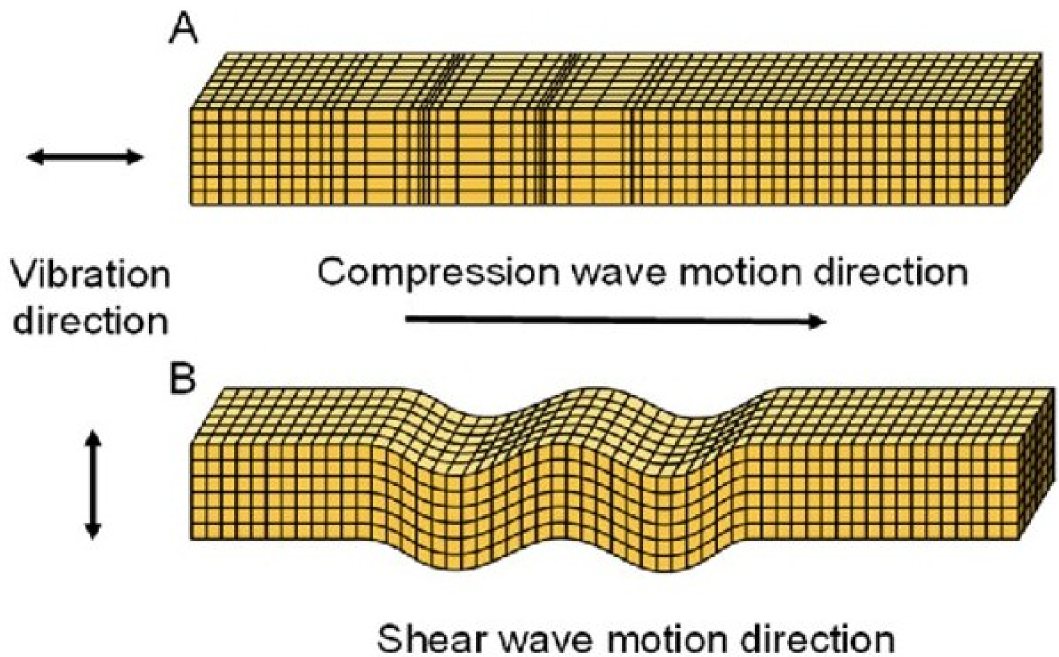

Figure 2.1: Diagram of the two types of acoustic waves. The top wave is longitudinal compressing and decompressing the space between particles. The bottom wave is a shear wave in which the particles move in either direction perpendicular to wave propagation. Illustration accredited to [76].

One can use these basic concepts for Lagrangian mechanics [77] (as shown in Appendix A.1) to derive the well known translational equation of motion all acoustic or elastic waves follow.

$$\rho \frac{\partial^2 \boldsymbol{u}}{\partial t^2} = \nabla \cdot T \tag{2.1}$$

On the left hand side, ρ represents the materials density the acoustic wave travels through, and $\boldsymbol{u}$ is the particle displacement vector, which is responsible for the profile of the wave. On the right hand side we are taking the gradient of stress tensor T which can be thought of as the self interacting forces acting on the particles. The addition of other external forces on the particles can be added to the right hand side to solve for any scenario one might consider.

Other important relations on how the particles self interact is the strain equation

$$S_{kl} = \frac{1}{2}\left(\frac{\partial u_k}{\partial r_l} + \frac{\partial u_l}{\partial r_k}\right) \tag{2.2}$$

and strain to stress conversion

$$T_{ij} = c_{ijkl} S_{kl} \tag{2.3}$$

The tensor c is the elastic stiffness tensor whose elements are dependent on the material chosen and sometimes rewritten in the form of Bulk's and Young's modulus [73]–[75], [78]. All subscripts $(ijkl)$ represent the usual cartesian coordinates (xyz). Depending on ones research scenario, any acoustic wave can be found from the known relations above.

For our case we take the isotropic conditions of the YIG/GGG materials and the elastic stiffness tensor explicitly takes the form

$$c = \begin{pmatrix} \begin{pmatrix} c_{xxxx} & 0 & 0 \\ 0 & c_{xxyy} & 0 \\ 0 & 0 & c_{xxzz} \end{pmatrix} & \begin{pmatrix} 0 & c_{xyxy} & 0 \\ c_{xyyx} & 0 & 0 \\ 0 & 0 & 0 \end{pmatrix} & \begin{pmatrix} 0 & 0 & c_{xzxz} \\ 0 & 0 & 0 \\ c_{xzzx} & 0 & 0 \end{pmatrix} \\ \begin{pmatrix} 0 & c_{yxxy} & 0 \\ c_{yxyx} & 0 & 0 \\ 0 & 0 & 0 \end{pmatrix} & \begin{pmatrix} c_{yyxx} & 0 & 0 \\ 0 & c_{yyyy} & 0 \\ 0 & 0 & c_{yyzz} \end{pmatrix} & \begin{pmatrix} 0 & 0 & 0 \\ 0 & 0 & c_{yzyz} \\ 0 & c_{yzzy} & 0 \end{pmatrix} \\ \begin{pmatrix} 0 & 0 & c_{zxxz} \\ 0 & 0 & 0 \\ c_{zxzx} & 0 & 0 \end{pmatrix} & \begin{pmatrix} 0 & 0 & 0 \\ 0 & 0 & c_{zyyz} \\ 0 & c_{zyzy} & 0 \end{pmatrix} & \begin{pmatrix} c_{zzxx} & 0 & 0 \\ 0 & c_{zzyy} & 0 \\ 0 & 0 & c_{zzzz} \end{pmatrix} \end{pmatrix} \tag{2.4}$$

The symmetry of these components and physical properties of an isotropic material help define the elements in c as

$$c_{ijkl} = \lambda \delta_{ij}\delta_{kl} + \mu(\delta_{ik}\delta_{jl} + \delta_{il}\delta_{jk}) \tag{2.5}$$

where λ and μ are the Lamé constants with values 110.5GPa and 90GPa respectively [73], [78], [79] and $\delta_{ij(kl)}$ is Kronecker delta. These Lamé constants are related to Young's modulus (E) and Bulk's modulus (K) also in the following way

$$E = \frac{\mu(3\lambda + 2\mu)}{\lambda + \mu} \tag{2.6a}$$

$$K = \lambda + \frac{2}{3}\mu \tag{2.6b}$$

2.1.1 Surface Acoustic Waves

The specific acoustic wave we studied is a SAW. There are two main types of SAWs: Love and Rayleigh. The first SAW, the Love wave [73]–[75] moves the particles in a perpendicular motion similar to a shear wave. The difference is the side-to-side motion of particles, that is parallel to the surface, is felt less and less by particles deeper within a medium. Love waves are difficult to work with in a simple homogeneous medium, as they will not propagate nor manifest (seen in experimentally related ME work [32], [63]). This is due to the nature of the wave needing a change in wave velocity via inhomogeneous structures [73], which also is needed for other subcategory SAWs. In general, we did not consider Love waves, because they cannot be reliably excited using standard excitement techniques as cited in these related works [28], [32], [63].

The second SAW type is called a Rayleigh wave [73]–[75] which we mainly use in this work. This SAW has more of a rotating motion for particles as they will be compressed and decompressed like longitudinal waves, but also have up-down shear motion, perpendicular to the surface, as well. A nice visual example of both waves are shown in Fig. 2.2. These SAWs were discovered by [68] through mathematical predictions via properties acoustic wave types only appearing at the surface of a medium. A small example of this theoretical work is shown in Appendix A.1 as we derive the profile of a Rayleigh wave under certain conditions, and obtaining the group velocities of longitudinal and shear waves. Even though SAWs are unique they still follow a linear dispersion relationship $\omega = vk$ for any mode, where ω, v, and k are the frequency, speed, and wavevector of the wave. Our well studied SAWs have been researched for many decades [28], [66], [81]–[86]. While almost any medium has SAWs, these waves are mainly studied experimentally using piezoelectric materials [31], [87]–[91]. These piezoelectric materials get there name by the conversion of electric energy to mechanical energy or vice versa.

This is how SAWs are used in technology and research today. To induced or absorb the mechanical energy of a SAW wiring is placed on top of the piezoelectric film or waveguide in an interlocking comb like pattern. First developed and shown off by [92].

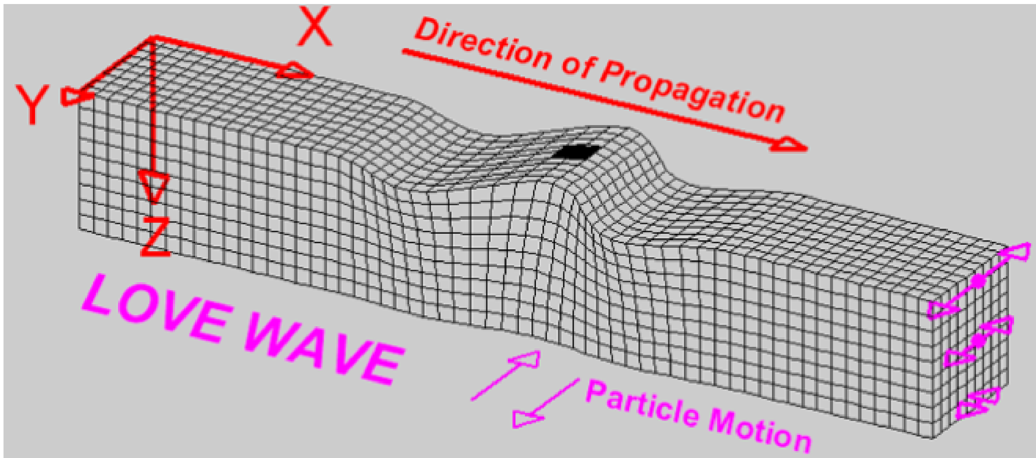

(a) Love wave

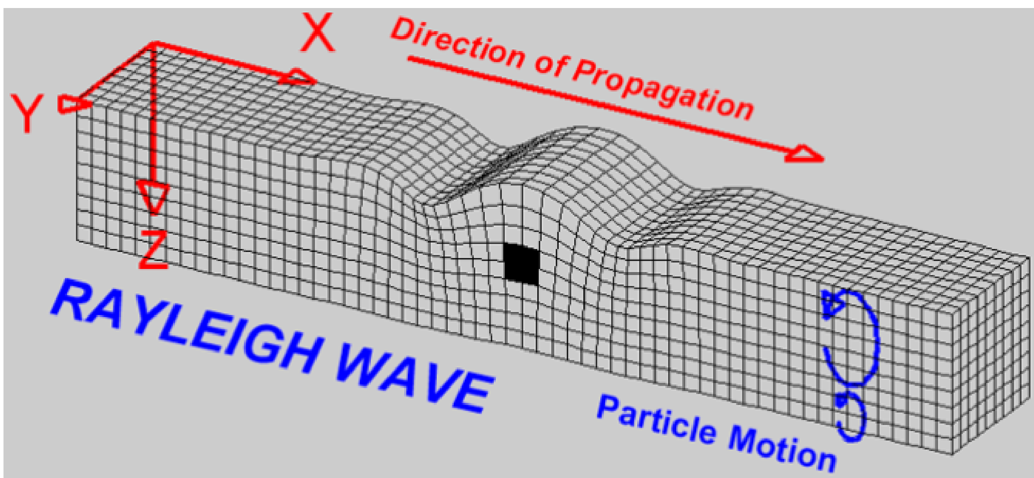

(b) Rayleigh wave

Figure 2.2: Two examples of SAWs and how particle motion is affected visually. Love waves have shear motion side-to-side parallel to surface. Rayleigh waves are rotational with longitudinal and up-down shear motion. Illustration accredited to [80].

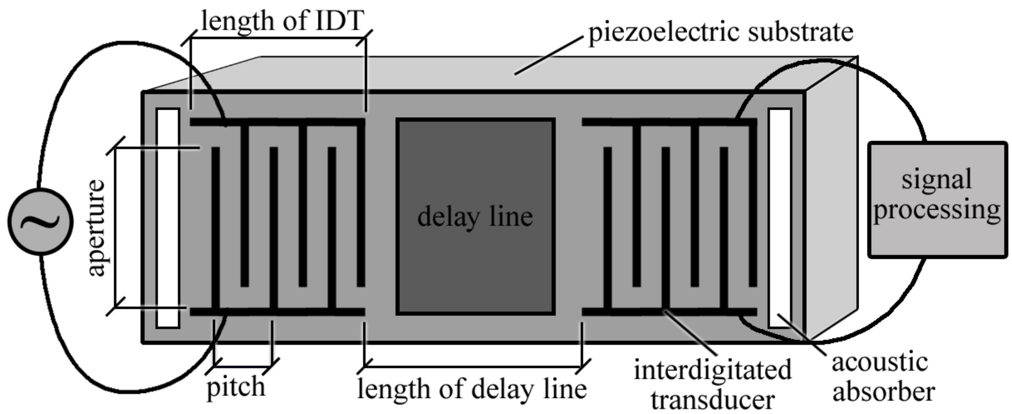

Figure 2.3: General structure of a SAW sensor with connections to an AC-voltage source and a signal processing unit. Acoustic absorbers appear on the ends, but can be replaced with reflectors to decrease insertion loss. Illustration accredited to [93].

This design technique is called an inter-digital transducer (IDT). A simple schematic is shown in Fig. 2.3.

When exciting a SAW, an AC-voltage is applied and a dynamic electrical field is felt by the charged particles within the piezoelectric material. The resulting affect on the particles cause them to expand and contract, creating the oscillating acoustic wave within the medium. From Fig. 2.3, the pitch is equal to the wavelength, or spacing between the teeth of the interlocking combs is half the wavelength [94]. Other designs give different effects on SAWs such as; standing waves, phase changes, extra filtering, focal points, etc, [95], [96]. Compared to other waves that usually need a current to excite, the input power is most efficiently transferred into a SAW considering there is no joule heating loss. Many every day devices use SAWs as three main functions for filtering, resonators, and sensors [97]–[101]. These devices include, television/wifi frequency filters, touchscreens, pressure monitors, biosensors, actuators, and many more.

This leads into one of the over used intrinsic properties of acoustic waves. They are reciprocal, meaning acoustic waves are symmetrical with mirrored movement in any direction. While useful in some devices that employ resonant effects of SAW excitation, reciprocal wave propagation prevents SAW used in other cases. Reflected waves are conceptually harmful for devices adding noise or interference when trying to measure an output. This is one reason why we would want to couple a reciprocal mechanical wave to a nonreciprocal magnetic wave.

2.2 Spin Waves

Perhaps too far back, SW essentially started with the discovery of electron spin from [102]. From that experiment a semi-classical approach with quantum mechanics shows how an atom forms its magnetic moment [51], [52], [103]–[105]. Modern textbooks reference extensive details in mathematical derivations providing a strong foundation for understanding of the atomic lattice interactions with electrons and their quantum behavior. All subatomic particles have a spin and magnetic moment.

However, the scale of interaction our work is theorized on is volumetric. Building from the ground up, the outer shell of electrons of an atom contribute to the atomic magnetic moment we will discuss. The atomic magnetic moments exhibit many interactions with its surroundings within the atomic lattice of a material. A few interactions include; electromagnetic forces via dipolar fields, spin-orbit coupling, electron-phonon scattering, critical temperature changes, etc. [106]–[108]. Magnetic fields from atoms, or external sources, interact with each other in complicated dynamical ways. In any crystallographic structured material, the static states of the atoms magnetization are randomized and would interact randomly with its neighbors in an unpredictable way. This is why SWs need certain requirements from the material as a whole.

This is beneficial because only magnetically ordered materials can support the existence of SWs. The magnetically ordered magnetic moments have a definitive stationary structure, and will exhibit collective behavior as a total magnetization summed from the magnetic moments. Depending on the strength of the magnetization of an element, there is a range of magnetically ordered materials to work with that can support SWs. Most texts today will discuss ferromagnets (FMs), antiferromagnets, ferrimagnets, and altermangets. A full list with definitions is provided in [51], [52]. In this work we have the added benefit only considering FMs where all the magnetic moments within the structure or medium are aligned parallel to each other within the material for a net magnetization.

The alignment of these magnetic moments in FMs is due to the exchange interaction found from quantum mechanics. The thought process to explain natural FM is the overlap of electron orbitals between atoms following the Pauli exclusion principle with the wave functions of electrons determining the coupling constant only for nearest neighbor spins. This exchange phenomena conceptually follows the Heisenberg Hamiltonian of coupled neighbors described as $H = -\sum_{i,j} \frac{J}{\hbar^2} S_i S_j$. This leads to many other topics outside the scope of our work, but further reading can be done with [51], [52], [109]–[113]. Notable facts to take away from the exchange interaction is that momentum and energy will always be conserved and quantized by the spin from the electron. This neighbor to neighbor exchange interaction is stronger than the long range dipolar interaction magnetic moments have with each other. The individual magnetic moments are described as a vector with direction and magnitude. The magnetic moments will precess about itself and keep a constant magnetization length. This magnetization vector is $\boldsymbol{m}$ which is dimensionless and always satisfies $|\boldsymbol{m}|^2 = 1$.

One will then wonder where magnetic units factor in to match a magnetic field as is our topic. In FM materials, when all magnetic moments are perfectly aligned a total net magnetization occurs and the FM becomes saturated. This magnetization saturation M_s is defined as a constant for that magnetized material with units Amps/meter matching a magnetic field. The saturation magnetization M_s is the unit factor for the magnetization vector $\boldsymbol{m}$. The $\boldsymbol{m}$ is normalized to the density of magnetization as will be shown later. The magnetization vector $\boldsymbol{m}$ provides unitary direction for magnetization of the material and the density of magnetization for any volume and with units have a magnitude of M_s. That way, mathematically, our unit vector $\boldsymbol{m}$ stays conservative, and the main magnetic equation everyone follows incorporates this feature helping us to know how far magnetization may deviate from its static state.

With a structural foundation of our magnetic system we wish to understand mathematically how SWs function with many dynamically interacting magnetic fields. This leads to our main well known Landau-Lifshitz equation

$$\frac{\partial \boldsymbol{m}}{\partial t} = |\gamma| \boldsymbol{B}_{\text{eff}} \times \boldsymbol{m} \tag{2.7}$$

where $\boldsymbol{B}_{\text{eff}}$ is the effective magnetic field of the entire system and the constant $|\gamma|$ is the electron gyromagnetic ratio.

Magnetization of a material is essentially determined by the sum of magnetic fields acting internally and externally on your system via $\boldsymbol{B}_{\text{eff}}$. Some magnetic fields mainly discussed in literature are external fields, anisotropy field, dipole field, exchange field, ME field, calorimetry field, optical field, etc., [51], [52], [104], [114]–[117]. We only need to consider the dipolar field $\mu_0 \boldsymbol{H}_{\text{dip}}$, exchange field $\boldsymbol{B}_{\text{ex}}$, and an external field $\boldsymbol{B}_{\text{ext}}$.

The expression for the dipolar field following historic notation, $\mu_0 \boldsymbol{H}_{\text{dip}}$, is not an exact solution, but rather a symbolic one. Starting with Maxwell's equations in derivative form we assume a magnetostatic approximation. This is for when a magnetic wave (our SW) is orders slowly than an electromagnetic wave, but still has long range interactions. Conceptually, the SW has frequency ω and can interact with its surroundings a length l away. When compared to the electromagnetic wave $\omega l << c$ and we drop the time derivative terms ($\partial E \big/ \partial t, \partial B \big/ \partial t$) for both fields. The last assumption is that no current is flowing through the magnetic material dropping the current density $\boldsymbol{J}$ term. This leaves us with $\nabla \cdot \boldsymbol{B} = 0$ and $\nabla \times \boldsymbol{H} = 0$ from Maxwell's equations. Using $\boldsymbol{B} = \mu_0(\boldsymbol{H} + M_s\boldsymbol{m})$, knowing $\boldsymbol{H}$ and $\boldsymbol{m}$ contain all magnetic components of a system, one substitutes $\boldsymbol{B}$ into the divergent expression. One would then find $\nabla \cdot \boldsymbol{H} = -M_s \nabla \cdot \boldsymbol{m}$. Following the same thought process solving Maxwells equations normally, one assumes $\boldsymbol{H} = \nabla \psi$ where the magnetic field is the gradient of the magnetic scalar potential ψ. Solving for ψ as a function of the magnetization $\boldsymbol{m}$, in the conceptual sense, as $\psi = -M_s \nabla^{-2} \nabla \cdot \boldsymbol{m}$, we see that the magnetic field comes from magnetization rather than a magnetic field producing magnetization. Back substituting what we found conceptually for $\boldsymbol{H}$, the dipolar field, $\boldsymbol{B}_{\text{dip}}$, takes the form

$$\mu_0 \boldsymbol{H}_{\text{dip}} = -\mu_0 M_s \nabla \nabla^{-2} \nabla \boldsymbol{m} \tag{2.8}$$

multiplied by $\mu_0 M_s$ for proper units as $\boldsymbol{m}$ is dimensionless. Dependent on the case one wishes to study this *gradient term* could be anything due to the complexity of long range interactions possible in a system. Two simple cases to substitute the *gradient term* with are plane waves using a tensor product of the unit wavevector $\hat{\boldsymbol{k}}$ or with uniform precession using the demagnetizing tensor $\hat{\mathbf{N}}$.

The exchange field is found via Lagrangian mechanics applied to an expanded Heisenberg Hamiltonian assuming non-uniform magnetization [51], [52], [117]. Rewriting the energy Hamiltonian expanded as two terms; one for the ground state energy of parallel spins and one for the dynamic SW interaction between nearest neighbors. We take the variational derivative of the Hamiltonian with respect to magnetization gives the exchange field. The final expression for how the exchange field $\boldsymbol{B}_{\text{ex}}$ depends on magnetization $\boldsymbol{m}$ is

$$\boldsymbol{B}_{\text{ex}} = -\mu_0 M_s \lambda_{\text{ex}}^2 \nabla^2 \boldsymbol{m} \tag{2.9}$$

where λ_{ex} represents the exchange length. The exchange length is a constant found from material parameters with units of length.

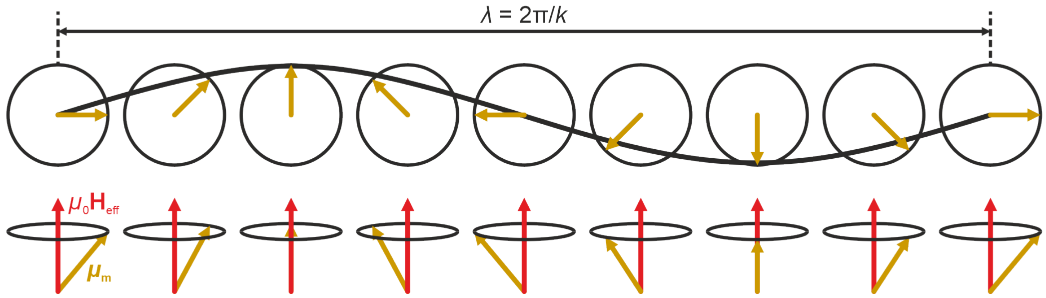

Figure 2.4: Magnetic moments (orange) precessing around the effective magnetic field (red). Initially, the magnetic moments were perfectly aligned with the effective field, but a disturbance 'kicks' a magnetic moment and it precesses around effecting its neighbors down the row. Illustration accredited to [119].

The external field $\boldsymbol{B}_{\text{ext}}$ is the magnetic field we can completely control. The external field helps set the magnetized geometry of our system. Normally when physically creating a magnetically ordered structure, the material is magnetized to an external field and sets the static state of magnetization.

Using the Landau-Lifshitz equation, and our three magnetic fields (dipolar, exchange, external) we begin looking for a solution to the magnetization vector, $\boldsymbol{m}$, which will detail our behavior for SWs. An exact method used in this work to solve for explicit SW profiles and approximate dispersion relations is shown in Appendix A.2 with a simple example. However, dipole-exchange interactions increase the complexity of the problem and numerical methods were used to solve for SW profiles and SW spectrum using [61], [118]. This involved SWs in FM films where (2.7) is linearized near the static magnetization state and the magnetic fields from (2.8) and (2.9) were expanded into an infinite series of algebraic equations.

Under the right conditions, any change to any magnetic field creates a perturbation within the previously stable magnetostatic system and excites the SW. To begin describing an explicit SW consider the illustration depicted in Fig. 2.4 we consider an untouched

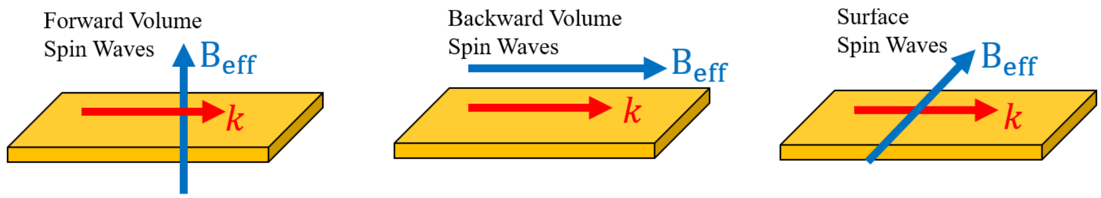

(a) Spin Wave Geometry

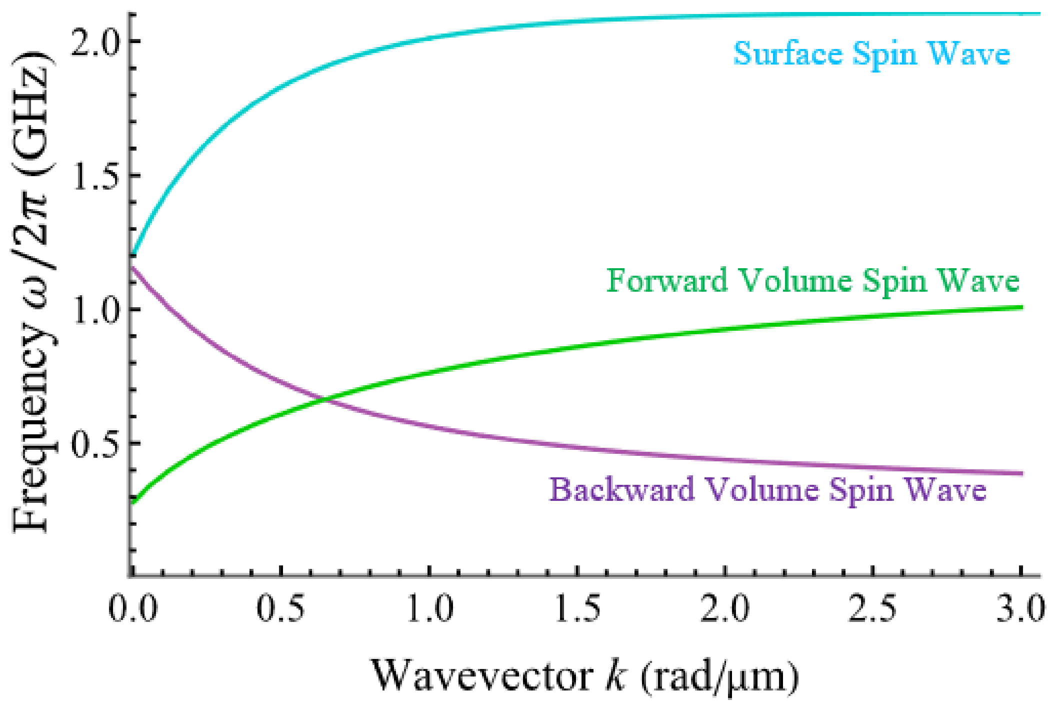

(b) Spin Wave Spectrum's

Figure 2.5: (a) SW propagation defined by the wavevector k (red arrow) and the effective magnetic field oriented three different ways to induce different SW affects. (b) SW spectra for each magnetic field geometry. Spectrum was plotted with YIG film thickness 1µm and internal magnetic field 10mT.

stable magnetostatic system. If we theoretically perturbed just one of these atomic magnetic moments the magnetization direction (dark yellow vector in Fig. 2.4) will be misaligned from the overall effective magnetic field (red vector in Fig. 2.4). This misalignment eventually realigns from damping factors, but not before the magnetization precesses around its static axis defined by the effective magnetic field. This precession about the magnetic dipole from the magnetization is felt by its neighboring atom and its magnetization will begin precessing itself around the static magnetized state. Soon a line of magnetic moments will precess in a wave-like fashion as shown in Fig. 2.4.

As with acoustic waves, there exists many different types of SWs. All solution types are found via Landau-Lifshitz equation (2.7) given the parameters for the problem. In this work we focus on three simple cases in the magnetostatic case. As shown in Fig. 2.5a, there are three cases defined by the orientation of the effective magnetic field with respect to the propagation of the SW. In these different geometrical set-ups the SWs have different profiles and features related to the interplay of the summed magnetic fields. The three magnetostatic SWs are, again like acoustic waves, considered to be modes of SWs. These SW modes are found to be a very nice feature of FMs.

SW modes are affected dynamically by the summed magnetic fields. It is best to clarify that under specific parameters, and for simplicity, one magnetic field can be more important than the other in the wave spectrum. The main consequence is that it will contribute to different SW behavior. Any of the three magnetostatic SWs can be dominated by either the dipole moments or the exchange neighbor interactions for example. Dipole moments dominate when magnetization is able to interact long distance with other magnetized states across the medium or material. Exchange energy dominates SWs when magnetization only interacts with their closet neighbors. Referring to Fig. 2.5b, where the plotted dispersion relations of SWs are shown with approximated solutions from (2.7) for a YIG film of thickness 1μm and magnetic field 10mT. The slopes of these curves for each dispersion relation depends on the film thickness, and the range of frequencies for each wave can be tuned via magnetic field strength. This is why SWs are an attractive form of signal processing, as the frequency of the SW can be dynamically tuned in real time with the strength of the net magnetic field. Essentially, as the magnetic field strength increases the frequency of the SW modes will increase proportionately and vice versa.

These approximations in Fig. 2.5b for the three magnetostatic SW modes is for the dipolar region where k is relatively small. Magnetic interactions are dominated by dipolar effects. All three dispersion relations (not obvious for BVSW, see (2.11) below) follow similar behavior where eventually at large enough k's the frequency plateaus. However, in this plateau region, both dipole and exchange interactions effect SWs having same order of energy interacting on SWs. Beyond this plateau dipole-exchange region the larger k's for SWs become dominated by nearest neighbor exchange interactions and and the frequency follows quadratic behavior as $\omega \sim k^2$. All three of the magnetostatic SW modes show the exact same quadratic dependence. Technology to excite very short wavelengths, for either wave, as k increases is difficult to create with great quality. This is why for Fig. 2.5b we focus on the dipolar region where more interesting phenomena with the SAW occurs.

The most notable effect for long range interactions is the ferromagnetic resonance (FMR). The FMR effect is the precession of magnetization everywhere all through out the medium ideally in perfect precessing synchronization. This concept happens when $k \approx 0$ or the wavelength is infinite compared to the small magnetic materials one experiments on. As shown in [51], [52], [61], [116], [118], FMR has been solved for mathematically and this natural feature of has had much research done to exploit this effect for technological use [120]–[126]. However, our range of wavevectors and wavelengths are for the microwave region and don't reach the infinite or zero limit, depending on your perspective.

This FMR effect is similar to another resonating feature in the microwave region. The complex exchange magnetic field holds certain interactions, that in comparison to a vibrating structure, will naturally have higher order standing SW resonant modes. For many cases, these higher order standing modes play a role in how any SW spectrum will appear. Mathematically, when you look for SW solutions that include exchange interactions, one will end up finding these higher order resonating SW modes in the FM. In the dipole range these resonant SW modes will be standing waves. Ideally, standing waves follow the same concept of a string pinned on both ends and again vibrates at specific frequencies with an increasing number of nodes as the frequency increases. These higher order resonant SW modes branch out at different discrete frequencies starting from $k \approx 0$. These higher order standing SWs are equally spaced frequencies dependent on the length between the boundaries of the FM film.

The SW resonant modes will interact with the three magnetostatic SW modes, and will some change the appearance of the SW spectrum. As shown in Fig. 2.6, our magnetostatic SW modes are hidden within this spectrum of higher order SWs resonant modes. The exception is the BVSW which does not cross with the higher order SW resonant modes, but does still affect the resonant mode spectrum. When the spectrum does become more complex, analysis of each SW line, at a specific wavevector value, will give a wave profile. This helps identify where the magnetostatic SW mode, such as for the forward volume or surface spin wave, is located using the previously discussed theories from [61], [118]. These SW resonant modes, same as the magnetostatic SW modes, can be dynamically tuned with the magnitude of the magnetic field.

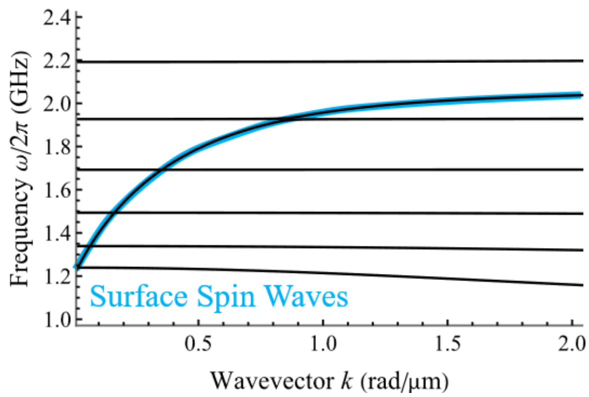

(a) Surface Spin Wave with Resonant Modes

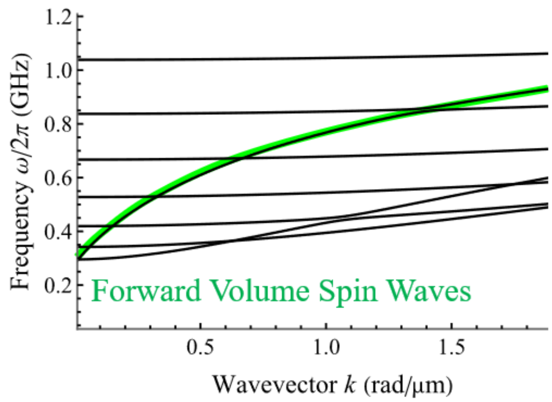

(b) Forward Volume Spin Wave with Resonant Modes

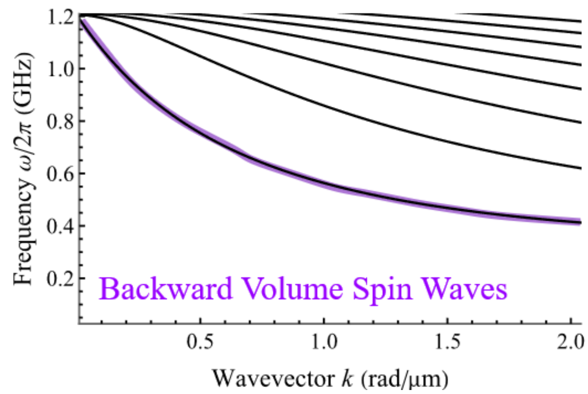

(c) Backward Volume Spin Wave with Resonant Modes

Figure 2.6: Black lines represent higher order standing SWs resonant modes. (a) Light blue highlights the SSW. (b) Green highlights the forward volume spin wave. (c) Purple highlights the BVSW. The higher order SW resonant modes cross the magnetostatic SW modes complicating the SW spectrum. Spectrum's where plotted with YIG film thickness 1μm and internal magnetic field 10mT.

2.2.1 Surface Spin Waves

Referring to Fig. 2.5, consider the far right case. This system of static magnetization is perpendicular to the propagation direction of the SW which is called the SSW mode. The main interesting feature of the SSW is that it can appear either at the either the top or bottom surface of FM film. This behavior is dependent on the sign of the wavevector k while also being perpendicular to the magnetization direction. These magnetostatic SSWs are nonreciprocal in this sense.

SSWs were first mathematically predicted and experimentally observed by [127]. Under simple assumptions using only the dipolar magnetic field (2.8) and solving (2.7) an approximated dispersion relation for the angular frequency of the SSW is found as

$$\omega^{(\mathrm{SSW})} = \sqrt{\omega_{\mathrm{B}}(\omega_{\mathrm{B}} + \omega_{\mathrm{M}}) + \frac{\omega_{\mathrm{M}}^2}{4}(1 - e^{-2kL})\sin(\phi)^2} \tag{2.10}$$

Mainly dominated by dipolar field effects, this dispersion relation serves as a good approximation with $\omega_{\mathrm{B}} = |\gamma|B_{\mathrm{ext}}$ and $\omega_{\mathrm{M}} = |\gamma|\mu_0 M_s$ as angular frequencies related to the external field and saturation magnetization. The angle ϕ is between the external magnetic field and wave propagation direction. The constant L is the thickness of the FM film and k is the wavevector. The dispersion relation can be explicitly found following the guide in Appendix A.2.

This phenomena to tune the SSWs frequency with the magnetic field strength and still exhibit nonreciprocal wave behavior has excited many to research SSWs over the decades [128]–[137]. For this reason many researchers continued to pursue utilizing SSWs with reciprocal SAW. As a result of ME coupling between SSWs and SAWs will exhibit nonreciprocal features, while still having advantages of both waves. Several decades of theoretical [33]–[35] and experimental [38]–[40] research revealed many interesting properties of the hybrid ME waves and showed their high potential for practical applications [32], [43]–[47], [138]. While a ton of work already has been done with SSWs alone, there is still more that can be done to couple SAWs and SSWs.

2.2.2 Backward Volume Spin Waves

Previously discussed SSWs are one of three magnetostatic SWs. The next one we will consider from Fig. 2.5a is the middle magnetostatic wave. The BVSW will be our main focus for ME coupling in the last two chapters. Many unique features will arise just from simple considerations. This geometric set-up is also easier in every sense since magnetization and wave propagation are parallel.

Referring to Fig. 2.5a the last magnetostatic SW is forward volume spin wave. While they have their own features, we found found BVSWs more exciting and easy for experimental set-up to test theories. Out-of-plane magnetization is tricky to apply to a film without it affecting other components of an experiment.

Back to BVSWs, they were predicted mathematically and experimentally observed by [139]. This SW is truly unique from the perspective of the waves' dispersion relation in many instances. Most notably, the special interest of BVSW takes place in the dipole region where magnetization interactions can happen for long distances. In this regime, as the wavevector of the BVSW increases the frequency of the BVSW actually decreases. Best seen from its approximated dispersion relation, found under the same conditions as the SSW,

$$\omega^{(\mathrm{BVSW})} = \sqrt{\omega_{\mathrm{B}}\left(\omega_{\mathrm{B}} + \frac{\omega_{\mathrm{M}}}{kL}(1 - e^{-kL})\right)} \tag{2.11}$$

The profile of this wave is a bulky bump in magnetization similar to the ground state of a vibrating string (see Fig. 5.1). As stated before the dispersion relation can be found explicitly following the guide in Appendix A.2.

They have been studied both theoretically [140]–[147] and experimentally [148]–[155] to exploit the BVSW special properties in new spintronic devices. Other unique BVSW phenomena may be observed with solitons, Bose-Einstein condensates, inverse Doppler effect, left-handed system, etc.

One struggle has been the consistency to excite and use BVSW in practical applications, especially with magnetic damping and their slow speed [156]–[161]. One possible solution would be using another wave to excite or convert BVSW to travel greater distances via SAWs. Our work with SAW-BVSW coupling lead us to new ideas on how we can achieve the same results as filters, isolators, channel flipping, information carrying, optical effects, quantum behavior, etc.

2.3 Magneto-Elastic Coupling

Researchers immediately sought ways to exploit these magnetic systems using well defined acoustic waves. Decades of research go as far back to the 1940's [162]–[164] which inspired many others to continue ME work throughout the century [165]–[183] and much much more for anyone to explore. This field may be just under a century old, but research continues in because of the ever expanding magnetic materials that arise with new magneto-acoustic phenomena. We hope in this work it will act as a easier foundation to catch up to modern work.

Today's modern work of ME coupling includes a vast range of studies [50]. These fields have expanded throughout the decades studied both theoretically [33]–[35], [64], [184]–[188] and experimentally [38]–[42], [189]–[199]. Modern work reveals incredible features of dual magneto and acoustic waves that demonstrate exceptional potential for practical applications [32], [43]–[49], [200]. Notable mechanisms of ME interaction in ferromagnetic materials have been shown off by [32], [53], [201]–[206] ME coupling exists in other magnetic materials such as antiferromagnets shown in [43], [54], [207]–[212]. One field with strong growth involves ME coupling in systems of quantum nature [55]–[57], [213]. Other studies describe the impact of acoustic behavior on spin current manipulation [214]–[217]. Additional areas of interest include SAW-induced domain wall movement [59], [218], [219]. and skyrmion or vortex manipulation [60], [220].

Conceptually, how the two waves interact is simple. From the perspective of the static magnetic system, an acoustic wave propagates through and disturbs magnetization causing dipolar interactions one example. From (2.7) an additional term is added as

$$\frac{\partial \boldsymbol{m}}{\partial t} = |\gamma|\boldsymbol{B}_{\text{eff}} \times \boldsymbol{m} + |\gamma|\boldsymbol{B}_{\text{ME}} \times \boldsymbol{m} \tag{2.12}$$

The ME magnetic field $\boldsymbol{B}_{\text{ME}}$ can be included in the effective field, but is brought outside to as a better visual. When viewed from the elastic system, the magnetic dipolar interactions create a force acting on the atomic lattice generating an acoustic wave.

$$\rho \frac{\partial^2 \boldsymbol{u}}{\partial t^2} = \nabla \cdot T + \boldsymbol{F}_{\text{ME}} \tag{2.13}$$

The term $\boldsymbol{F}_{\text{ME}}$ is the ME force acting on the acoustic system. Under the right conditions using a specific frequency where both spin and acoustic waves cross in the spectrum one wave will generate the other with great efficiency.

Mathematically, building off the previous works of [46], [79], [221]–[224], we derive the ME energy, E_{ME}, which is the shared energy between the magnetic and elastic systems. The added ME terms take the form $\boldsymbol{B}_{\text{ME}} = -M_s^{-1} \delta E_{\text{ME}}/\delta \boldsymbol{m}$ and $\boldsymbol{F}_{\text{ME}} = -\delta E_{\text{ME}}/\delta \boldsymbol{u}$ for effective ME magnetic field and ME force, respectively. This gives our known energy formula as

$$E_{\text{ME}} = \int_V \frac{1}{M_s^2} b_{\alpha\beta\gamma\zeta} \frac{\partial u_\alpha}{\partial r_\beta} M_\gamma M_\zeta d^3\mathbf{r} \tag{2.14}$$

This describes coupling between the spin and elastic degrees of freedom. Here, $b_{\alpha\beta\gamma\zeta}$ is the magnetostriction tensor where the Greek indices $\alpha\beta\gamma\zeta$ arbitrarily are xyz coordinates. The magnetostriction tensor components are material dependent, same as the elastic stiffness tensor.

2.4 Material Parameters

The work presented in this dissertation uses the bi-layer system YIG/GGG with well known parameters used everyday in other research. Taking isotropic conditions for the FM YIG film, as with the elastic stiffness tensor c_{ijkl}, the magnetostriction tensor also has off diagonal symmetrical components $b_{\alpha\beta\alpha\beta} = b_{\beta\alpha\alpha\beta} = b_{\alpha\beta\beta\alpha} = b_{\beta\alpha\beta\alpha} = b_2$ and diagonal components with $b_{\alpha\alpha\alpha\alpha} = b_1$. d The values of the magnetostriction tensor elements found in YIG are $b_1 = 0.35\text{MJ/m}^3$ and $b_2 = 0.7\text{MJ/m}^3$ with respect to [79], [180], [221], [222]. The magnetostriction tensor is shown explicitly below.

$$b = \begin{pmatrix} \begin{pmatrix} b_1 & 0 & 0 \\ 0 & 0 & 0 \\ 0 & 0 & 0 \end{pmatrix} & \begin{pmatrix} 0 & b_2 & 0 \\ b_2 & 0 & 0 \\ 0 & 0 & 0 \end{pmatrix} & \begin{pmatrix} 0 & 0 & b_2 \\ 0 & 0 & 0 \\ b_2 & 0 & 0 \end{pmatrix} \\ \begin{pmatrix} 0 & b_2 & 0 \\ b_2 & 0 & 0 \\ 0 & 0 & 0 \end{pmatrix} & \begin{pmatrix} 0 & 0 & 0 \\ 0 & b_1 & 0 \\ 0 & 0 & 0 \end{pmatrix} & \begin{pmatrix} 0 & 0 & 0 \\ 0 & 0 & b_2 \\ 0 & b_2 & 0 \end{pmatrix} \\ \begin{pmatrix} 0 & 0 & b_2 \\ 0 & 0 & 0 \\ b_2 & 0 & 0 \end{pmatrix} & \begin{pmatrix} 0 & 0 & 0 \\ 0 & 0 & b_2 \\ 0 & b_2 & 0 \end{pmatrix} & \begin{pmatrix} 0 & 0 & 0 \\ 0 & 0 & 0 \\ 0 & 0 & b_1 \end{pmatrix} \end{pmatrix} \tag{2.15}$$

For simplicity and how it is handle in labs, we do assume that the elastic parameters of the YIG and GGG layers are the same as in reality they differ by about 10% [37], [62], [63], [65], [73], [74], [79], [224]. Another technically note is that YIG is a ferrimagnet based upon the definition of the word and the alignment of magnetization within the material. It is easier to think of YIG as a weaker FM based on its magnetization saturation [225]. For our discussion and work we consider YIG a FM which can be thought of as a regular magnet for all in tense in purpose.

Using this bi-layer system we reference [47], [51], [73], [74], [78], [79] to find parameters for a thin YIG film with thickness L in µm, magnetization saturation 139kA/m, density 5170 kg/m^3, exchange length λ_{ex}^2 =3 10^{-16}m^2 and acoustic parameters (Lamé constants) with $\lambda = 110.5$GPa and $\mu = 90$GPa. The magnetic field parameter for a thin YIG film isn't necessarily the magnitude of the effective magnetic field $\boldsymbol{B}_{\text{eff}}$. The effective field is a dynamic field dependent on the amplitude of the SWs. For this reason, and for realistic simplicity, we consider the static internal magnetic field for a thin film magnetized in-plane which coincides closely with the external magnetic field $\boldsymbol{B}_{\text{ext}}$ all in units of mT. Further details from [36], [44], [51], [52], [226]–[230] show why this is possible due to magnetization along the easy axis for a thin film and having negligible anisotropic and demagnetizing effects. In the perspective of SWs, our future technology, YIG is the best choice due to the lowest damping recorded. The added benefit of using YIG is the elasticity of the material to support acoustic waves as well in the same spectra regime as SWs.

A practical detail to keep in mind is the damping or relaxation rate of the two waves. Damping is a phenomenological effect on any wave in nature. The wave is always interacting with its surroundings in free space. The condensed energy of the wave, seen as the amplitude of the wave, essentially distributes itself outward till disappears. The best analogy is tossing a rock into a pond. Where the rock lands there are large ripples in the water, but dissipate as the ripples spread across the pond eventually settling back to a calm bed of water. While damping is not our main focus, there are specific devices that benefit from damping. On the other hand, damping does normally hurt the ME coupling effects if the coupling rate is less than the damping rate. Damping is discussed by [114], [163], [182], [183], [200], [206], [211], [214] in many ways, but for this theoretical work we take an effective damping of rate of $\eta = 0.35$MHz for SAWs and $\Gamma = 1$MHz for SWs. These factors can be applied to any mathematical step when calculating the hybridized ME system.

CHAPTER THREE

THEORY: COUPLING COEFFICIENT DERIVED WITH EXAMPLES

In this chapter we cover how the coupling coefficient is derived from a method of expansion of vector modes from each wave. This expansion is substituted into the ME energy, E_{ME} (2.14) and solved for the complex amplitudes of the waves. We only consider linear terms when we use our equations of coupled waves (3.2) for quick and easy approximations to check how a system may couple. The coupling coefficient, or coupling rate, will be shown as the overlap of wave profiles as the core of coupling between two waves. Once coupling is found we perform an analysis on material parameters to find optimal conditions for ME coupling. Then the coupled wave equations can be used to plot wave coupled spectrum and see how coupling interactions occur in a system changing in time and space.

3.1 Coupling Coefficient Derived

We have two vectors in the ME energy (2.14) representing their respective system, $\boldsymbol{u}(\boldsymbol{r}, \boldsymbol{t})$ and $\boldsymbol{M}(\boldsymbol{r},t)$ as acoustic and magnetic waves. As stated earlier, we expand these vectors as a series of modes a system may contain described in [221], [222], [224] as

$$\boldsymbol{u}(\boldsymbol{r},t) = \sum_{\kappa} A_{\kappa}(t)\boldsymbol{u}_{\kappa}(\boldsymbol{r}) + c.c. \tag{3.1a}$$

$$\boldsymbol{M}(\boldsymbol{r},t) = M_s[\boldsymbol{m}_0(\boldsymbol{r}) + \sum_{\xi} S_{\xi}(t)\boldsymbol{m}_{\xi}(\boldsymbol{r}) + c.c.] \tag{3.1b}$$

For (3.1a) the particle displacement vector is expanded over κ modes with a time varying complex amplitude as $A_{\kappa}(t)$ and a spatial dependent acoustic wave profile $\boldsymbol{u}_{\kappa}(\boldsymbol{r})$. For (3.1b) the magnetization vector is set up similarly, expanded over ξ modes with $S_{\xi}(t)$ as the complex amplitude and $\boldsymbol{m}_{\xi}(\boldsymbol{r})$ as the profile of the SW. There is an added singular term in (3.1b), $\boldsymbol{m}_0(\boldsymbol{r})$, which tells us the static magnetization direction. The static magnetization, $\boldsymbol{m}_0(\boldsymbol{r})$, is spatially dependent as some systems may have multi-layers or sub-lattices with different directions. The units for (3.1b) come from the saturation magnetization constant M_s outside the brackets, telling us $\boldsymbol{m}_0(\boldsymbol{r})$ and $\boldsymbol{m}_\xi(\boldsymbol{r})$ are unit vectors. Lastly, the additional *c.c.* term in (3.1) is the complex conjugate of the previous term.

The exceptional benefits we receive with this method is developing a system solvable for the amplitudes of the waves, and that the wave profiles are found independently of any coupling from their own respective system of equations. Following [51], [61], [114] we find the SW profile $\boldsymbol{m}_\xi(\boldsymbol{r})$, and from [73]–[75], [77] the acoustic wave profile $\boldsymbol{u}_\kappa(\boldsymbol{r})$. As with all wave profiles the wavevector k, depending on its value, will produce specific modes of the amplitude and profiles of the acoustic/spin waves. Specific cases with their solutions will be discussed later.

The coupled wave system, using their amplitudes will become

$$\frac{\mathrm{d}A_\kappa}{\mathrm{d}t} = -i\omega_\kappa^{(\mathrm{AW})} A_\kappa(t) - i\frac{1}{P_\kappa}\frac{\partial E_{\mathrm{ME}}}{\partial A_\kappa^*} \tag{3.2a}$$

$$\frac{\mathrm{d}S_\xi}{\mathrm{d}t} = -i\omega_\xi^{(\mathrm{SW})} S_\xi(t) - i\frac{1}{Q_\xi}\frac{\partial E_{\mathrm{ME}}}{\partial S_\xi^*} \tag{3.2b}$$

where $\omega_\kappa^{(\mathrm{AW})}$ and $\omega_\xi^{(\mathrm{SW})}$ are the acoustic and spin wave frequencies of a particular mode. Normally with complex wave amplitudes we have the simple relation $\frac{\mathrm{d}}{\mathrm{d}t} \to -i\omega$, but waves are coupled giving the added far right terms in (3.2). The partial derivative is the amount of energy one wave gives to the other through their wave amplitudes. The Q_ξ and P_κ terms are the normalization factors for the expanded SW and acoustic wave series. They take their forms as

$$P_\kappa = 2\omega_\kappa^{(\mathrm{AW})} \int_V \rho(\boldsymbol{r})[\boldsymbol{u}_\kappa^*(\boldsymbol{r}) \cdot \boldsymbol{u}_\kappa(\boldsymbol{r})] d^3\mathbf{r}, \tag{3.3a}$$

$$Q_\xi = \frac{iM_s}{\gamma} \int_V \boldsymbol{m}_\xi^*(\boldsymbol{r}) \cdot [\boldsymbol{m}_0(\boldsymbol{r}) \times \boldsymbol{m}_\xi(\boldsymbol{r})] d^3\mathbf{r} \tag{3.3b}$$

with action units (Joules·seconds) from the combined references [51], [73], [74], [114], [116]. Returning to (2.14), the ME energy E_{ME}, we use (3.1) to rewrite (3.2) into a simpler solvable form. Expanding (2.14) with substitutions from (3.1) we get

$$E_{\mathrm{ME}} = \int_V b_{\alpha\beta\gamma\zeta} \left[\frac{\partial}{\partial r_\beta} \sum_\kappa A_\kappa(t) u_{\kappa,\alpha}(\boldsymbol{r}) + c.c. \right] \times \\ \left[m_{0,\gamma}(\boldsymbol{r}) + \sum_\xi S_\xi(t) m_{\xi,\gamma}(\boldsymbol{r}) + c.c. \right] \left[m_{0,\zeta}(\boldsymbol{r}) + \sum_\xi S_\xi(t) m_{\xi,\zeta}(\boldsymbol{r}) + c.c. \right] d^3\mathbf{r} \tag{3.4}$$

If one distributed all the components one would end up with eight-teen different terms. To reduce the number of terms let us considering expanding (3.4) using only the magnetic components. One will notice a symmetrical pattern with terms containing combined components $m_{0,\gamma}m_{0,\zeta}$, $m_{0,\gamma}m_{\xi,\zeta}$, $m_{0,\zeta}m_{\xi,\gamma}$, and $m_{\xi,\gamma}m_{\xi,\zeta}$. This includes all combinations with their complex conjugates as well. The static magnetization term $m_{0,\gamma}m_{0,\zeta}$ is apart of the static energy that can be produced from stress on a magnet already incorporated in the SW system. The many SW component terms $m_{\xi,\gamma}m_{\xi,\zeta}$ are second order in magnetization dynamics considering small non-linear interactions. These lead to parametric pumping of waves as [114], [222], [231]–[234] have described before hand. Our work only considers first order linear interactions leaving only $m_{0,\gamma}m_{\xi,\zeta}$ and $m_{0,\zeta}m_{\xi,\gamma}$ terms, with their complex conjugates included in the ME energy formula.

Eliminating the above terms in (3.4) reduces the ME energy to

$$E_{\mathrm{ME}} = \int_V b_{\alpha\beta\gamma\zeta} \left[\frac{\partial}{\partial r_\beta} \sum_\kappa A_\kappa(t) u_{\kappa,\alpha}(\boldsymbol{r}) + c.c \right] \times \\ \left[\sum_\xi S_\xi(t) \Big(m_{0,\gamma}(\boldsymbol{r}) m_{\xi,\zeta}(\boldsymbol{r}) + m_{0,\zeta}(\boldsymbol{r}) m_{\xi,\gamma}(\boldsymbol{r}) \Big) + c.c. \right] d^3\mathbf{r} \tag{3.5}$$

The symmetry of the magnetostriction tensor helps simplify the magnetic half of the coupled system. With $b_{\alpha\beta\gamma\zeta} = b_{\alpha\beta\zeta\gamma}$, the combination of added terms $m_{0,\gamma}(\boldsymbol{r})m_{\xi,\zeta}(\boldsymbol{r})$ and $m_{0,\zeta}(\boldsymbol{r})m_{\xi\gamma}(\boldsymbol{r})$ are the same. This doubling of terms gives us a two in the magnetic expansion. Rewriting (3.5) gives

$$E_{\mathrm{ME}} = 2\int_V b_{\alpha\beta\gamma\zeta}\left[\frac{\partial}{\partial r_\beta}\sum_\kappa A_\kappa(t)u_{\kappa,\alpha}(\boldsymbol{r}) + c.c\right]\times \\ \left[\sum_\xi S_\xi(t)m_{0,\gamma}(\boldsymbol{r})m_{\xi,\zeta}(\boldsymbol{r}) + c.c.\right]d^3\mathbf{r} \tag{3.6}$$

Having reduced our number of terms for ME energy, the full expansion takes the form

$$\begin{aligned} E_{\mathrm{ME}} = 2\int_V b_{\alpha\beta\gamma\zeta}\sum_{\kappa,\xi}\Bigg[&A_\kappa(t)\frac{\partial u_{\kappa,\alpha}}{\partial r_\beta}S_\xi(t)m_{0,\gamma}(\boldsymbol{r})m_{\xi,\zeta}(\boldsymbol{r}) \\ &+A_\kappa(t)\frac{\partial u_{\kappa,\alpha}}{\partial r_\beta}S^*_\xi(t)m_{0,\gamma}(\boldsymbol{r})m^*_{\xi,\zeta}(\boldsymbol{r}) \\ &+A^*_\kappa(t)\frac{\partial u^*_{\kappa,\alpha}}{\partial r_\beta}S_\xi(t)m_{0,\gamma}(\boldsymbol{r})m_{\xi,\zeta}(\boldsymbol{r}) \\ &+A^*_\kappa(t)\frac{\partial u^*_{\kappa,\alpha}}{\partial r_\beta}S^*_\xi(t)m_{0,\gamma}(\boldsymbol{r})m^*_{\xi,\zeta}(\boldsymbol{r})\Bigg]d^3\mathbf{r} \end{aligned} \tag{3.7}$$

An important part of ME interactions is the small frequency difference between spin and acoustic waves. From (3.7) there are complex wave amplitude terms as multiped factors: $A_\kappa S_\xi$, $A_\kappa S^*_\xi$, $A^*_\kappa S_\xi$, and $A^*_\kappa S^*_\xi$. Here we apply the rotating wave approximation [235], [236]. This means that we can ignore doubling frequencies with the same sign as these oscillations are too large and fast due to resonance effects. Conceptually, it is the small difference between wave frequencies that holds the evolutionary transition between waves, a.k.a. the coupling coefficient we want to study.

Dropping these doubled frequency terms, the ME energy is

$$E_{\mathrm{ME}} = 2\int_V b_{\alpha\beta\gamma\zeta}\sum_{\kappa,\xi}\left[A_\kappa(t)\frac{\partial u_{\kappa,\alpha}}{\partial r_\beta}S^*_\xi(t)m_{0,\gamma}(\boldsymbol{r})m^*_{\xi,\zeta}(\boldsymbol{r}) + c.c.\right]d^3\mathbf{r} \tag{3.8}$$

Let us rewrite the ME energy in a form where the complex wave amplitudes are the variables for the coupled system (3.2) we plan to study.

$$E_{\mathrm{ME}} = \sum_{\kappa,\xi}\left[2\int_V b_{\alpha\beta\gamma\zeta}m_{0,\gamma}(\boldsymbol{r})\frac{\partial u_{\kappa,\alpha}}{\partial r_\beta}m^*_{\xi,\zeta}(\boldsymbol{r})d^3\mathbf{r}\right]A_\kappa(t)S^*_\xi(t) + c.c. \tag{3.9}$$

Replacing the bracketed terms with a new term of constants

$$E_{\text{ME}} = \sum_{\kappa,\xi} \left[g_{\kappa,\xi} \sqrt{P_\kappa Q_\xi} \right] A_\kappa(t) S^*_\xi(t) + c.c. \tag{3.10}$$

We find the coupling rate coefficient $g_{\kappa,\xi}$ to be defined as

$$g_{\kappa,\xi} \sqrt{P_\kappa Q_\xi} = \int 2b_{\alpha\beta\gamma\zeta} m_{0,\gamma}(\boldsymbol{r}) \frac{\partial u_{\kappa,\alpha}}{\partial r_\beta} m^*_{\xi,\zeta}(\boldsymbol{r}) d^3\mathbf{r} \tag{3.11}$$

The most important dependence we can see instantly is how the coupling coefficient is defined as the overlap of spatial wave profiles. The coupling coefficient is then very dependent on the specific wavevector value k as the wave profiles $\boldsymbol{u}_\kappa$, $\boldsymbol{m}_\zeta$ as they are defined in a general sense. The coupling coefficient, better described as the coupling rate, has units in frequency (Hertz). The coupling rate $g_{\kappa,\xi}$ describes the strength of the ME interaction between acoustic wave modes with SW modes in the spectrum. This rate can be readily calculated once the profiles of both modes are known and found from their independent systems.

To complete the theory, we return to the coupled wave amplitude equations (3.2). The coupled system of wave amplitudes is rewritten with substituting (3.10) and becomes

$$\frac{\mathrm{d}A_\kappa}{\mathrm{d}t} = -i\omega_\kappa^{(\text{AW})} A_\kappa(t) - i\sum_\xi g^*_{\kappa,\xi} S_\xi(t) \tag{3.12a}$$

$$\frac{\mathrm{d}S_\xi}{\mathrm{d}t} = -i\omega_\xi^{(\text{SW})} S_\xi(t) - i\sum_\kappa g_{\kappa,\xi} A_\kappa(t) \tag{3.12b}$$

The new coupled system (3.12) are the most interesting and important equations we deal with in determining results of how well the acoustic and spin waves couple. For the simplest case where we ignore the summations, we see how effectively one acoustic wave interacts with one SW from the spectrum. Equations for acoustic wave and SW amplitudes can follow the harmonic solution $\frac{\mathrm{d}}{\mathrm{d}t} \to -i\omega$, with the addition of the ME interaction. The system (3.12) can then be solved analytically as an eigen value problem yielding the two branches of the hybrid wave spectrum as

$$\omega_k = \frac{\omega_k^{(\mathrm{AW})} + \omega_k^{(\mathrm{SW})}}{2} \pm \sqrt{\left(\frac{\omega_k^{(\mathrm{AW})} - \omega_k^{(\mathrm{SW})}}{2}\right)^2 + |g_k|^2} \tag{3.13}$$

Equation (3.13) describes a conventional anti-crossing mode with a frequency gap from the ME interaction where the two different wave dispersion relations cross at a specific wavevector value k. At the crossing point we'll have a ME gap defined as

$$\Delta\omega_{\mathrm{ME}} = 2|g_k| \tag{3.14}$$

for any crossing point between the spin and acoustic wave in the spectrum.

3.2 Coupling Coefficient with Plane Waves

As an example use of the coupling rate $g_{\kappa,\xi}$ let us consider plane wave profiles for both waves. For plane acoustic and spin waves we can find optimal conditions in which these two arbitrary waves will couple to one another. We can also find which parameters will effect our coupling rate the most between these two plane waves. As stated before we derive the acoustic and SW profiles independently before analyzing the coupled ME system. Acoustic waves follow the translation equation of motion (2.1), and SW follow Landau-Lifshitz equation (2.7).

Starting with the magnetic system, the Landau-Lifshitz equation (2.7) is dynamically intertwined as the magnetization vector $\boldsymbol{m}$ appears on both sides. We begin by linearizing this expression in the sense of small deviations for $\boldsymbol{m}$ and reduce the expansion of SW modes to a single plane SW. Our magnetic wave becomes

$$\boldsymbol{m}(\boldsymbol{r},t) = \boldsymbol{m}_0 + \boldsymbol{m}_k e^{-i\omega t + i\boldsymbol{k}\cdot\boldsymbol{r}} \tag{3.15}$$

The SW profile here $\boldsymbol{m}_k$ is dependent on the wavevector. Additional conditions required are $|\boldsymbol{m}_0|^2 = 1$ and $\boldsymbol{m}_0 \cdot \boldsymbol{m}_k = 0$, maintaining proper formalism following [114].

The system considered here will be an infinite medium of YIG. The static magnetization vector $\boldsymbol{m}_0$, the ground state of magnetization, will be oriented in the $+z$-direction. Our plane SW profile then will have components only in the xy-plane. The contributing magnetic fields will be an external field $\boldsymbol{B}_{\text{ext}}$, the dipolar field $\mu_0\boldsymbol{H}_{\text{dip}}$, and the inhomogeneous exchange field $\boldsymbol{B}_{\text{ex}}$.

The effective magnetic field $\boldsymbol{B}_{\text{eff}}$ is shown as the addition of all magnetic fields we are considering in this plane wave example.

$$\boldsymbol{B}_{\text{eff}} = B_{\text{ext}}\boldsymbol{m}_0 + \mu_0\boldsymbol{H}_{\text{dip}} + \boldsymbol{B}_{\text{ex}} \tag{3.16}$$

For simplicity the static magnetization is aligned with the external field. For the dipolar field (2.8), note it was solved symbolically and needs a proper operator to perform work on the plane SW. We use the same tricks before for $\boldsymbol{H}_{\text{dip}}$ where $\nabla \times \boldsymbol{H}_{\text{dip}} = 0$ and $\nabla \cdot \boldsymbol{H}_{\text{dip}} = -M_s \nabla \cdot \boldsymbol{m}$. Along with $\nabla = -i\boldsymbol{k}$ under the condition that the wavevector $\boldsymbol{k}$ is parallel to $\boldsymbol{B}_{\text{dip}}$, we find this expression

$$\boldsymbol{B}_{\text{dip}} = -\mu_0 M_s (\hat{\boldsymbol{k}} \otimes \hat{\boldsymbol{k}}) \cdot \boldsymbol{m} \tag{3.17}$$

The wavevector $\boldsymbol{k}$ usually should be parallel to the x-axis as with normal wave propagation. However, this wavevector is more arbitrary in the sense that the wave may propagate at an angle off of the internal static magnetic field orientation. This will be the case for the in-plane magnetostatic SW modes in our main study. This makes the unit wavevector $\hat{\boldsymbol{k}} = \sin(\theta)\hat{\mathbf{x}} + \cos(\theta)\hat{\mathbf{z}}$. The dipolar field then becomes

$$\mu_0\boldsymbol{H}_{\text{dip}} = -\mu_0 M_s \begin{pmatrix} \sin^2\theta & 0 & \sin\theta\cos\theta \\ 0 & 0 & 0 \\ \sin\theta\cos\theta & 0 & \cos^2\theta \end{pmatrix} \cdot \boldsymbol{m} \tag{3.18}$$

Now substituting (3.18) into (3.16) we have the full expression for the effective magnetic field

$$\boldsymbol{B}_{\text{eff}} = B_{\text{ext}}\boldsymbol{m}_0 - \mu_0 M_s \begin{pmatrix} \sin^2\theta & 0 & \sin\theta\cos\theta \\ 0 & 0 & 0 \\ \sin\theta\cos\theta & 0 & \cos^2\theta \end{pmatrix} \cdot \boldsymbol{m} - \mu_0 M_s \lambda_{\text{ex}}^2 \nabla^2 \boldsymbol{m} \tag{3.19}$$

Now we can begin to simplify the Landau-Lifshitz Equation (2.7) by substituting (3.15) for $\boldsymbol{m}$ and (3.19) for $\boldsymbol{B}_{\text{eff}}$. When substituting the magnetization vector (3.15) into the dipolar field (2.8) and exchange field (2.9) the static magnetization term will disappear as each field has the gradient operator applied to it initially. Only the SW term with $\boldsymbol{m}_k$ will survive, and any second order terms are discarded following [114]. When fully simplified solving for ω first, the dispersion relation of plane SWs is

$$\omega^{(\text{PSW})} = \sqrt{(\omega_{\text{B}} + \omega_{\text{M}}\lambda_{\text{ex}}^2\boldsymbol{k}^2 + \omega_{\text{M}}\sin^2\theta)(\omega_{\text{B}} + \omega_{\text{M}}\lambda_{\text{ex}}^2\boldsymbol{k}^2)} \tag{3.20}$$

where ω_{B} and ω_{M} are the same as stated in section 2.2.1. Following mathematical formalism from [114] we can also derive an analytical solution for the SW profile of the plane wave. An example for this method is shown in Appendix A.2. Our plane SW profile has the form

$$\boldsymbol{m}_k = \begin{pmatrix} -i\sigma & 1 & 0 \end{pmatrix} \tag{3.21}$$

where σ is the fraction

$$\sigma = \frac{\sqrt{\omega_B + \omega_M \lambda_{ex}^2 k^2}}{\sqrt{\omega_B + \omega_M \lambda_{ex}^2 k^2 + \omega_M \sin^2\theta}} \tag{3.22}$$

which shows elliptical behavior of the SW profile. We have everything we need to analyzing coupling for the magnetic system; SW dispersion relation and profile.

Turning our attention to acoustic waves as plane waves. This reduces our expansion of modes (3.1a) to a single wave as

$$\boldsymbol{u}(\boldsymbol{r},t) = \boldsymbol{u}_c e^{-i\omega t + i\boldsymbol{k}\cdot\boldsymbol{r}} \tag{3.23}$$

where $\boldsymbol{u}_c$ is the acoustic plane wave profile dependent on material constants. Here we instantly plug (3.23) into the translation equation of motion (2.1). The assumption we do make is taking the infinite medium of YIG our plane waves exist in as an isotropic geometry. For a complete break down of this derivation see Appendix A.1. Essentially, the translation equation of motion is simplified into an eigenvalue problem which can be written as

$$\rho\omega^2\boldsymbol{u}_c = A\boldsymbol{u}_c \tag{3.24}$$

The matrix A here for plane waves is an operator formed from the gradient of the stress tensor which contains the components of the acoustic plane wave. After proper substitution of our single acoustic plane wave into the translation equation of motion, we will end up with three different expressions opening up the brackets between matrix A and the profile vector $\boldsymbol{u}_c$. Moving everything to one side sets all expressions equal zero. Isolate the elements of the acoustic profile by factoring them out and we explicitly get

$$u_x[\rho\omega^2 - k^2(\mu\cos^2(\theta) + \sin^2(\theta)(\lambda + 2\mu))] - u_z[k^2\cos(\theta)\sin(\theta)(\lambda + \mu)] = 0 \tag{3.25a}$$

$$u_y[\rho\omega^2 - k^2\mu] = 0 \tag{3.25b}$$

$$u_z[\rho\omega^2 - k^2(\mu\sin^2(\theta) + \cos^2(\theta)(\lambda + 2\mu))] - u_x[k^2\cos(\theta)\sin(\theta)(\lambda + \mu)] = 0 \tag{3.25c}$$

where μ and λ are the Lamé constants from [73], [74], [78] defined from the physical material. The three expressions in (3.25) are written this way to because the matrix notation for A from (3.24) is too big to fit this dissertation formatting. If one solved for eigen values of matrix A, you would find the shear and longitudinal dispersion relations.

However, since our plane wave contains both of these components, the dispersion relation for the acoustic plane wave takes the form

$$\omega^{(\mathrm{PAW})} = k\sqrt{\frac{X\mu}{\rho}} \tag{3.26}$$

where X is a coupling factor between traversal and longitudinal movement. The value X can be found via the polynomial

$$X^3 - X^2(4+\varepsilon) + X(5+2\varepsilon) - \varepsilon - 2 = 0 \tag{3.27}$$

where ε is the ratio of Lamé constants λ/μ.

Returning to (3.25) rewritten in matrix notation and solving for the eigen vectors, we find a solution for how the profile $\boldsymbol{u}_c$ will behave. The full expression of the acoustic plane wave profile is

$$\boldsymbol{u}_c = \begin{pmatrix} \tau & 1 & 2\cos(\theta)\sin(\theta) \end{pmatrix} \tag{3.28}$$

where τ is another fractional expression representing

$$\tau = \frac{\lambda + 3\mu - 2(\lambda + 2\mu)\cos^2(\theta) - 2\mu\sin^2(\theta)}{\lambda + \mu} \tag{3.29}$$

We have obtained both components from the acoustic system needed to begin analyzing of ME coupling between plane acoustic and plane spin wave.

We begin by plotting the spectrum of the plane waves. Seen in Fig. 3.1, there are five plotted dispersion relations. The solid red line represent the acoustic plane wave. This line is solid unlike the rest to represent this is always the fixed case for acoustic modes being material dependent only. The other four dashed lines arbitrarily represent where the plane SW mode can appear as it propagates at an angle θ away from the static magnetization $\boldsymbol{m}_0$. We show multiple in Fig. 3.1 for a quicker analysis of all the angles in one plot.

The two parameters we concern ourselves with to optimize the ME coupling rate are the angle θ between wave propagation and static magnetic field direction and the magnitude of the external magnetic field. The magnitude of the external magnetic field is important as it affects the magnitude of the effective magnetic field, or in the main case study the internal magnetic field. Even more importantly, as described before if one were to increase the magnitude of the magnetic field this would not only change the SW spectrum, but also the crossing point where ME coupling takes place between the two different waves. Changing the magnetic field is an extremely vital parameter to consider. These ME interactions will change as the waves change their crossing point within the spectra. Our main case study will cover finding optimal conditions for not only the magnetic field, but the angle of magnetization with respect to wave propagation, the thickness of a magnetic material, and the speed of the waves.

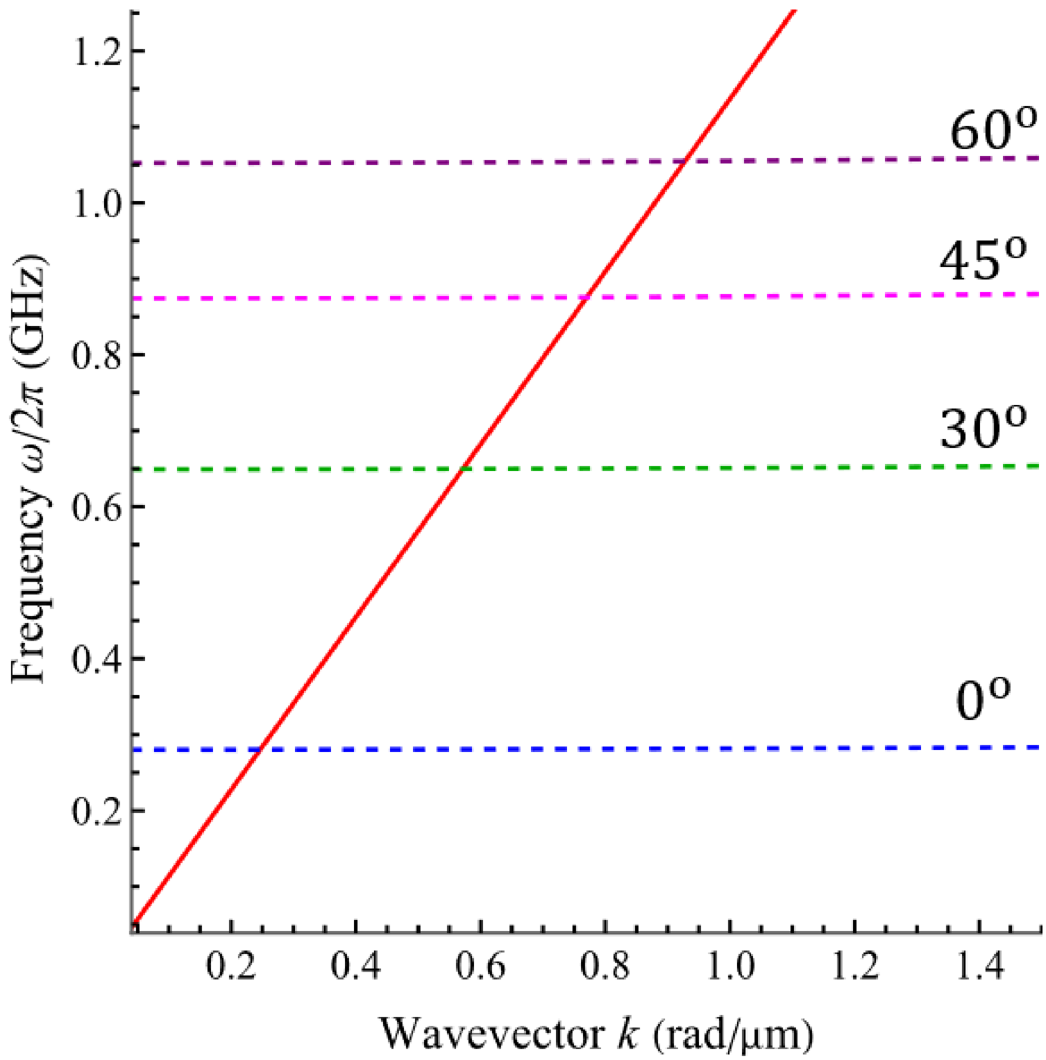

Figure 3.1: Five plane wave dispersion relations are plotted: plane SW at 0° (blue), plane SW at 30° (green), plane SW at 45° (magenta), plane SW at 60° (purple), and a plane acoustic wave (red). The acoustic wave is a solid line representing a fixed spectrum. The dashed lines for plane SW represent an arbitrary spectrum where the SW dispersion relations may be plotted using specific conditions. Parameters: $B_{\text{ext}} = 10\text{mT}$

Now we have a visual understanding of what parameters will be important for plane waves, let us derive the ME coupling rate explicitly. We have profiles to plug into the coupling rate (3.9). The plane waves reduce the partial derivative $\frac{\partial}{\partial r_\beta} \to ik_\beta$ in the integral. Taking isotropic conditions, from YIGs magnetostriction tensor b where $b_1 = 0.35\text{MJ/m}^3$ and $b_2 = 0.7\text{MJ/m}^3$. Then (3.9) can be simplified explicitly to

$$g = ib_2\sqrt{\frac{\gamma}{\omega^{(\text{PAW})}\rho|\boldsymbol{u}_c|^2 M_s\sigma}}\left[i\tau\sigma + 1 + 2i\sigma\sin^2(\theta)\right]k\cos(\theta) \tag{3.30}$$

Since neither wave profile is dependent on the xyz cartesian coordinates the volume integral for the coupling rate g cancels with the volume integrals from the normalization constants P and Q. Also, note this coupling is highly dependent on the cosine term which is why we did not choose to use 90° in the plane SW dispersion relation.

Coupling is tested between the acoustic plane wave and four modes of the plane SW at angles 0°, 30°, 45°, and 60°. Using the material parameters found from [47], [51], [73], [74], [78], [79] for YIG with a constant $B_{\text{ext}} = 10\text{mT}$ throughout, magnetization saturation 139 kA/m, density 5170 kg/m^3 and acoustic parameters (Lamé constants) λ =110.5GPa and μ =90GPa. Note the coupling rate appears in equations with the angular frequency, so we must divide by 2π to get our final answer. Coupling between the plane acoustic and plane spin wave with each angled mode, gives us

$$g_1/2\pi = 10.2 \text{ MHz} \tag{3.31a}$$

$$g_2/2\pi = 14.5 \text{ MHz} \tag{3.31b}$$

$$g_3/2\pi = 16.8 \text{ MHz} \tag{3.31c}$$

$$g_4/2\pi = 15.4 \text{ MHz} \tag{3.31d}$$

where the subscript numbers are for the θ angles 0°, 30°, 45°, and 60° respectively.

Using equations (3.31) we can substitute all the arbitrary plane SWs as modes into (3.10) and we can plot the coupled spectrum. Figure 3.2 shows the coupled spectrum of plane waves. In comparison to Fig. 3.1, we see the highlight lines corresponding back to the differently angled propagating plane waves, with exception for the acoustic wave.

These ME anti-crossing gaps do exist for each angle as predicted. This gap is the ME frequency gap $\Delta\omega_{ME}$ that is double the coupling rate. Curiously, the trend in the coupling rate had a steady increase with the angle until somewhere between 45° to 60°.

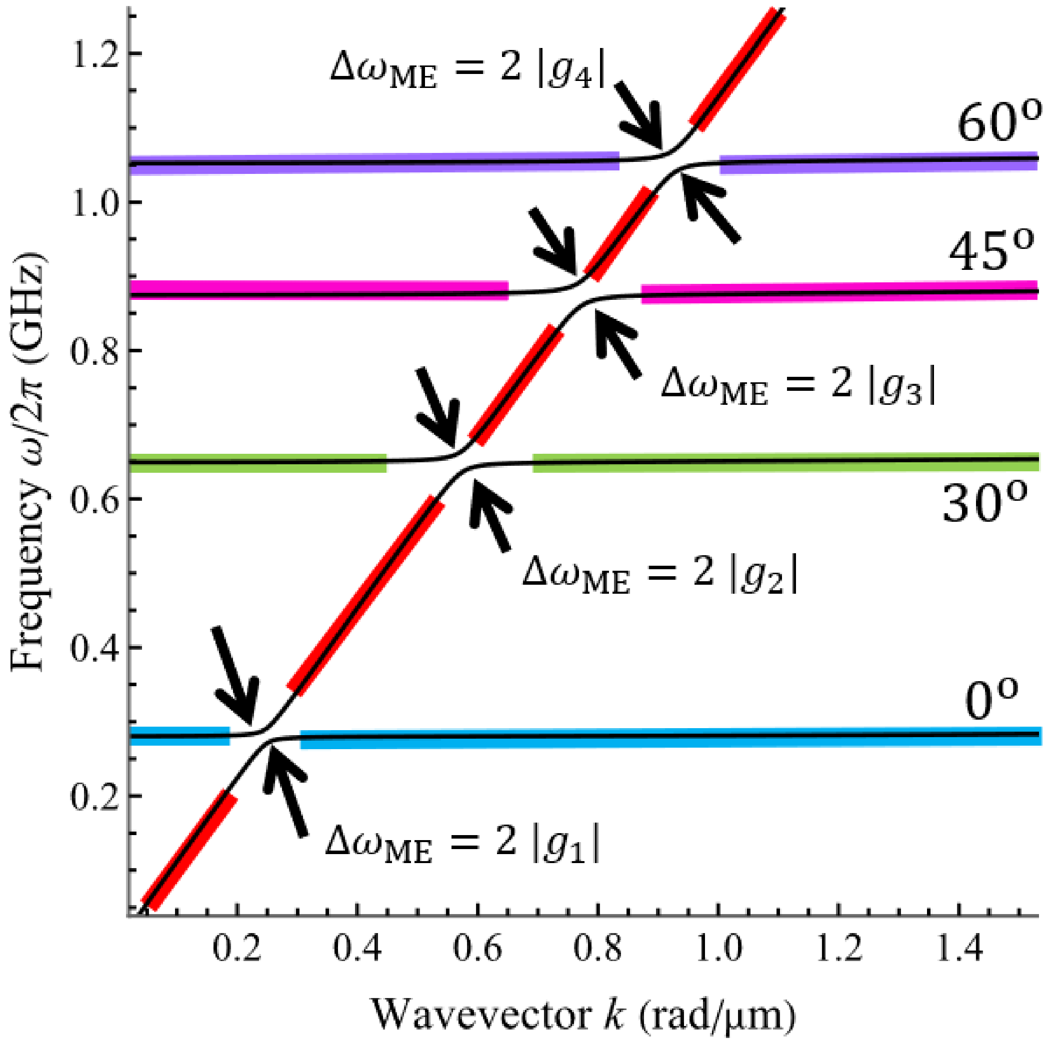

Figure 3.2: Coupled plot of plane wave dispersion relations between a single plane acoustic wave and multiple plane SWs. Highlighted lines indicate: plane SW at 0° (blue), plane SW at 30° (green), plane SW at 45° (magenta), plane SW at 60° (purple), and a plane acoustic wave (red). Anti-crossing gaps between plane waves are found in equations (3.31). Parameters: $B_{\mathrm{ext}} = 10\mathrm{mT}$

Figure 3.2 provides us a nice example of how important the magnetic field will play role for the ME coupling rate. We have an acoustic wave (red highlighted line) crossing four plane SW (highlighted blue, green, magenta, and purple) lines. As the angle increases, so does the frequency of the SW. This behavior also happens when the external magnetic field B_{ext} increases as well, which was previously pointed out. When B_{ext} is increased, all plane SW modes will rise in frequency simultaneously. The main take away here is that when the acoustic wave crosses one of these SW modes an anti-crossing gap opens up between these waves.

Fixing all parameters, and varying only the magnitude of the external magnetic field, we see the clear picture of ME coupling between plane acoustic and plane spin waves. For larger and larger magnetic fields, the ME coupling rate rises for all scenarios of plane acoustic and plane spin waves. However, for very low fields, 40mT and below, certain components seem to dominate over the others for different angles. The fractional components τ and σ play a huge role in how big coupling behaves for the lower fields. The more important fractional factor is from the SWs, because for extremely low magnetic fields

$$\sigma \approx \frac{\sqrt{\omega_M \lambda_{ex}^2 k^2}}{\sqrt{\omega_M \lambda_{ex}^2 k^2 + \omega_M \sin^2\theta}} \tag{3.32}$$

because the external magnetic field contributes to ω_B and is relatively small compared to the other natural constants. This is when the angle for σ plays a bigger role in the elliptical behavior it posses with the angle in the denominator. This also applies for τ which can value between -1 and 1 for angles 0° and 90° respectively. Only when the external magnetic field increases does it start to dominate and σ begins to approach 1. The larger angles still have a lower coupling rate thanks to the cosine term out front that decreases with larger angles. This is only countered by the $\sin^2(\theta)$ for a small sweet spot, because as some point while the 60° purple curve in Fig. 3.3 seems good, increasing the angle pass a critical angle will eventually drop the coupling rate down to 0MHz since $\cos(90°) = 0$.

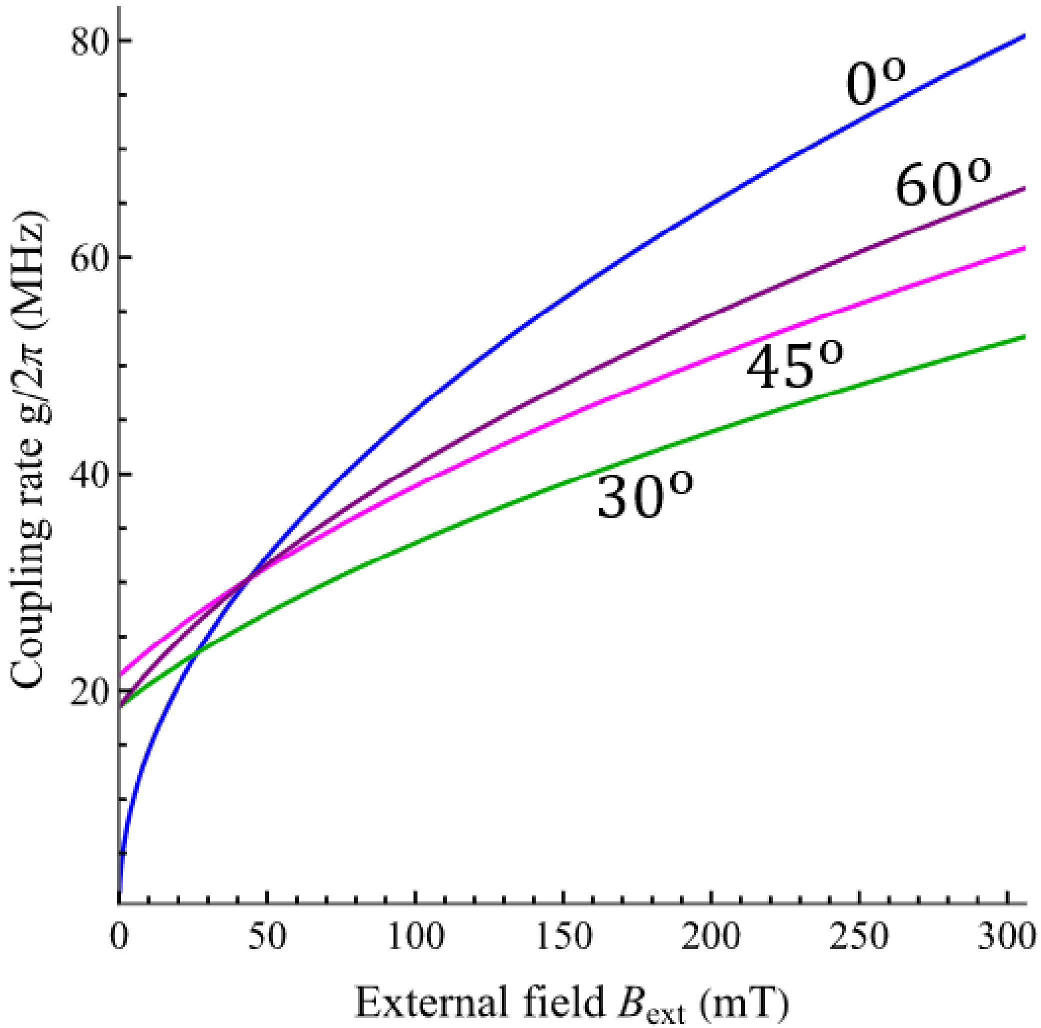

Figure 3.3: Arbitrary plane SWs are calculated with θ at 0° (blue), 30° (green), 45° (magenta), 60° (purple) and coupled to the plane acoustic wave. The coupling rate g between plane acoustic waves the four plane SWs show similar behavior for larger and larger magnetic fields. For low to no fields certain components begin to dominate dependent on the angle of plane wave propagation.

3.3 Coupling between SAWs and In-Plane Magnetized SWs

For our main research focus, we considered ME coupling between SAWs and in-plane magnetized SWs, including the SSW and BVSW. The expressions for ME coupling (3.11) and the coupled wave amplitude system (3.12) will begin to simplify as we make more theoretical assumptions. First, we only consider one acoustic mode (the SAW). Second, both the acoustic and spin wave profiles are spatially dependent only the variable z, being the depth into the bi-layer system in Fig. 3.4. Lastly, magnetization is uniformly distributed and constant within our YIG film.

Now we define our system of parameters and how they will incorporate into the the coupling rate (3.11). As described in Fig. 3.4, we have the bi-layer system of YIG/GGG where only YIG is a magnetic material. As stated before, YIG and GGG are assumed to have the same acoustic properties meaning the SAW profile appears through both layers. The SW profile, arbitrarily represented a low order resonant mode in blue, only exists in the FM film layer. This FM layer of YIG has a thickness defined as L along the z-axis. The static internal field within the YIG layer lies in the xy-plane and magnetization will be controlled via the external magnetic field $\boldsymbol{B}_{\text{ext}}$. The external magnetic field will be at an angle ϕ to the x-axis. Both the SAW and in-plane SWs will propagate along the x-axis either in the positive or negative direction depending on parameters used for case by case scenarios. The substrate GGG is the standard practice YIG is grown upon with matching lattice constants and is considered with a normal thickness of 500μm.

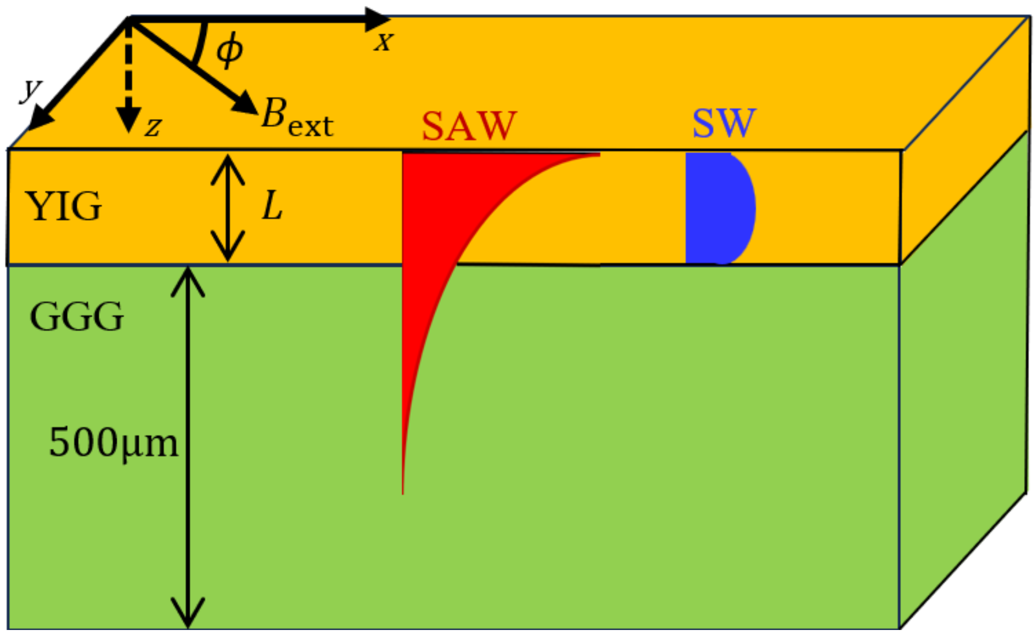

Figure 3.4: Generic visualization of system describing parameters affecting ME coupling between SAWs and magnetized in-plane SWs. The SAW profile expands through both layers of the system. The SW profile (lowest resonant mode) is blue and only exists in the magnetic layer of YIG with a thickness L in the z-direction. The external magnetic field $\boldsymbol{B}_{\text{ext}}$ is in the xy-plane at an angle ϕ to the direction of wave propagation along the x-axis. The substrate GGG is the standard practice YIG is grown upon with matching lattice constants and is considered with a normal thickness of 500µm.

From (3.11) we simplify the integral by considering the wave profiles are spatially dependent only on the depth z into the medium for an infinite plane. This changes the vectors $\boldsymbol{m}_{\xi}(\boldsymbol{r}) \to \boldsymbol{m}_{\xi}(z)e^{-i\boldsymbol{k}'\cdot\boldsymbol{r}}$ and $\boldsymbol{u}_{\kappa}(\boldsymbol{r}) \to \boldsymbol{u}(z)e^{-i\boldsymbol{k}\cdot\boldsymbol{r}}$ for both wave types. The subscript κ is removed for acoustic waves as only the SAW mode is considered any further. With static magnetization held constant, dependent only on the direction and magnitude of $\boldsymbol{B}_{\text{ext}}$ and choosing to keep all other possible variables constant (density, magnetostriction tensor, wavevector) we have chosen a system set-up that allows for easy derivation of in-plane coupling. We rewrite (3.9) into

$$g_\xi = \frac{2}{\sqrt{PQ_\xi}} \iiint b_{\alpha\beta\gamma\zeta} m_{0,\gamma} \left(\frac{\partial u_\alpha}{\partial z} + ik_\beta u_\alpha \right) m^*_{\xi,\zeta}(z) e^{i(\boldsymbol{k}'-\boldsymbol{k})\cdot\boldsymbol{r}} dxdydz \tag{3.33}$$

Our ME waves propagate within the xy-plane of the medium making $k_z = k'_z = 0$. Only the exponential has the variables xy in a form as shown in (3.33). This integral can be integrated using the property that comes with delta functions and Fourier transforms from [77]

$$\delta(x - x_0) = \frac{1}{2\pi} \int_{-\infty}^{\infty} e^{iu(x-x_0)}\, du \tag{3.34}$$

This property shows simply that the period length is 2π with a shifted phase allowing us to substitute in a δ function into our coupling rate expression. The only terms that survive are when $k_x = k'_x$, $k_y = k'_y$ equal each other. Meaning when $\boldsymbol{k} = \boldsymbol{k}'$ are the same. This mathematical property of the δ function also follows that we have found the 'period lengths' from the xy integrals. However, these 'period lengths' vanish as they cancel by the fact the normalization factors P_κ and Q_ξ from (3.3) will also have the same substitution of our vectors $\boldsymbol{u}_\kappa$ and $\boldsymbol{m}_\xi$. We can then rewrite our normalization constants as

$$P = 2\omega^{(\mathrm{SAW})} \int \rho \boldsymbol{u}^*(z) \cdot \boldsymbol{u}(z) dz, \tag{3.35a}$$

$$Q_\xi = \frac{iM_s}{\gamma} \int \boldsymbol{m}^*_\xi(z) \cdot [\boldsymbol{m}_0 \times \boldsymbol{m}_\xi(z)] dz \tag{3.35b}$$

To continue the derivation we must find the individual wave profiles. Using references [61], [114], [221] the SW vector $\boldsymbol{m}_\xi$ has two magnetization components, in and out of plane. The static magnetization vector $\boldsymbol{m}_0$ will stay in-plane and help determine which magnetostatic SW mode we are investigating. Recall Fig. 2.5a, where we see two cases with magnetization in-plane. Our static magnetization and SW vector take the form as

$$\boldsymbol{m}_0 = \begin{pmatrix} \cos\phi & \sin\phi & 0 \end{pmatrix} \tag{3.36a}$$

$$\boldsymbol{m}_{\xi}(z) = \begin{pmatrix} m_{\xi}^{\mathrm{IP}}(z)\sin\phi & m_{\xi}^{\mathrm{IP}}(z)\cos\phi & m_{\xi}^{\mathrm{OP}}(z) \end{pmatrix} \tag{3.36b}$$

where m_{ξ}^{IP} is the in-plane component and m_{ξ}^{OP} is out-of-plane component. The calculation of these SW profile components, m_{ξ}^{IP} and m_{ξ}^{OP}, is done numerically from the theory of dipole-exchange SWs in FM films [61]. This method involves linearization of (2.7) near the equilibrium state and expansion of the transversal SW profile $\boldsymbol{m}_{\xi}(z)$ as a Fourier series. Following [61], the Landau-Lifshitz equation is expanded into an infinite series of algebraic equations, which can be numerically solved using a finite number of expansion terms. For the numerical calculations used of various thicknesses for YIG in the proceeding chapters, note we use at most 50 terms when solving the infinite series of the the Landau-Lifshitz equation. The reason for this is so the in-plane magnetostatic modes, BVSW and SSW, are accurately calculated on how their wave profiles and spectrum behave when interacting with the higher order SW resonant modes, see Fig. 2.6. Further details on this numerical procedure are seen in [237] and its supplementary work on talking points about the convergence properties of this method. The numerical solution of all the SWs modes is an eigen value problem which provides SW frequencies $\omega_{\xi}^{(\mathrm{SW})}$ and transversal profiles $\boldsymbol{m}_{\xi}(z)$, used to analyze SAW-SW phenomena.

The calculation of the SAW profile, $\boldsymbol{u}(z)$, can be done using existing theories for pure elasticity [73], [74], [77] The SAW profile is derived in extensive detail in Appendix A.1. Found from the homogeneous translation equation of motion (2.1) using the boundary conditions $T \cdot \hat{\mathbf{n}} = 0$ at $z = 0$ and $\boldsymbol{u}(z) \to 0$ as $z \to \infty$ with assumed plane wave dependence $\propto e^{i\boldsymbol{k}\cdot\boldsymbol{r}}$ in the film plane [73], [74], [77]. For isotropic mediums, the stiffness tensor has the Lamé constants, $\lambda = c_{iijj}$ and $\mu = c_{ijij} = c_{ijji}$ as its two independent constants [73], [74], [78]. The resulting SAW profile is described by

$$\boldsymbol{u}(z)=\begin{pmatrix} \frac{1-Y\varepsilon/2}{k\sqrt{1-Y\varepsilon}}e^{-zk\sqrt{1-Y\varepsilon}}-\frac{1}{k\sqrt{1-Y}}e^{-zk\sqrt{1-Y}} \\ 0 \\ -\frac{i}{k}\left(\frac{1-Y\varepsilon/2}{1-Y\varepsilon}e^{-zk\sqrt{1-Y\varepsilon}}-e^{-zk\sqrt{1-Y}}\right) \end{pmatrix} \tag{3.37}$$

where Y is the solution of the algebraic equation

$$Y^3-8\varepsilon Y^2+16\varepsilon^2 Y(3/2-\varepsilon)-16\varepsilon^3(1-\varepsilon)=0 \tag{3.38}$$

and $\varepsilon=\mu/(\lambda+2\mu)$ is a ratio of shear and longitudinal factors. The elastic eigenvalue problem also defines the dispersion relation for pure SAW, $\omega^{(\mathrm{SAW})}=v^{(\mathrm{SAW})}k$, where $v^{(\mathrm{SAW})}=\sqrt{Y(\lambda+2\mu)/\rho}$ is the SAW velocity. The solution of our SAW profile describes the so-called Rayleigh SAW [68], [73], [74] we discussed earlier.

With these completed expressions for the both wave profiles, and using the YIG constants b_1, b_2 for the magnetostriction tensor b, we again rewrite the ME coupling rate as

$$g_\xi=\frac{b_1}{\sqrt{PQ_\xi}}\int_0^L\left[ik_xu_xm_\xi^{\mathrm{IP}*}\sin(2\phi)+4\left(\frac{\partial u_x}{\partial z}+ik_xu_z\right)m_\xi^{\mathrm{OP}*}\cos(\phi)\right]dz, \tag{3.39}$$

and equations for coupled mode amplitudes (3.12) as

$$\frac{\mathrm{d}A}{\mathrm{d}t}=-i\omega^{(\mathrm{SAW})}A(t)-i\sum_\xi g_\xi^* S_\xi(t) \tag{3.40a}$$

$$\frac{\mathrm{d}S_\xi}{\mathrm{d}t}=-i\omega_\xi^{(\mathrm{SW})}S_\xi(t)-ig_\xi A(t) \tag{3.40b}$$

These equations (3.39) and (3.40) we will solve numerically due to our method for the SW profile, but are still good general expressions one can solve analytically for simpler interactions. They are used for analysis of the ME coupling rate dependencies and for the coupled hybridized spectrum.

CHAPTER FOUR

SURFACE ACOUSTIC WAVES AND SURFACE SPIN WAVES

In this chapter, we begin discussing results of ME coupling between SAW and in-plane SWs. The first in-plane SW we consider is the SSW as both the acoustic and spin wave are localized at the surface naturally. Our results will discuss how ME from (3.39) is affected by the three main parameters that directly relate to the SSW: YIG thickness L, magnetization angle to wave propagation ϕ, and magnitude of the external magnetic field B_{ext}. Optimal conditions can then be found for ME coupling in current YIG/GGG devices. One big distinction here for SSWs is that they can appear at both the top free surface of YIG and at the boundary transitioning from YIG to GGG as this acts as a "surface" for the magnetic layer for SWs. Referring to Fig. 4.1, keeping the magnetization angle and magnitude constant, if the SSW propagates right ($+x$ direction) it will appear at the top surface. If the SSW propagates left ($-x$ direction) it will appear at the "bottom" surface. This leads into a major topic of non-reciprocity of wave propagation some technological advancements rely on.

As discussed in section 3.2, our system reference is the same with YIG/GGG films that lye in the xy plane as shown schematically in Fig. 4.1. While the excitation of a wave is important for any working device, it is not discussed here as our focus is only to find optimal conditions between two specific waves. This will be the consideration for this chapter and the next for ME coupling between a SAW and the two SWs; SSW and BVSW.

Another important note for the simulations shown from here forth are solved via SW system from [61]. We used 15 terms at minimum to ensure convergence with an estimated relative error of $\sim 10^{-3}$ and a maximum of 50 terms for the thickest YIG films considered to ensure that the desired magnetostatic SW mode is consistent within the SW spectrum of higher order SW resonant modes. The numerical solution of the SW eigenvalue problem provides SW frequencies $\omega_{\xi}^{(\mathrm{SW})}$ and transversal profiles $\boldsymbol{m}_{\xi}(z)$, used below to analyze the ME phenomena.

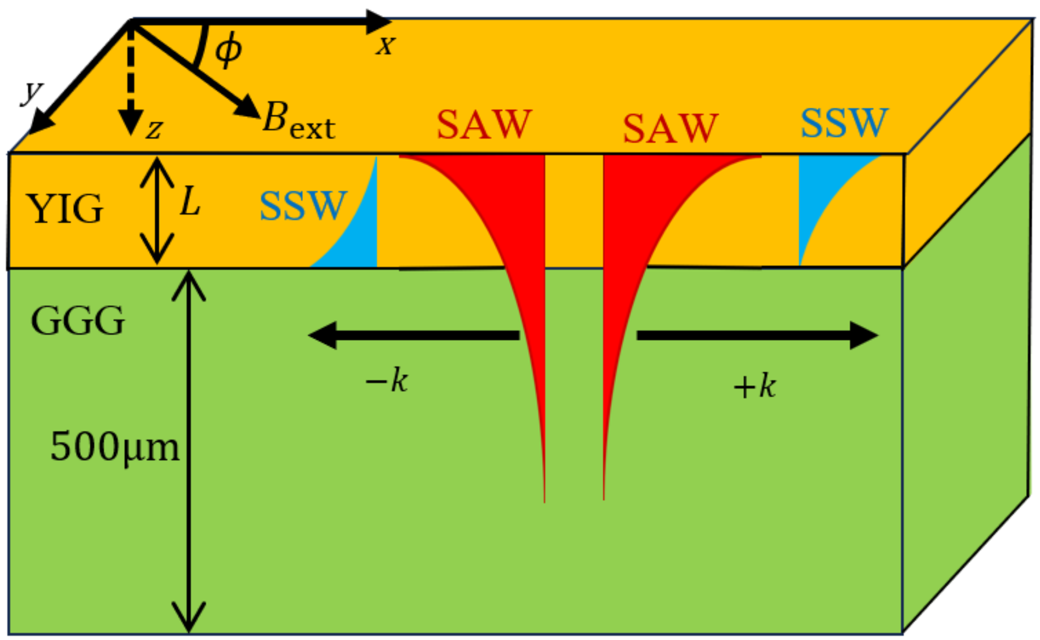

Figure 4.1: Geometry of the system under study: magnetic YIG/nonmagnetic GGG bi-layer magnetized at an angle ϕ with respect to the wave propagation direction. Red (blue) shaded areas show schematically profiles of SAW (SSW) propagating in $\pm x$ directions

We begin by analyzing the spectrum of these two waves, shown in Fig. 4.2, and see the crossing point of the SAW-SSW dispersion relations at a specific wavevector value $|k_0|$. As stated before in the SSW case we consider waves propagating in the $\pm x$ directions. This is why in Fig. 4.2 we show a mirrored spectrum indicating waves with a negative wavevector $(-k)$ propagating to the left. Direction of SSW propagation gives the property of non-reciprocity to the SSW profiles (shown via blue profiles in Fig. 4.1). This will result in non-reciprocal ME coupling with SAWs, which are only localized near the top free surface of the bi-layer system regardless of the direction of propagation (shown via red profiles in Fig. 4.1).

Figure 4.2 shows a coupled ME hybrid wave spectrum calculated using (3.40) with parameters $\phi = 45^\circ$, $B_{\text{ext}} = 10\text{mT}$, and $L = 1\mu\text{m}$. These parameters are chosen from later talking points. The highlighted lines in Fig. 4.2 show the dispersion relations of the uncoupled SAW (red) and SSW (blue) modes. The black lines in Fig. 4.2 represent the higher-order SW resonant modes. This higher order SW resonant modes do couple to the SAW but are significantly smaller than the ME coupling between SAWs-SSWs and can be ignored. In addition these higher order SW resonant modes have low to no propagation velocity and will be shown later to limit our ME interaction between SAWs and SSWs. These resonant SWs modes are also affected by the three main parameters.

While the frequency spectrum in Fig. 4.2 seems completely reflective for wave propagation direction, there is the exceptional difference in the ME coupling rate. We can see from Fig. 4.2, the SAW and SSW branches intersect at $k_0 \approx 3.5\text{rad}/\mu\text{m}$, where a well-pronounced anti-crossing region with the gap $\Delta\omega$ (defined from (3.14)) is shown in the smaller dashed circles. For waves propagating to the right ($+x$ direction), where the SSW is localized at the free surface, the ME coupling rate produces a $\Delta\omega_+/2\pi = 61\text{MHz}$ gap (enhanced by right circle in Fig. 4.2). For waves propagating to the left ($-x$ direction), where the SSW is localized at the YIG/GGG interface, the ME coupling rate produces a $\Delta\omega_-/2\pi = 26\text{MHz}$ gap (enhanced by left circle in Fig. 4.2). The gap $\Delta\omega_\pm$ substantially exceeds both SAW and SW damping rates, meaning SAW-SSW coupling can be easily observed experimentally. This system shows nonreciprocal behavior arising from the SSW properties. Non-reciprocity is measured by the ratio of $\Delta\omega_+/\Delta\omega_-$. For the case of Fig. 4.2 the non-reciprocity ratio is theoretically 2.33.

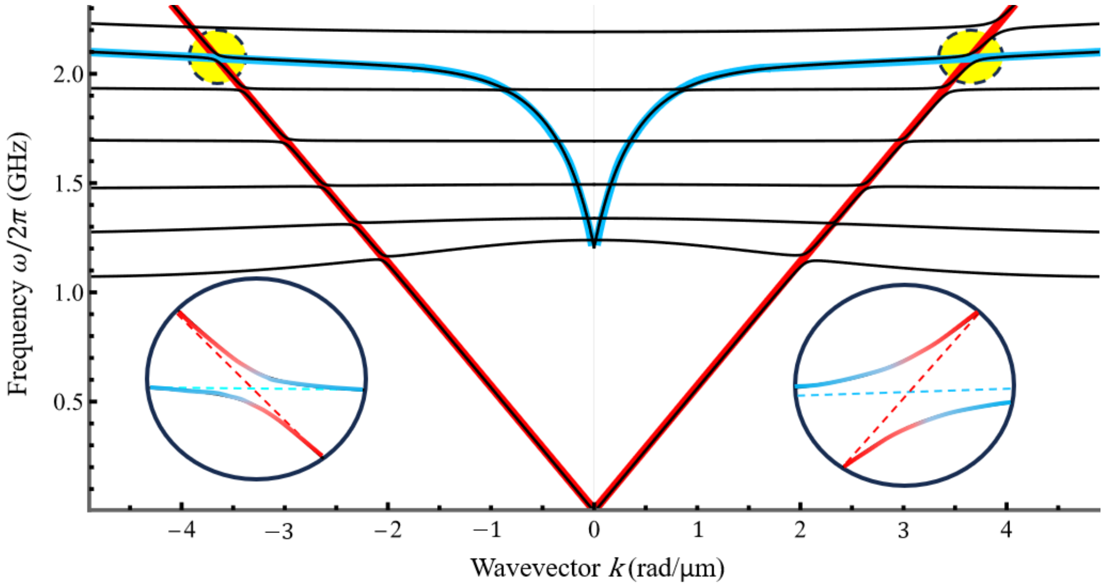

Figure 4.2: Spectrum of the hybrid ME waves in YIG/GGG bi-layer. Highlighted branches correspond to SAW (red) and SSW (blue) waves. The left side corresponds to propagation to the left, and the right side has waves propagating to the right. The circled frames show the size of ME coupling of SAWs to nonreciprocal SSWs. Parameters: YIG film thickness $L = 1$μm, internal bias field 10mT applied in-plane at an angle of 45° to the direction of wave propagation.

When considering propagating wave directions, non-reciprocity in our ME coupled system is shown to be dependent on the coupling rate g_ξ. From the ME coupling rate (3.39) the first parameter analyzed is the angle ϕ in the sine and cosine terms. Referring to Fig. 2.5a, SSW exists in the geometry that magnetization is perpendicular to wave propagation. While both SAWs and SSWs can exist in this system the two waves will never couple using $\phi = 90°$ in (3.39). The parameter ϕ's optimal angle is found with a constant magnetic field and thickness. Referring to Fig. 4.3, with a constant internal magnetic field of 10mT and YIG film thickness 1μm, one can see for various magnetization directions, 45° gives the largest ME coupling rate. From these numerical calculations of (3.39) in Fig. 4.3, the magnetization angle at $\phi = 45°$ should always give the largest ME coupling stemming from the dominant in-plane term with $\sin(2\phi)$. A purely numerical calculation at 30° was done further for confirmation of our theoretical understandings.

Another feature, from Fig. 4.3 is the arch behavior of the ME coupling rate. This comes from the SSW mode crossing one of the SW resonant modes. As stated before the spectrum of the SSW and higher order SW resonant modes change with the magnitude of the magnetic field. The SSW increases faster with the increasing magnetic field than the SW resonant modes. The SSW will eventually cross one of these resonant modes and ME coupling between SAW-SSW becomes mixed with an extra SW mode. Not only does this interaction reduce the coupling rate, but one will not know which SW property or effect will be measured or shared with the SAW.

This leads to the limiting factor from the magnitude of the magnetic field B_{ext}. As one can see from other angles in Fig. 4.3, the SSW can exist in a low enough bias magnetic field at a relatively high angle away from SSW geometry. If the external magnetic field B_{ext} is increased the asymmetry of the SSW profile would be lost to the resonant mode. Caution is only mentioned here for those who wish use 45° not to increase your field to the point of destroying your SSW. All-in-all, 45° will be optimum for study of SAW-SSW interaction since the ME interaction is already strong enough over damping factors. This carries over as well for the magnitude of B_{ext} at low fields, such as 10mT, where there exists a well-pronounced surface wave in the SW spectrum.

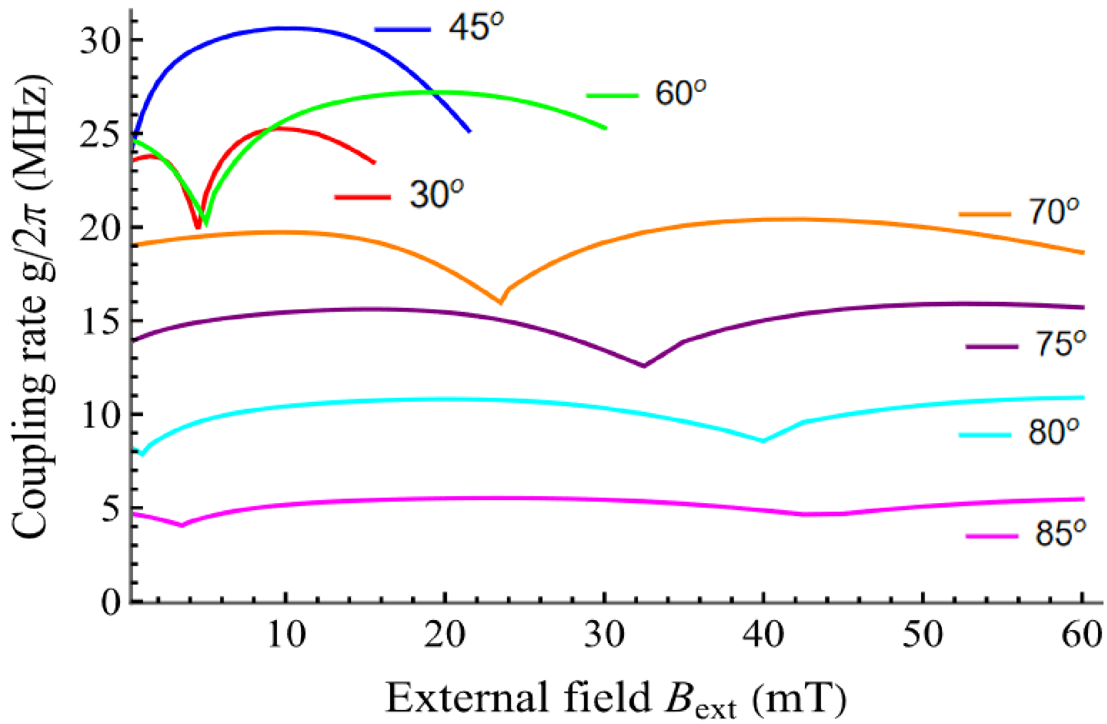

Figure 4.3: SAW-SSW coupling rate as a function of internal magnetic field for various angles. The arch structure comes from the SSW mode jumping from one resonant mode branch to another as magnetic field changes. Parameters: YIG film thickness 1μm.

Numerically calculating the ME coupling rate of SAW-SSW between these blue and red dispersion relations in Fig. 4.2 with wavevector k as our variable for a fixed YIG thickness and magnetic field. The blue curve in Fig. 4.4 is ME coupling between SAW-SSW in the $+x$ direction. The red curve is ME coupling between SAW-SSW in the $-x$ direction. As the ME coupling rate uses the profiles of the waves, the wavevector k sets the profiles. The boundary k_B between this reciprocal and nonreciprocal region of k's occurs approximately at $k_B = \pi/2L$ (solid vertical line in Fig. 4.4). At this point nonreciprocal non-uniformity of SSW profile becomes important. As one can see to the left of this k_B boundary line, the coupling rate of SAW to the differently profiled SSW is reciprocal. Not until we increase k to the right side of k_B does the profile of the SAW become more localized within the YIG film, and the coupling rate gives nonreciprocal behavior. The reasoning being SAW becomes more and more localized at the free surface. Conceptually, the whole SAW profile would be encased in the YIG film. The SAW won't touch the YIG/GGG interface at large wavevectors where the $-x$ propagating SSW exists. Note the importance of the profiles of these waves on the ME coupling rate g_ξ. This comparison of k_B and k_0 should serve as a quick check to see if your crossing point of the two waves will give reciprocal or nonreciprocal ME behavior.

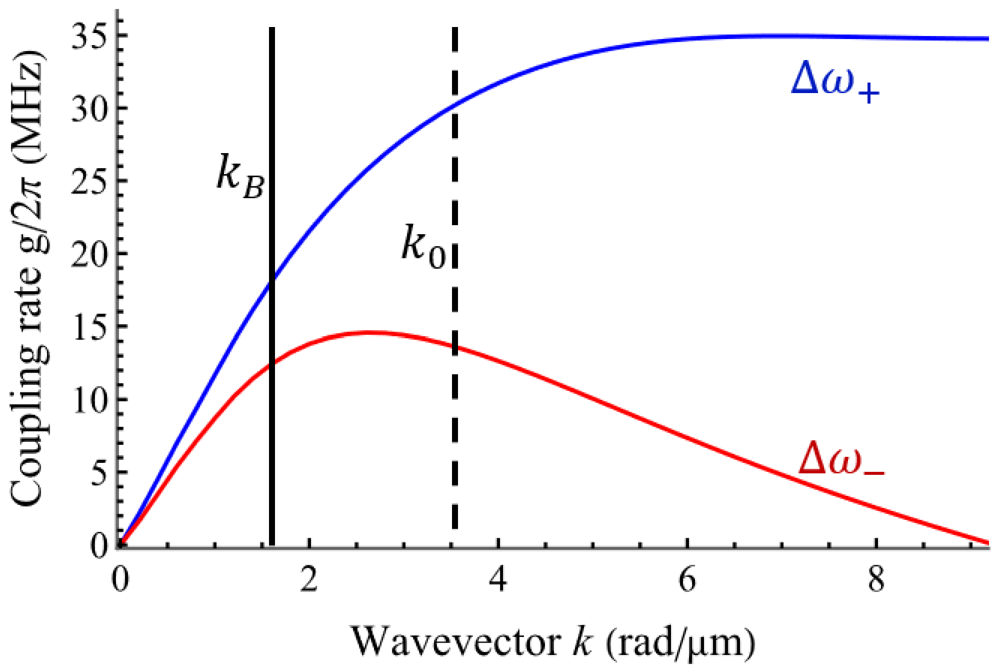

Figure 4.4: Numerically calculated coupling rate at various wavevectors k between the SAW and SSW dispersion relations. The blue (red) line is coupling between SAW and SSW localized at the free surface (YIG/GGG interface). The dashed line k_0 is where the acoustic and spin wave dispersion relations actually cross. The solid black line k_B is boundary between reciprocal and nonreciprocal regions of ME coupling between SAWs and SSWs. Parameters: YIG film thickness 1μm, internal magnetic field 10mT, magnetization angle 45°.

Back to Fig. 4.2, the SAW and SSW branches cross at a "plateau" region in the SW spectrum. This happens for all typical experimental conditions and allows one to easily estimate the position of the crossing point k_0. This "plateau" frequency can be found from the approximated SSW dispersion relation (2.10) at low magnetic fields and a relatively thick magnetic film as $\omega^{(\text{SSW-plateau})} = (\omega_M/2)\sin(\phi)$. The SAW dispersion relation $\omega^{(\text{SAW})}$ can easily be set equal to $\omega^{(\text{SSW-plateau})}$ to solve for a minimum film thickness. Thus, observation of nonreciprocal ME interaction requires use of YIG films with thickness at least

$$L_{min} = \frac{\pi}{2k_0} = \frac{\pi v^{(\text{SAW})}}{\omega_M \sin(\phi)} \tag{4.1}$$

For YIG material magnetized at $\phi = 45^\circ$ this gives $\omega_0/2\pi \approx 2\text{GHz}$ as the same in Fig. 4.2. The ME wavevector k_0 at the crossing point can then be found from the SAW dispersion relation as $k_0 = \omega_0/v^{(\text{SAW})} \approx 3.5$ rad/μm, which comes to a wavelength of approximately 2μm. These are relatively short waves, but not impossible to excite. At a fixed wavevector k, this ratio is virtually independent of the magnetization angle and bias field, but strongly depends on the YIG film thickness L. This is illustrated by Fig. 4.5.

As one can see from Fig. 4.5, the ME gaps for oppositely propagating waves $\Delta\omega_+ \approx \Delta\omega_-$ are close in value. The hybrid ME waves stay almost reciprocal for YIG thicknesses below 0.5μm. For such thin YIG films, the SSW has approximately a uniform profile across the film. Also, this thickness is smaller than the SAW localization depth, and only a small fraction of the SAW profile interacts with SSW, giving the small values of the ME gap. With the increase of YIG thickness, the coupling rate for SSWs localized near the free YIG surface reaches a max value, while the coupling rate for the opposite propagation direction decreases. This decrease is explained by localization of SAW and SSW at the opposite ends of the YIG film (compare figures 4.1, 4.4) and gradual decreases the overlap of the wave profiles. As one can see the thicker films support a larger non-reciprocity ratio.

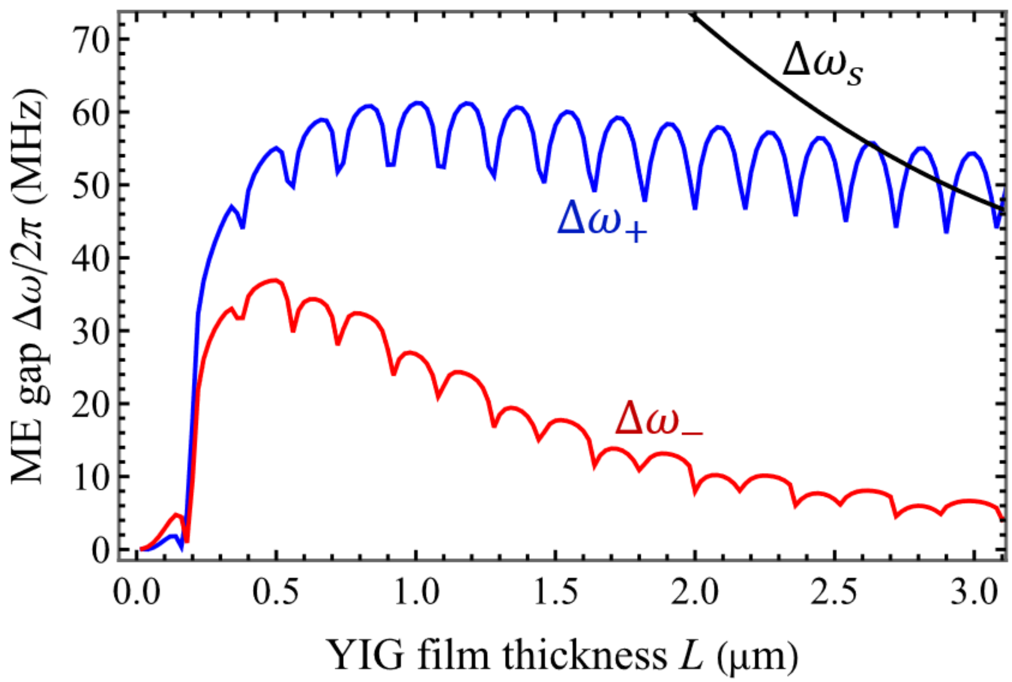

Figure 4.5: ME gap $\Delta\omega$ for SSW propagating in $+x$ ($\Delta\omega_+$, blue line) and $-x$ ($\Delta\omega_-$, red line) directions as a function of YIG thickness L. Solid black line shows the exchange splitting between SW modes $\Delta\omega_s$. Parameters: Internal magnetic field 10mT applied in-plane at an angle of 45° to the $+x$ axis

The periodic structure of humps in Fig. 4.5 arises from hybridization of SSW with higher-order SW resonant modes. As the YIG thickness increases, the frequency gaps between the higher order SW resonant modes is less and less. The SSW will stay fixed at the "plateau" frequency as thickness of the YIG film only affects the curve of the SSW dispersion relation, see Eq. (2.10) and Fig. 2.6. Thus, when the YIG film increases, the SSW will cross with a higher order SW resonant mode complicating the point of ME coupling between SAW and SSW modes. At this point, the SSW loses its well-pronounced surface characteristics and the ME coupling rate dips. This is the same effect as described in Fig. 4.3 when three modes mix at a single point. For changes in YIG thickness as small as ($\sim$0.1μm) may lead to significant variations of the ME gap. These presence of higher-order SW modes imposes another restriction on the thickness of YIG film. Namely, when the exchange splitting (frequency gap) between these resonant modes $\Delta\omega_s \approx \pi\omega_M\lambda_{ex}/L$ (shown by black curve in Fig. 4.5), becomes smaller than the ME gap $\Delta\omega_\pm$, several SW resonant modes fall within the ME gap. This leads to modification of the spectrum of the hybrid ME waves.

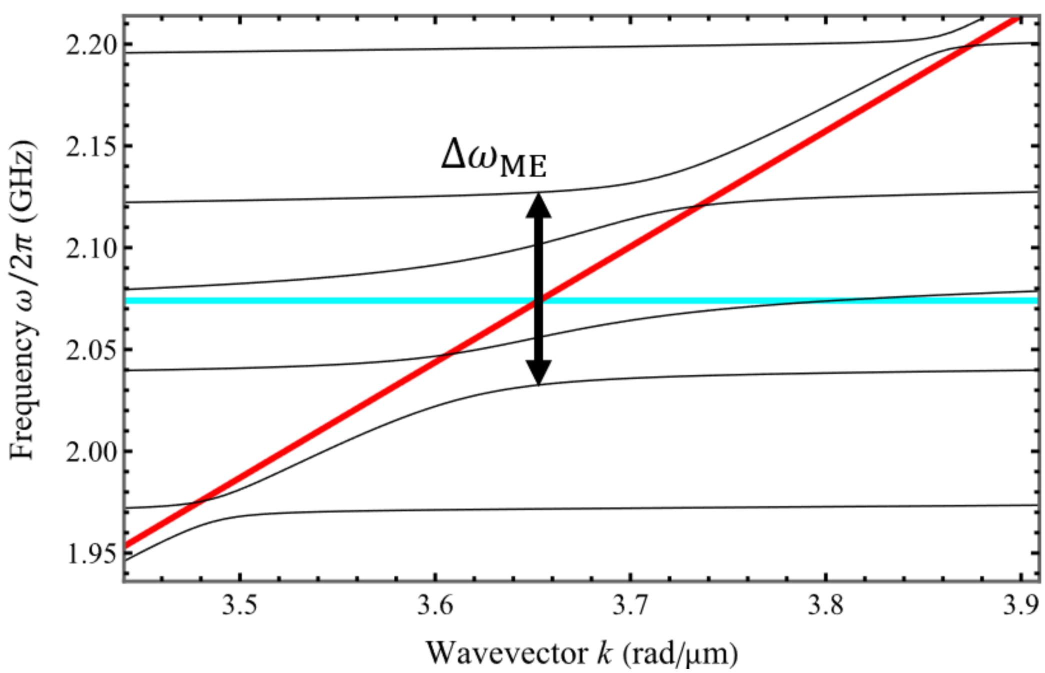

Figure 4.6: Spectrum of hybrid ME waves for thick YIG film $L = 3.7$μm (black). Highlighted red line shows the SAW dispersion relation, while blue line shows the approximate SSW dispersion relation. The ME anti-crossing gap is not well defined as SAW-SSW coupling is mixed with SAW and resonant SW modes. The ME gap, $\Delta\omega_{\mathrm{ME}} = 0.052$GHz, is larger than the frequency gap between resonant SW modes, $\Delta\omega_S = 42$MHz. Parameters: Bias field 10mT, magnetization angle 45° with respect to $+x$ axis

Figure 4.6 illustrates the importance of precise selection of YIG film thickness for observation and analysis of isolated SAW-SSW interactions. For YIG thickness $L = 3.7\mu m$ with $B_{ext} = 10mT$ at $\phi = 45^{\circ}$, this scenario does not have a simple "anti-crossing" shape anymore as observation and practical use of nonreciprocal SAW-SSW coupling. The ME gap $\Delta\omega_{ME}/2\pi = 52MHz$ is greater than the exchange splitting gap $\Delta\omega_{S}/2\pi = 42MHz$. This verifies our reasoning, but add evidence can be seen by looking at the very top and bottom ME gap. These anti-crossing gaps are for SAW and SW resonant modes coupling that have normal anti-crossing gaps as small as 8MHz. When compared to the neighboring SW resonant modes next to the SSW these ME gaps are larger at most 26MHz. The ME gaps between SAW-SSW and SAW-SW are confirmed to overlap for a wider range of mixed ME coupling. This wider range is indicated by double arrow shown in Fig. 4.6

The presence of higher-order resonant SW modes imposes an upper limit on the YIG film thickness for clear observation of SAW-SSW interaction:

$$L_{max} = \frac{\pi\lambda_{ex}}{2\Delta\omega_{\pm}} \tag{4.2}$$

As one can see from Fig. 4.5, this happens at YIG film thicknesses above 2.5μm. Thus, the best YIG thickness to observe non-reciprocal SAW-SSW coupling is from 1μm to 2μm.

These optimal conditions for SAW-SSW coupling give the ideal nonreciprocal behavior one would want in any device with a low magnetized YIG film at 45° of thickness between 1μm to 2μm.

Depending on ones set-up, some limitations may be subverted, or enhanced. Choosing a higher angle allows for lower ME coupling which could sneak under the exchange splitting gap (black curve) in Fig. 4.5. Choosing a higher angle also gives a higher range of magnetic field strengths to consider.

Be careful for practical devices considering damping factors. For both acoustic and spin waves, the damping rate should always be smaller than the ME coupling rate to see any effects. The optimal case to view damping is taken with the same parameters used to plot Fig. 4.2. Adding the damping terms η and Γ for SAWs and SSWs, respectively, we are able to view how the damping rate is affected in this ME coupled system. For a simple picture, we will calculate how the SAW damping rate is affected when coupled to the SSW.

Figure 4.7 shows three damping rates for the SAW. The black dashed line is the SAW effective damping rate η =0.35MHz without any interactions. The red curve is SAW damping for when both the SAW-SSW propagate together along the free surface of the YIG/GGG system. The darker red curve is SAW damping for when the SAW-SSW have mismatching profiles propagating in the opposite direction when the SSW appears at the YIG/GGG interface. The peaks of the curves happen at the exact frequency, $\omega/2\pi = 2.07$GHz, where the two dispersion relations cross for both directions of propagation. The wider red curve says ME coupling is larger in this case when the surface waves have matching profiles.

One will notice in Fig. 4.7 that damping is greater for a wave when coupling is greater. The non-reciprocal behavior of SAW-SSW is shown here in the form of the damping rates and their approximate lifetimes. Taking the ratio of the damping rates between wave propagation directions we can find the largest non-reciprocal behavior of 1.9. This value of non-reciprocity happens at frequencies 2.04GHz and 2.1GHz due to the symmetry of the SAW damping rate curves. Essentially, for an isolator or filter, you need to tune your magnetic field to have the anti-crossing gap just above or below your excited waves frequency. This way when two waves, in oppositely propagating directions, will have different lifetimes in reference to our non-reciprocal damping ratio of 1.9. One wave will dissipate twice as fast compared to the opposite propagating wave.

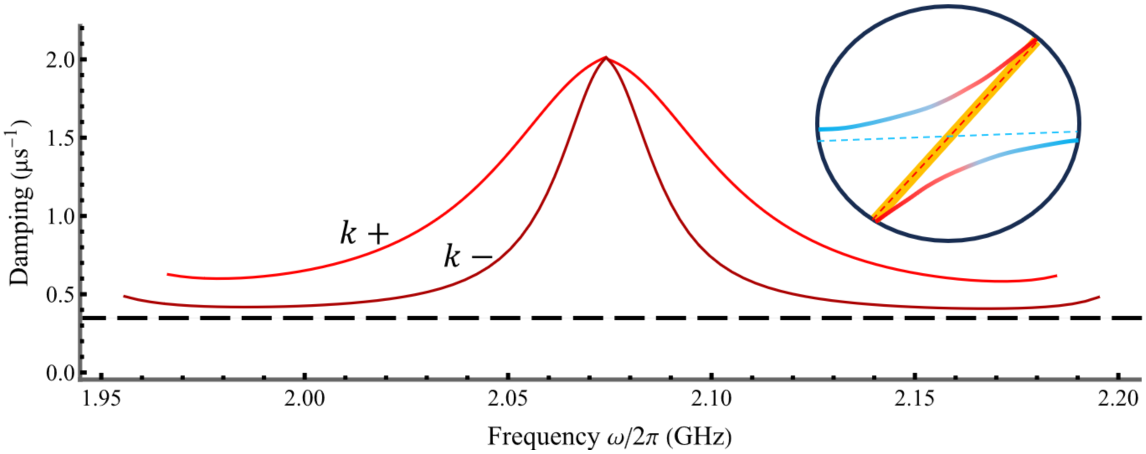

Figure 4.7: Red (darker red) curve is hybridized damping of SAW with SSW in $+k$ ($-k$) direction. Black dashed line represents SAW damping in YIG. Circle top right is ME anti-crossing point of SAW-SSW. Normal SAW spectra is highlighted to indicate the shown damping in the plot is from the SAW at the ME anti-crossing point. Parameters: Bias field 10mT, magnetization angle 45° with respect to $+x$ axis, $L = 1\mu$m, SAW effective damping 0.35MHz, SW effective damping 1MHz.

CHAPTER FIVE

SURFACE ACOUSTIC WAVES AND BACKWARD VOLUME SPIN WAVES

In this chapter, we analyze ME coupling between BVSWs, the second in-plane magnetized SW, with SAWs. This geometry is simple considering wave propagation and magnetization are parallel to one another referring to Fig. 2.5a. A uniformly in-plane magnetized film has controlled via external magnetic field B_{ext} applied parallel to the wave propagation direction along the x-axis. The same reference system is used, a YIG/GGG bi-layer lying in the xy-plane and having in-plane magnetization as shown schematically in Fig. 5.1. The difference in this case here is the direction of propagation between the two waves that will be important for this case and in the next chapter. We add a piezoelectric layer with a built on IDT to help indicate the direction of the SAW to the right $+x$ direction. The BVSW direction of propagation, as the name suggests, will propagate backwards compared to the forward propagating SAW. Important to note and will be discussed, is the BVSW will propagate opposite to SAWs, as shown in Fig. 5.1, but only when the wavevector k is relatively small in the rad/μm dipole region. Further details for this are shown from figures 5.3, 5.4, 5.5.

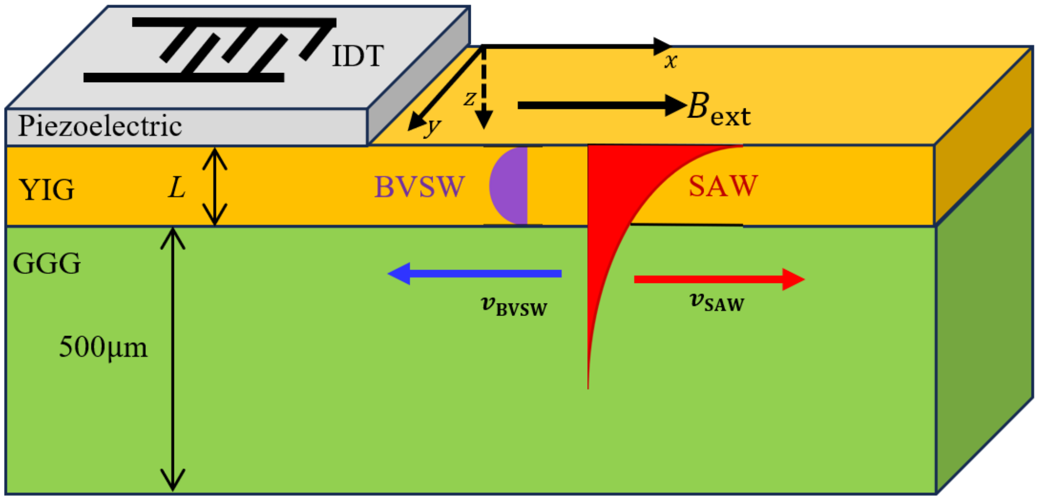

Figure 5.1: Geometry of the system under study: magnetic (YIG)/nonmagnetic (GGG) bi-layer magnetized in the x direction parallel to wave propagation direction. Red (purple) shaded areas show schematically profiles of SAW (BVSW) propagating to the right (left).

Starting from the ME coupling rate g_ξ, magnetization and wave propagation are parallel in this geometry giving $\phi = 0°$. We rewrite (3.39) with this applied angle

$$g_\xi = \frac{4b_1}{\sqrt{PQ_\xi}} \int_0^L \left(\frac{\partial u_x}{\partial z} + ik_x u_z \right) m_\xi^{\text{OP}*} dz \tag{5.1}$$

The out-of-plane component $m_\xi^{\text{OP}*}(z)$ of the SW profile $\boldsymbol{m}_\xi(z)$ is the dominant component in this case compared to SAW-SSW coupling dominated by in-plane magnetization. We only consider YIG film thickness L and the magnitude of the external magnetic field B_{ext} as the variables to ME coupling as in the previous chapter.

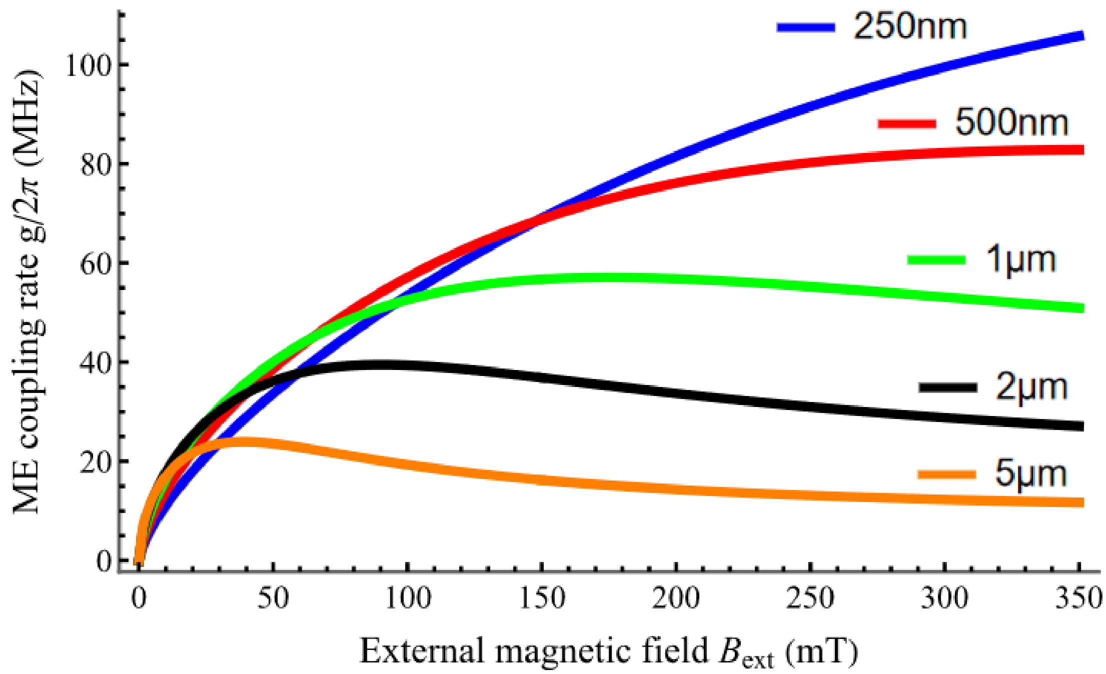

Figure 5.2: ME coupling rate g for SAW-BVSW as a function internal bias magnetic field with varying YIG thickness L.

Figure 5.2 shows the coupling rate for fixed YIG film thicknesses and different internal magnetic fields strengths. As stated before g_ξ is extremely dependent on the wave profiles at the specific wavevector k_0 where the dispersion relations cross. The thickness and magnetic field strength are integral to understanding how the wave profiles at k_0 change. As the external magnetic field B_{ext} uniformly increases or decreases throughout the YIG film the wavevector k_0 will proportionally increase and decrease with the field magnitude. For the SAW profile, as k_0 increases, becomes more localized at the top free surface of the YIG film. The BVSW profile becomes localized too in the thinner films leading to a small region of space where energy between the waves must be transferred more intensely leading to the larger coupling rate. In the thicker films the BVSW profile is spread more top to bottom in the YIG film. Increasing the field and therefore the wavevector, the SAW profile continues to be localized only at the top having less and less overlap of complete profiles. This leads to a decreasing plateau of the coupling rate from the SAW profile. Theoretically, even the coupling rate g_{ξ} will plateau even for the 250nm thick YIG film, but in reality we will reach a strain limit on the acoustic wave and the region of interaction we have at high magnetic fields is not yet fully realizable for today's technology. This case for thinner films and larger fields is examined first naturally, as we wish to see the spectrum where ME coupling is strongest and why we should avoid these conditions for now.

Figure 5.3 shows the spectrum of the hybrid ME waves calculated using (3.40) with parameters $L = 500$nm and $B_{\text{ext}} = 350$mT. The highlighted lines in Fig. 5.3 show the dispersion relations of the uncoupled SAW (red) and BVSW (purple) modes. The anti-crossing point highlighted in the circled frame of Fig. 5.3 shows a ME gap $\Delta\omega_{\text{ME}}/2\pi = 165$MHz. The black curve in Fig. 5.3 shows one higher-order SW resonant mode. Everything we learned about ME coupling between SAW and the higher order SW resonant modes carries over from the previous chapter. The benefit here is that the BVSW magnetostatic mode lies in the lowest SW mode from all the resonant modes.

As one can see from Fig. 5.3, this region of the wave spectrum is for relatively high wavevectors at $k \approx 15-20$rad/μm, or 315-420nm wavelengths. These values have their own practical problems as really short wavelengths for SAW that are challenging to excite [28], [50], [63]. Also, the magnetic material is dominated by a bundle of exchange interactions of SWs [51], [52], [61]. [109], [110], [112]. As a last word of caution, when one does decide to use thicker YIG films at high magnetic fields, one must consider the exchange spin splitting frequency gap $\Delta\omega_s$ between the higher-order SW resonant modes or else they mix into the large ME coupling gap. For these reasons, experimentalists require something much more reasonable, and theoretically what makes the BVSW special is its dipolar region. The dipolar region for BVSWs has a rare phenomena not normally found in nature. As the wavevector increases, frequency decreases giving the BVSW a negative group velocity via the slope of the dispersion relation, see Fig. 2.5b.

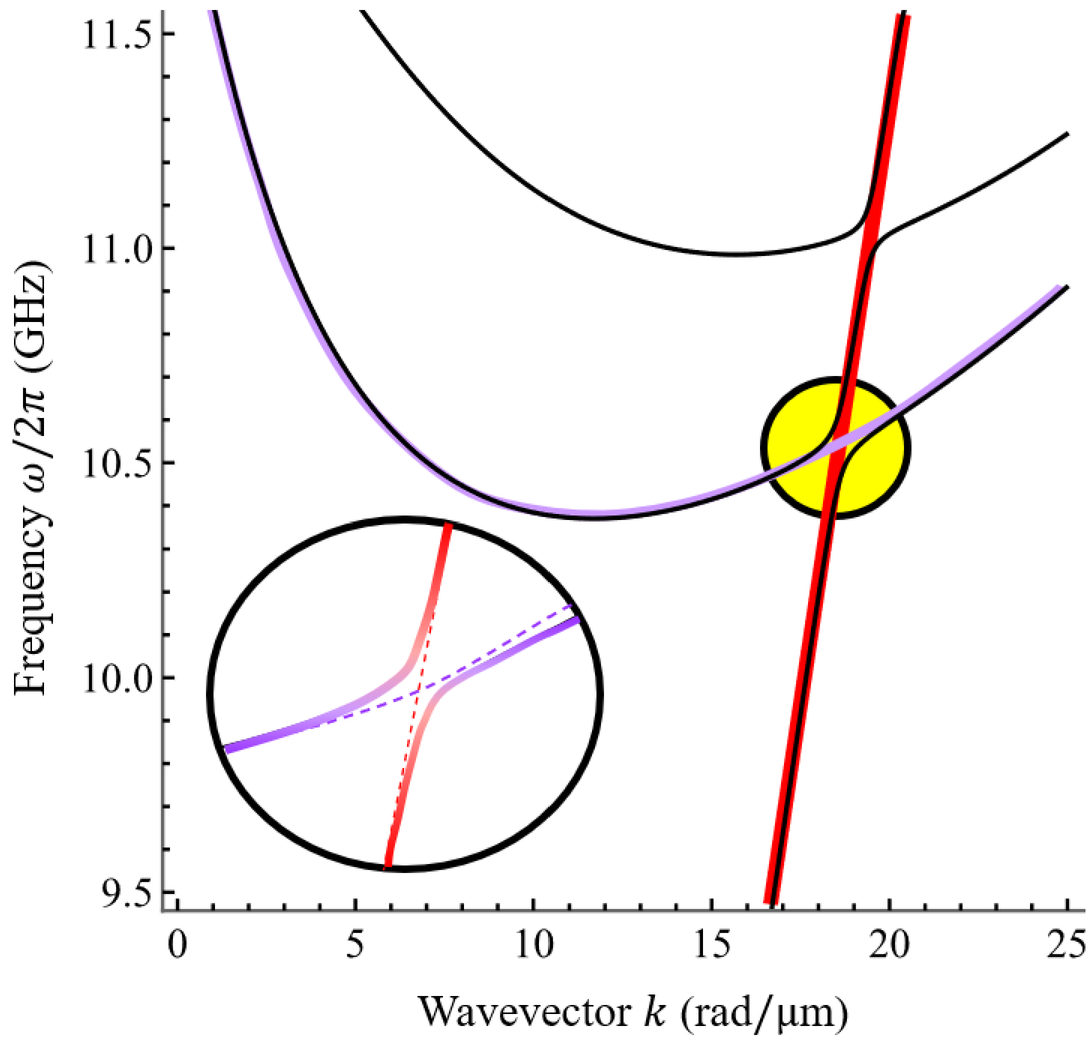

Figure 5.3: Spectrum of the hybrid ME waves in YIG/GGG bi-layer. Highlighted branches correspond to SAW (red) and BVSW (purple). Yellow highlight circle features the zoomed in region of the ME coupling. Parameters: YIG film thickness $L = 500$nm, internal magnetic field 350mT applied in-plane parallel to the direction of wave propagation.

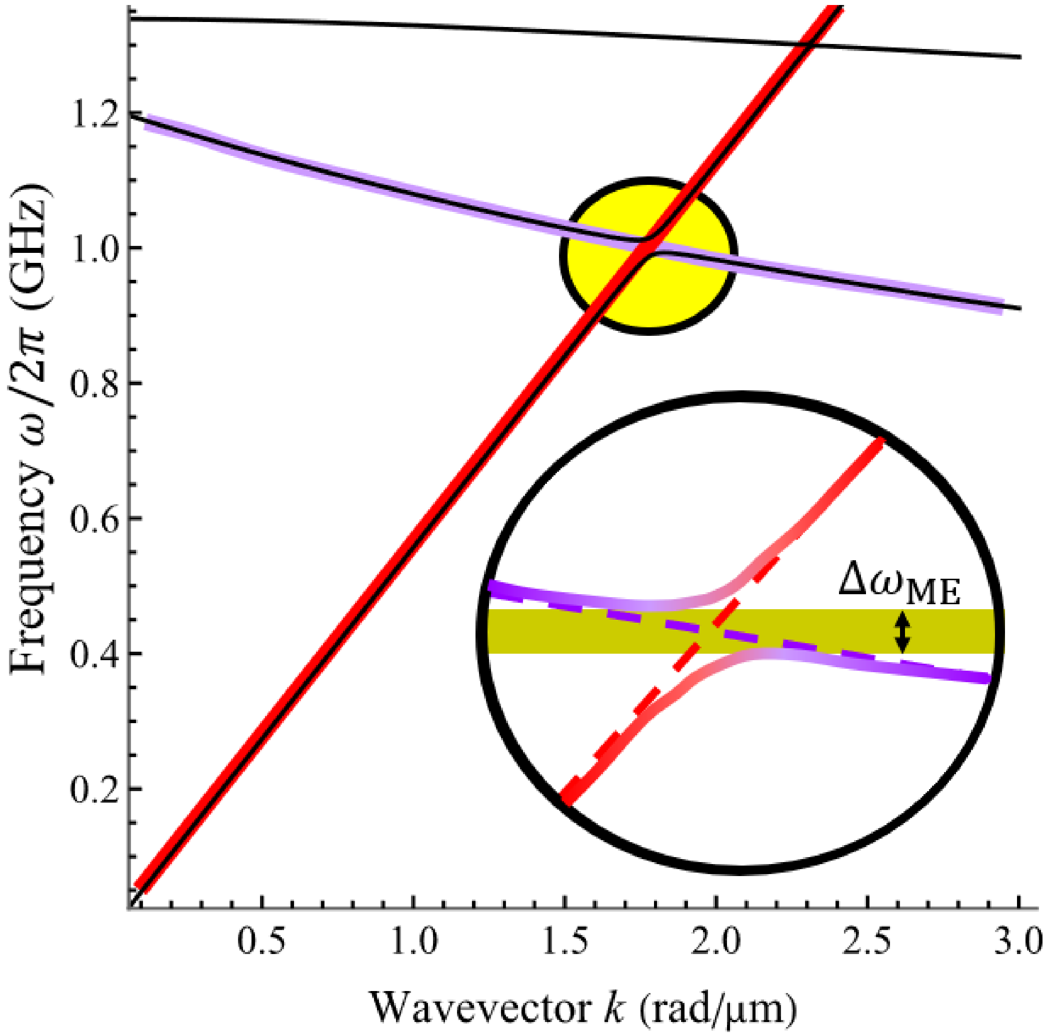

Figure 5.4: Spectrum of the hybrid ME waves in YIG/GGG bi-layer. Highlighted branches correspond to SAW (red) and BVSW (purple). Yellow circle shows zoomed in feature of frequency band gap $\Delta\omega_{\mathrm{ME}}/2\pi = 13$MHz from the ME coupling anti-crossing. Parameters: YIG film thickness $L = 500$nm, internal bias field 10mT applied in-plane parallel to the direction of wave propagation.

We decrease the internal magnetic field to 10mT and keep YIG thickness at 500nm. Figure 5.4 shows this new coupled spectrum with a new feature. The circle frame of the zoomed in view of the ME crossing point has a dark yellow bar where neither dispersion relation in this coupled system enters this range of frequencies. The dark yellow bar in Fig. 5.4, is a forbidden frequency gap that can be clearly defined as a gap of width $\Delta\omega_{\mathrm{ME}}$. This forbidden frequency gap is a powerful feature of this system.

Conceptually, think of a SAW propagating through any material that is elastic and FM. If that SAW propagates toward our YIG/GGG system, it won't be able to enter. This is because, when it touches the boundary to our YIG/GGG system, the SAW would "feel" this boundary as a "mirror" and immediately and completely convert into a BVSW that now propagates back to where it started from. This propagating SAW at approximately 1GHz is not allowed to enter our YIG/GGG system, because that frequency is in the forbidden frequency gap. The only interaction that can happen then is the SAW transforms and converts all of its energy into a BVSW which will propagate away from this forbidden region of space, where either wave in this range of frequencies, $\Delta\omega_{\mathrm{ME}}$, cannot exist.

As before with SSW, a good quick check to see if one might obtain a frequency gap to find where the SAW dispersion relation crosses the approximated BVSW dispersion relation (2.11). If SAW crosses the BVSW in the plateau region, a forbidden frequency gap will not appear.

One other important factor to consider at the forbidden frequency gap, is the group velocity of the wave. We would like the speed of the BVSW is be on par with the SAW to travel far distances due to higher damping for SWs. Consider Fig. 5.4, and the slopes of the highlighted dispersion relations of the two waves. The SAW will always have a constant speed for the YIG material at $v^{(\mathrm{SAW})} = 3,567$m/s. The BVSW in Fig. 5.4 only has a velocity of -557m/s. The ME crossing point at k_0 has a low BVSW speed compared to the SAW. To optimize this parameter, we check the two variables L and B_{ext} and see how the BVSW speed compares at different crossing points with the SAW.

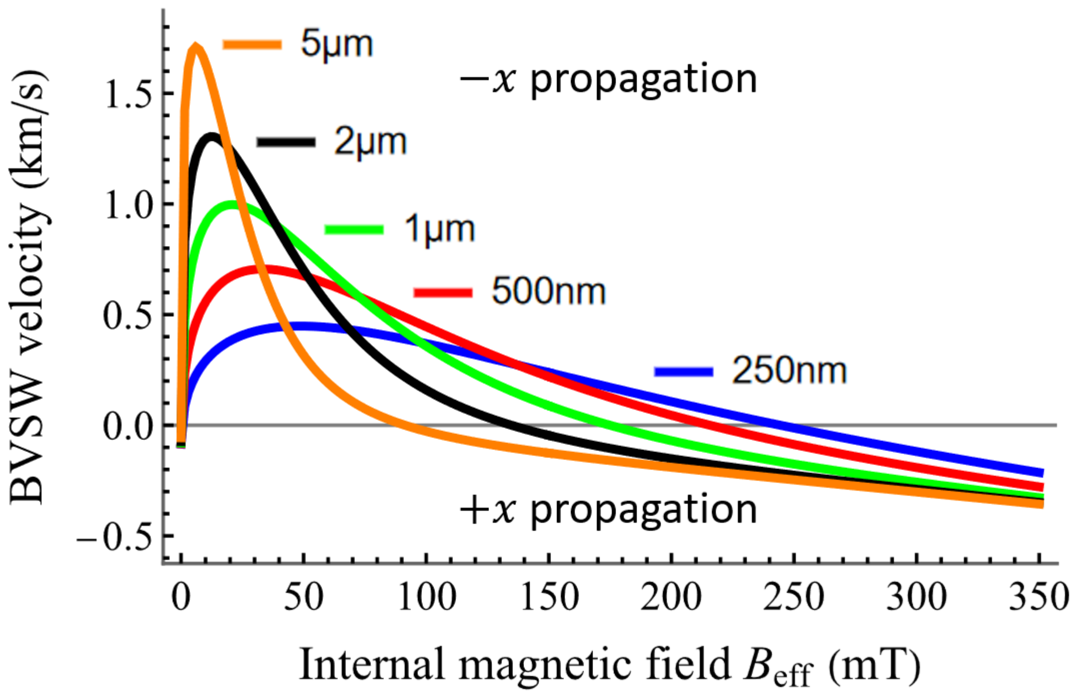

Figure 5.5: Velocity of the BVSW at the crossing point between the SAW and BVSW dispersion relations.

This search for a higher BVSW speed produces Fig. 5.5 As described by the $\pm x$ directions, the BVSW has its highest negative group velocity at lower fields, less than 50mT, in thicker films, greater than 1μm. This leads us to a better situation as we look at Fig. 5.6, where the thickest film of 5μm at $B_{\text{ext}} = 10$mT gives the BVSW a velocity of -1636m/s. The thicker film will benefit us in a way one might not find intuitively, in comparison to the initial ME coupling rate data in Fig. 5.2.

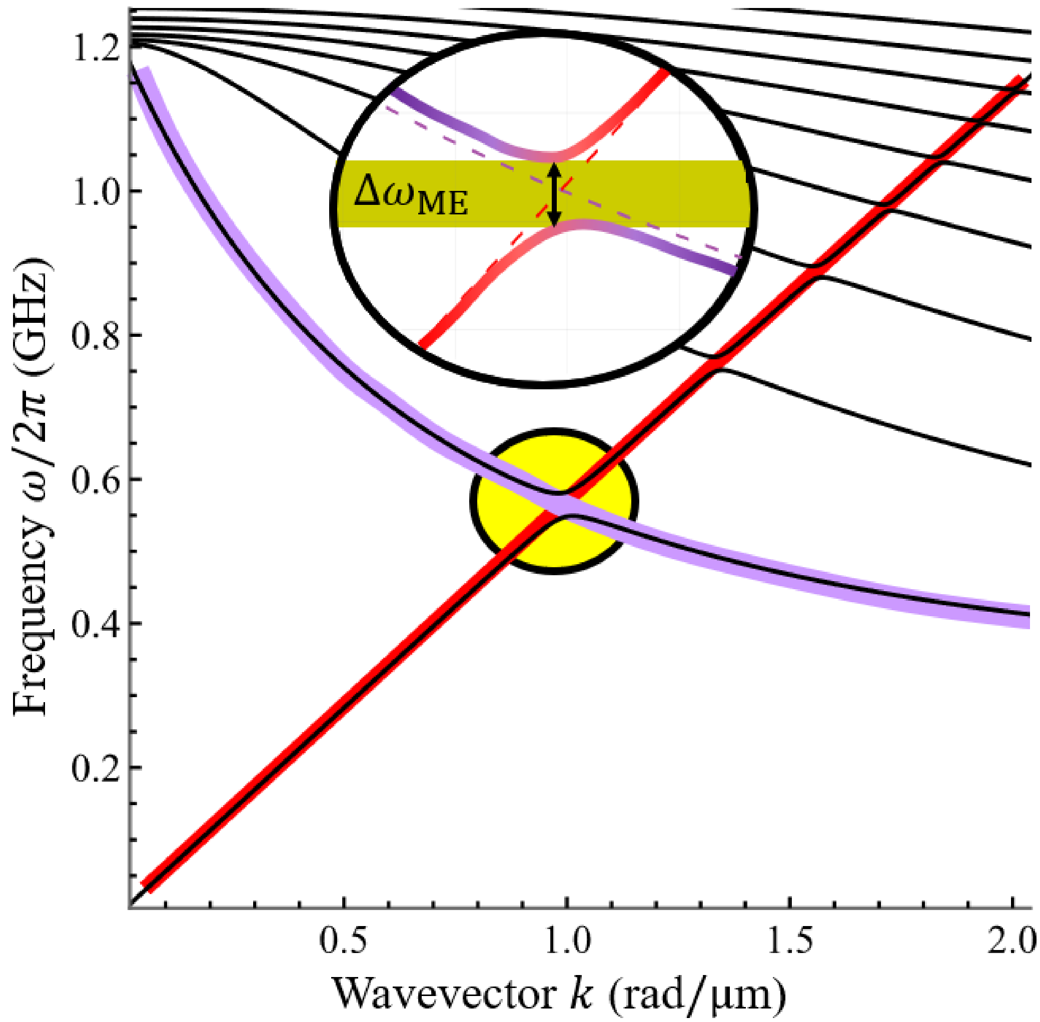

Figure 5.6: Spectrum of the hybrid ME waves in YIG/GGG bi-layer. Highlighted branches correspond to SAW (red) and BVSW (purple). Yellow circle shows zoomed in feature of frequency band gap $\Delta\omega_{\mathrm{ME}}/2\pi = 17$MHz from the ME coupling anti-crossing. Parameters: YIG film thickness $L = 5$μm, internal bias field 10mT applied in-plane parallel to the direction of wave propagation.

As stated earlier, the harm of using thicker films is the decrease in exchange spin splitting frequency gap $\Delta\omega_s$. However, for this thicker YIG film at $L = 5$μm with a low magnetic field strength of $B_{\mathrm{ext}} = 10$mT, the BVSW curves down faster and stays away from the higher order SW resonant modes. As one might see from the BVSW dispersion relation for the dipolar approximation (2.11), the thicker film supports a steeper curve and higher negative (backward) velocity of the SW.

Compared to Fig. 5.4's coupling rate $g/2\pi = 13\text{MHz}$, we have the added benefit that the coupling rate in Fig. 5.6's case is $g/2\pi = 17\text{MHz}$. We have slightly increased the coupling rate and by directly expanding the prohibited frequency gap defined by (3.14). Numerically, the ME interaction gap for Fig. 5.4 is $\Delta\omega_{\text{ME}}/2\pi = 26\text{MHz}$ and Fig. 5.6 has a frequency band gap of $\Delta\omega_{\text{ME}}/2\pi = 34\text{MHz}$

This unique situation allows for easier control of filtering/isolating signals as one can vary an external magnetic field to change the BVSW dispersion relation and therefore the frequency band gap to interact or not with almost any excited SAW or BVSW at a fixed frequency. This situation is even better in the fact that the propagation of the waves are opposite at this point in space. The SAW-BVSW interaction will depend both on the thickness of a magnetic layer and magnitude of film magnetization. We emphasize that a balance or choice of preference must be made in choosing physical parameters between the ME coupling rate and BVSW group velocity at the coupling point. In any sense, the optimal conditions for more practical devices comes down to what exactly needs to be achieved. This unique scenario though of SAW-BVSW coupling will provide many opportunities for future ME phenomena as we will discuss in the next chapter.

CHAPTER SIX

MANIPULATION OF PULSES IN AN INHOMOGENEOUS SYSTEM

In this chapter we wish to show how to exploit the use of the unique situation of ME coupling between SAW and BVSW. Specifically, we examine the power of this forbidden frequency band gap, produced from the ME coupling between SAW-BVSW. We will discuss manipulation of these waves by using a timed pulse of electrical current creating an inhomogeneous field localized within the YIG film. This will allow one to essentially turn ME coupling on or off in a device and either allow a SAW to pass through the system or reflect into a BVSW or vice versa. Beginning with a simple case of a static inhomogeneous magnetic field in the YIG film. This inhomogeneous system leads into many interesting phenomena one might not intuitively think would be there for a system coupling two waves. The inhomogeneity of the magnetic field generated from the wire changes the SW spectrum in both time and space leading our YIG film to be considered a space-time meta material [238]. We analyze simulations of waves propagating in this system changing the spatial dimensions of the wire, then expand on finding reflection and transmission coefficients of these wave interactions with this inhomogeneous magnetic field. From those results we move on to testing possible operations that can be done with this ME coupled system. The potential of this ME coupling opens up many practical applications of use be able to manipulate two waves with different characteristics within the same system.

Looking at Fig. 6.1, we begin our set-up essentially the same as before in Chapter 5 (see Fig. 5.1), but a wire has been added on top of the YIG film oriented parallel to the *y*-axis. A current *I* applied within the wire induces the magnetic field within YIG to have an inhomogeneous distribution along the *x*-direction. Note the direction of the current will also determine if the magnetic distribution of the YIG film will be either lowered or raised in this region of space underneath the wire. An extra factor to consider will be the size of the wire. The region under the wire will have the strongest effect on the YIG films internal magnetic field along the x-axis. In this case, we actually have an external magnetic field produced from the wire. To help differentiate the between the two previous scenarios, we will have two magnetic fields in this system. One will be for the YIG film, a bias internal magnetic field at a value of B_{YIG} that is kept uniformly constant everywhere. The other will be an explicitly external field produced from the wire, which will have a mathematical expression (see (6.4)). While we have chosen to show a straight simple wire in Fig. 6.1, any number of wires or different designs can be used as long as the same inhomogeneous magnetic field is produced as discussed in later sections to measure and compare our theoretical results.

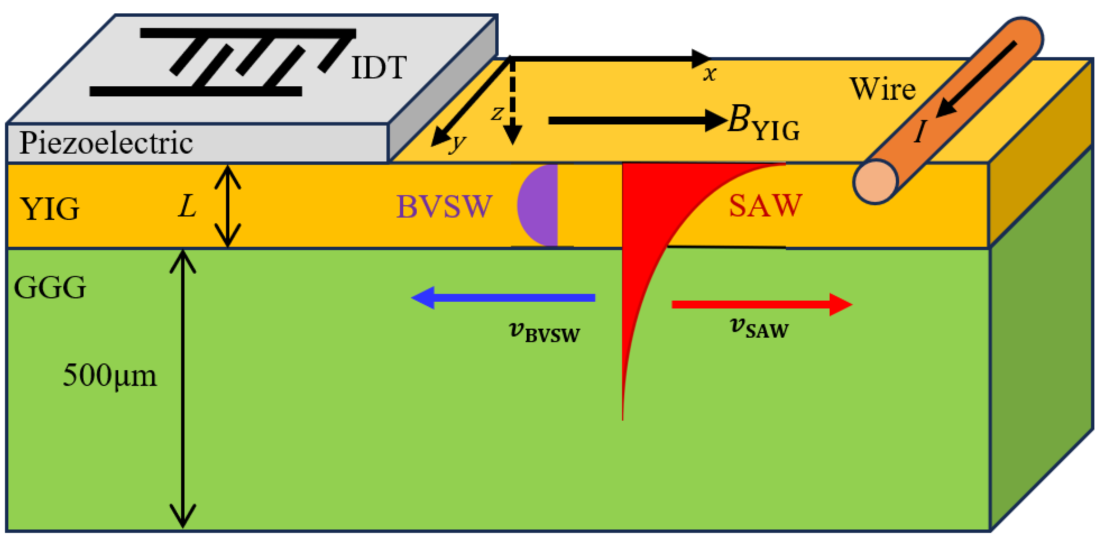

Figure 6.1: Geometry of the system under study: magnetic (YIG)/nonmagnetic (GGG) bi-layer magnetized in the x direction parallel to wave propagation direction. Red (purple) shaded area shows schematic profile of SAW (BVSW) propagating to the right (left). Orange cylinder is copper wire placed atop YIG film with current orientated in $+y$-direction for inhomogeneous magnetic field along x-axis.

6.1 Theory

To analyze the manipulation of pulsed waves we need to define an expression of these waves propagating in linear space. They will be dependent on the inhomogeneous magnetic field to determine if coupling, or transformation, of either wave is possible. We start with our main wave equations (3.40) in k-space and transform them to real space. We can then solve for the scenario when an excited wave (SAW or BVSW) propagates along the x-axis and interacts with this inhomogeneous magnetic field created from the wire.

Simplifying the mathematics, our focus for this model is the magnetic dipole region where we will have small values of wavevector k, and we will always have the forbidden frequency band gap $\Delta\omega_{\mathrm{ME}}$. We choose to ignore all the higher order SW resonance modes as the BVSW intersection is far enough away to not worry about SW modes mixing even with the relatively $L = 5$ μm thick YIG film. Therefore, in (3.40) we drop the summation and index ξ for SWs and the SAW will couple only to the BVSW mode, leaving us only

$$\frac{\mathrm{d}A_k}{\mathrm{d}t} = -i\omega_k^{(\mathrm{SAW})}A_k - ig_k^*S_k \tag{6.1a}$$

$$\frac{\mathrm{d}S_k}{\mathrm{d}t} = -i\omega_k^{(\mathrm{BVSW})}S_k - ig_kA_k \tag{6.1b}$$

Now we have the most simplistic version of coupled waves in (6.1) and note all components lie in momentum space. We will focus much more carefully around the ME interaction point. This is the only point of the ME coupling interaction and will be designated as (k_0, ω_0) for the frequency and wavevector at the crossing point of dispersion relations. With this only point of interaction, we assume the ME coupling rate be constant and change notation from $g_k \to g_0$. At this crossing point between SAW-BVSW dispersion relations, we apply a Taylor expansion to the first order to linearize our ME interaction. They will take the form

$$\omega^{(\mathrm{SAW})} = \omega_0 + \frac{\partial \omega}{\partial k}\Delta k \tag{6.2a}$$

$$\omega^{(\mathrm{BVSW})} = \omega_0 + \frac{\partial \omega}{\partial k}\Delta k + \frac{\partial \omega}{\partial B}\Delta B(x,t) \tag{6.2b}$$

Notice the BVSW frequency is dependent on both wavevector k and the magnetic field value $\Delta B(x,t)$. This $\Delta B(x,t)$ term means the difference between the YIG films internal magnetic field and the magnetic field value produced from the wire. This is abstractly shown in Fig. 6.2 from a spatial perspective. In order to achieve coupling of waves the dispersion relations both have to cross at the point (k_0, ω_0) where the term $\Delta B(x,t) = 0$. The other magnetic term $\frac{\partial \omega}{\partial B}$, is conceptually described as the effective gyromagnetic ratio γ_{eff} and solved for numerically. This constant γ_{eff} linearly shows the change of frequency from the change in magnetic field as $\Delta\omega = \gamma_{\mathrm{eff}}\Delta B$. The shared term $\frac{\partial \omega}{\partial k}$ is the group velocity for the wave.

After substitution of our linearized frequency forms into (6.1) we then apply a Fourier transform. All details of mathematical conversion are shown in Appendix B.1. Essentially, we have converted our equations of motion from k-space to real space where they take the form

$$\frac{\partial A}{\partial t} = -v^{(\mathrm{SAW})}\frac{\partial A}{\partial x} - ig_0 S \tag{6.3a}$$

$$\frac{\partial S}{\partial t} = -v^{(\mathrm{BVSW})}\frac{\partial S}{\partial x} - ig_0 A - i\gamma_{\mathrm{eff}}\Delta B(t,x)S \tag{6.3b}$$

Here in equation (6.3), S and A are the complex wave amplitudes dependent on both variables x and t. The constants $v^{(\mathrm{SAW})}$ and $v^{(\mathrm{BVSW})}$ are the group velocities of SAW and BVSW at the ME crossing point, respectively. To solve the partial differential equation (6.3) numerically, one must set initial and boundary conditions. Initial conditions are defined at $t = 0$ and position a wave or waves at any initial position in space. Boundary conditions stay constant in time at fix points in space. This helps set the direction propagation of waves, such as saying that A at the left boundary is zero means the SAW propagates right. If the SAW did propagate left, it would reach this boundary that states no acoustic wave should exist at this boundary and destroy itself or give large numerical errors. The chosen initial and boundary conditions of our system must then reflect our idea to prove one excited wave reflects and transforms into the other.

6.2 Results for a Single Wire with Current

We begin by describing a simple inhomogeneous system where the spectrum of our waves changes how they propagate through space within the YIG film. From Fig. 6.1, assume we only have a single wire with a constant current always running to keep a static inhomogeneous magnetic field. This changes the inhomogeneity term $\Delta B(x,t)$ in (6.3) to $\Delta B(x)$. Figure 6.2 is an abstract visualization this scenario. We see in Fig. 6.2a, the magnetic field distribution within the YIG film. The black dashed line is the YIG films constant internal magnetic field B_{YIG}. The solid black line is the actually magnetic field where at the position of the wire (x_W) the magnetic field is locally raised to a peak value of $B_{\text{YIG}} + B_W$ where B_W is the max magnetic field produced from the wires current. The inhomogeneous magnetic field can be generically expressed as

$$B(x) = B_{\text{YIG}} + B_W \frac{r_W^2}{r_W^2 + (x - x_W)^2} \tag{6.4}$$

The constant r_W in (6.4) is the radius of the wire. The width of the wire does play a role in the effectiveness of ME coupling between waves. Essentially, the wire constant r_W helps determine how fast or slow the gradual change is of the magnetic field. In other words, the wire's width is directly proportional to the width of the inhomogeneous magnetic field bump.

Back to Fig. 6.2, consider we excite a SAW or BVSW at an excited frequency ω_0 far away from the wire. When the excited wave is far from the wire the wave exists in this

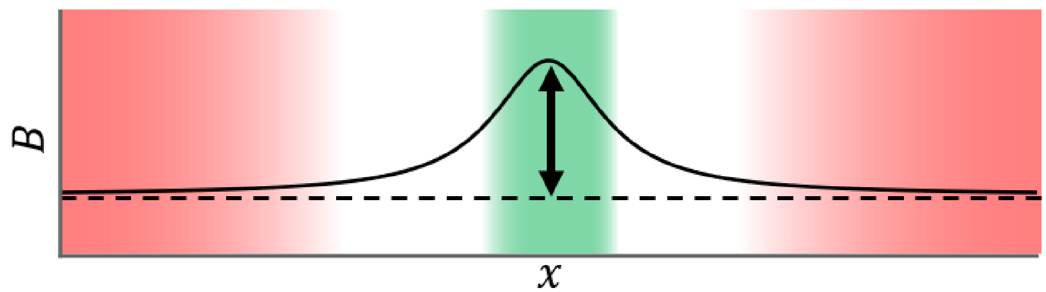

(a) Inhomogeneous field distribution in YIG film

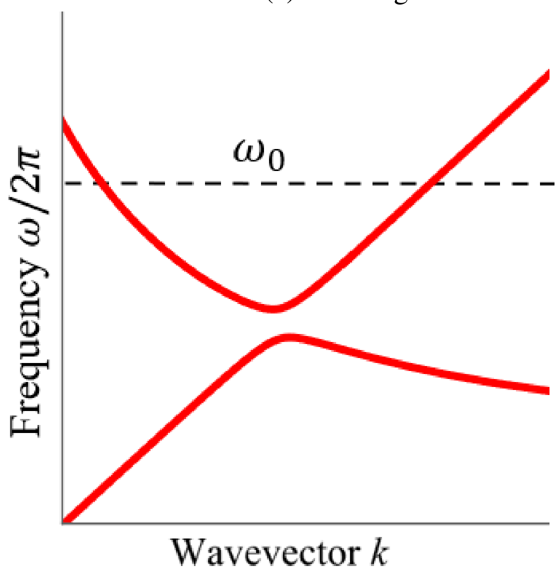

(b) Wave spectrum away from wire

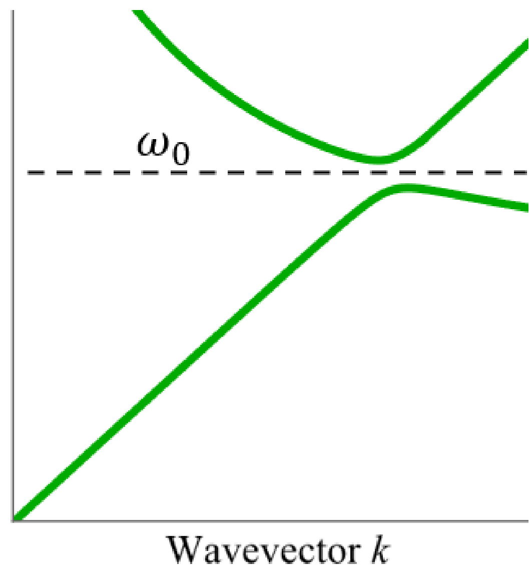

(c) Wave spectrum underneath wire

Figure 6.2: (a) Solid black line represents inhomogeneous magnetic field strength in YIG film. Dashed black line represents a constant internal magnetic field in YIG film. Double arrow represents how the wire creates the inhomogeneous magnetic field and where the peak magnetic field value is positioned. Red shaded region corresponds to spectrum of waves away from wire. Green shaded region corresponds to spectrum of waves directly underneath the wire. (b) Spectrum of waves away from wire. Straight line is SAW, curve is BVSW spectrum in YIG film from internal magnetic field. The frequency ω_0 is the frequency of the excited SAW. (c) Spectrum of waves in region of space directly underneath the wire. Straight line is SAW, curve is BVSW. In this region of space the SAW traveling with frequency ω_0 couples to the BVSW via ME coupling band gap.

red region shown in Fig. 6.2a. The red region relates to the red wave spectrum shown in Fig. 6.2b. From 6.2b, one can see that for either wave, excited at a frequency ω_0, they do not "feel" each other in the sense the dispersion relations don't cross at this frequency value. However, as either wave moves in space toward the green shaded region in Fig. 6.2a, we end up moving the BVSW mode. In the green region of space, which is directly related to being underneath the wire, we have the dispersion relation of both waves shown in Fig. 6.2c. The green spectrum in Fig. 6.2c shows that the excited wave with frequency ω_0 interacts with the ME coupling point. As stated previously, but visually seen now, when a wave enters this green region with the forbidden frequency band gap, that wave will immediately transform into the other wave. This is because that waves dispersion relation and frequency intersect in this region of space. Once the initial wave transforms it will propagate to to its original starting point as the other wave. As an important reminder the BVSW changes with the magnetic field, thus we can change the ME coupling interaction point to match that of the excited wave frequency ω_0 as needed. This is key to applicable devices requiring tunability.

To simulate this scenario and prove our theory we need to solve (6.3) using (6.4) for part of the inhomogeneous magnetic field. As we choose to solve (6.3) numerically we must pick initial and boundary conditions. We begin by describing how our simulations are evaluated. We chose to initially start with a SAW at a fixed frequency ω_0 and not have any BVSW at $t = 0$. This simple illustration is to avoid confusion as the frequency of the BVSW will vary with the magnetic field, while having the BVSW traveling backwards as it is properly named. This hones in our idea to prove as one wave reflects off the raised magnetic field and transforms into the other wave and propagate backwards. We give our system the following initial and boundary conditions expressed as

$$A(x,0) = e^{-\left(\frac{x-x_0}{w}\right)^2} \tag{6.5a}$$

$$S(x,0) = 0 \tag{6.5b}$$

$$A(-x_R,t) = 0 \tag{6.5c}$$

$$S(+x_R,t) = 0 \tag{6.5d}$$

The initial conditions (6.4a) and (6.4b) show our SAW takes the form of a Gaussian wave packet at a starting position x_0 with a width of w. The BVSW does not initially exist in our system so it does not matter where it starts, but the BVSW will be created when the SAW Gaussian packet transforms via ME coupling. The boundary conditions are set by the constant x_R which is the region of space we allow our waves to move through and interact with the inhomogeneous magnetic field from the wire. As described previously, the boundary conditions also indicate the directions the SAW and BVSW will propagate through this region of space x_R.

6.2.1 Simulation Results

For the specific parameters and initial conditions chosen we are still in a good region where the ME coupling rate (g_0) is still greater than both damping rates of either wave. The SAW pulse is w =50μm wide, with wavevector k_0 = 1rad/μm and frequency $\omega_0/2\pi$ =0.565GHz traveling from left to right. The SAW is traveling in a spatial region of YIG with an internal magnetic field B_{YIG} = 7mT. Meaning the BVSW dispersion relation does not intersect the with the traveling excited SAW frequency (see Fig. 6.2b). The SAW will not couple to the BVSW until the SAW reaches green region (see Fig. 6.2a) where the local magnetic field is raised by B_W = 3mT by the wire. The reason we decided on the parameters of L = 5μm and $B_{\text{YIG}} + B_W$ = 10mT for ME coupling to occur is due to the group velocity of the BVSW. The linear SAW has a constant group velocity 3,567 m/s predetermined from the materials elastic properties. The BVSW group velocity is dependent on both L and B_{YIG}, along with where it intersects the SAW spectra. Back to

Fig. 5.5, the SAW-BVSW crossing point for various thicknesses and fields has the highest value of $\sim$1,636 m/s for the BVSW group velocity with $L = 5\mu\text{m}$ and $B_{\text{YIG}} = 10\text{mT}$ as the parameters. This is another reason why we only increase the magnetic field in YIG as our internal magnetic field is pretty low initially.

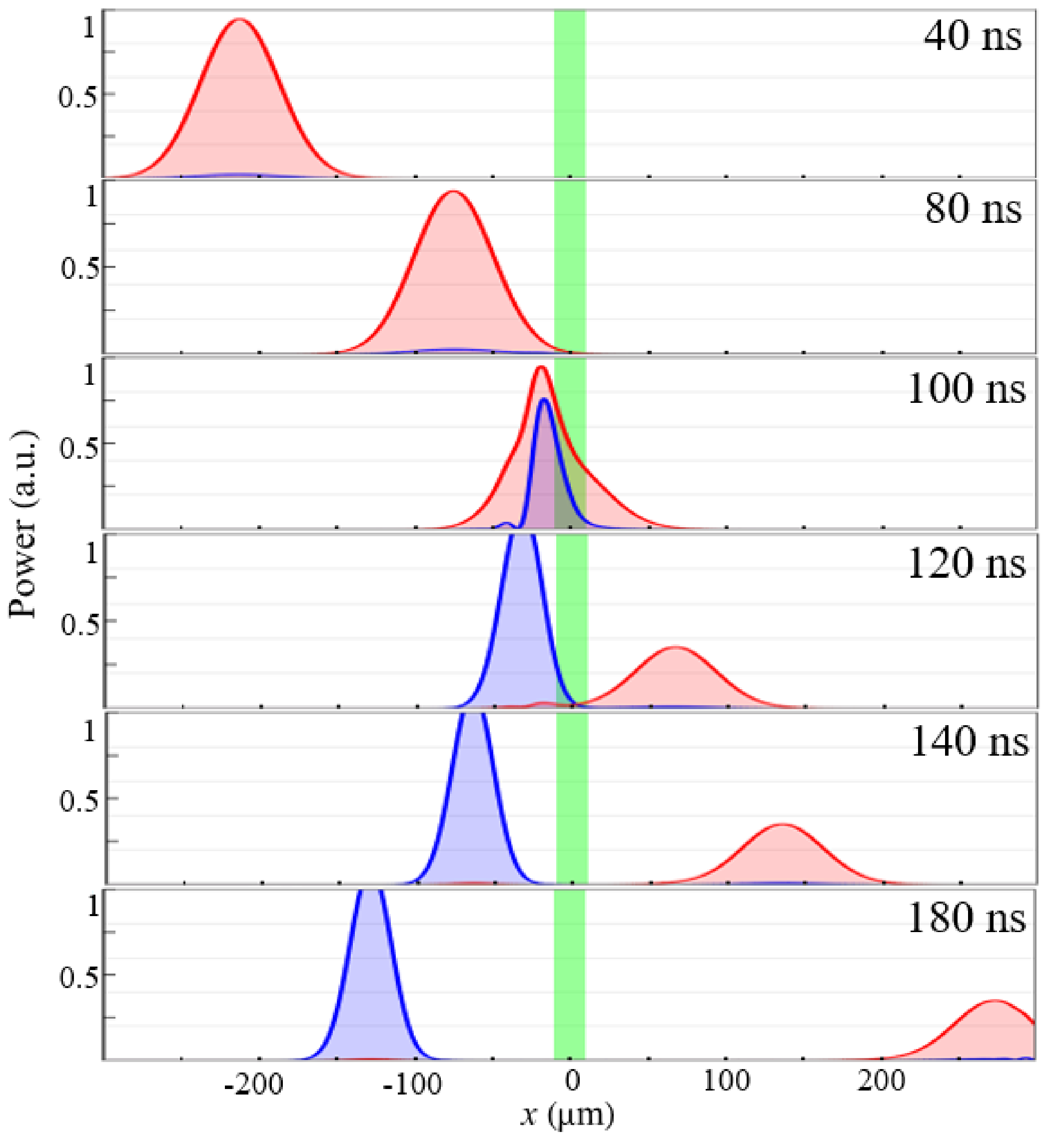

Figure 6.3: SAW (red) traveling in the $+x$ direction and BVSW (blue) traveling in $-x$ direction. Green region is space where magnetic field raises BVSW dispersion relation to interact with SAW at $k_0 = 1$rad/μm. Parameters: $L = 5$μm, $B_{\text{YIG}} = 7$mT, $B_W = 3$mT, $r_W = 10$μm

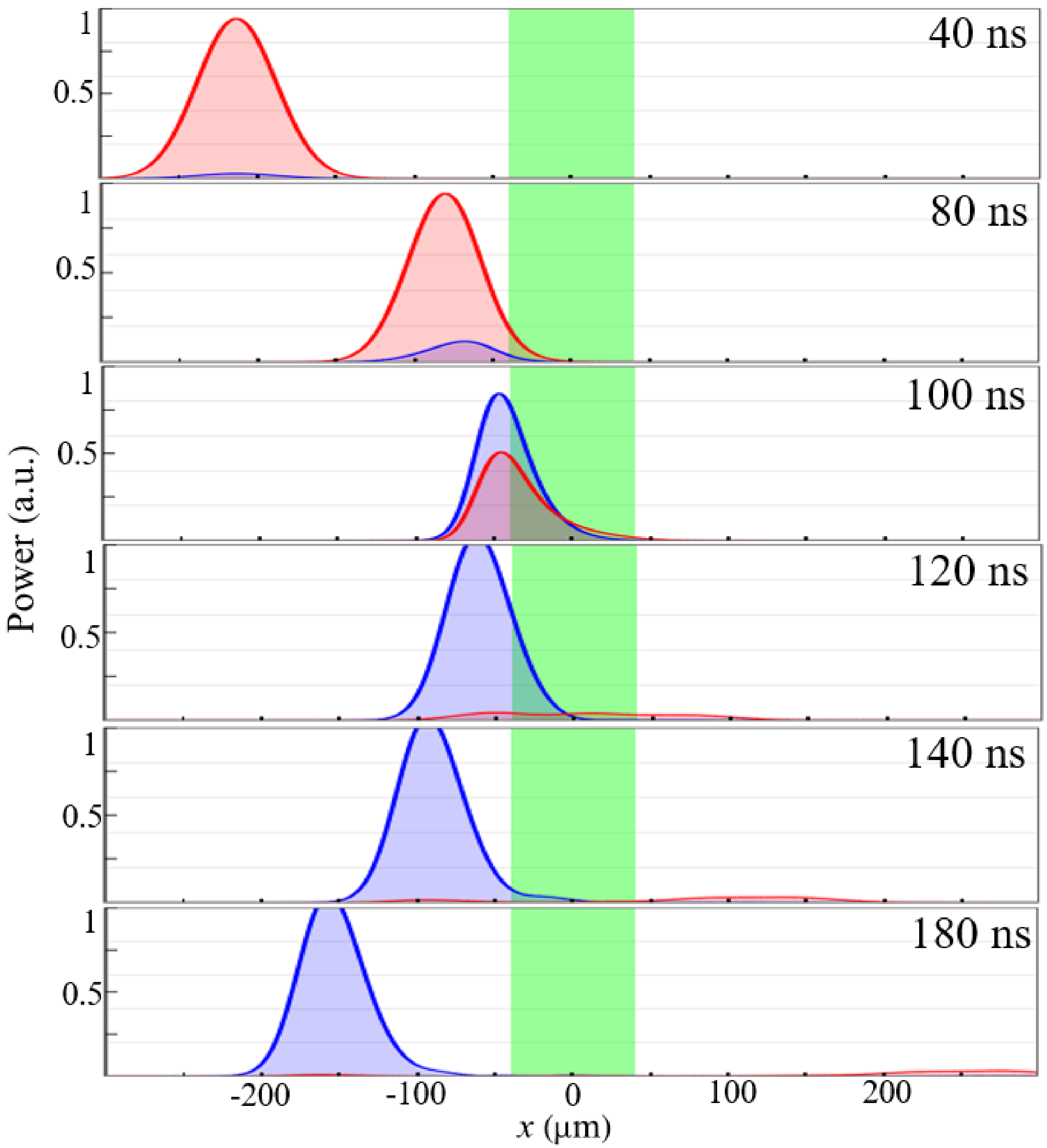

Figure 6.4: SAW (red) traveling in the $+x$ direction and BVSW (blue) traveling in $-x$ direction. Green region of is space where magnetic field raises BVSW dispersion relation to interact with SAW at $k_0 = 1$rad/μm. Parameters: L =5μm, $B_{\text{YIG}} = 7$mT, $B_W = 3$mT, $r_W = 40$μm

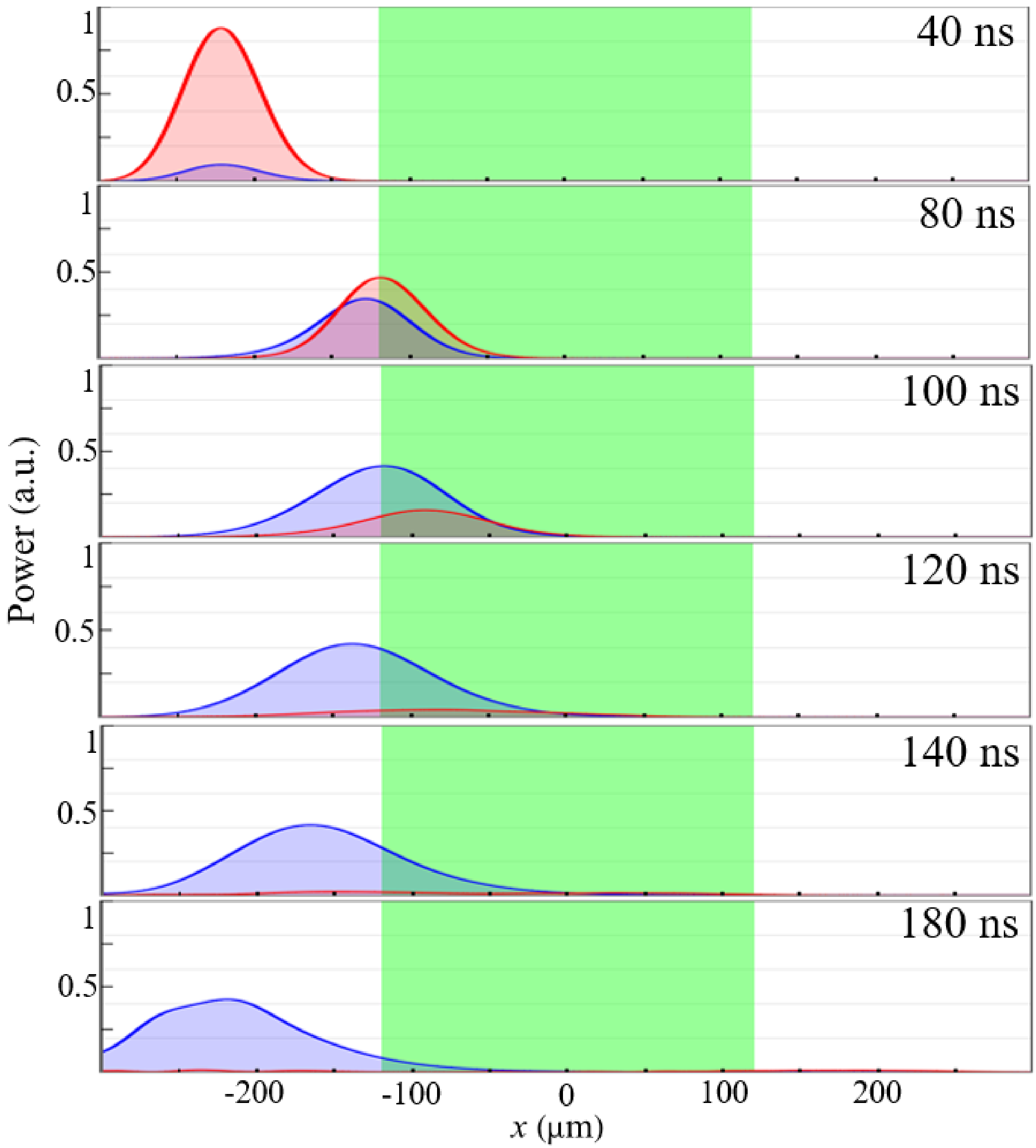

Figure 6.5: SAW (red) traveling in the $+x$ direction and BVSW (blue) traveling in $-x$ direction. Green region is space where magnetic field raises BVSW dispersion relation to interact with SAW at $k_0 = 1$rad/μm. Parameters: $L = 5$μm, $B_{\text{YIG}} = 7$mT, $B_W = 3$mT, $r_W = 120$μm

Solving (6.3) using the above parameter constants with conditions (6.5) and inhomogeneous magnetic field (6.4) we run simulations to see and understand the transformation of a SAW into a BVSW. In comparison to Fig.'s 6.2a, 6.2c, the green region where ME coupling takes place in the spectrum (matching the excited SAW frequency with the ME band gap varied by field) is also shown in Figures 6.3-6.5. We begin analyzing by visual differences changing the wire radius r_W which changes how slow or fast the spatial change from the internal field (red region Fig. 6.2a) is to the added peak field from the wire B_W (green region Fig. 6.2a). Figures 6.3-6.5 show the exact width of this green region of the ME anti-crossing gap as $2r_W$ for radii 10μm, 40μm, and 120μm used respectively.

One note on these wave pulses is that the width of the pulse does correspond to a range of frequencies within the spectrum. At the peak of the SAW packet (red Fig. 6.3) is the center frequency at which we excite our wave $\omega_0/2\pi$ =0.565GHz. The range of frequencies is found by taking the width of the pulse, $w = 50$μm for our case, and have it divide the speed of the packet $v^{(SAW)} = 3567$m/s. This gives us a frequency range of 71MHz with the high and low points at frequencies 0.6GHz and 0.529GHz. This information is important because as the magnetic field gradually increases, and raises the BVSW spectra. The SAW packet with the lower frequency side will convert to the BVSW packet (blue Fig. 6.3) even before touching the green region. Best shown by two frames in Fig 6.5 at the 80ns mark, and in Fig. 6.4 at the 140ns mark, a closer look at the BVSW packet reveals an asymmetric shape of the wave packet as it the SAW converts into the BVSW. As the magnetic field continues to raise the BVSW spectrum, the ME interaction gap rises along with the field and the lower frequencies in the SAW packet will convert before the center frequency.

In Fig. 6.3 , we consider a small wire radius of 10μm. In this case the SAW packet moves too fast, meaning not enough time is given for the ME coupling rate to convert the

SAW to the BVSW. As one can see at the time mark 180ns a substantial amount of SAW power passes through this coupling region not giving 100% effectiveness. One exceptional feature show cased here, and in Fig. 6.4, is that the width of the BVSW is thinner than the SAW packet, leading to a more concentration of power for that wave. This effect happens because of the difference in magnitude of the waves group velocities. Before the BVSW has the chance to move away from the coupling region, the next interval of the SAW have already converted to a BVSW.

In Fig. 6.4, we consider a medium case of wire with radius r_W =40μm. This simulation shows great conversion effectiveness of the whole SAW converting into a full BVSW packet. We get a BVSW packet of higher peaked power (from difference in group velocities magnitude) and is slightly wider too.

In Fig. 6.5, our case here is for a drastically large wire radius r_W =120μm. The width of the inhomogeneous magnetic field is significantly wider in this case shown by the magnetic component of the quasi-SAW packet at the 40ns mark compared to the other cases. This simulation shows a much wider BVSW packet in the YIG film, but greatly reduced in concentration of power.

To emphasize why the smaller wires are favorable, at the 120ns mark the SAW is fully converted to BVSW in all the cases. The difference though is the peak of power. The last two-time marks in all the figures (6.3-6.5) emphasizes the BVSW is slower than SAW, and that the BVSW travels in the opposite direction of SAW. The slow speed and low power is important when damping considered in real devices. Its lifetime and detection would be significantly shorter than the rest due to damping factors. For this reason in the last case the BVSW packet will not be considered when looking at the effectiveness of wave reflection.

6.2.2 Reflection Results

The reflection and transmission coefficients determine how effective the inhomogeneous magnetic field is in transforming these acoustic and spin waves back and forth These coefficients are dependent on the excited frequency of the pulse, gradient change of the field, and magnitude of the field from the wire. Numerically they are found from (6.3) under monochromatic conditions. Using the same constant parameters as the case beforehand, we see how well the SAW will reflect and convert to the BVSW from this change in magnetic field in the film at various frequencies.

This magnetic barrier affects all frequencies the BVSW dispersion relation crosses with the SAW as the wire raises or lowers the magnetic field in reference to YIGs constant bias field. One would expect to see 100% reflection of waves when calculating pulses at excited frequencies between ME resonance with the YIG film and at the peak value of the crossing point between SAW-BVSW dispersion relations directly beneath the wire.

The concept of monochromatic conditions is a single infinite wave propagating through time and space. This wave will behave in a certain way depending on ones spatial or temporal conditions, like our inhomogeneous magnetic field in space. We compare the wave amplitude values for both waves on opposite sides of the inhomogeneous spatial distribution to calculate the transmission and reflection coefficients. The system under monochromatic conditions where both complex wave amplitudes A and S are described as

$$\begin{pmatrix} A(x,t) \\ S(x,t) \end{pmatrix} = e^{i(k_0 x - \omega_0 t)} \begin{pmatrix} A(x) \\ S(x) \end{pmatrix} \tag{6.6}$$

will allow us to transform (6.3) into a matrix format as

$$\frac{d}{dx}\begin{pmatrix} A(x) \\ S(x) \end{pmatrix} = \begin{pmatrix} \frac{i(\omega-\omega_0)}{v^{(\mathrm{SAW})}} & \frac{-ig_0}{v^{(\mathrm{SAW})}} \\ \frac{-ig_0}{v^{(\mathrm{BVSW})}} & \frac{i(\omega-\omega_0)-i\gamma_{\mathrm{eff}}\Delta B(x)}{v^{(\mathrm{BVSW})}} \end{pmatrix} \cdot \begin{pmatrix} A(x) \\ S(x) \end{pmatrix} \tag{6.7}$$

The derivation for (6.7) is shown in Appendix B.2. Essentially, the newly added ω variable is the frequency of the pulse one chooses to excite. This will be our free variable that will help us determine and analyze the reflection and transmission coefficients of our inhomogeneous system. All other terms are treated as constants already previously defined.

While the monochromatic system (6.7) is difficult to solve in general, we use the Magnus expansion method [239], [240] to solve numerically.

$$\begin{pmatrix} A(x) \\ S(x) \end{pmatrix} = \Phi(x,x_0) \begin{pmatrix} A(x_0) \\ S(x_0) \end{pmatrix} \tag{6.8a}$$

$$\Phi(x,x_0) = \Phi(x,x_n)\Phi(x_n,x_{n-1})...\Phi(x_2,x_1)\Phi(x_1,x_0) \tag{6.8b}$$

As described by (6.8) we must define a starting position assuming the final conditions of the wave amplitudes A and S. The matrix $\Phi(x,x_0)$ is a matrix taking integral steps in any domain showing how the wave amplitudes evolve. Our initial condition will be

$$\begin{pmatrix} A(x_R) \\ S(x_R) \end{pmatrix} = \Phi(x_R,x_R) \begin{pmatrix} 1 \\ 0 \end{pmatrix} \tag{6.9}$$

saying that for all SAWs excited, propagating to the right, only one SAW passes through the very strong magnetic barrier and reaches the right boundary. The evolving matrix $\Phi(x,x_0)$ gives an output of two numbers at the boundary $-x_R$. These two numbers are taken as the wave amplitudes of the SAWs and BVSW. We compare these wave amplitude values at the left boundary $-x_R$ as a ratio of $S(-x_R)/A(-x_R)$ to get the reflection coefficient. Physically meaning the percent of SAWs reflected off the inhomogeneous magnetic field into BVSW. This is the correct method, because if we take the ratio of the SAW wave amplitude at the left boundary $-x_R$ to the right boundary $+x_R$ we get

$A(+x_R)/A(-x_R) = 1/A(-x_R)$ which is the transmission coefficient. The percent chance of a SAW passing through the inhomogeneous field in space with certain parameters.

In Fig. 6.6-6.9, we see how the reflection coefficient varies with the excited SAW frequency, wire radius, and magnitude of the wire's magnetic field. We will consider the parameters previously taken for the simulations shown in Fig. 6.3-6.4 where the BVSW power is greater than the initial SAW that will counter damping in real devices. We will not consider a wire with any larger radii than 40μm. For example, in Fig. 6.5 the power of the BVSW is less than the initial SAW power in comparison to the other two previous cases.

Starting with Fig. 6.8 for the ideal appearance of results, the wire has radius $r_W = 40$μm and raises the field in YIG by $B_W = +3$mT. The YIG film is $L = 5$μm with internal magnetic field $B_{\text{YIG}} = 7$mT. Using frequencies less than 0.47GHz for the free variable ω in (6.7), the excited SAW propagates through the inhomogeneous magnetic field region without any interaction in the YIG film. For frequencies between roughly 0.47-0.5GHz a gray region appears where data was collected, but cannot be interpreted as real values.

The reason no real values of reflection exist in the gray region, is because the YIG film is initially kept at a homogeneous magnetic field of magnitude $B_{\text{YIG}} = 7$mT. The BVSW dispersion relation with this 7mT field crosses the SAW spectrum and creates the forbidden ME band gap for frequencies 0.47-0.5GHz. If a SAW was excited, it would immediately convert to a BVSW and vice versa creating a standing wave transforming back and forth in one spot. Since there is no propagation in the system, there is no reflection from the inhomogeneous magnetic field, thus no real data could be acquired.

As we continue to excite SAWs at higher frequencies, above the fixed ME band gap (gray range of frequencies) we do achieve 100% reflection of SAW into BVSW up to a certain frequency. This range of frequencies where reflection is 100% relates back to the change of the BVSW frequency as the magnetic field changes within the YIG film. As the excited SAW frequency rises a proportion of the magnetic field needs to rise too in order for the BVSW dispersion relation to cross the SAW spectrum at that frequency. Compare Figures 6.2b and 6.2c. The ME band gap actually moves up with the BVSW dispersion relation as the magnetic field rises from the inhomogeneity. It is within this range of frequencies where reflection is 100% as no wave can pass through this white/green region (Fig. 6.2a) due to the ME band gap sliding along the SAW dispersion relation. This physical effect happens from the frequency boundary of the right gray dashed line to the green dashed line.

The green dashed line in figures 6.6-6.9 and figures 6.11-6.14 represents the upper boundary of the ME band gap directly beneath the wire. The highest frequency for reflection is expressed as $\omega_0 + g_0$ and directly relates to Fig. 6.2c. Ironically, our results do not 'reflect' this physical phenomenon completely accurate. This deviation, between our reflection results and where reflection should peak, stems from our method approximating the change in the dispersion relations from the magnetic field linearly from (6.2) and solving (6.7). In the case of Fig. 6.8, the max frequency of reflection is about 0.584GHz$= \omega_0 + g_0 = 0.567 + 0.017$GHz represented by the green dashed line. The dispersion relations intersect at $\omega_0 = 0.567$GHz in the middle of the ME band gap slightly left of the green dashed line, but show the complete reflection result one might expect. If a more complicated expression for how the ME band gap moves in space with the magnetic field their results would be more accurate and a very strong reflection of SAW would carry to the maximum frequency of the green dashed line. This deviation, from a linear approximation, is more prominent using larger magnetic fields from the wire in Figures 6.7 and 6.9.

Continuing to excite SAWs at any frequencies higher would result in near 0% reflection. The BVSW dispersion relation cannot rise any further due to the maxed out magnetic field produced from the wire. This provides us a nice range of frequencies to test and play around with SAW reflecting and converting into a BVSW, especially if we raise the max magnetic field from the wire even higher.

To compare Fig. 6.8 parameters with the other figures (6.7, 6.9, 6.10) we must explain the anomaly of these two vertical lines in the reflection range. This is a very interesting feature within our range of reflecting waves, which will require a more detailed analysis. In Fig. 6.8, there are two prominently defined vertical lines or dips in reflection. These vertical lines are dips in reflection with extremely small widths between 1-10kHz. Conceptually, these gaps can be thought of as certain energy levels (frequency levels) where a wave is allowed to 'tunnel' through the magnetic barrier. This scenario is analogous to a potential well in quantum mechanics, or more specifically, resonant tunneling through a double barrier. Please, compare [103], [241] for a more detailed understanding.

Figure 6.2a shows a symmetric inhomogeneous magnetic field that is similar to a quantum mechanical case of a potential energy well. Within these potential energy wells there exists resonant conditions that allows the energy of one wave to pass through, or tunnel through, the energy barriers that create the potential well. For our case, a wave of either type may tunnel through the 'magnetic' barrier not interacting with the ME band gap. This 'magnetic well' allows for a unique phenomena for real devices to act as a resonator with this simple system.

Consider Fig. 6.10 which show the simulation of continuous excitation of SAWs at a frequency of $\omega/2\pi = 0.52$GHz using all the same parameters used in Fig. 6.8. At the 10ns mark the continuously excited SAW approaches the inhomogeneous magnetic field. The wire is still positioned at $x_W = 0$μm, but the green shaded region as shown in Figures 6.3-6.5 is not displayed for easier examination of the resonance at later times. This SAW at frequency equal to 0.52GHz interacts with the inhomogeneous magnetic field in this

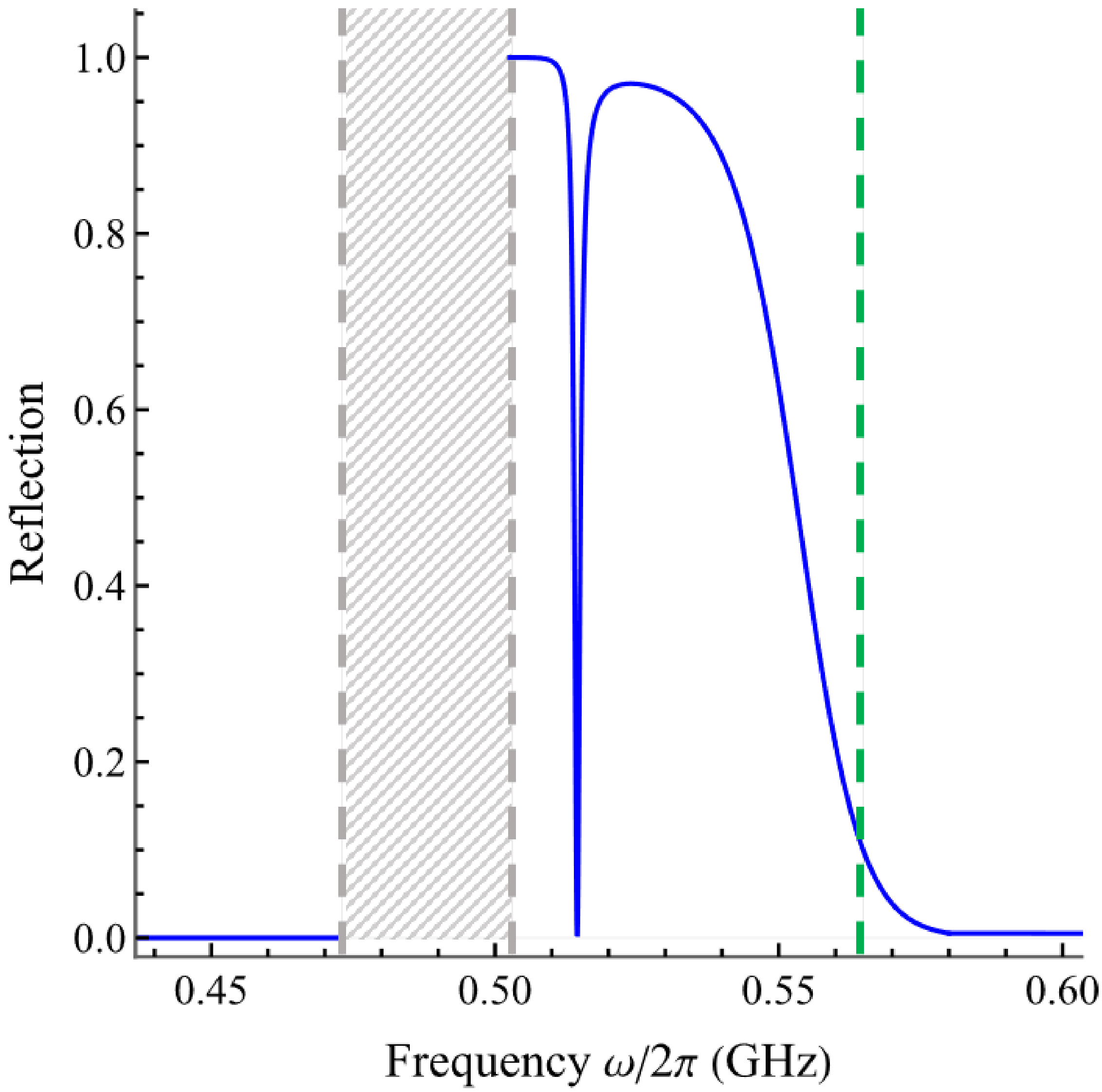

Figure 6.6: Percentage of SAWs reflected from wire generated magnetic field. Gray region shows where ME coupling takes place from bias internal field B_{YIG} in film. Green dashed line shows BVSW-SAW crossing frequency ω_0 from added magnetic field B_W from wire. Parameters: $L = 5\mu\mathrm{m}$, $B_{\mathrm{YIG}} = 7\mathrm{mT}$, $B_W = +3\mathrm{mT}$, $r_W = 10\mu\mathrm{m}$.

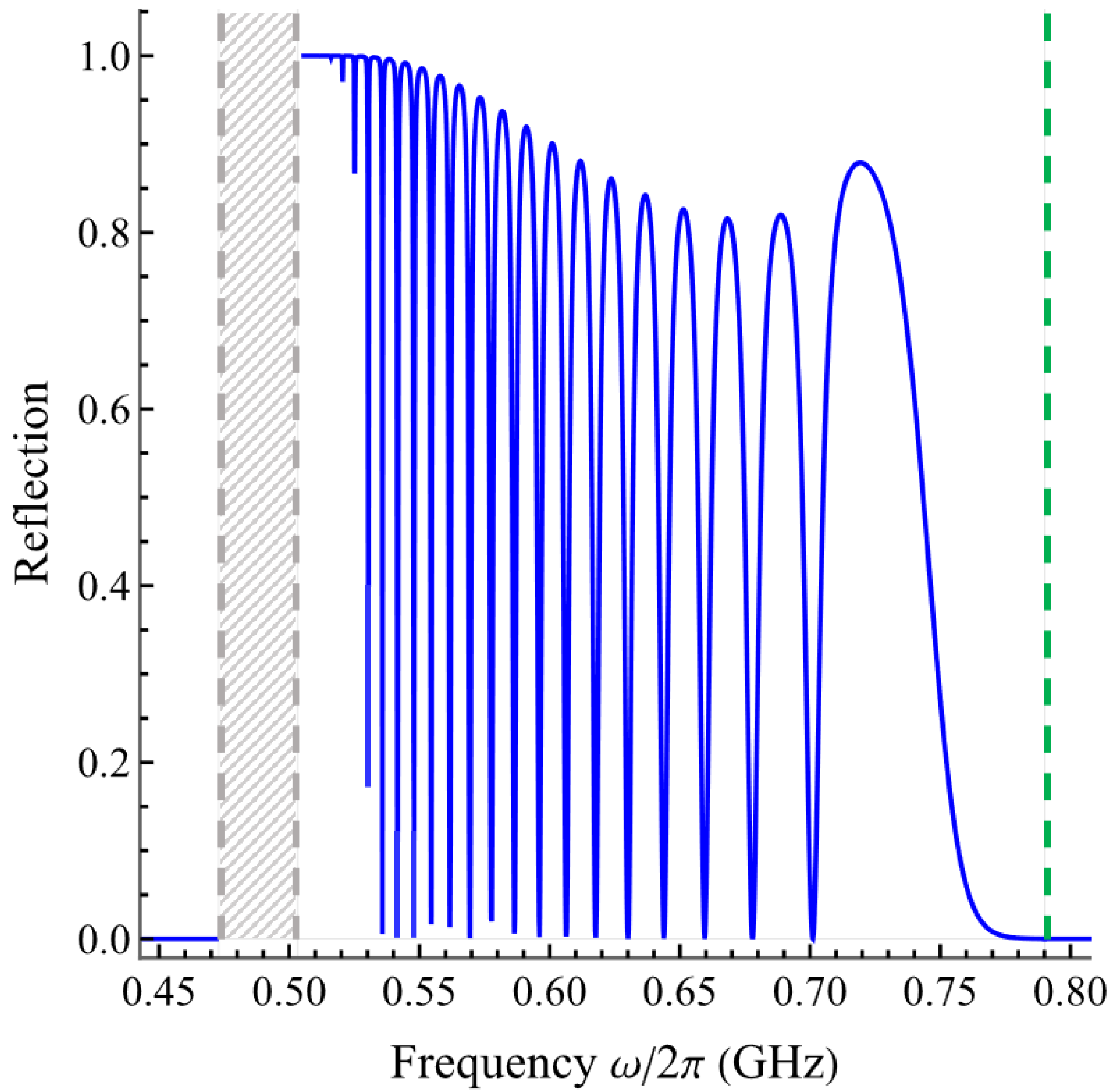

Figure 6.7: Percentage of SAWs reflected from wire generated magnetic field. Gray region shows where ME coupling takes place from bias internal field B_{YIG} in film. Green dashed line shows BVSW-SAW crossing frequency ω_0 from added magnetic field B_W from wire. Parameters: $L = 5\mu\mathrm{m}$, $B_{\mathrm{YIG}} = 7\mathrm{mT}$, $B_W = +13\mathrm{mT}$, $r_W = 10\mu\mathrm{m}$.

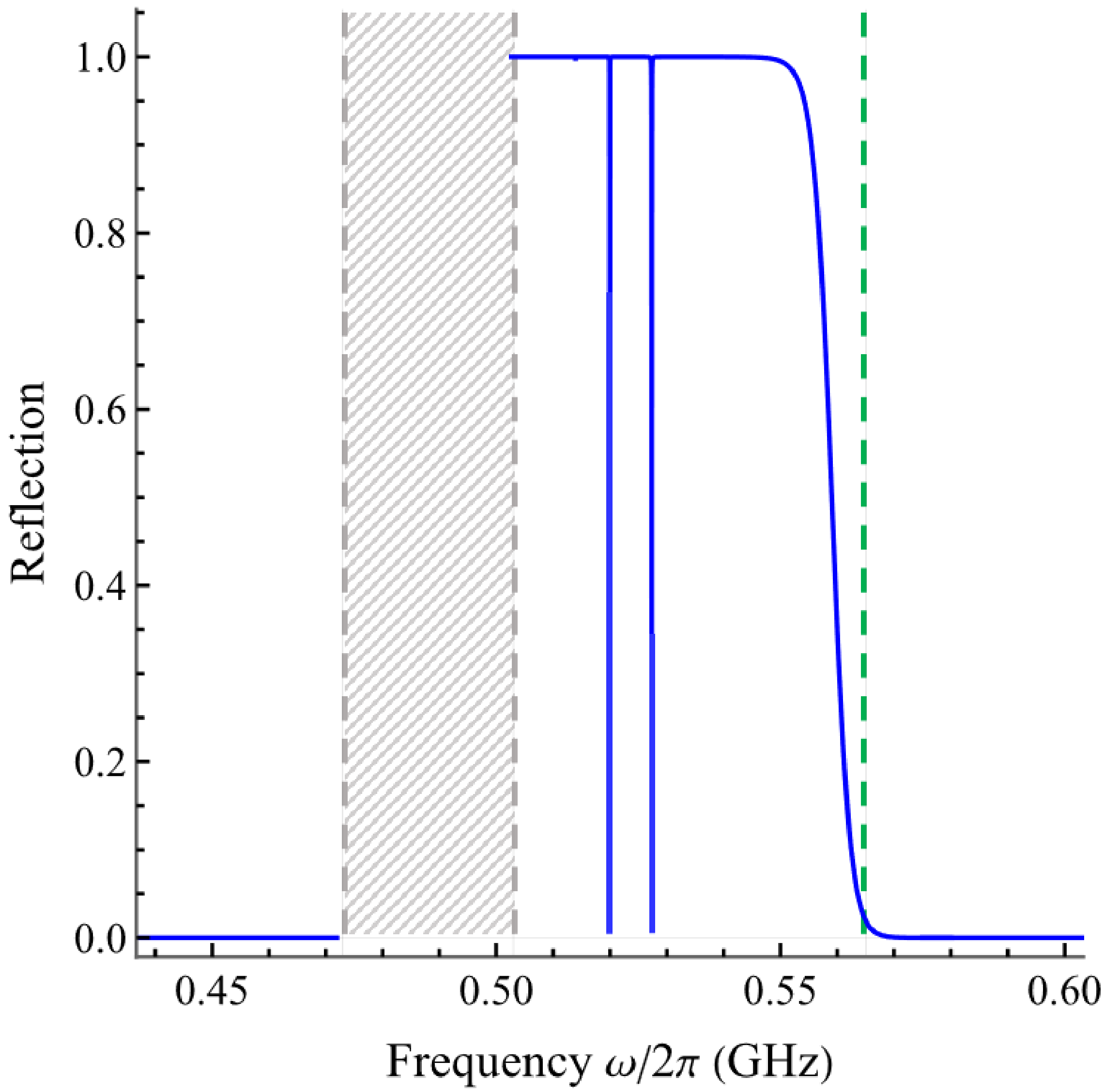

Figure 6.8: Percentage of SAWs reflected from wire generated magnetic field. Gray region shows where ME coupling takes place from bias internal field B_{YIG} in film. Green dashed line shows BVSW-SAW crossing frequency ω_0 from added magnetic field B_W from wire. Parameters: $L = 5\mu\text{m}$, $B_{\text{YIG}} = 7\text{mT}$, $B_W = +3\text{mT}$, $r_W = 40\mu\text{m}$.

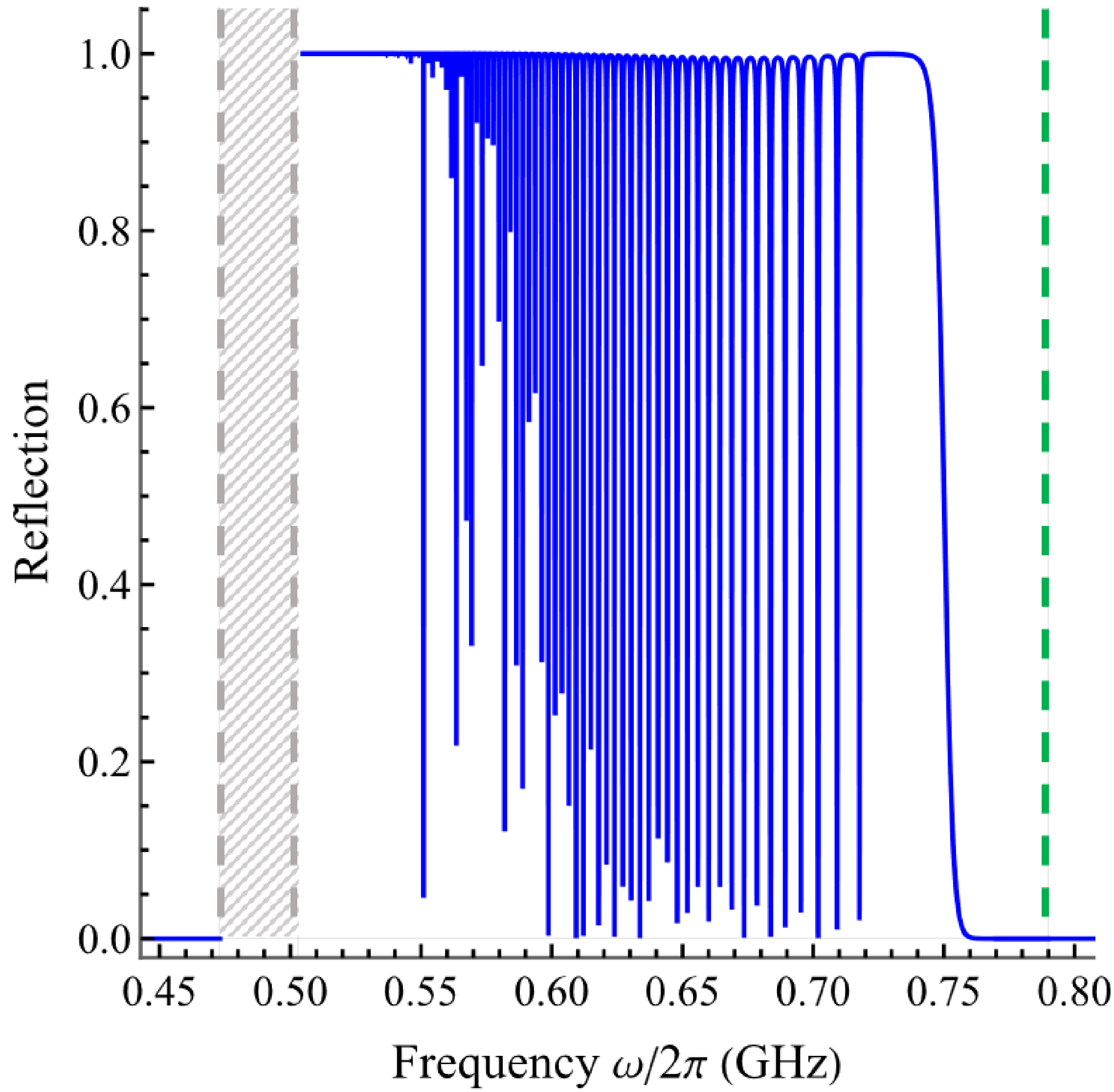

Figure 6.9: Percentage of SAWs reflected from wire generated magnetic field. Gray region shows where ME coupling takes place from bias internal field B_{YIG} in film. Green dashed line shows BVSW-SAW crossing frequency ω_0 from added magnetic field B_W from wire. Parameters: $L = 5\mu\mathrm{m}$, $B_{\mathrm{YIG}} = 7\mathrm{mT}$, $B_W = +13\mathrm{mT}$, $r_W = 40\mu\mathrm{m}$.

orange region (white region in Fig. 6.2a). This is because it only takes a small increment of the magnetic field to raise the BVSW dispersion relation to cross the SAW at this frequency. While a majority of the energy of the SAW is still reflected into a BVSW, which is now continuously excited from reflection, a small amount of energy leaks/tunnels into the 'magnetic well'. As time goes on the energy of the waves resonating within the 'magnetic well' begins to rise functioning as a resonating device. Within the well the SAW still propagates right and reflects, and the BVSW still propagates left and reflects. Eventually, as time goes on enough energy will build up in the resonator and leak to the other side of the inhomogeneous magnetic field opposite to where the SAW is continuously excited. The only draw back to due to the narrow width of the band shown in Fig. 6.8. Even for a long time of 500ns the power scale shown in Fig. 6.10 is still only 40% comparing the resonating wave to the excited SAW. Either way, the features of this ME are strongly shows on why this system should be favorable with future spintronic devices.

Back to our discussion on the remaining reflection results for Figures 6.6, 6.7, and 6.9. In comparison to Fig. 6.8 shows super narrow gaps, if we decreased the radius of the wire down to 10μm, wider tunneling frequency gaps appear as shown in Figures 6.6 and 6.7.

Comparing Figures 6.6 and 6.8 the only difference in parameters is the wire radius. The result to consider is you will get wider resonant gaps, but fewer of them. Even though we are only comparing one plot with one resonant gap and one plot with two resonant gaps, if we increase the magnetic field magnitude from the wire B_W the results of reflection will help confirm our previous statements.

For Fig. 6.7, still having a small wire radius of 10μm, but increasing the strength of the generated magnetic field from the wire, $B_W = +13$mT, reveals many more resonant tunneling gaps for SAWs and BVSWs in this system. The reflection factor may not be as

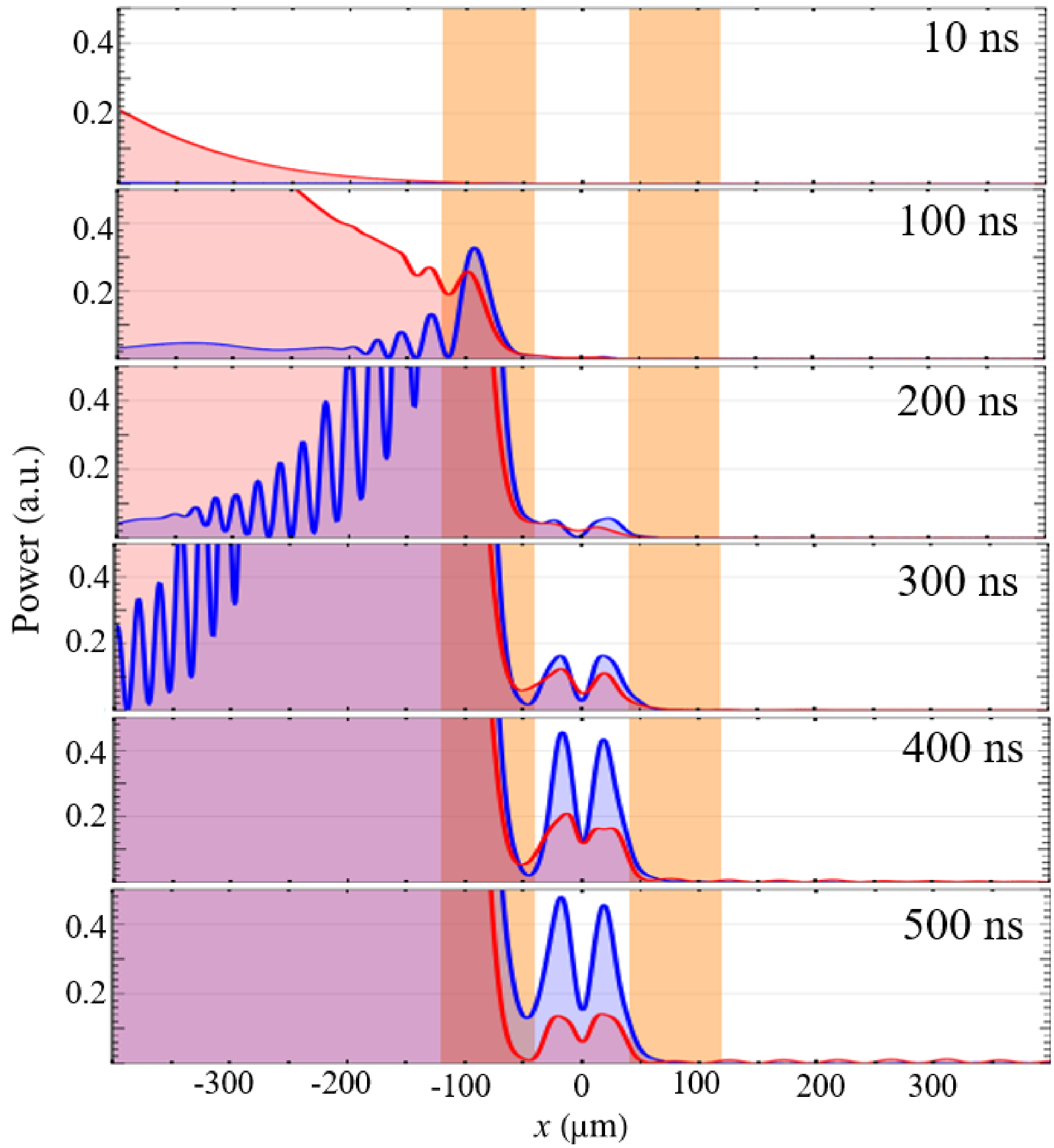

Figure 6.10: Orange bars represent the reflection point of the gradient magnetic field for waves at lower frequencies. Red shaded area is continuous excitation of SAWs. Blue shaded area is continuous excitation of BVSWs from reflection of SAW. Parameters: $\omega/2\pi = 0.52$GHz, $L = 5$μm , $B_{\mathrm{YIG}} = 7$mT, $B_W = +3$mT, $r_W = 40$μm.

strong with smaller wires, but new statements can be made about this system. Starting from the far right hump in Fig. 6.7 we see a wide resonant gap for our acoustic and spin waves, however, as frequency is lowered this gap becomes thinner and the jumps in 'frequency levels' become less and less.

These statements are confirmed for the last case in Fig. 6.9 using parameters as those for Fig. 6.8, but with $B_W = +13\text{mT}$. The somewhat raw data here has the better chance of reflection of acoustic and spin waves due to the much narrower widths of the resonant gaps. As one can see the jump between gaps does become smaller as frequency is lowered and we would eventually get a blue shaded region. Clearly, the number of data points need to be increased for accuracy.

Using concepts from quantum mechanics in a semi-classical approach we do offer a qualitative expression to help find the width and frequencies of these resonant gaps.

$$\int_0^{l(\omega)} \Big[k_a(x,\omega) + k_s(x,\omega)\Big]\, dx = 2\pi n \tag{6.10}$$

Here $l(\omega)$ is the length of the region between the points of the magnetic field needed to match the BVSW frequency with the excited SAW. The terms k_a and k_s are the quasi-wavevectors of the ME hybrid wave dependent on the spatial changes of the spectrum and frequency changes. The right hand side $2\pi n$ is usually πn in context of [103], [241], but because we have two waves in resonance it takes an extra phase for the system to repeat itself.

However, for real devices wanting to use these resonant effects damping must be considered which will greatly affect our results. Damping can be included in our matrix from (6.7). The top left entry will have the extra term $\eta/v^{(\mathrm{SAW})}$ as damping for SAW in space, and the bottom right entry has the extra term $\Gamma/v^{(\mathrm{BVSW})}$ as damping for the BVSW in space. Remember that coupling should always be greater than both wave damping factors to see any effects. These new reflection results from (6.7) with damping are shown

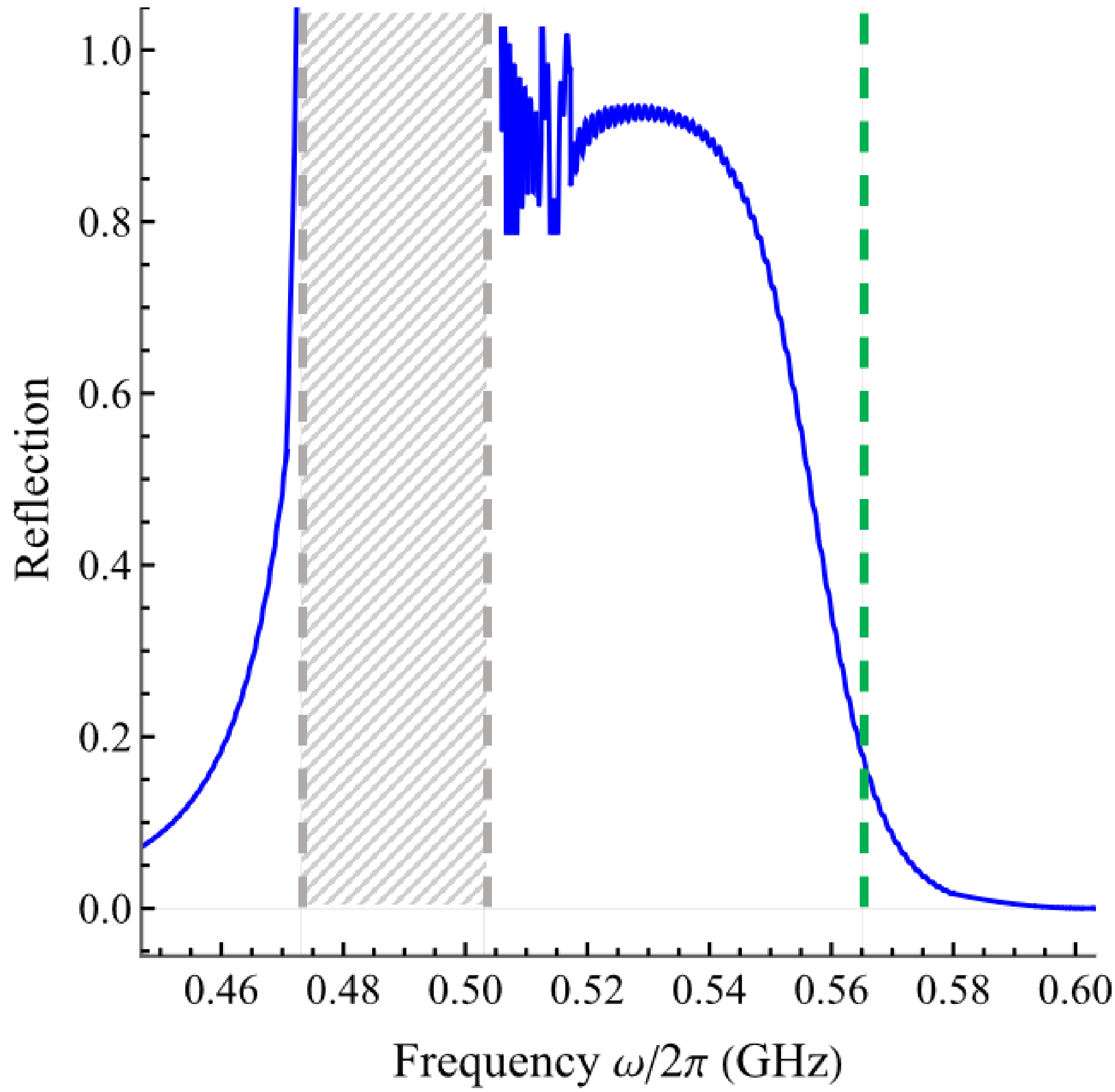

Figure 6.11: Percentage of SAWs reflected from wire generated magnetic field. Gray region shows where ME coupling takes place from bias internal field B_{YIG} in film. Green dashed line shows BVSW-SAW crossing frequency ω_0 from added magnetic field B_W from wire. Parameters: $L = 5\mu\text{m}$, $B_{\text{YIG}} = 7\text{mT}$, $B_W = +3\text{mT}$, $r_W = 10\mu\text{m}$.

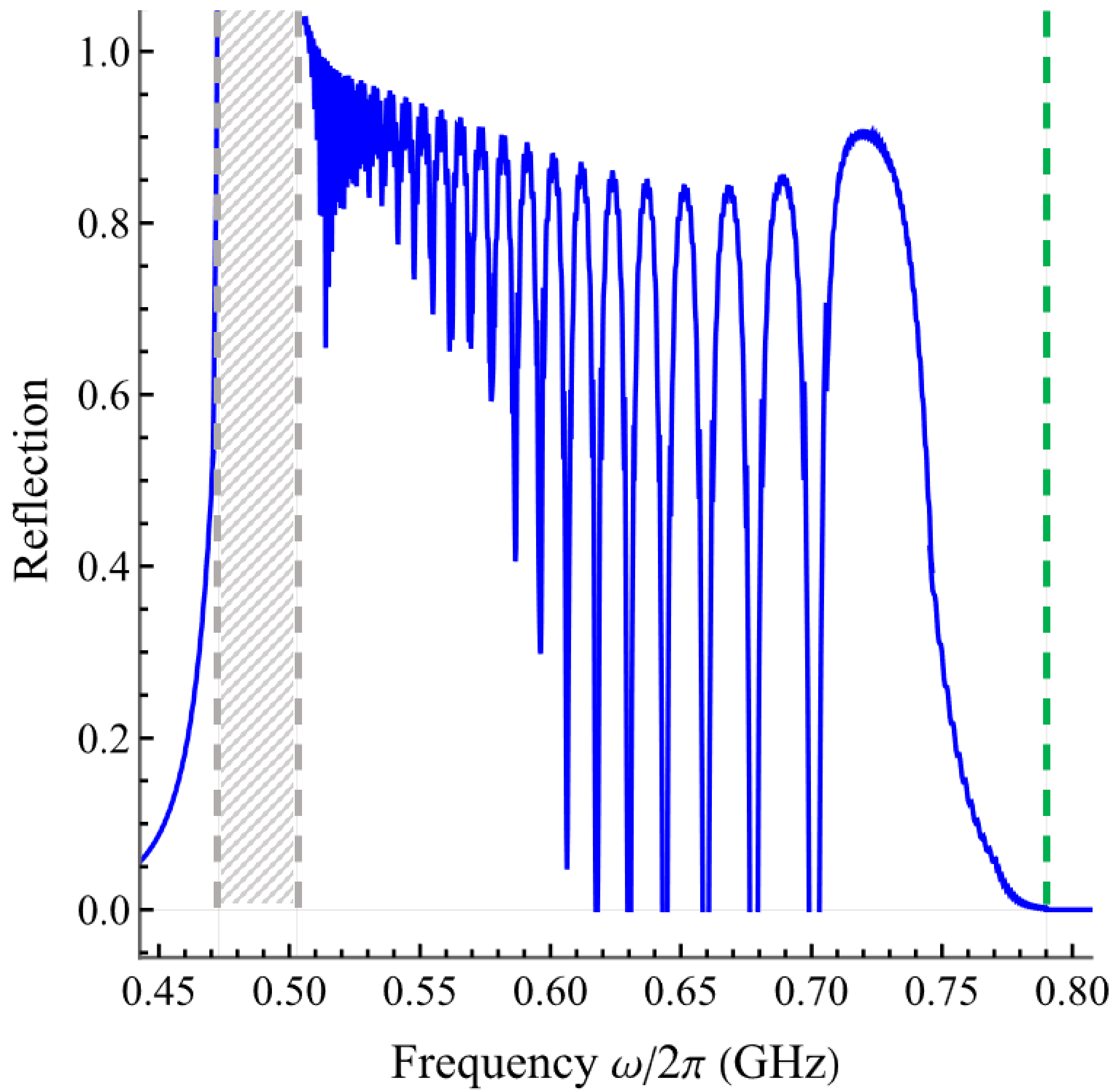

Figure 6.12: Percentage of SAWs reflected from wire generated magnetic field. Gray region shows where ME coupling takes place from bias internal field B_{YIG} in film. Green dashed line shows BVSW-SAW crossing frequency ω_0 from added magnetic field B_W from wire. Parameters: $L = 5\mu\text{m}$, $B_{\text{YIG}} = 7\text{mT}$, $B_W = +13\text{mT}$, $r_W = 10\mu\text{m}$.

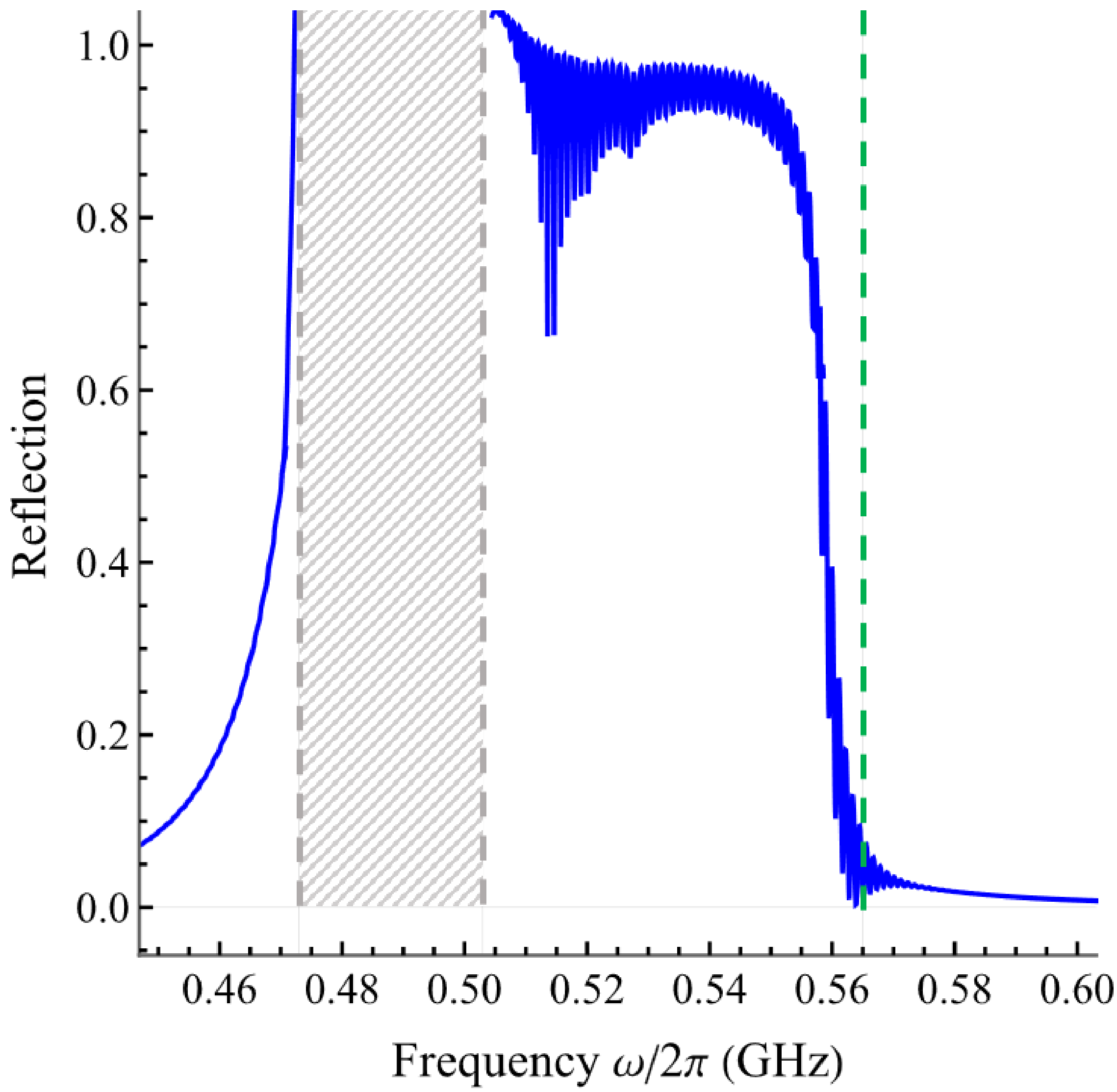

Figure 6.13: Percentage of SAWs reflected from wire generated magnetic field. Gray region shows where ME coupling takes place from bias internal field B_{YIG} in film. Green dashed line shows BVSW-SAW crossing frequency ω_0 from added magnetic field B_W from wire. Parameters: $L = 5\mu\text{m}$, $B_{\mathrm{YIG}} = 7\text{mT}$, $B_W = +3\text{mT}$, $r_W = 40\mu\text{m}$.

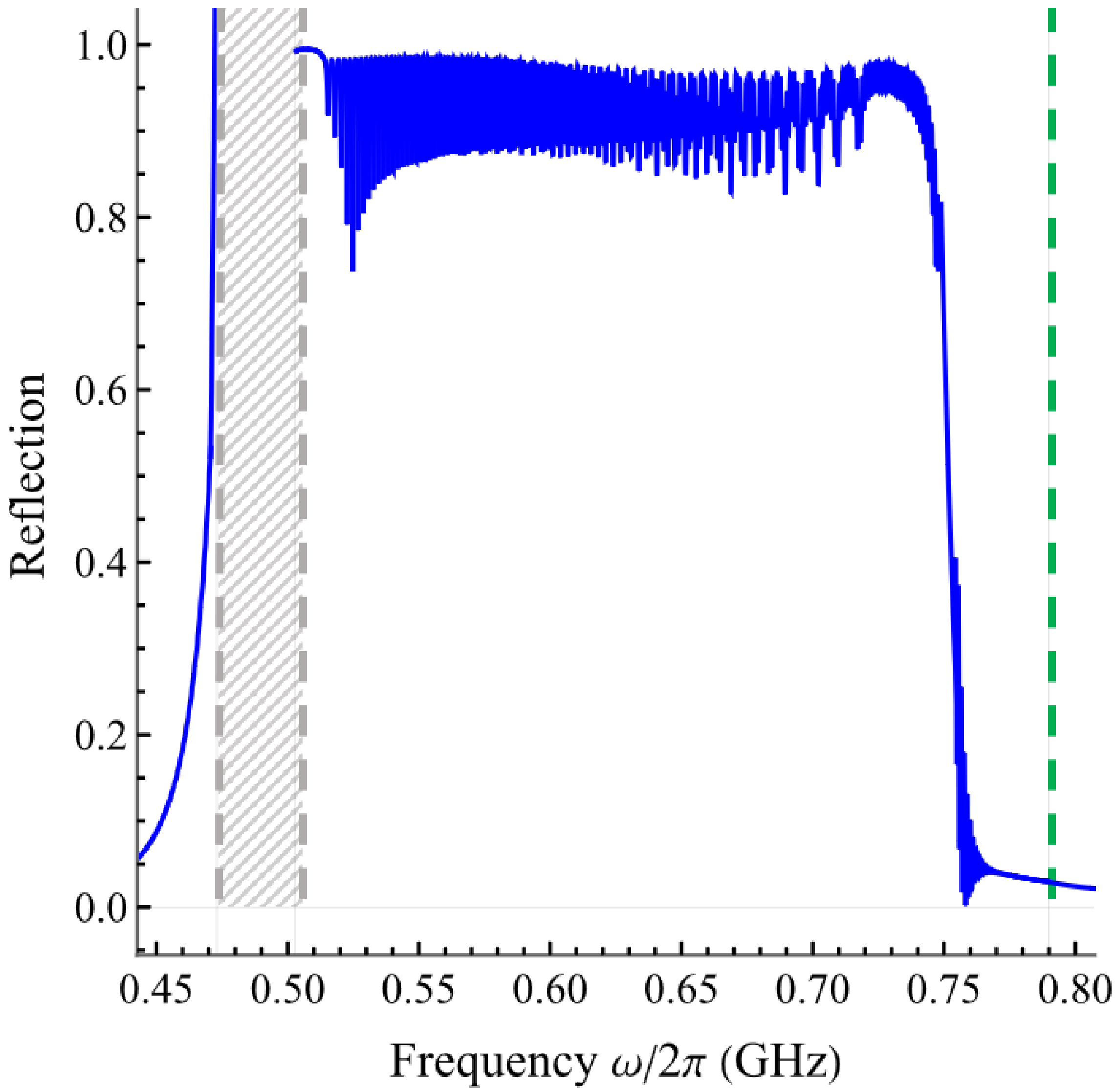

Figure 6.14: Percentage of SAWs reflected from wire generated magnetic field. Gray region shows where ME coupling takes place from bias internal field $B_{\rm YIG}$ in film. Green dashed line shows BVSW-SAW crossing frequency ω_0 from added magnetic field B_W from wire. Parameters: $L = 5\mu$m , $B_{\rm YIG} = 7$mT, $B_W = +13$mT, $r_W = 40\mu$m.

in Figures 6.11-6.14. They are presented in the same order as Figures 6.6-6.9 in context of material parameters.

Introducing damping to our very first case of calculating reflection (Fig. 6.8), damping in Fig. 6.13 does destroy our nice resonant tunneling gaps. The same result is found when increasing B_W for Fig. 6.14 (Fig. 6.9 with damping factors). However, hope of an applicable resonating device is still possible when considering a smaller wire radius. In Fig. 6.11 (Fig. 6.6 with damping), we lose our single wide resonant gap when the increase of B_W is small. But when the magnetic field from the wire B_W is large and the radius is small $r_W = 10\mu\text{m}$, we still have resonant tunneling of the ME hybrid system. This is shown in Fig. 6.12 (Fig. 6.7 with damping).

The fact we achieve similar behavior of reflection next to the gray range of frequencies says, at least numerically, that these frequencies feel the almost infinitely many 'frequency levels' allowed to support resonant tunneling. This would explain the dip in reflection near the gray region for all damping figures. One would argue this situation is analogous to electron energy levels in an atom where the outer shell quantized levels from the potential well begin to stack on top one another.

While these reflection results may not give the best ideal scenario to support real resonant devices a sweet spot can be found when considering slightly thicker wires that definitely would support the larger currents for more tunability. Either way having the BVSW interact with SAW or not is great for spintronic devices. This mainly can act as a filter for BVSW (or vice versa with SAWs). This feature acts as a switch that can be turned on and off. Referring to Fig. 6.2, if we excite either wave at frequency ω_0 where the YIG film is kept at a bias internal magnetic field (red region Fig. 6.2a), both waves will propagate through YIG with no interactions. However, if the current in the wire is turned on to raise or lower the magnetic field locally somewhere in YIG for a moment (green region Fig. 6.2a) the dispersion relations would intersect at this frequency and one wave will transform and reflect backward. The added benefit to mention is the added quantum tunneling feature that allows for more configuration with more than one excited frequency. More benefits of this ME hybrid system will be shown when manipulating the magnetic field in real time as discussed in the next section.

6.3 Results on ME coupling from Manipulation of the Magnetic Field

Looking back at Figures 6.3 and 6.4, we notice the SAW, at time mark 40ns, is propagating in a region of space away from the wire (green region) and this also applies to the BVSW as well at the time mark of 180ns. In the region away from the wire (red region Fig. 6.2a) we have a fixed hybridized spectrum as shown in Fig. 6.2b. We clearly know the initial wavevector k and frequency $\omega/2\pi$ that the SAW has, but what about the BVSW? Where would the BVSW be found on its curved dispersion relation in the red region (Fig. 6.2c) away from the wire? We refer to our mathematical techniques for finding the BVSW wavevector and frequency.

Our system of equations for waves in real space (6.3) are dependent on the linearized form of the wave dispersion relations in (6.2). We are able to plot a coupled hybrid system of (6.2) using (3.13) as shown in Fig. 6.15. The yellow bar in Fig. 6.15 is the forbidden frequency gap of the coupled wave spectrum, and is shown for a region of space far away from the wire. Our initial SAW in Figures 6.3 and 6.4 has wavevector $k = 1$rad/μm and frequency $\omega/2\pi = 0.565$GHz. After the SAW transforms to the BVSW, that newly created BVSW must lie on the dispersion relation shown in Fig. 6.15 as it propagates in the YIG film away from the wire. We highlight two spots, using empty white circles in Fig. 6.15, on the BVSW dispersion relation for the possible wave coordinates of the propagating BVSW. The solution to determine which spot on the purple dashed line is correct is to perform a Fourier Analysis [77] on the BVSW at the very last time stamp of 180ns in Fig. 6.3 and 6.4.

Figure 6.16 shows the Fourier analysis specifically for Fig. 6.4 for the first and last time stamps in comparing the SAWs and BVSWs wavevector and frequency coordinates. Previously stated, the width of the propagating wave packet has a range of frequencies and wavevectors centered around the initial SAW one wishes to excite exactly. From Fig. 6.16 the 40ns time shows the SAW has a central wavevector of $k = 1$rad/μm and frequency $\omega/2\pi = 0.565$GHz corresponding to our stated initially excited SAW. The frames below give us the central wavevector and frequency of the BVSW for the films (Figures 6.3-6.5). The smaller red humps in these frames are the remnants of the SAW packet that did not successful transform. Analyzing the blue hump tells us the wavevector and frequency of the BVSW. The central wavevector of the BVSW is found roughly to be $k = 0.578$rad/μm with a frequency of $\omega/2\pi = 0.565$GHz. This means there was a shift in the wavelength only when the wire transformed the SAW into a BVSW. This is a truly fascinating result.

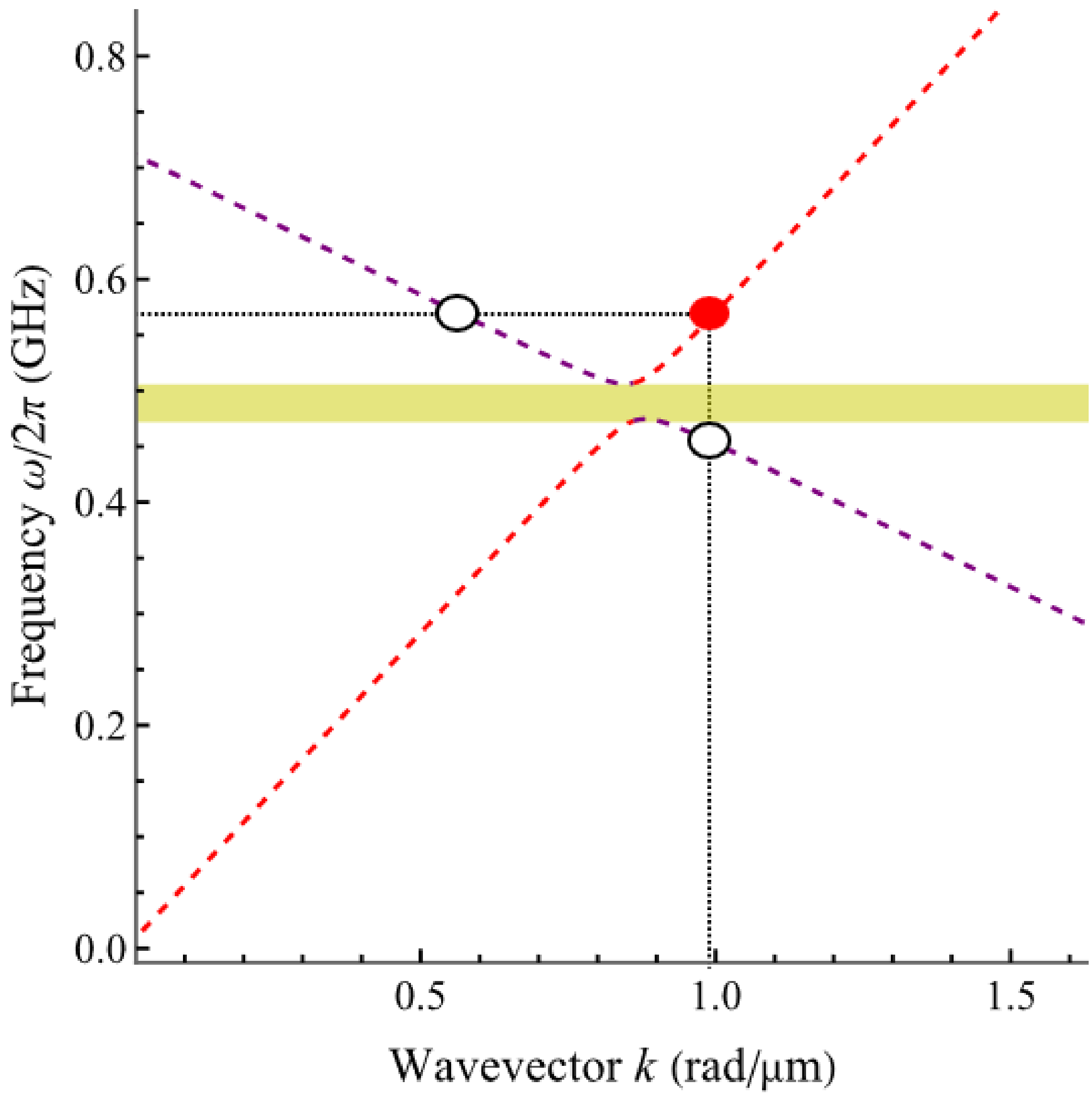

Figure 6.15: Linearized system of ME coupling of SAW-BVSW. Red dot shows initial excited SAW with defined frequency and wavevector from black dotted lines. Empty circles represent possible BVSW locations after transformation of SAW. Parameters: $L = 5$μm , $B_{\mathrm{YIG}} = 7$mT.

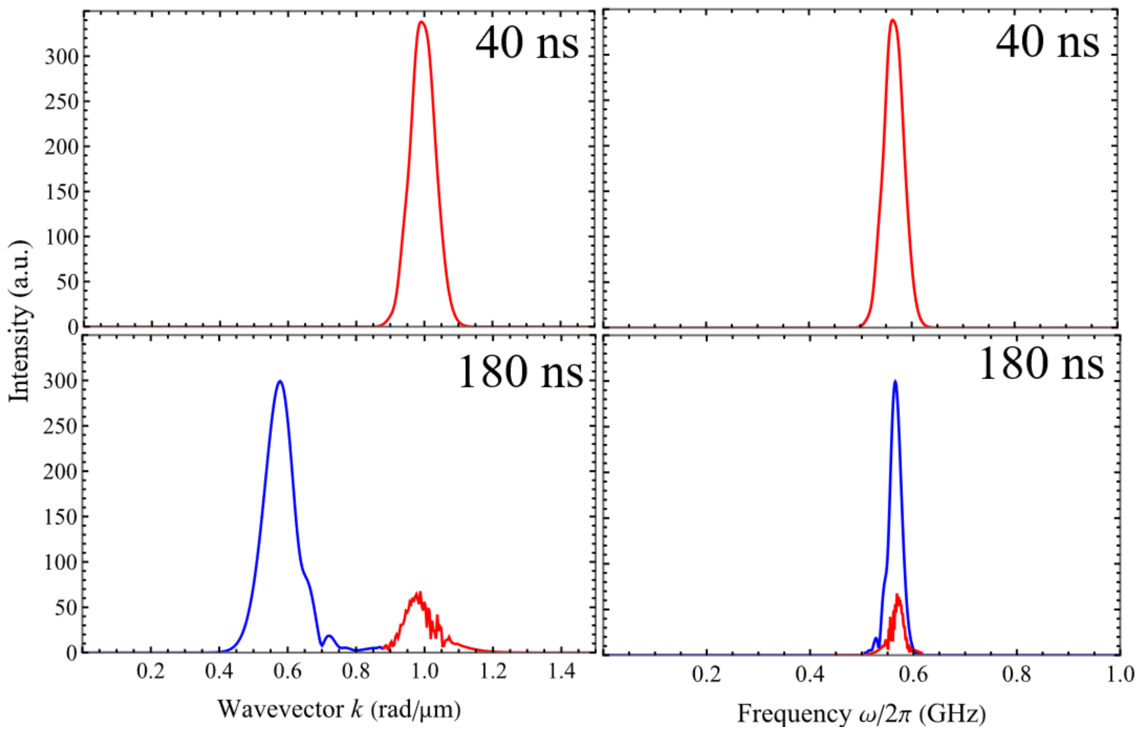

Figure 6.16: Plotted wavevector and frequency intensity of propagating wave packets from the first three simulations. Initially at the 40ns time mark only the SAW traveling with central wavevector $k = 1$rad/μm and frequency $\omega/2\pi = 0.565$GHz. At the 180ns time mark, BVSW is propagating with a central wavevector of $k = 0.55$rad/μm and frequency $\omega/2\pi = 0.565$GHz. Parameters: $L = 5$μm , $B_{\text{YIG}} = 7$mT, $B_W = +3$mT

Back to Fig. 6.15, we can confidently state the BVSW lies on the purple dashed line at wavevector $k = 0.578$rad/μm and frequency $\omega/2\pi = 0.565$GHz. A shift in the wavevector number is significant and, as we'll show later, helps lead into a larger topic of possible signal operations. This is only possible due to the physical property from the YIG films magnetic field. The magnetic field changes the properties of the YIG film and which type of SWs it may or may not support. As the localization of the wire above the YIG film introduces spatial changes to the film, the magnetic field can change in time homogeneously throughout the YIG film leading to a temporal effect. These features categorize the YIG film as what is known as a space-time meta-material. A further detailed reading on these materials and their functions can be found in [238], [242]–[244]. The reason their was a shift in the wavevector number was because the spatial localization of the wire's inhomogeneous magnetic field affects the momentum space. The SAW is propagating along with some momentum and feels this "magnetic barrier" from ME coupling. The SAW wave packet then reflects off this "magnetic barrier" as a BVSW as one of the two consequences. The other consequence being the change in wavevector number due to the change in momentum from both direction and magnitude.

However, due to the properties of a space-time meta material, such as YIG, we can also show how the SAW packet may transform to a BVSW changing only frequency. We refer back to Fig. 6.15 where the BVSW packet can follow the vertical dashed line and end up at a lower frequency than the initial SAW frequency. If the internal magnetic field in the YIG film changed harmoniously in time this would affect the temporal domain of the wave packet via frequency.

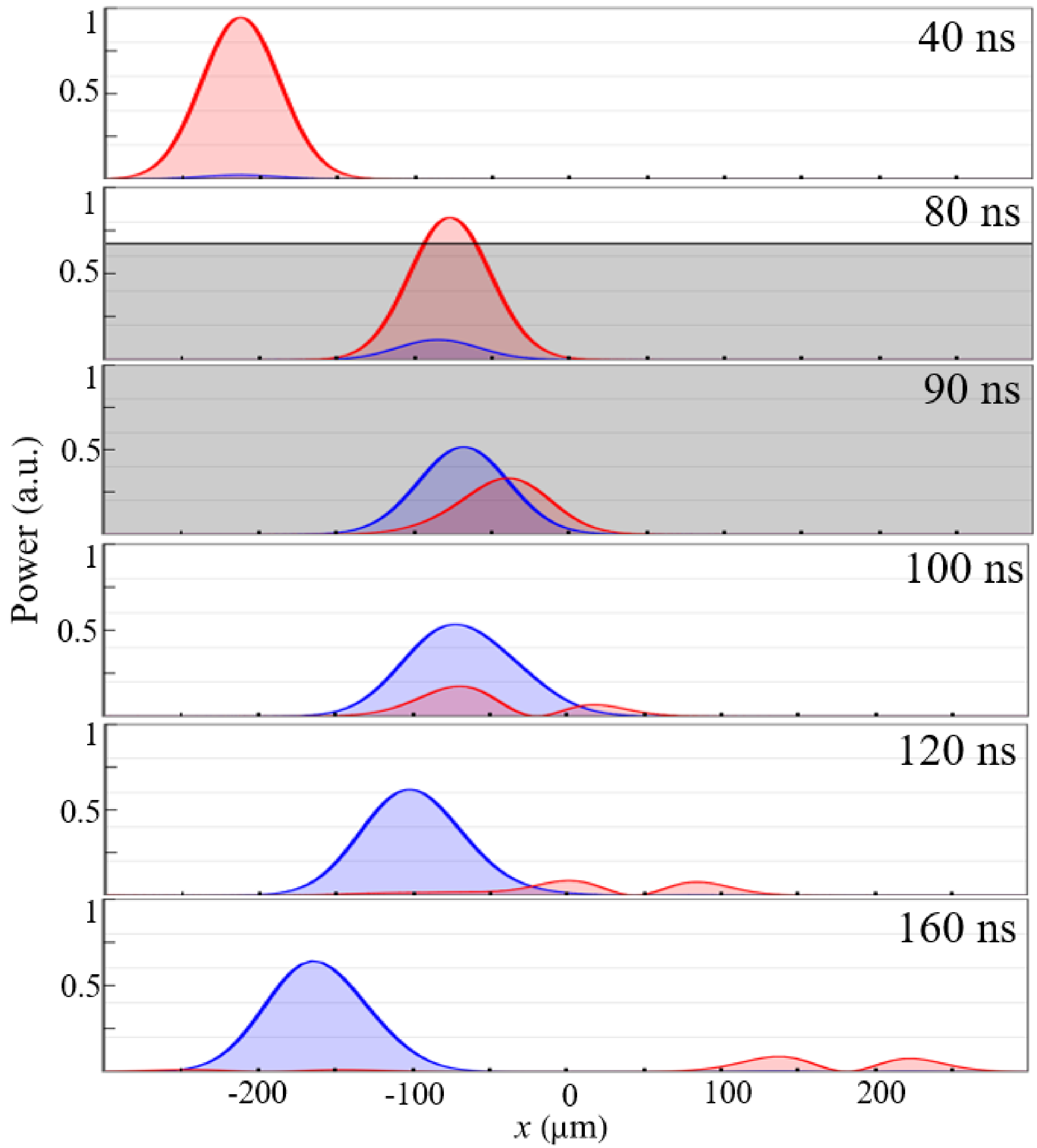

Figure 6.17: Simulation of SAW (red hump) propagating in YIG film. In 80ns time frame the (gray shaded region) internal magnetic field is increasing from $B_{\mathrm{YIG}} = 7\mathrm{mT}$ to $B_{\mathrm{YIG}} = 10\mathrm{mT}$. At 90ns time frame magnetic field continues to increase while SAW converts to BVSW (blue hump). At 100ns time frame the YIG film's internal magnetic field immediately reverts back to $B_{\mathrm{YIG}} = 7\mathrm{mT}$ and hybrid waves settle. Last two time frames emphasize group velocity of different waves and effectiveness of conversion via power magnitude. Parameters: $L = 5\mu\mathrm{m}$, B_{YIG} =7mT, $\Delta B(t) = +3\mathrm{mT}$

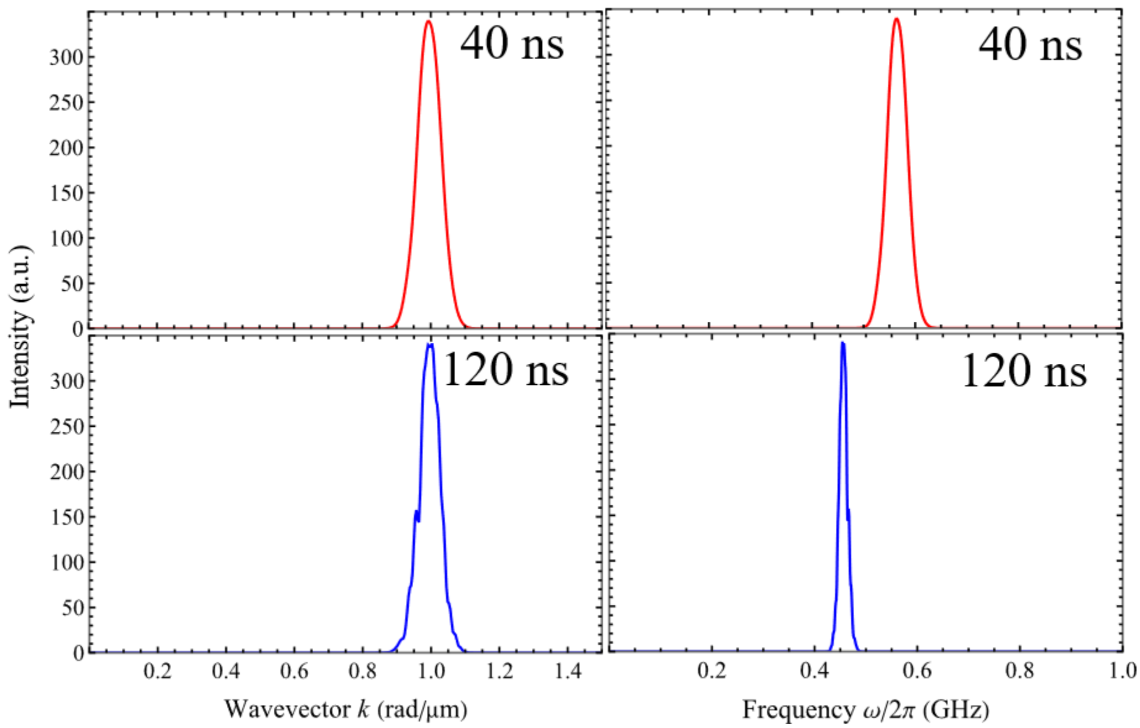

Figure 6.18: Plotted wavevector and frequency intensity of propagating wave packets from simulation in Fig. 6.17. Initially at the 40ns time mark only the SAW traveling with central wavevector $k = 1$rad/μm and frequency $\omega/2\pi = 0.565$GHz. At the 180ns time mark, BVSW is propagating with a central wavevector of $k = 1$rad/μm and frequency $\omega/2\pi = 0.456$GHz. Parameters: $L = 5$μm , $B_{\text{YIG}} = 7$mT, $\Delta B(t) = +3$mT

We prove the above statements by running another simulation where the whole internal magnetic field B_{YIG} for YIG is dependent on time. The initial state of the simulation is the same with the SAW having wavevector $k = 1$rad/μm and frequency $\omega/2\pi = 0.565$GHz. The YIG film starts with $B_{\text{YIG}}(t = 0) = 7$mT and is 5μm thick. Figure 6.17 shows this simulation with the same notations of the SAW being the red hump and the BVSW as the blue hump. The difference here is that no wire is shown via the green region. Instead in time frames 80ns and 90ns their is a gray shaded region that rises between the two frames. This gray region indicates that the internal magnetic field everywhere in the YIG film is rising from 7mT to 10mT harmoniously. The next frame at 100ns shows the hybrid system settling after a sharp decrease back to the initial $B_{\text{YIG}} = 7$mT. The timing to stop the increase of the films internal magnetic field and let it revert back to the films original field is proportionate to a quarter of the ME coupling rate. This allows for the best power conversion between the two waves. In the last two frames of Fig. 6.17, we successfully converted the SAWs central frequency range into the BVSW. The two small SAW humps show the end points of the wider SAW frequency range that did not fit into the ME frequency gap $\Delta\omega_{\text{ME}}$.

Performing the same Fourier analysis on this simulation reveals the intriguing affects of a space-time meta-material. Figure 6.18 shows the intensity of the wavevector for both the SAW at the 40ns and the BVSW at the 120ns from Fig. 6.17. In this case when the whole film changed magnetic field magnitude the wavevector stayed the same. However, looking to the right in Fig. 6.18 we notice a shift in intensity of frequency. The BVSW has a lower frequency of $\omega/2\pi = 0.456$GHz compared to the initial SAW frequency of $\omega/2\pi = 0.565$GHz. These results in comparing Figures 6.16 and 6.18 show that a ME coupled system with respective magnetic field changes, via localized external wire or internally throughout the whole film, may have different varying affects on the initial and final wavevector and frequency numbers of the waves.

6.3.1 Frequency Inversion Technique

We now provide a simple example of a device functionality that could be expanded upon in future outlooks. Utilizing both the change of magnetic field from the wire and internal field of the whole film, we are able to change the wavevector number and frequency for either wave. We continue with the simple basis built from earlier, an initial SAW is excited at some frequency and transforms to a BVSW via inhomogeneous magnetic field from a wire. The BVSW then transforms into a SAW by a change in the films internal magnetic field. The new SAW will have a different wavevector and frequency than the initial excited SAW.

We show in Fig. 6.19, this change of wavevector and frequency for two SAWs as this operation is known as frequency inversion. Again, the dashed lines represent the SAW (red) and BVSW (purple) dispersion relations using (6.2) for a 5μm thick YIG film at 7mT. Initially, we begin with two SAWs indicated by the red and orange dots with wavevectors 0.93rad/μm, 0.97rad/μm, and frequencies 0.53GHz, 0.55GHz, respectively. The first step in this operation is to use the inhomogeneous magnetic field from the wire to change the wavevector. For the BVSW disperion to interact with these SAW frequencies we must raise the magnetic field. The red (orange) SAW then becomes the blue (cyan) BVSW. The new wavevector numbers for the BVSW are 0.71rad/μm for the cyan wave and 0.63rad/μm for the blue wave. The next step is having the BVSWs interact with the SAW spectrum again, but with a change in frequency this time. By decreasing the YIG films whole internal magnetic field, the BVSW dispersion relation will move the blue and cyan BVSW done to the point where the ME gap will transform the waves. The final red and orange SAWs will have wavevectors 0.71rad/μm, 0.63rad/μm, and frequencies 0.4GHz and 0.36GHz. Notice initially the red SAW had a lower frequency than the orange and the difference between them was 0.2GHz. The final red SAW now has a higher frequency with a difference of roughly 0.4GHz. This operation is how frequency inversions in devices works conceptually, with the added bonus of our system expanding the frequency difference between them. This is due to the difference of group velocities from two different waves.

Figure 6.20 shows the simulation we ran following the steps described previously for Fig. 6.19 showing a frequency inversion operation. We initially, in the 5ns time frame, have the two SAWs red and orange propagating to the right with their quasi-magnetic components. The red wave is out front and the orange behind initially. The red and orange wave packets are wider with a width of $w = 150\mu m$ to tighten the range of frequencies they hold to avoid interaction with the fixed ME gap in the YIG film with thickness 5μm and internal field 7mT. At the 130ns time frame the wires inhomogeneous magnetic field (gray shaded region) is shown to raise the local magnetization by $B_W = +3mT$. This is the same scenario as the first three simulations in Figures 6.3-6.5. The red SAW is almost fully transformed and the orange SAW has just reached the wire's region of influence. In the 260ns time frame the blue and cyan BVSWs propagate, with half the speed of a SAW, to the left. The power of these waves are higher with thinner widths as well. In the 300ns time frame, below the wave packets is a gray region that appears throughout space. This gray region indicates that the magnetic field is decreasing everywhere in the whole YIG film from $B_{\text{YIG}} = 7mT$ to $B_{\text{YIG}} = 2mT$. The 345ns time frame shows when the films internal magnetic field is decreased enough so the BVSWs convert back to SAWs.

This timing is even trickier with two waves. We don't want to have the blue BVSW, that requires less of a magnetic field change, to become a standing resonant wave. This is because the blue BVSW feels the ME gap twice. This 0.4GHz frequency point (blue-red conversion) feels the gap once when the magnetic field decreases to the 0.36GHz frequency point (cyan-orange conversion) and again when the magnetic field resets back to its initial homogeneous state in the film.

Analyzing the last time frame at 450ns, notice the red SAW in now behind the orange SAW. The two wave packets have swapped positions, and become more localized via peak power and width of wave packet. While this exciting consequence is fascinating we have yet to begin to discuss the potential connecting operations that could be done with this ME coupling tunability. Before that we must confirm the frequency inversion of these SAW was successful as well.

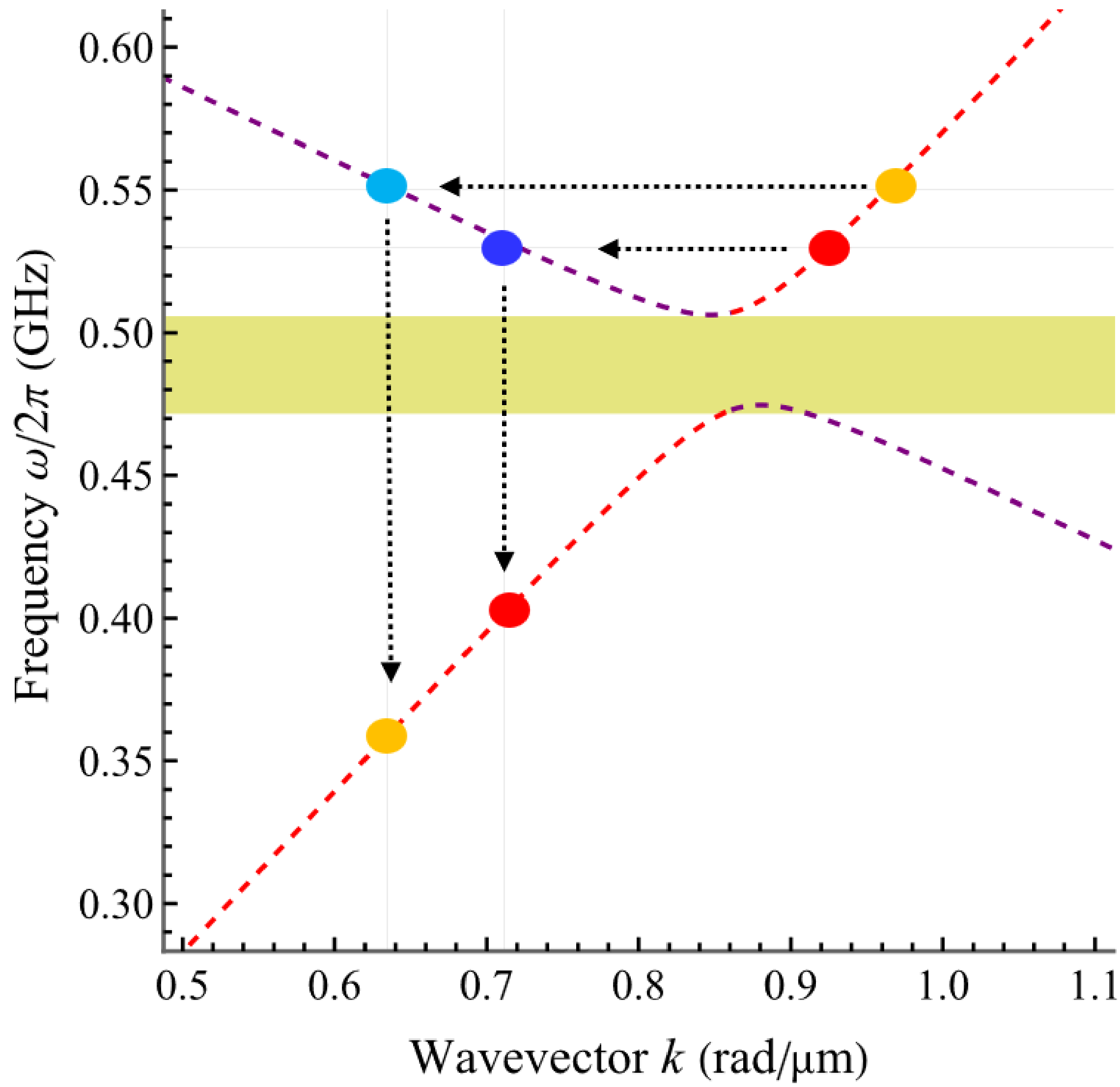

Figure 6.19: Plotted spectrum of hybridized waves using (6.2). Dots indicate waves with specific wavevectors and frequencies. Black dotted arrows indicate steps of frequency inversion from converting one wave to another. Horizontal arrows indicate change via inhomogeneous magnetic field from wire in space. Vertical arrows indicate change via magnitude of internal magnetic field in whole films in time. Parameters: $L = 5$µm , $B_{\mathrm{YIG}} = 7$mT, $B_W = +3$mT, $\Delta B(t) = -5$mT.

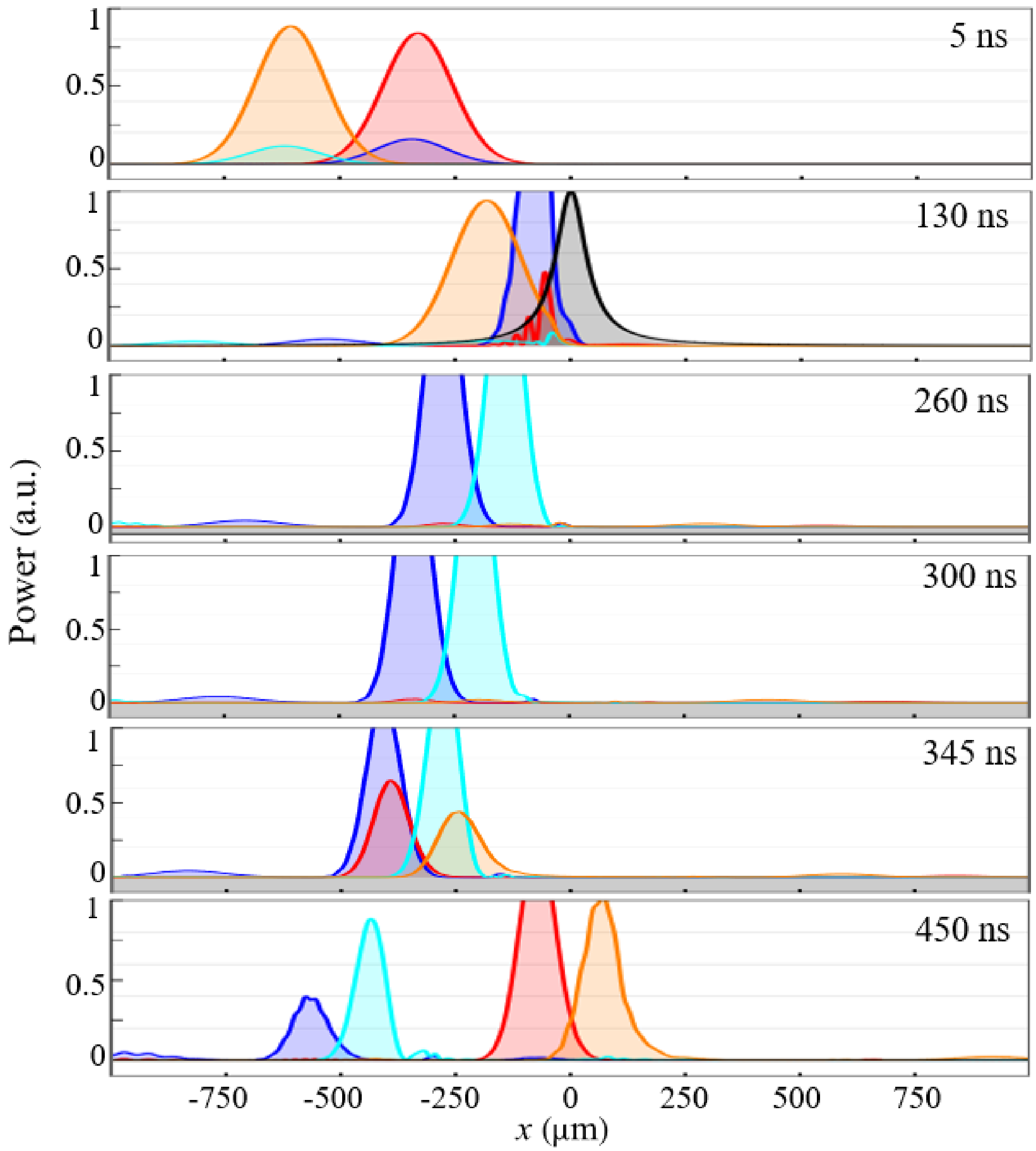

Figure 6.20: Simulation of SAWs (red, orange) at two different initial frequencies propagating in YIG film. The 130ns time frame shows the inhomogeneous magnetic field change from the wire (gray shaded region). At 260ns time frame the BVSWs (blue, cyan) propagate slower to the left. At 300ns time frame the YIG film's internal magnetic field begins to decrease in magnitude from $B_{\mathrm{YIG}} = 7\mathrm{mT}$ to $B_{\mathrm{YIG}} = 2\mathrm{mT}$. At 345ns the BVSWs transform into SAWs. At 450ns difference in power levels, position of waves, and widths of SAWs are shown to be different than starting wave packets. Parameters: $L = 5\mu\mathrm{m}$, $B_{\mathrm{YIG}} = 7\mathrm{mT}$, $B_W = +3\mathrm{mT}$, $\Delta B(t) = -5\mathrm{mT}$, $\omega^{(\mathrm{SAW})}_{\mathrm{Red}}/2\pi = 0.53\mathrm{GHz}$, $\omega^{(\mathrm{SAW})}_{\mathrm{Orange}}/2\pi = 0.55\mathrm{GHz}$

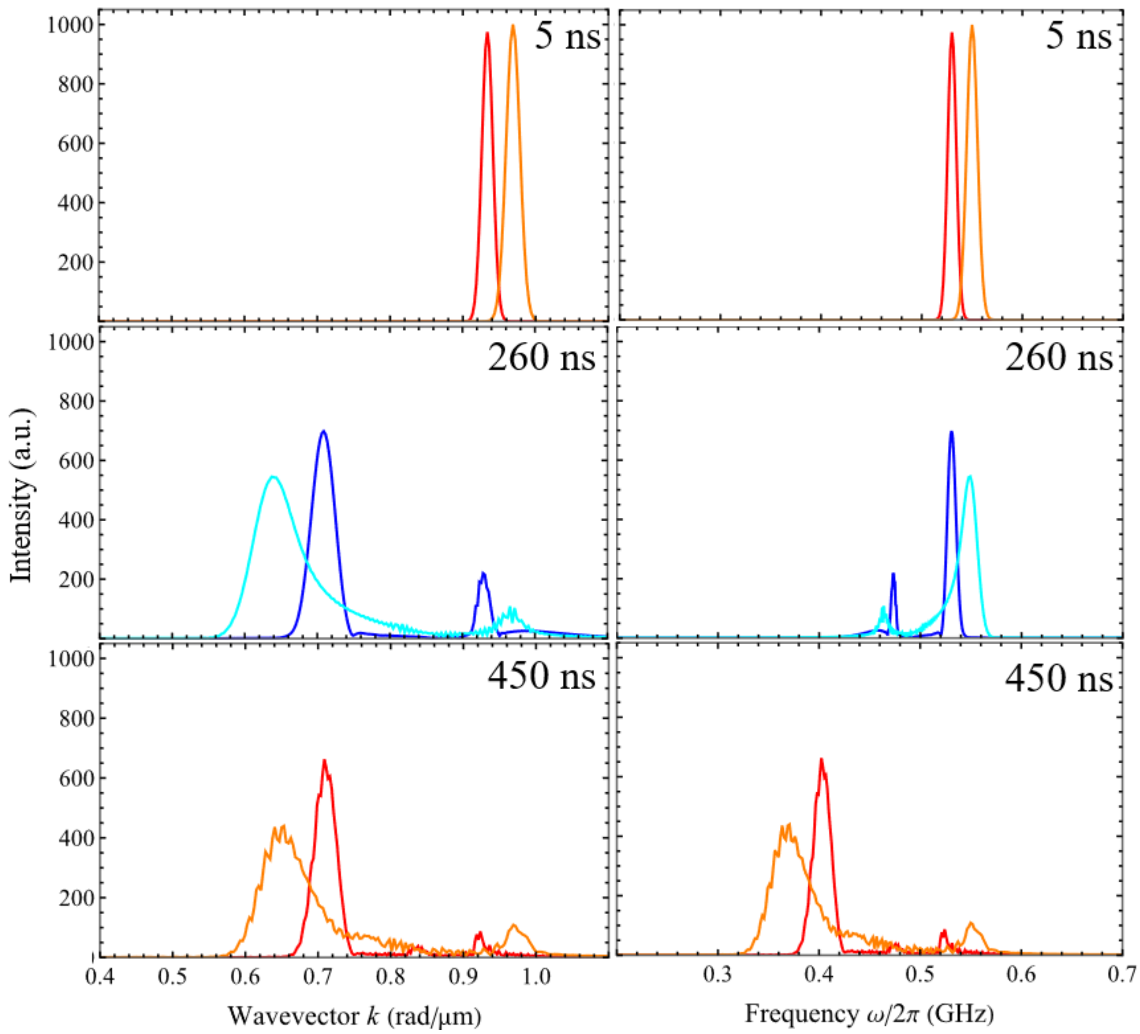

Figure 6.21: Plotted wavevector and frequency intensity of propagating wave packets from simulation in Fig. 6.20. Both SAWs have same width. At 5ns both SAWs have initial wavevectors 0.93rad/μm, 0.97rad/μm, and frequencies 0.53GHz, 0.55GHz, for red and orange respectively. At 260ns snapshot Fourier analysis is done on BVSWs which have wavevectors 0.71rad/μm, 0.63rad/μm, and frequencies 0.53GHz, 0.55GHz, for blue and cyan respectively. Final Fourier analysis of system is done at 450ns snapshot on SAWs with red and orange having wavevectors 0.71rad/μm, 0.63rad/μm, and frequencies 0.4GHz, 0.36GHz, respectively. Parameters: $L = 5$μm, $w = 150$μm, $B_{\mathrm{YIG}} = 7$mT, $B_W = +3$mT, $\Delta B(t) = -5$mT.

Figure 6.21 provides snapshots in time showing the success of the frequency inversion of the SAWs in the SAW spectrum. As a big picture detail, since we increased the width of the wave packets from 50μm in all the simulations before to 150μm in Fig. 6.20, the intensity has increased as well. The higher peaks confirm where our central wavevectors and frequencies are located along the axes. Initially, at 5ns, both SAWs have initial wavevectors 0.93rad/μm, 0.97rad/μm, and frequencies 0.53GHz, 0.55GHz, for red and orange respectively. As the two previous figures show, interaction with the wire's inhomogeneous magnetic field shifts the wavevector number, but frequency should stay the same. Fourier analysis of the 260ns snapshot shows this effect explain in detail previously. The BVSWs have wavevectors 0.71rad/μm, 0.63rad/μm, and frequencies 0.53GHz, 0.55GHz, for blue and cyan respectively. Taking a final Fourier analysis at the 450ns snapshot on the SAWs we have peaks for wavevectors at 0.71rad/μm, 0.63rad/μm, and peaks for frequencies at 0.4GHz, 0.36GHz, for red and orange respectively. This frequency inversion not only shows an operation, but also tells us that for any acoustic or spin wave, interaction with the ME gap, via local or temporal change, we can shift a waves wavevector or frequency up or down in anyway we choose. The best example is to simply reverse the process of the frequency inversion we showed here as a way to increase the frequency for a SAW. These scenarios are only possible due to the tunable magnetic field of the YIG material that controls the BVSW dispersion relation and from there the ME gap location on the frequency axis. This is why we attempt to expand upon some ideas utilizing YIG as a space-time meta-material.

CHAPTER SEVEN

CONCLUSION

We have theoretically derived and studied multiple SAW-SW coupling in YIG/GGG bi-layers and determined the optimum conditions for conversion of these hybrid ME waves with operational value for foundational uses in devives today. We also derived an analytical expression for the system that considers a dynamic inhomogeneous magnetic field. The mathematical foundations we hope are simplified enough for introductory scientists to perform quick calculations for their specific geometry and waves. This should help reach new experimental goals not only for spintronics, but for acoustic devices as well.

The results we analyzed in this dissertation produced many interesting phenomenal effects that are relevant for signal processes. This includes, but not limited to: SW transducers, filters, isolators, hybrid resonators, time reversal operations, frequency/wavevector inversions, excitation of short wavelength SW, channel swapping, etc,. The dynamics of SWs are improved upon by ME interactions with SAW with unidirectional potential wells, nonreciprocal effects, frequency and wavevctor variations, and so much more. We hope that our results will be useful for the experimental observation of the ME coupling and for the development of practical magneto-acoustic devices.

APPENDIX A

ANALYTICAL MATHEMATICAL PROBLEMS

A.1 Acoustic Wave Derivations

Please, note in this appendix there are subscript notations following historical elasticity descriptions. Also, be aware of how indices appear as subscripts on certain symbolic notations. We will note when certain changes are made through the derivations.

Beginning with the derivation for the translational equation of motion for all acoustic waves. Start with Euler's formula [77]

$$\frac{\partial f}{\partial y} - \frac{\partial}{\partial x}\frac{\partial f}{\partial y_x} = 0 \tag{A.1}$$

where y_x is derivative of y with respect to x. Take what we know about acoustic waves from [73], [74] to see the kinetic energy (K) and potential energy (V) as

$$K = \frac{\rho|\dot{\boldsymbol{u}}|^2}{2} \tag{A.2a}$$

$$V = \frac{1}{2}S_{ij}c_{ijkl}S_{kl} \tag{A.2b}$$

where $\dot{\boldsymbol{u}}$ is the derivative of the particle displacement vector (acoustic wave) with respect to time and S_{ij} is an element of the strain matrix defined by (2.2). The symbol c represents the elastic stiffness tensor as discussed in Chapter 2. The potential energy comes from stored energy in the elastic deformation of the material. Note the indices $ijkl = xyz$ are the same as in the main text.

Before taking our energies as the Lagrangian and plugging them into Euler's formula, we first simplify, V. With substitution from the strain definition the potential energy from the particle displacement vector is

$$V = \frac{1}{8}\left[\left(\frac{du_i}{dr_j} + \frac{du_j}{dr_i}\right)c_{ijkl}\left(\frac{du_k}{dr_l} + \frac{du_l}{dr_k}\right)\right] \tag{A.3}$$

From here, we apply a change in derivative notation which will make expressions easier to read when the Lagrangian of our elastic system is applied to Euler's formula

(A.1). We change notation as

$$\frac{\partial u_i}{\partial r_j} = u_{ij} \tag{A.4}$$

where the element of a vector component i is taken as a derivative of j.

Back to (A.3), we recall the general symmetry of the elastic stiffness tensor where $c_{ijkl} = c_{jikl}$ and $c_{ijkl} = c_{jilk}$. This reduces the potential energy to

$$V = \frac{1}{2} u_{ij} c_{ijkl} u_{kl} \tag{A.5}$$

Subtracting the kinetic energy (A.2a) from the new potential energy (A.5) gives us the Lagrangian.

$$\mathscr{L} = \frac{1}{2}\rho(|\dot{u}_x|^2 + |\dot{u}_y|^2 + |\dot{u}_z|^2) - \frac{1}{2} u_{ij} c_{ijkl} u_{kl} \tag{A.6}$$

This Lagrangian (A.6) will be plugged into Euler's formula (A.1). For Euler's formula there are four independent variables, x, y, z, and t, and one dependent variable $\boldsymbol{u}$. This changes Euler's formula from (A.1) to

$$\frac{\partial \mathscr{L}}{\partial u_i} - \sum_j \frac{\partial}{\partial r_j} \frac{\partial \mathscr{L}}{\partial u_{ij}} - \frac{\partial}{\partial t} \frac{\partial \mathscr{L}}{\partial \dot{u}_i} = 0 \tag{A.7}$$

Now we begin the process of simplifying and rewriting (A.7) into the translation equation of motion. The first term on the left hand side $\partial \mathscr{L} / \partial u_i = 0$. This is because the Lagrangian doesn't depend on any direct component of $\boldsymbol{u}$, just its derivatives. We then take the third term on the left hand side of (A.7) and move it to the other side. Our expression then becomes

$$\frac{\partial}{\partial t} \frac{\partial \mathscr{L}}{\partial \dot{u}_i} = -\sum_j \frac{\partial}{\partial r_j} \frac{\partial \mathscr{L}}{\partial u_{ij}} \tag{A.8}$$

The left hand side of (A.*) simplifies to

$$\frac{\partial}{\partial t} \frac{\partial \mathscr{L}}{\partial \dot{u}_i} = \rho \ddot{u}_i \tag{A.9}$$

which matches the translational equation of motions (2.1) already, just formatted in tensor notation.

For the right hand side of (A.8) will require some mathematical tricks. Writing out the right hand side of (A.8) explicitly

$$\frac{\partial \mathscr{L}}{\partial u_{ij}} = \frac{\partial}{\partial u_{ij}}\left[-\frac{1}{2}u_{ij}c_{ijkl}u_{kl}\right] \tag{A.10}$$

we will need to make some changes to express and simplify the many combinations of terms we have in total. Abstractly, $ijkl$ are only dummy indices or placeholders for xyz. Therefore replacing $ijkl$ with indices $\alpha\beta\gamma\zeta$ makes no mathematical impact within the bracketed portion of the expression (A.10). Following the chain rule of derivatives for functions (A.10) is rewritten as

$$\frac{\partial \mathscr{L}}{\partial u_{ij}} = -\frac{1}{2}\left(\frac{\partial u_{\alpha\beta}}{\partial u_{ij}}c_{\alpha\beta\gamma\zeta}u_{\gamma\zeta} + u_{\alpha\beta}c_{\alpha\beta\gamma\zeta}\frac{\partial u_{\gamma\zeta}}{\partial u_{ij}}\right) \tag{A.11}$$

These derivative forms in the brackets will be substituted respectively via sneaky trick using the expression

$$\frac{\partial u_{\alpha\beta}}{\partial u_{ij}} = \delta_{\alpha i}\delta_{\beta j} \tag{A.12}$$

Our (A.11) expression is rewritten with the Kronecker deltas as

$$\frac{\partial \mathscr{L}}{\partial u_{ij}} = -\frac{1}{2}\left(\delta_{\alpha i}\delta_{\beta j}c_{\alpha\beta\gamma\zeta}u_{\gamma\zeta} + u_{\alpha\beta}c_{\alpha\beta\gamma\zeta}\delta_{\gamma i}\delta_{\zeta j}\right) \tag{A.13}$$

The only surviving terms are when all conditions are satisfied: $\alpha = i, \beta = j, \gamma = i, \zeta = j$. The starting indices ij have been determined from the Kronecker delta terms. We then replace the remaining Greek indices $\alpha\beta\gamma\zeta$ to kl respectively with their c counterparts. Exploiting the symmetry of the elastic stiffness tensor c_{ijkl} again, we reduce (A.10) to a simplified version as

$$\frac{\partial \mathscr{L}}{\partial u_{ij}} = -c_{ijkl}u_{kl} \tag{A.14}$$

Now taking (A.9) and (A.14) and plugging them into (A.8) we have

$$\rho \ddot{u}_i = \sum \frac{\partial}{\partial r_j} c_{ijkl} u_{kl} \tag{A.15}$$

Recall our u_{kl} notation is just $\partial u_k / \partial l$ and the elastic stiffness tensor c_{ijkl} is made of material constants. We can rewrite (A.15) again to become

$$\rho \ddot{u}_i = \sum c_{ijkl} \frac{\partial^2 u_k}{\partial r_j \partial r_l} \tag{A.16}$$

which is the translational equation of motion (2.1), written in tensor notation. For further proof this is for acoustic waves following elastic theory from [73], [74] we will find the Hamiltonian.

Starting with the generalized form for momentum

$$\boldsymbol{p} = \frac{\partial \mathscr{L}}{\partial \dot{\boldsymbol{u}}} = \rho \dot{\boldsymbol{u}} \tag{A.17}$$

Theoretically following the same mechanics, the Hamiltonian is

$$H = \sum (p_i q_i) - \mathscr{L} \tag{A.18}$$

where $q_i = \dot{u}_i$, a derivative component of the particle displacement vector with respect to time. One will then see the Hamiltonian gives total energy for the system as

$$H = \frac{1}{2} \rho \left(|\dot{u}_x|^2 + |\dot{u}_y|^2 + |\dot{u}_z|^2 \right) + \frac{1}{2} u_{ij} c_{ijkl} u_{kl} \tag{A.19}$$

Next we consider the velocity of the two basic acoustic waves; P and S. These velocities are important because their components will help describe how a wave propagates in comparison to how the particles are displaced. There are two general directions in which the particles may move with respect to wave propagation; either parallel or perpendicular. For simplicity, starting from the condition that our material is isotropic, the elastic stiffness tensor explicitly takes the form

$$c = \begin{pmatrix} c_{11} & c_{12} & c_{12} & 0 & 0 & 0 \\ c_{12} & c_{11} & c_{12} & 0 & 0 & 0 \\ c_{12} & c_{12} & c_{11} & 0 & 0 & 0 \\ 0 & 0 & 0 & c_{44} & 0 & 0 \\ 0 & 0 & 0 & 0 & c_{44} & 0 \\ 0 & 0 & 0 & 0 & 0 & c_{44} \end{pmatrix} \tag{A.20}$$

following elasticity theory notation from [73]. This elastic stiffness tensor components c_{IJ} have these capital subscripts to indicate numbers.

A change in classical elastic notation to cartesian coordinates is provided in Table A.1. The elastic stiffness tensor in cartesian coordinates is written as

I	ij	J	kl
1	xx	1	xx
2	yy	2	yy
3	zz	3	zz
4	yz,zy	4	yz,zy
5	xz,zx	5	xz,zx
6	xy,yx	6	xy,yx

Table A.1: Change of indices from numbers to cartesian coordinates

$$c = \begin{pmatrix} \begin{pmatrix} c_{xxxx} & 0 & 0 \\ 0 & c_{xxyy} & 0 \\ 0 & 0 & c_{xxzz} \end{pmatrix} & \begin{pmatrix} 0 & c_{xyxy} & 0 \\ c_{xyyx} & 0 & 0 \\ 0 & 0 & 0 \end{pmatrix} & \begin{pmatrix} 0 & 0 & c_{xzxz} \\ 0 & 0 & 0 \\ c_{xzzx} & 0 & 0 \end{pmatrix} \\ \begin{pmatrix} 0 & c_{yxxy} & 0 \\ c_{yxyx} & 0 & 0 \\ 0 & 0 & 0 \end{pmatrix} & \begin{pmatrix} c_{yyxx} & 0 & 0 \\ 0 & c_{yyyy} & 0 \\ 0 & 0 & c_{yyzz} \end{pmatrix} & \begin{pmatrix} 0 & 0 & 0 \\ 0 & 0 & c_{yzyz} \\ 0 & c_{yzzy} & 0 \end{pmatrix} \\ \begin{pmatrix} 0 & 0 & c_{zxxz} \\ 0 & 0 & 0 \\ c_{zxzx} & 0 & 0 \end{pmatrix} & \begin{pmatrix} 0 & 0 & 0 \\ 0 & 0 & c_{zyyz} \\ 0 & c_{zyzy} & 0 \end{pmatrix} & \begin{pmatrix} c_{zzxx} & 0 & 0 \\ 0 & c_{zzyy} & 0 \\ 0 & 0 & c_{zzzz} \end{pmatrix} \end{pmatrix} \tag{A.21}$$

the same way as described in Chapter 2. Note again the symmetrical tensor relations, $c_{ijkl} = c_{jikl} = c_{ijlk} = c_{jilk} = c_{klij}$ between components. These symmetrical relations between components help reduce the translation equation of motion (A.16). The tensor components $c_{12} = c_{11} - 2c_{44}$ then define two independent constants. Transforming the elastic notation expression $c_{12} = c_{11} - 2c_{44}$ into a cartesian coordinates via Table A.1 gives $c_{xxyy} = c_{xxxx} - 2c_{xyxy}$ as one example.

As described in Chapter 2 by (2.5) the elastic stiffness tensor for isotropic conditions can be defined by the expression

$$c_{ijkl} = \lambda \delta_{ij}\delta_{kl} + \mu(\delta_{ik}\delta_{jl} + \delta_{il}\delta_{jk}) \tag{A.22}$$

The independent constants λ and μ are known as the Lamé constants in reference to [76], [78].

Substituting (A.22) into (A.16) we get a long expression for the translation equation of motion under isotropic conditions. The summation will be for the all permutations of the subscripts jkl with the subscript i set by the left hand side of (A.16).

$$\rho \ddot{u}_i = \sum_{jkl} \left[\lambda \delta_{ij}\delta_{kl} + \mu(\delta_{ik}\delta_{jl} + \delta_{il}\delta_{jk})\right] \frac{\partial^2 u_k}{\partial r_j \partial r_l} \tag{A.23}$$

We open the brackets to see how each variation of the Kronecker delta affects the double derivative of the particle displacement vector.

$$\rho \ddot{u}_i = \sum_{jkl} \lambda \delta_{ij} \delta_{kl} \frac{\partial^2 u_k}{\partial r_j \partial r_l} + \sum_{jkl} \mu \delta_{ik} \delta_{jl} \frac{\partial^2 u_k}{\partial r_j \partial r_l} + \sum_{jkl} \mu \delta_{il} \delta_{jk} \frac{\partial^2 u_k}{\partial r_j \partial r_l} \tag{A.24}$$

For the right hand side of (A.24) which ever subscript is matched with the i subscript on the Kronecker will be replaced with the i to match the left hand side. Specifically, the first and third terms on the right side of (A.24) with have the j and l indices, respectively, will be replaced with an i in the double derivative. For the second Kronecker delta that does not contain an i subscript, you may choose either index to replace with the other. As an example, the first and third terms again from (A.24), we will replace the l and j indices, respectively, with k to keep math simple. Our new expression after applying the rules of the Kronecker deltas is

$$\rho \ddot{u}_i = \sum_{k} \lambda \frac{\partial^2 u_k}{\partial r_i \partial r_k} + \sum_{j} \mu \frac{\partial^2 u_i}{\partial r_j \partial r_j} + \sum_{k} \mu \frac{\partial^2 u_k}{\partial r_k \partial r_i} \tag{A.25}$$

One can then combine the summation terms with k and factor out a $\partial \big/ \partial r_i$ to get a reduced derivative expression.

$$\rho \ddot{u}_i = (\lambda + \mu) \frac{\partial}{\partial r_i} \sum_{k} \frac{\partial u_k}{\partial r_k} + \mu \sum_{j} \frac{\partial^2 u_i}{\partial r_j^2} \tag{A.26}$$

From here one might notice similarities between the derivative summations and vector operators. From (A.26) the first derivative summation is the component expression of the gradient applied to the divergence of the particle displacement vector. The second derivative summation is the Laplacian opertor written in terms of components. Rewriting (A.26) into vector notation we see the translational equation of motion for acoustic waves in isotropic materials. Transforming summations into vector form.

$$\rho \ddot{\vec{\mathbf{u}}} = (\lambda + \mu) \nabla (\nabla \cdot \vec{\mathbf{u}}) + \mu \nabla^2 \vec{\mathbf{u}} \tag{A.27}$$

Recall our goal is to understand how the wave propagates in comparison to the particle movement. Keeping the math simple, we take the plane wave formula and substitute it into (A.27). As stated previously, we consider two cases where the particle displacement vector, $\boldsymbol{u}$, is parallel and perpendicular to the wavevector $\boldsymbol{k}$. Our plane wave formula is

$$\boldsymbol{u}(\boldsymbol{r},t) = \boldsymbol{u}_0 e^{-i\omega t + i\boldsymbol{k}\cdot\boldsymbol{r}} \tag{A.28}$$

where $\boldsymbol{u}_0$ is the acoustic plane wave profile. The gradients and Laplacian in (A.27) transform as $\nabla \to i\boldsymbol{k}$ and $\nabla^2 \to -|\boldsymbol{k}|^2$ respectively for the plane wave approximation. The next step plugging (A.28) into (A.27) and deriving

$$-\rho\omega^2\boldsymbol{u}_0 e^{-i\omega t + i\boldsymbol{k}\cdot\boldsymbol{r}} = (\lambda+\mu)i\boldsymbol{k}(i\boldsymbol{k}\cdot\boldsymbol{u}_0)e^{-i\omega t + i\boldsymbol{k}\cdot\boldsymbol{r}} - \mu|\boldsymbol{k}|^2\boldsymbol{u}_0 e^{-i\omega t + i\boldsymbol{k}\cdot\boldsymbol{r}} \tag{A.29}$$

At this point we go case by case for the particles movement. For the first case where $\boldsymbol{u}_0$ is perpendicular to $\vec{\mathbf{k}}$, are the Shear waves, The (A.29) expression becomes

$$-\rho\omega^2\boldsymbol{u}_0 e^{-i\omega t + i\boldsymbol{k}\cdot\boldsymbol{r}} = -\mu k^2\boldsymbol{u}_0 e^{-i\omega t + i\boldsymbol{k}\cdot\boldsymbol{r}} \tag{A.30}$$

where the middle term is zero due to the dot product of vectors. Solving (A.30) for the shear waves phase velocity, we end up with

$$v_s = \frac{\omega}{k} = \sqrt{\frac{\mu}{\rho}} \tag{A.31}$$

which is dependent only on the materials density and the off diagonal constant μ in the elastic stiffness tensor.

For the second case with pressure waves, or longitudinal waves, we note $\boldsymbol{u}_0 = \alpha\boldsymbol{k}$. The α is just a scalar constant because $\boldsymbol{u}$ and $\boldsymbol{k}$ are never one-to-one. Substituting this new condition in (A.29) we end up with

$$-\rho\omega^2\alpha\boldsymbol{k}e^{-i\omega t + i\boldsymbol{k}\cdot\boldsymbol{r}} = -(\lambda+\mu)\alpha k^2\boldsymbol{k}e^{-i\omega t + i\boldsymbol{k}\cdot\boldsymbol{r}} - \mu\alpha k^2\boldsymbol{k}e^{-i\omega t + i\boldsymbol{k}\cdot\boldsymbol{r}} \tag{A.32}$$

Focusing on the constants in front of each vector, the exponentials and α cancel. This leaves us with an easy solve for the longitudinal waves phase velocity as

$$v_l = \frac{\omega}{k} = \sqrt{\frac{\lambda + 2\mu}{\rho}} \tag{A.33}$$

This solution for how the wave moves uses both constants, but this addition of constants $\lambda + 2\mu$ is found only when all the indices in the elastic stiffness tensor are the same. This completes our velocity derivations for longitudinal and shear waves. The importance of these foundational velocities is because acoustic waves will generally have both particle movements, perpendicular and parallel, when compared to the waves propagation direction.

We now move on to the derivation for the SAW used in the main text. To begin the SAW profile we define our coordinate system similar to Fig. 3.4 and assume SAW in only one medium. The SAW will take the form

$$\boldsymbol{u}(\boldsymbol{r},t) = A(t)e^{i(k_x x - \omega t)} \begin{pmatrix} u_x(z) \\ 0 \\ u_z(z) \end{pmatrix} \tag{A.34}$$

where the SAW propagates only along the x-axis as indicated by $\boldsymbol{k} = \begin{pmatrix} k_x & 0 & 0 \end{pmatrix}$ and only has two components for its wave profile dependent on the depth z into the material. This is normal as the influence of the surface wave has less of an affect on particle movement deeper in the medium. The time dependent variable $A(t)$ is the complex wave amplitude. The profile is chosen to have only u_x and u_z components as following our choice of using a Rayleigh wave. That means no shear component, or particle movement in the y direction. This is because the Rayleigh wave is defined by particles having counter-clockwise movement as the surface wave propagates. While the solution we show does not reflect this description, we are solving for the envelope, wave profile, of how much the particles are affected by this motion at a certain depth. In our solution, we do see both longitudinal and shear constants appearing in the u_x and u_z component indicating this rotational movement. Now we find the functions for $u_x(z)$ and $u_z(z)$ to define our SAW profile.

Starting with strain (2.2), we plug in our SAW approximation to get

$$S = A(t)e^{i(k_x x - \omega t)} \begin{pmatrix} ik_x u_x(z) & 0 & \frac{1}{2}(ik_x u_z(z) + u_x'(z)) \\ 0 & 0 & 0 \\ \frac{1}{2}(ik_x u_z(z) + u_x'(z)) & 0 & u_z'(z) \end{pmatrix} \tag{A.35}$$

where the derivative notation is simplified to an apostrophe. The only variable the acoustic components are dependent on is z, so a single apostrophe is $\partial/\partial z$ and a double apostrophe means $\partial^2/\partial z^2$. Then we convert strain to stress via relationship (2.3) where the elastic stiffness tensor c is substituted for an isotropic material. We again use the Lamé constants, λ and μ, as the associated as material constants. The elastic stiffness tensor c then is explicitly

$$c = \begin{pmatrix} \begin{pmatrix} \lambda+2\mu & 0 & 0 \\ 0 & \lambda & 0 \\ 0 & 0 & \lambda \end{pmatrix} & \begin{pmatrix} 0 & \mu & 0 \\ \mu & 0 & 0 \\ 0 & 0 & 0 \end{pmatrix} & \begin{pmatrix} 0 & 0 & \mu \\ 0 & 0 & 0 \\ \mu & 0 & 0 \end{pmatrix} \\ \begin{pmatrix} 0 & \mu & 0 \\ \mu & 0 & 0 \\ 0 & 0 & 0 \end{pmatrix} & \begin{pmatrix} \lambda & 0 & 0 \\ 0 & \lambda+2\mu & 0 \\ 0 & 0 & \lambda \end{pmatrix} & \begin{pmatrix} 0 & 0 & 0 \\ 0 & 0 & \mu \\ 0 & \mu & 0 \end{pmatrix} \\ \begin{pmatrix} 0 & 0 & \mu \\ 0 & 0 & 0 \\ \mu & 0 & 0 \end{pmatrix} & \begin{pmatrix} 0 & 0 & 0 \\ 0 & 0 & \mu \\ 0 & \mu & 0 \end{pmatrix} & \begin{pmatrix} \lambda & 0 & 0 \\ 0 & \lambda & 0 \\ 0 & 0 & \lambda+2\mu \end{pmatrix} \end{pmatrix} \tag{A.36}$$

The stress tensor, after substitution of (A.36) and (A.35) into (2.2), then becomes

$$T = A(t)e^{i(k_x x-\omega t)}.$$

$$\begin{pmatrix} ik_x[\lambda+2\mu]u_x(z)+\lambda u_z'(z) & 0 & \mu[ik_x u_z(z)+u_x'(z)] \\ 0 & \lambda[ik_x u_z(z)+u_z'(z)] & 0 \\ \mu[ik_x u_z(z)+u_x'(z)] & 0 & ik_x\lambda u_x(z)+[\lambda+2\mu]u_z'(z) \end{pmatrix} \tag{A.37}$$

Continuing with substitution of (A.37) and (A.34) into the translational equation of motion (2.2). Noting again we are taking the envelope of the wave to see its surface profile. For this reason we discard all time derivative terms taken with respect to the complex wave amplitude. Skipping these extra algebraic steps and moving all terms to the left side we have complicated expression as

$$A(t)e^{i(k_x x-\omega t)} \begin{pmatrix} (-k_x^2(\lambda+2\mu)+\rho\omega^2)u_x(z)+ik_x(\lambda_+\mu)u_z'(z)+\mu u_x''(z) \\ 0 \\ (-k_x^2\mu+\rho\omega^2)u_z(z)+ik_x(\lambda_+\mu)u_x'(z)+(\lambda+2\mu)u_x''(z) \end{pmatrix} = \boldsymbol{0} \tag{A.38}$$

To begin solving this expression consider a general solution for the SAW vector profile components as $u_x = u_z = e^{\xi z}$. The derivatives can easily be found as $u_x' = u_z' = \xi e^{\xi z}$ and $u_x'' = u_z'' = \xi^2 e^{\xi z}$, for first and second order with respect to z. At this point we can suppress the y component of this vector as it will not be needed past this point. The same is said for the complex wave amplitude $A(t)$ and the wave exponential to simplify the problem. We rewrite everything into matrix form as $C \cdot \boldsymbol{u} = 0$, we can solve for ξ via $\det|C| = 0$ just like an eigen value problem. Our eigen value problem comes from the matrix expression

$$\begin{pmatrix} \mu\xi^2-((\lambda+2\mu)k_x^2-\rho\omega^2) & ik_x(\lambda+\mu)\xi \\ ik_x(\lambda+\mu)\xi & (\lambda+2\mu)\xi^2-(\mu k_x^2-\rho\omega^2) \end{pmatrix} \cdot \begin{pmatrix} u_x(z) \\ u_z(z) \end{pmatrix} = \boldsymbol{0} \tag{A.39}$$

Solving this eigen value problem one would get four solutions to ξ. However, as one of the natural boundary conditions for a surface wave the SAW profile must decay as $z \to \infty$. Therefore we throw away the positive ξ solutions leaving us with two eigen values

$$\xi_1 = -\sqrt{k_x^2 - \frac{\rho\omega^2}{\mu}}, \tag{A.40a}$$

$$\xi_2 = -\sqrt{k_x^2 - \frac{\rho\omega^2}{\lambda + 2\mu}} \tag{A.40b}$$

With these eigen values for ξ we plug them into the matrix from (A.39). Each eigen value of ξ, we will produce an eigenvector which will be added together into the general solution as

$$\begin{pmatrix} u_x(z) \\ u_z(z) \end{pmatrix} = c_1 \begin{pmatrix} 1 \\ \frac{ik_x}{\sqrt{k_x^2 - \frac{\rho\omega^2}{\mu}}} \end{pmatrix} e^{\xi_1 z} + c_2 \begin{pmatrix} 1 \\ \frac{i}{k_x}\sqrt{k_x^2 - \frac{\rho\omega^2}{\lambda+2\mu}} \end{pmatrix} e^{\xi_2 z} \tag{A.41}$$

While we have solved for a general solution, we need to find the specific solution for the SAW. To solve for the constants c_1, c_2, we use the other boundary condition for the SAW at $z = 0$ where the surface of our material begins. This boundary condition is expressed as

$$T \cdot \begin{pmatrix} 0 \\ 0 \\ 1 \end{pmatrix} = 0 \tag{A.42}$$

where the stress tensor is dotted by the normal vector perpendicular to the plane of the materials surface. Taking our stress tensor from (A.37) we end up with the expression

$$\begin{pmatrix} \mu[ik_x u_z(0) + u_x'(0)] \\ ik_x \lambda u_x(0) + [\lambda + 2\mu] u_z'(0) \end{pmatrix} = \boldsymbol{0} \tag{A.43}$$

Plugging (A.41) into the boundary condition (A.43) we will end up with a second matrix. Pulling out the constants, c_1 and c_2, we will have a matrix D dotted with a vector of components c_1 and c_2 set equal to zero. In this case the variable ω is our eigen value. Our eigen value problem then takes the form

$$\begin{pmatrix} \frac{-2k_x^2\mu+\rho\omega^2}{\sqrt{k_x^2-\frac{\rho\omega^2}{\mu}}} & -2\mu\sqrt{k_x^2-\frac{\rho\omega^2}{\lambda+2\mu}} \\ -2ik_x\mu & -2ik_x\mu+\frac{i\rho\omega^2}{k_x} \end{pmatrix} \cdot \begin{pmatrix} c_1 \\ c_2 \end{pmatrix} = \boldsymbol{0} \tag{A.44}$$

However, for this eigen value problem the eigen values will be extremely difficult to derive. Surprisingly, we have technically already solved for the ω eigen values. Recall how the frequency is dependent on the phase velocity multiplied by the wavevector k. We did this for the Hamiltonian of acoustic waves under isotropic conditions with the planes wave solution. This was done for two cases, shear and longitudinal. In our case for the SAW the shear and longitudinal movements of particles are coupled in a rotational behavior as defined for a Rayleigh wave. Thus the eigen values for matrix D in (A.44) are expressed as

$$\omega_s = k_x\sqrt{\frac{X\mu}{\rho}} \tag{A.45a}$$

$$\omega_l = k_x\sqrt{\frac{Y(\lambda+2\mu)}{\rho}} \tag{A.45b}$$

where X and Y are numerical constants representing couplng between components. We numerically find a these values for X and Y in our ω's by plugging each ω into matrix D in (A.44), one-by-one respectively, and solving for the determinant of D. One will two polynomials to numerically solve.

$$0 = X^3 - 8X^2 + 16X\left(\frac{3}{2}-\varepsilon\right) - 16(1-\varepsilon) \tag{A.46a}$$

$$0 = Y^3 - 8Y^2\varepsilon + 16Y\varepsilon^2\left(\frac{3}{2}-\varepsilon\right) - 16\varepsilon^3 \tag{A.46b}$$

The constant $\varepsilon = \mu/(\lambda+2\mu)$ is the ratio of Lamé constants and we have the relation $Y = X\varepsilon$ between the numerical constants. One will have to solve for either X or Y and find that both relations between ω and k give the same numerical answer for the speed of the SAW.

Back to our main problem for the SAW profile, we now can solve for the constants c_1 and c_2. Taking (A.44) and either ω eigen value you will end up with two expressions.

$$\frac{X-2}{\sqrt{1-X}} k_x \mu c_1 - 2\mu k_x c_2 \sqrt{1-\frac{X\mu}{\lambda+2\mu}} = 0 \tag{A.47a}$$

$$-2c_1 + c_2(X-2) = 0 \tag{A.47b}$$

For these expressions in (A.47) we specifically used the eigen value ω_s. Rewriting the second expression, we have

$$c_1 = c_2\left(\frac{X}{2}-1\right) \tag{A.48}$$

where we define $c_2 = 1$. Now take everything and substitute what we got for the constants (c_1, c_2) and ω's into the general solution (A.41). One will get a full expression for the SAW profile as

$$\boldsymbol{u}(z) = \begin{pmatrix} \frac{1-Y\varepsilon/2}{k\sqrt{1-Y\varepsilon}} e^{-zk\sqrt{1-Y\varepsilon}} - \frac{1}{k\sqrt{1-Y}} e^{-zk\sqrt{1-Y}} \\ 0 \\ -\frac{i}{k}\left(\frac{1-Y\varepsilon/2}{1-Y\varepsilon} e^{-zk\sqrt{1-Y\varepsilon}} - e^{-zk\sqrt{1-Y}}\right) \end{pmatrix} \tag{A.49}$$

For this final expression we show for the SAW profile we did perform a "change of basis" from X's to Y's for a reduction in number of symbols shown.

A.2 Spin Wave derivation using Vector Hamiltonian Formalism

In this section we provide an example use of [114] which helps one derive the dispersion relation and vector profiles for various SW. Our example will be consistent with the main text of this dissertation using a ferromagnetic thin film in the xy-plane and z axis perpendicular to the thin film. As always with any magnetic system, we begin with the Landau-Lifshitz equation (2.7). However, in [114] this formula is transformed in the linear limit of the Hamiltonian for SWs.

The new formula we will be using is

$$L_0 \cdot \frac{d\boldsymbol{s}}{dt} = H_0 \cdot \boldsymbol{s} \tag{A.50}$$

The vector s is our SW, L_0 is a skew-symmetric operator and H_0 is the linear Hamiltonian operator. The skew-symmetric operator is defined as

$$L_0 \cdot v = -L_s \boldsymbol{m}_0 \times \boldsymbol{v} \tag{A.51}$$

where $L_s = M_s/\gamma$ and v is an arbitrary vector used to solve for L_0 with the static magnetization vector m_0. The γ is the gyromagnetic ratio and M_s is a materials saturation magnetization.

The Hamiltonian operator H_0 is defined as

$$H_0 = P_0 \cdot (H + M_s B_0 I) \cdot P_0 \tag{A.52}$$

where P_0 is the projection operator, H is the magnetic field Hermitian operator, and B_0 is the static internal magnetic field. The I is the identity matrix used to defined the projection operator as

$$P_0 = I - \boldsymbol{m}_0 \otimes \boldsymbol{m}_0 \tag{A.53}$$

For both the magnetic field operator H and internal magnetic field B_0, these are found after defining your system. The magnetic field operator H is essentially the sum of all magnetic fields with exception for the $\boldsymbol{B}_{\text{ext}}$. These fields together form the $\boldsymbol{B}_{\text{eff}}$ as

$$\boldsymbol{B}_{\text{eff}}(\boldsymbol{m}) = \boldsymbol{B}_{\text{ext}} - M_s^{-1} H \cdot \boldsymbol{m} \tag{A.54}$$

where $\boldsymbol{m}$ is the general magnetization vector. Examples of magnetic field operators are provided by [114] and are

$$H_{ex} = -\mu_0 M_s^2 \lambda_{ex}^2 \nabla^2 \tag{A.55a}$$

$$H_{dip} = \mu_0 M_s^2 \nabla \nabla^{-2} \nabla \tag{A.55b}$$

$$H_{am} = -M_s B_{an} \boldsymbol{n}_{am} \otimes \boldsymbol{n}_{an} \tag{A.55c}$$

$$H_{DMI} = T_{DMI} \cdot \nabla \tag{A.55d}$$

The field operators (A.55a), (A.55b) are the exchange and dipolar field we discuss in Chapter 2, just without the magnetization vector. The extra examples of field operators, (A.55c), (A.55d), are the anisotropy, and Dzyaloshinskii-Moriya interaction fields, respectively.

To complete our new formal method for SWs, we need two more formulas: normalization and damping. The SW vector is normalized via

$$\hbar = -i \int_V \boldsymbol{s} * \cdot L_0 \cdot \boldsymbol{s} d\boldsymbol{r} \tag{A.56}$$

Damping for SW follows as

$$\Gamma = \alpha_G \omega \hbar^{-1} \int_V L_s |\boldsymbol{s}|^2 d\boldsymbol{r} \tag{A.57}$$

This concludes the necessary expressions required to solve for a real system of SWs using a linearized form of energy substituted into the Landau-Lifshitz equation.

Proceeding with our thin film example problem, in this simple case only the dipolar field $\boldsymbol{H}_{\mathrm{dip}}$ will contribute to the overall effective field. The exchange, anisotropy, and Dzyaloshinskii Moriya interaction fields are smaller in magnitude and negligible. The dipolar field is reduced to the demagnetizing tensor N.

$$\boldsymbol{H}_{\text{dip}} = \mu_0 M_s^2 N = \mu_0 M_s^2 \begin{pmatrix} 0 & 0 & 0 \\ 0 & 0 & 0 \\ 0 & 0 & 1 \end{pmatrix} \tag{A.58}$$

The demagnetizing tensor takes this form because the normal vector is perpendicular to the xy-plane the thin film lies in. Before plugging our dipolar field operator into H, the sum of magnetic fields (A.54) is substituted with the static magnetization vector m_0. This is because we are in a system defined for weak non-linear dynamics for SWs that literally revolves around the static magnetization vector and damping brings magnetization back to alignment with the static vector. The total effective magnetic field takes the form then as

$$\boldsymbol{B}_{\text{eff}}(\boldsymbol{m}_0) = \boldsymbol{B}_{\text{ext}} - M_s^{-1} H \cdot \boldsymbol{m}_0 = B_0 \boldsymbol{m}_0 \tag{A.59}$$

The $\boldsymbol{B}_0$ is the new net magnetic field as the internal magnetic field is now defined by the static magnetization vector.

Defining the rest of our system, the external field $\boldsymbol{B}_{\text{ext}}$ will lye along the x-axis, and the ground state magnetization can have three components.

$$\boldsymbol{m}_0 = \begin{pmatrix} m_x & m_y & m_z \end{pmatrix} \tag{A.60}$$

Taking the external field, (A.58), and (A.60), everything is plugged into (A.59) and three rows of expressions are found as

$$B_{\text{ext}} = B_0 m_x \tag{A.61a}$$

$$0 = B_0 m_y \tag{A.61b}$$

$$-\mu_0 M_s m_z = B_0 m_z \tag{A.61c}$$

Very clearly m_y=0 always, but we also have the condition

$$\boldsymbol{m}_0 \cdot \boldsymbol{m}_0 = 1 \tag{A.62}$$

that must be satisfied. This can be done for two cases.

The first case is when $m_z = 0$. Then we have $m_x^2 = 1$ and $B_{\text{ext}} = B_0$ for the most trivial case. The second case is more interesting where neither m_0-component is zero. Then the magnetic fields are $B_0 = -\mu_0 M_s$ and $B_{\text{ext}} = -\mu_0 M_s m_x$ making

$$\boldsymbol{m}_0 = \begin{pmatrix} -\cos\theta & 0 & \sin\theta \end{pmatrix} \tag{A.63}$$

to satisfy the theoretical condition in (A.62). We chose m_0 with this configuration, because we wish to see how the static magnetization, at an initial angle θ in the xz-plane away from the external magnetic field oriented in the $+x$ direction, will damp towards a true stable state.

In order to solve both of these cases for SW damping, dispersion relation, and vector, we transform (A.50) into an eigen value problem we can easily solve. We begin by solving for harmonic solutions where $d/dt \to -i\omega$. This changes (A.50) to

$$-i\omega L_0 \cdot \boldsymbol{s} = H_0 \cdot \boldsymbol{s} \tag{A.64}$$

Taking advantage of some theoretical properties discussed in [114] we can use

$$L_0^2 = -L_s^2 P_0 \tag{A.65a}$$

$$P_0 \cdot \boldsymbol{s} = \boldsymbol{s} \tag{A.65b}$$

to rearrange (A.64) into a standard eigen value problem. Our normal eigen value problem, $\lambda \cdot \boldsymbol{s} = A \cdot \boldsymbol{s}$, for the SW vector has the following definitions

$$\lambda = -i\omega \tag{A.66a}$$

$$A = -L_s^{-2} L_0 \cdot H_0 \tag{A.66b}$$

for the eigen values λ and matrix A. We now have a defined system and are ready to solve the two different cases for SWs using this eigen value problem.

Starting with the first case where $m_z = 0$, $m_x^2 = 1$ and $B_{\text{ext}} = B_0$, we can find the operators P_0 and L_0 can be found using the static magnetization vector. Using the operator definitions (A.53) and (A.51) with the static vector in this first case we have

$$P_0 = \begin{pmatrix} 0 & 0 & 0 \\ 0 & 1 & 0 \\ 0 & 0 & 1 \end{pmatrix} \tag{A.67a}$$

$$L_0 = \begin{pmatrix} 0 & 0 & 0 \\ 0 & 0 & \frac{M_s}{\gamma} \\ 0 & -\frac{M_s}{\gamma} & 0 \end{pmatrix} \tag{A.67b}$$

The operator H_0, following (A.52), needs the internal magnetic field. In this case, the internal field magnetic is equal to the external field. Using (A.67a) in (A.52) will give

$$H_0 = \begin{pmatrix} 0 & 0 & 0 \\ 0 & B_{\text{ext}} M_s & 0 \\ 0 & 0 & B_{\text{ext}} M_s + \mu_0 M_s^2 \end{pmatrix} \tag{A.68}$$

Taking matrices (A.68) and (A.67b) and using them for (A.66b) gives us our eigen value problem matrix A as

$$A = \begin{pmatrix} 0 & 0 & 0 \\ 0 & 0 & -\gamma(B_{\text{ext}} + \mu_0 M_s) \\ 0 & \gamma B_{\text{ext}} & 0 \end{pmatrix} \tag{A.69}$$

Solving (A.69) for eigenvalues λ gives us three expressed as

$$\lambda_1 = 0 \tag{A.70a}$$

$$\lambda_2 = -i\gamma\sqrt{B_{\text{ext}}(B_{\text{ext}} + \mu_0 M_s)} \tag{A.70b}$$

$$\lambda_3 = i\gamma\sqrt{B_{\text{ext}}(B_{\text{ext}} + \mu_0 M_s)} \tag{A.70c}$$

For the eigen value λ_1, this corresponds to the tivial solution where $\boldsymbol{s} = \boldsymbol{m}_0$. After finding the eigen vectors one will see this is not a real solution for SWs. With these eigen values $\lambda_{2,3}$ and their relation to the angular frequency (A.66a), we also have the dispersion relation for this SW. The angular frequency is only dependent on the external magnetic field.

The eigen vectors from (A.69) require more attention to detail. The eigen vectors for matrix A, listed in order with their corresponding eigen values from (A.70), are

$$\boldsymbol{s}_1 = \begin{pmatrix} 1 & 0 & 0 \end{pmatrix} \tag{A.71a}$$

$$\boldsymbol{s}_2 = \begin{pmatrix} 0 & -\frac{i}{B_{\text{ext}}}\sqrt{B_{\text{ext}}(B_{\text{ext}} + \mu_0 M_s)} & 1 \end{pmatrix} \tag{A.71b}$$

$$\boldsymbol{s}_3 = \begin{pmatrix} 0 & \frac{i}{B_{\text{ext}}}\sqrt{B_{\text{ext}}(B_{\text{ext}} + \mu_0 M_s)} & 1 \end{pmatrix} \tag{A.71c}$$

The extra details here is to ensure the answers one may derive are theoretical accurate to the method in [114]. Two tests are performed to check your work: From [114] we use the conditions

$$P_0 \cdot \boldsymbol{s} = \boldsymbol{s} \tag{A.72a}$$

$$\boldsymbol{m}_0 \cdot \boldsymbol{s} = 0 \tag{A.72b}$$

The first eigen value and eigen vector does not pass these tests and is not considered since they are mathematically trivial solutions. The next step is to normalize the eigen vectors $\boldsymbol{s}_2$ and $\boldsymbol{s}_3$ using (A.56). We end with

$$\hbar_2 = \frac{2M_s V_s\sqrt{B_{\text{ext}}(B_{\text{ext}} + \mu_0 M_s)}}{B_{\text{ext}}\gamma} \tag{A.73a}$$

$$\hbar_3 = -\frac{2M_s V_s \sqrt{B_{\text{ext}}(B_{\text{ext}} + \mu_0 M_s)}}{B_{\text{ext}}\gamma} \tag{A.73b}$$

as our normalization constants for the eigen vectors. At this step, we point out we got two solutions for the SW vector, $\boldsymbol{s}_2$ and $\boldsymbol{s}_3$. Which SW vector solution is the physically real one? We are able to answer this question looking at the normalization constants. The normalization constant whose sign is positive says that $\boldsymbol{s}_2$ is the real SW vector one would use say for ME coupling.

All that is left is finding the damping factor for this SW. Following from (A.57) for damping we use $\omega = i\lambda_2$ and $\boldsymbol{s}_2$ we find damping to be

$$\Gamma = \frac{1}{2}\alpha_G \gamma (2B_{\text{ext}} + \mu_0 M_s) \tag{A.74}$$

Damping is found to be a positive value, as it should, knowing in most wave equation expression we see damping takes energy away in a term usually expressed as $-i\Gamma$. The realism here is that for stronger external magnetic fields damping increases proportionally. Magnetization wants to stay aligned with the strong stable static state.

We now move on to the second case where magnetization is oriented somewhere in the xz-plane. As a refresh of the circumstances we have in this case, neither m_0-component is zero in (A.61), except for m_y. The magnetic fields are $B_0 = -\mu_0 M_s$ and $B_{\text{ext}} = -\mu_0 M_s m_x$ where static magnetization m_0 is defined in (A.63). We again start with finding our matrix operators from (A.51)-(A.53).

$$P_0 = \begin{pmatrix} \sin^2\theta & 0 & \cos\theta\sin\theta \\ 0 & 1 & 0 \\ \cos\theta\sin\theta & 0 & \cos^2\theta \end{pmatrix} \tag{A.75a}$$

$$L_0 = \frac{M_s}{\gamma} \begin{pmatrix} 0 & \sin\theta & 0 \\ -\sin\theta & 0 & -\cos\theta \\ 0 & \cos\theta & 0 \end{pmatrix} \tag{A.75b}$$

$$H_0 = -\mu_0 M_s^2 \begin{pmatrix} \sin^4\theta & 0 & \cos\theta\sin^3\theta \\ 0 & 1 & 0 \\ \cos\theta\sin^3\theta & 0 & \cos^2\theta\sin^2\theta \end{pmatrix} \tag{A.75c}$$

These operators produce our eigen value problem matrix A, from (A.66b) as

$$A = \gamma\mu_0 M_s \begin{pmatrix} 0 & \sin\theta & 0 \\ -\sin^3\theta & 0 & -\cos\theta\sin^2\theta \\ 0 & \cos\theta & 0 \end{pmatrix} \tag{A.76}$$

Repeating the same steps as before in the first case, the eigen values (and SW dispersion relation) are evaluated to

$$\lambda_1 = 0 \tag{A.77a}$$

$$\lambda_2 = -i\gamma\mu_0 M_s \sin\theta \tag{A.77b}$$

$$\lambda_3 = i\gamma\mu_0 M_s \sin\theta \tag{A.77c}$$

which give the following eigen vectors.

$$s_1 = \begin{pmatrix} -\cot\theta & 0 & 1 \end{pmatrix} \tag{A.78a}$$

$$s_2 = \begin{pmatrix} \tan\theta & -i\tan\theta & 1 \end{pmatrix} \tag{A.78b}$$

$$s_3 = \begin{pmatrix} \tan\theta & i\tan\theta & 1 \end{pmatrix} \tag{A.78c}$$

We test these eigen vectors following from (A.72) to check if they are theoretically correct. The first eigen vector s_1 does not pass, which can be determined from the corresponding eigen value of $\lambda_1 = 0$. Continuing with normalization (A.56), we confirm which is the real SW vector.

$$\hbar_2 = -2V\frac{M_s}{\gamma}\sec\theta\tan\theta \tag{A.79a}$$

$$\hbar_3 = 2V\frac{M_s}{\gamma}\sec\theta\tan\theta \tag{A.79b}$$

We see the second eigen vector is real SW, because it has a positive normalization factor. Damping from (A.57) is then found for both to be

$$\Gamma = \frac{1}{4}\alpha_G\gamma\mu_0 M_s(-3+\cos 2\theta) \tag{A.80}$$

Before making any analytical observations, we choose to substitute the $\cos 2\theta$ to a magnetic variable. From our condition for the static vector $\boldsymbol{m}_0$ from (A.63), we make our own formula from the condition (A.62) and substitution of $B_0 = -\mu_0 M_s$ into $B_{\text{ext}} = -\mu_0 M_s m_x$. We derive the expression can see that after a few substitutions

$$\sin^2\theta = 1 - \left(\frac{B_{\text{ext}}}{\mu_0 M_s}\right)^2 \tag{A.81}$$

between the angle in the xz-plane to the external field pointing in the $+x$ direction. We use the trigonometric relation

$$\cos 2\theta = 1 - 2\sin^2\theta \tag{A.82}$$

to substitute for the cosine term in (A.80). This transforms our damping coefficient into

$$\Gamma = -\frac{1}{2}\alpha_G\gamma\mu_0 M_s\left(2 - \left[\frac{B_{\text{ext}}}{\mu_0 M_s}\right]^2\right) \tag{A.83}$$

This damping is negative under the condition that $B_{\text{ext}}/(\mu_0 M_s) < \sqrt{2}$. This means the amplitude of precession for the SW is actually increasing. What is physically happening is the SW vector rotates with a larger and larger radius, because we are at an angle $\theta > 90^o$. When the external field is large enough to a point where

$B_{\text{ext}}/(\mu_0 M_s) > \sqrt{2}$ the angle $\theta < 90^o$ and the SW has a positive damping factor that will stabilize the internal magnetic field along with the very strong external field.

In this case when static magnetization is initially at some angle larger than 90^o from the $+x$ axis the damping factor actually behaviors as a gaining factor, where the SW amplitude grows. The other condition in which we can see this effect comes from the dispersion relation found from (A.77). When using our relation between the angle and external field (A.81), the dispersion relation becomes

$$\omega = \sqrt{(\gamma\mu_0 M_s)^2 - (\gamma B_{\text{ext}})^2} \tag{A.84}$$

As long as $(\gamma\mu_0 M_s)^2 > (\gamma B_{\text{ext}})^2$ we will have this gain effect.

All these SW results for a simple ferromagnetic thin film with various static magnetization cases are accredited to the theoretical work in [114].

APPENDIX B

DERIVATION OF INHOMOGENEOUS PARTIAL DIFFERENTIAL EQUATIONS

B.1 Fourier Transform of coupled Partial Differential Equations

Starting from (3.40) we have the complex amplitude wave equations in k-space and must convert them to a real space system to actually see the waves transform in real time from SAW to BVSW or vice versa. The index ξ for the summation is dropped because the BVSW is in the lowest SW mode and the ME gap $\Delta\omega_{\mathrm{ME}}$ won't mix with the higher-order SW resonant modes. Generally, speaking this derivation can be applied for any SW interaction with an acoustic wave. The k-space coupled wave amplitude system is

$$\frac{\mathrm{d}A_{\boldsymbol{k}}}{\mathrm{d}t} = -i\omega_{\boldsymbol{k}}^{(\mathrm{SAW})} A_{\boldsymbol{k}} - i g_{\boldsymbol{k}} S_{\boldsymbol{k}} \tag{B.1a}$$

$$\frac{\mathrm{d}S_{\boldsymbol{k}}}{\mathrm{d}t} = -i\omega_{\boldsymbol{k}}^{(\mathrm{SW})} S_{\boldsymbol{k}} - i g_{\boldsymbol{k}} A_{\boldsymbol{k}} \tag{B.1b}$$

Before converting these k-space wave equations, we perform a Taylor series expansion to simplify our work. We analyze the ME coupling point where the two wave dispersion relations cross. Focusing closely at the ME coupling point, the waves will be linearized by taking only the first order terms in the Taylor series expansion. Staying close to the ME coupling point, which is defined as (k_0, ω_0), will have a coupling rate that won't change considerably from g_0 The ME coupled point at (k_0,ω_0) with a coupling rate g_0 will be for a specific magnetic field at B_0. The Taylor series expansion for both the SAW and BVSW are presented as

$$\omega_{\boldsymbol{k}}^{(\mathrm{SAW})} = \omega_0 + \frac{\partial \omega}{\partial k}(k - k_0) \tag{B.2a}$$

$$\omega_{\boldsymbol{k}}^{(\mathrm{SW})} = \omega_0 + \frac{\partial \omega}{\partial k}(k - k_0) + \frac{\partial \omega}{\partial B}(B - B_0) \tag{B.2b}$$

We will perform a change in variables from k and B to $k_0 + \Delta k$ and $B_0 + \Delta B$. We also convert $\partial\omega/\partial k$ to the group velocities for each wave, respectively. Lastly, the $\partial\omega\big/\partial B$ is treated as a constant called the effective gyromagnetic ratio. Depending on the initial starter field one might choose this effective gyromagnetic ratio simply states how how the angular frequency changes with a change in the magnetic field. The two Taylor expanded dispersion relations then transform to

$$\omega_{k_0+\Delta k}^{(\mathrm{SAW})} = \omega_0 + v^{(\mathrm{SAW})}\Delta k \tag{B.3a}$$

$$\omega_{k_0+\Delta k}^{(\mathrm{SW})} = \omega_0 + v^{(\mathrm{SW})}\Delta k + \gamma_{\mathrm{eff}}\Delta B \tag{B.3b}$$

Before substituting (B.3) back into (B.1), we must transform the inverse Fourier transform we are applying to our k-space equations. The reason for this is because of our change in variables, i.e. $k \to \Delta k$. The normal inverse Fourier transform [77] is

$$f(x,t) = e^{i\omega_0 t} \int f_k(t) e^{ikx} \frac{dk}{2\pi} \tag{B.4}$$

However, for our change of basis from $k \to k_0 + \Delta k$ we have the inverse Fourier transform as

$$f^{\sim}(x,t) = e^{ik_0 x} \int f_{k_0+\Delta k}(t) e^{i\Delta k x} \frac{d\Delta k}{2\pi} \tag{B.5a}$$

$$f(x,t) = e^{i(\omega_0 t - k_0 x)} f^{\sim}(x,t) \tag{B.5b}$$

which is a two step process to obtain the proper function $f(x,t)$ for a real space system. We perform our derivation this way so our result reflects a propagating wave packet and not propagating oscillations of a wave in real space. The math is also simplified working with both derivatives and integrals for two different variables for time and space.

We now take our dispersion relations (B.3) and substitute them into (B.1). Then with noted notation the following system becomes

$$\frac{d}{dt}A_{k_0+\Delta k}(t) = -i\omega_0 A_{k_0+\Delta k}(t) - iv^{(\mathrm{SAW})}\Delta k A_{k_0+\Delta k}(t) - ig_0 S_{k_0+\Delta k}(t) \tag{B.6a}$$

$$\frac{d}{dt}S_{k_0+\Delta k}(t) = -i\omega_0 S_{k_0+\Delta k}(t) - iv^{(\mathrm{SW})}\Delta k S_{k_0+\Delta k}(t) - ig_0 A_{k_0+\Delta k}(t) - i\gamma_{\mathrm{eff}}\Delta B S_{k_0+\Delta k}(t) \tag{B.6b}$$

Since both formulas in (B.6) need to be transformed via the same method, we will only show the mathematically process for one expression. We will show how (B.6b) is inversely Fourier transformed step-by-step, since this expression has the extra term with $\gamma_{\text{eff}}\Delta B$ for S.

Starting simply with the left hand side, we apply the inverse Fourier transform defined by (B.5a). The left hand side of (B.6b) becomes

$$e^{ik_0 x}\int \frac{d}{dt}S_{k_0+\Delta k}(t)e^{i\Delta kx}\frac{d\Delta k}{2\pi} \tag{B.7}$$

We then pull out the derivative, because the wave amplitude S here is only time dependent. Notice now S is transformed via the first step in the two step process from (B.5). We rewrite our time derivative wave amplitude as

$$\frac{\partial}{\partial t}S^{\sim}(x,t) \tag{B.8}$$

The left hand side of (B.6b) is done for the first step of transformation. Please note, for repetition reasons and obvious dependence in the final result, we will suppress the (x,t) variables next to the wave amplitudes to avoid confusion within the long expressions written below.

Now we inverse Fourier transform the much tricker right hand side of (B.6b) with (B.5a). Our terms are placed inside the integral as

$$\begin{aligned} e^{ik_0 x}\int \Big[& -i\omega_0 S_{k_0+\Delta k}(t) - iv^{(\text{SW})}\Delta k S_{k_0+\Delta k}(t) \\ & - ig_0 A_{k_0+\Delta k}(t) - i\gamma_{\text{eff}}\Delta B S_{k_0+\Delta k}(t)\Big] e^{i\Delta kx}\frac{d\Delta k}{2\pi} \end{aligned} \tag{B.9}$$

Distribute the integral to each term and pull out constants for the first, third, and forth terms. The second term, with $v^{(\text{SW})}\Delta k S_{k_0+\Delta k}(t)$, is where a math trick will be applied. Rewriting (B.9) with into a more simplified form gives

$$-i\omega_0 S^{\sim} - v^{(\text{SW})}e^{ik_0 x}\int S_{k_0+\Delta k}(t)i\Delta k e^{i\Delta kx}\frac{d\Delta k}{2\pi} - ig_0 A^{\sim} - i\gamma_{\text{eff}}\Delta B S^{\sim} \tag{B.10}$$

where we have transformed most of the wave amplitudes by the first step in (B.5a). The second term still having an integral has had its variables moved around in a way to help see the procedure. The term $i\Delta k e^{i\Delta kx}$ is the derivative of the exponential with respect to x. Rewriting the open integral with this derivative term inside we have

$$-i\omega_0 S^{\sim} - v^{(\mathrm{SW})} e^{ik_0 x} \int S_{k_0+\Delta k}(t) \left[\frac{d}{dx} e^{i\Delta kx} \right] \frac{d\Delta k}{2\pi} - ig_0 A^{\sim} - i\gamma_{\mathrm{eff}} \Delta B S^{\sim} \tag{B.11}$$

We can bring the derivative operator outside the integral, but not in front of the exponential with dependent on x. The integral is not reduced to $S^{\sim}$ just yet, because we need the exponential $e^{i\Delta kx}$ next to the integral to be equal to (B.5a). Our new expression for the right hand side of (B.6b) is

$$-i\omega_0 S^{\sim} - v^{(\mathrm{SW})} e^{ik_0 x} \frac{d}{dx} \int S_{k_0+\Delta k}(t) e^{i\Delta kx} \frac{d\Delta k}{2\pi} - ig_0 A^{\sim} - i\gamma_{\mathrm{eff}} \Delta B S^{\sim} \tag{B.12}$$

At this point we perform a sneaky double derivative trick by adding two of the same integrals with different signs into (B.12). This way the system is conserved and we have more variables to play around which will help eliminate terms. Our new expression is

$$\begin{aligned} -i\omega_0 S^{\sim} - v^{(\mathrm{SW})} \Bigg[& ik_0 e^{ik_0 x} \int S_{k_0+\Delta k}(t) e^{i\Delta kx} \frac{d\Delta k}{2\pi} - ik_0 e^{ik_0 x} \int S_{k_0+\Delta k}(t) e^{i\Delta kx} \frac{d\Delta k}{2\pi} \\ & + e^{ik_0 x} \frac{d}{dx} \int S_{k_0+\Delta k}(t) e^{i\Delta kx} \frac{d\Delta k}{2\pi} \Bigg] - ig_0 A^{\sim} - i\gamma_{\mathrm{eff}} \Delta B S^{\sim} \end{aligned} \tag{B.13}$$

Looking closely at the first and third integrals within the brackets above, the terms out front, thinking backwards, function following the double derivative rule. Rewriting (B.13) to show these derivatives produces

$$\begin{aligned} -i\omega_0 S^{\sim} - v^{(\mathrm{SW})} \Bigg[& \frac{d}{dx}\left(e^{ik_0 x}\right) \int S_{k_0+\Delta k}(t) e^{i\Delta kx} \frac{d\Delta k}{2\pi} + e^{ik_0 x} \frac{d}{dx} \left(\int S_{k_0+\Delta k}(t) e^{i\Delta kx} \frac{d\Delta k}{2\pi} \right) \\ & - ik_0 e^{ik_0 x} \int S_{k_0+\Delta k}(t) e^{i\Delta kx} \frac{d\Delta k}{2\pi} \Bigg] - ig_0 A^{\sim} - i\gamma_{\mathrm{eff}} \Delta B S^{\sim} \end{aligned} \tag{B.14}$$

Working backwards from the derivative chain rule for two functions, we reduce our number of integrals to two as one can see below.

$$-i\omega_0 S^{\sim} - v^{(\mathrm{SW})}\left[-ik_0 e^{ik_0x}\int S_{k_0+\Delta k}(t)e^{i\Delta kx}\frac{d\Delta k}{2\pi} + \frac{d}{dx}\left(e^{ik_0x}\int S_{k_0+\Delta k}(t)e^{i\Delta kx}\frac{d\Delta k}{2\pi}\right)\right] \\ - ig_0A^{\sim} - i\gamma_{\mathrm{eff}}\Delta BS^{\sim} \tag{B.15}$$

The integrals containing S now match (B.5a), so we can reduce $S \to S^{\sim}$ and distribute the $v^{(\mathrm{SW})}$ to each term.

$$-i\omega_0 S^{\sim} + v^{(\mathrm{SW})}ik_0S^{\sim} - v^{(\mathrm{SW})}\frac{\partial}{\partial x}S^{\sim} - ig_0A^{\sim} - i\gamma_{\mathrm{eff}}\Delta BS^{\sim} \tag{B.16}$$

For the linear system we described in (B.3) the velocity, or slope, $v^{(\mathrm{SW})}$ multiplied by a specific wavevector k_0 will give a specific angular frequency ω_0. With the two front terms being the same, but opposite in sign they will cancel leaving us with

$$-v^{(\mathrm{SW})}\frac{\partial}{\partial x}S^{\sim} - ig_0A^{\sim} - i\gamma_{\mathrm{eff}}\Delta BS^{\sim} \tag{B.17}$$

for the right hand side of (B.6b). The full differential equation in (B.6b) is now complete with the first step of the inverse Fourier transform following from (B.5a). The exact same method is applied to (B.6a) and we have the coupled system as

$$\frac{\partial}{\partial t}A^{\sim} = -v^{(\mathrm{SAW})}\frac{\partial}{\partial x}A^{\sim} - ig_0S^{\sim} \tag{B.18a}$$

$$\frac{\partial}{\partial t}S^{\sim} = -v^{(\mathrm{SW})}\frac{\partial}{\partial x}S^{\sim} - ig_0A^{\sim} - i\gamma_{\mathrm{eff}}\Delta BS^{\sim} \tag{B.18b}$$

Step one is complete following (B.5a). The next step (B.5b) is how we obtain the formal inverse Fourier transform, defined in (B.4). To prove the inverse transform was done correctly on our coupled system of wave amplitudes, we multiply both sides of (B.18) by $e^{i(\omega_0 t - k_0 x)}$ from the left side. Again, the same process is applied to both expression in (B.18), so we will show the steps only for one; (B.18b) with the extra term.

Starting with the simpler left hand side of (B.18b) we have

$$e^{i\omega_0 t - ik_0 x}\frac{\partial}{\partial t}S^{\sim} \tag{B.19}$$

We will open up $S^{\sim}$ into its integral form and cut the exponential out front into two components: $e^{i\omega_0 t}$, $e^{-ik_0 x}$. The second exponential component will be moved into the partial derivative term giving us

$$e^{i\omega_0 t}\frac{d}{dt}e^{-ik_0 x}e^{ik_0 x}\int S_{k_0+\Delta k}(t)e^{i\Delta kx}\frac{d\Delta k}{2\pi} \tag{B.20}$$

The exponentials will cancel, and we will perform the same double derivative trick again by adding more integrals. Our new expression for the left hand side of (B.18b) becomes

$$\begin{aligned} &i\omega_0 e^{i\omega_0 t}\int S_{k_0+\Delta k}(t)e^{i\Delta kx}\frac{d\Delta k}{2\pi} \\ &\qquad -i\omega_0 e^{i\omega_0 t}\int S_{k_0+\Delta k}(t)e^{i\Delta kx}\frac{d\Delta k}{2\pi} + e^{i\omega_0 t}\frac{d}{dt}\int S_{k_0+\Delta k}(t)e^{i\Delta kx}\frac{d\Delta k}{2\pi} \end{aligned} \tag{B.21}$$

The first and third terms, will be worked backwards again, from the derivative chain rule for two functions. The second term, with different variables, is the formal inverse Fourier transform and the integral can be reduced to S. The left hand side becomes

$$\frac{d}{dt}\left(e^{i\omega_0 t}\right)\int S_{k_0+\Delta k}(t)e^{i\Delta kx}\frac{d\Delta k}{2\pi} - i\omega_0 e^{i\omega_0 t}S + e^{i\omega_0 t}\frac{d}{dt}\int S_{k_0+\Delta k}(t)e^{i\Delta kx}\frac{d\Delta k}{2\pi} \tag{B.22}$$

Combining the integrals and derivatives into one term, following the chain rules we get

$$\frac{d}{dt}\left(e^{i\omega_0 t}\int S_{k_0+\Delta k}(t)e^{i\Delta kx}\frac{d\Delta k}{2\pi}\right) - i\omega_0 S \tag{B.23}$$

The term within the parentheses is shown to be the proper inverse Fourier transform, so we can reduce our expression once again.

$$\frac{\partial}{\partial t}S - i\omega_0 S \tag{B.24}$$

The left hand side is now complete as a properly inverse transformed system. While we may have two terms, one will cancel when we work on the right hand side of (B.18b) next.

For the right hand side of (B.18b), we will start again by splitting the exponential into two components: $e^{i\omega_0 t}$, $e^{-ik_0 x}$. Expand the right two wave amplitudes, with terms g_0 and γ_{eff} out front, into the integral form from (B.5a).

$$-v^{(\text{SW})}e^{-ik_0 x}\frac{\partial}{\partial x}e^{i\omega_0 t}S^{\sim} - ig_0 e^{i\omega_0 t}e^{-k_0 x}e^{ik_0 x}\int A_{k_0+\Delta k}(t)e^{i\Delta k x}\frac{d\Delta k}{2\pi} \\ - i\gamma_{\text{eff}}\Delta B e^{i\omega_0 t}e^{-k_0 x}e^{ik_0 x}\int S_{k_0+\Delta k}(t)e^{i\Delta k x}\frac{d\Delta k}{2\pi} \tag{B.25}$$

The exponentials with $e^{ik_0 x}$ and $e^{-ik_0 x}$ will cancel and a formal inverse Fourier transform can be seen. The last two terms are then reduced to simply wave amplitudes in a real space system.

$$-v^{(\text{SW})}e^{-ik_0 x}\frac{\partial}{\partial x}e^{i\omega_0 t}S^{\sim} - ig_0 A - i\gamma_{\text{eff}}\Delta B S \tag{B.26}$$

The first term with $S^{\sim}$ is being multiplied by the exponential $e^{i\omega t}$. When expand $S^{\sim}$ into the integral form from (B.5a), we essentially swap the exponentials out front to use the proper inverse Fourier transform on $S_{k_0+\Delta k}(t)$. Simply swapping exponentials changes the definition of the wave amplitude transformation.

$$-v^{(\text{SW})}e^{-ik_0 x}\frac{\partial}{\partial x}e^{ik_0 x}S - ig_0 A - i\gamma_{\text{eff}}\Delta B S \tag{B.27}$$

At this point we do the same math trick of applying the double derivative trick to by adding terms that cancel. The $v^{(\text{SW})}$ is pulled out front to see

$$-v^{(\text{SW})}\left[ik_0 e^{-ik_0 x}e^{ik_0 x}S - ik_0 e^{-ik_0 x}e^{ik_0 x}S + e^{-ik_0 x}\left(\frac{\partial}{\partial x}e^{ik_0 x}S\right)\right] - ig_0 A - i\gamma_{\text{eff}}\Delta B S \tag{B.28}$$

Don't cancel the exponentials just yet as we need them to work backwards for the two function derivative chain rule. This time we are using the second and third term within the brackets. Rewriting the right hand side of (B.18b) with derivative operators gives

$$-v^{(\text{SW})}\left[ik_0 e^{-ik_0 x}e^{ik_0 x}S + \frac{\partial}{\partial x}(e^{-ik_0 x})e^{ik_0 x}S + e^{-ik_0 x}\left(\frac{\partial}{\partial x}e^{ik_0 x}S\right)\right] - ig_0 A - i\gamma_{\text{eff}}\Delta B S \tag{B.29}$$

Working backwards with the double derivative rule reduces (B.28) to

$$-v^{(\mathrm{SW})}\left[ik_0 e^{-ik_0x}e^{ik_0x}S + \frac{\partial}{\partial x}\left(e^{-ik_0x}e^{ik_0x}S\right)\right] - ig_0A - i\gamma_{\mathrm{eff}}\Delta BS \tag{B.30}$$

Here we now cancel the exponential terms, distribute $v^{(\mathrm{SW})}$, and set (B.24) and the newly written (B.29) equal to each other.

$$\frac{\partial}{\partial t}S - i\omega_0 S = -v^{(\mathrm{SW})}ik_0S - v^{(\mathrm{SW})}\frac{\partial}{\partial x}S - ig_0A - i\gamma_{\mathrm{eff}}\Delta BS \tag{B.31}$$

Using the linear system described in (B.3), again, the terms $-i\omega_0 S$ and $-v^{(\mathrm{SW})}ik_0S$ will cancel because $\omega_0 = v^{(\mathrm{SW})}\Delta k$.

With those last terms canceling out from both sides and we have derived (6.3). This is the same general expression used for the simulations of wave transformations in Chapter 6. The exact same process is repeated for the acoustic differential equation (B.6a) to end up with for both waves

$$\frac{\partial}{\partial t}A = -v^{(\mathrm{SAW})}\frac{\partial}{\partial x}A - ig_0S \tag{B.32a}$$

$$\frac{\partial}{\partial t}S = -v^{(\mathrm{SW})}\frac{\partial}{\partial x}S - ig_0A - i\gamma_{\mathrm{eff}}\Delta BS \tag{B.32b}$$

coupled partial differential equations.

B.2 Monochromatic Condition of coupled Partial Differential Equations

Starting from (B.32), with the complex wave amplitudes as $A(x,t)$ and $S(x,t)$ for the real system of differential equations, reflection and transmission coefficients are obtained via monochromatic conditions. The monochromatic condition means that in all of time and space, a wave is fixed to a certain frequency making the complex wave amplitude vary in an environment accordingly to spatial parameters. This changes our wave amplitudes for A and S to a simplified version where

$$\begin{pmatrix} A(x,t) \\ S(x,t) \end{pmatrix} = e^{-i\omega_0 t + ik_0 x} \begin{pmatrix} A(x) \\ S(x) \end{pmatrix} \tag{B.33}$$

Plug (B.33) into (B.32) noting dependence now only on x for the wave amplitudes. The partial derivative $\partial/\partial t$ becomes $-i\omega$, and the exponentials cancel on both sides.

$$-i\omega_0 A(x) = -v^{(\mathrm{SAW})}\left[ik_0 A(x) + \frac{dA}{dx}\right] - ig_0 S(x) \tag{B.34a}$$

$$-i\omega_0 S(x) = -v^{(\mathrm{SW})}\left[ik_0 S(x) + \frac{dS}{dx}\right] - ig_0 A(x) - i\gamma_{\mathrm{eff}}\Delta B(x) S(x) \tag{B.34b}$$

Distributing the wave velocities among the terms in the brackets, the $-i\omega$ terms in (B.34) will cancel. This happens because we have the same linear relation $\omega = vk$ for both acoustic and spin waves.

$$0 = -v^{(\mathrm{SAW})}\frac{dA}{dx} - ig_0 S(x) \tag{B.35a}$$

$$0 = -v^{(\mathrm{SW})}\frac{dS}{dx} - ig_0 A(x) - i\gamma_{\mathrm{eff}}\Delta B(x) S(x) \tag{B.35b}$$

From (B.35) move the derivative terms to the left hand side and divide the top expression by $v^{(\mathrm{SAW})}$, the bottom expression by $v^{(\mathrm{SW})}$. Rewrite these new expressions in matrix format as

$$\frac{d}{dx}\begin{pmatrix} A(x) \\ S(x) \end{pmatrix} = \begin{pmatrix} 0 & \frac{-ig_0}{v^{(\mathrm{SAW})}} \\ \frac{-ig_0}{v^{(\mathrm{SW})}} & \frac{-i\gamma_{\mathrm{eff}}\Delta B(x)}{v^{(\mathrm{SW})}} \end{pmatrix} \cdot \begin{pmatrix} A(x) \\ S(x) \end{pmatrix} \tag{B.36}$$

This expression shows how the reflection and transmission coefficients behavior for SAW and SW in an inhomogeneous magnetic medium. Notice the only spatial parameter creating the environment for the waves comes from $\Delta B(x)$, so only magnetism affects the wave amplitudes. However, this is for monochromatic conditions with a fixed frequency ω_0 where the waves couple. Meaning the waves will always couple in this system at some point in space. To see how the waves behavior in this inhomogeneous magnetic medium for different frequencies, terms must be added that shift the frequency away from the coupling point.

From the diagonal elements of the matrix a more complete theoretical work is derived. The bottom right element says that $\gamma_{\text{eff}}\Delta B(x)$ is the frequency that offsets coupling via the magnetic field changing in space. We expand on this idea adding terms for two components of this matrix in (B.36). The 0 in the top left element says this is the frequency ω_0 of the ME crossing point. To excite either a SAW or a SW at a higher or lower frequency we input the term $i(\omega-\omega_0)/v$ into the (B.36) matrix for diagonal components top-left and bottom-right. This shifts the waves frequency so we are not always at the coupling point (k_0, ω_0), unless the free angular frequency $\omega = \omega_0$. Our new system in the matrix is

$$\frac{d}{dx}\begin{pmatrix} A(x) \\ S(x) \end{pmatrix} = \begin{pmatrix} \frac{i(\omega-\omega_0)}{v^{(\text{SAW})}} & \frac{-ig_0}{v^{(\text{SAW})}} \\ \frac{-ig_0}{v^{(\text{SW})}} & \frac{i(\omega-\omega_0)-i\gamma_{\text{eff}}\Delta B(x)}{v^{(\text{SW})}} \end{pmatrix} \cdot \begin{pmatrix} A(x) \\ S(x) \end{pmatrix} \tag{B.37}$$

This is the same expression as the one used in Chapter 6, (6.7). This is the system where we use the Magnus Expansion from [239], [240] to obtain the reflection results in discussed in Chapter 6.

APPENDIX C

CODE

All numerical calculations, creation of plots, and simulations were done in Mathematica. Important to note contributing work from Cody Trevillian. Cody created two programs used for his work with [19]. They come from [61], [237], [239], [240] as sources to create programs for finding SW profiles and dispersions, and numerically solving the Magnus Expansion. They will be referred to as "codySW" and "codyMagnus" when used in my programs.

Within the code presented there are a number of symbols representing different variables used to find the final result. Most are self explanatory, but for clarity and to help keep track of units, any unit names typed out, Joules, Hertz, Tesla, meters, etc., are all equal to 1. This excludes prefixes where; Giga, Mega, micro, nano, etc., represent the corresponding numbers 10^9, 10^6, 10^{-6}, 10^{-9}, respectively. Below is a list of the remaining symbols and their meaning.

Symbol	Description
k	wavevector magnitude
ϕ	in-plane magnetization angle
θ	out-of-plane magnetization angle
mat	material parameter
L	YIG film thickness
heff	magnitude of static magnetization
npts	number of points used for numerical analysis
SWmodes	number of Spin Wave modes in spectrum
n	integer number
klow	lowest wavevector number in spectrum
khigh	largest wavevector number in spectrum
Ymat	numerical constant for elastic system, see (3.38)

$\mathbb{L}$	thickness of GGG substrate
λ, μ	Lamé constants
Norm	normalization for the waves vector profile
Damp	damping rate for a wave
col	the column component or subscript for a matrix element
AWP, SWP	Acoustic/Spin wave packet
DelHx	inhomogeneous magnetic field
ExcitedFreq,	initial frequency of initial wave
ko	wavevector at crossing point between acoustic and spin wave dispersion relations
CR	coupling rate
GammaEff	γ_{eff} constant, see (6.2) and (6.3)
AccuracyPoints	limiter on numerical method solving partial differential equations

Table C.1: Symbols used for variables in calculations of theoretical results

```
SpinWaveProfile[k_, φ_, θ_, mat_, L_, heff_, specificMode_, npts_,
SWmodes_ ]:= (
 Φ = Table[Cos[ (n π)/L (ξ + L/2)], { n, Range[0, SWmodes - 1] } ,
{ ξ, Range[-L/2, L/2, L/npts]} ];
 cn = codySW[k , φ, θ, mat, L, heff, SWmodes];
 Transpose[{ cn[[2]][[specificMode]][[;; ;; 2]] .  Φ,
cn[[2]][[specificMode]][[2 ;; ;; 2]].Φ, Range[-L/2, L/2, L/npts] } ]
)
```

```
 FindSurfaceSpinWave[ k_, φ_, θ_, mat_, L_, heff_, SWmodes_] := (
 TakeLargest[ Abs[Table[
codySW[k, φ, θ, mat, L, heff, SWmodes][[2, mode, 2]],
{ mode, 1, SWmodes} ]] → "Index", 3] )
```

```
 rotateSpinWaveProfile[k_, φ_, θ_, mat_, L_, heff_, specificMode_,
npts_, SWmodes_] := (
 SWP = SpinWaveProfile[k, φ, θ, mat, L, heff, specificMode, npts,
SWmodes];
 sx = SWP[[All, 1]];
 sy = SWP[[All, 2]];
 zdepth = SWP[[All, 3]];
 SWPzdepth = Table[{ sx[[n]] { 0, 0, 1 } +
sy[[n]] {-Sin[φ], -Cos[φ], 0} }, { n, Range[1, npts]} ] [All, 1]];
 RotatedSWP = {
Interpolation[Reverse[{ Abs[zdepth[[# ]] - L/2], SWPzdepth[[# , 1]] }
& / @ Range[1, npts]]] ,
Interpolation[Reverse[{ Abs[zdepth[[# ]] - L/2], SWPzdepth[[# , 2]] }
& / @ Range[1, npts]]] ,
Interpolation[ Reverse[{ Abs[zdepth[[# ]] - L/2], SWPzdepth[[# , 3]] }
& / @ Range[1, npts]]] } [[1, All, 1]] )
```

```
FindkpointbetweenSAWandAllSWmodes[klow_, khigh_, npts_, ϕ_, θ_,
mat_, L_, heff_, SWmodes_, Ymat_, μ_, ρ_] := (
 krange = Range[klow, khigh, (khigh - klow)/ npts];
 SAWfreq[k_] := 1/(2 Pi) Sqrt[Ymat(λ+2μ)/ρ] k;
 SWfreq = codySW[# , ϕ, θ, mat, L, heff, SWmodes] & /@ krange;
 transposeSWfreq = Transpose[SWfreq[[All, 1]]];
 Quiet[Table[{ k /.  FindRoot[ { Interpolation[ Transpose[ { krange,
Re[transposeSWfreq[[mode]] ] } ] ] [k] == SAWfreq[k] } , { k, klow,
khigh }, WorkingPrecision → 5], mode } , { mode, 1, SWmodes} ]] )


 CouplingSAWtoSWmodes[k_, ϕ_, θ_, mat_, L_, heff_, npts_, SWmodes_,
ρ_, 𝕃_, λ_, μ_, Ymat_, specificMode_] := (
 rVector[x_, y_, z_] := { x, y, z } ;
 kvector = { k , 0.0, 0.0 } ;
 ωSAW = k Sqrt[Ymat(λ+2μ)/ρ];
 ε = μ/(λ+2μ)];
 SAWvector[z_, k, Y = Ymat] := { (1-Yε/2)/(k Sqrt[1-Yε]) Exp[-kz
Sqrt[1-Yε] ] -1/(k Sqrt[1-Y] ) Exp[-kz Sqrt[1-Y] ] , 0,
-i/k ( (1-Yε/2)/(1-Yε) ) Exp[-kz Sqrt[1-Yε] ] - Exp[-kz Sqrt[1-Y] ] }
 SWvector = rotateSpinWaveProfile[k, ϕ, θ, mat, L, heff,
specificMode, npts, SWmodes];
 m0 = { Cos[ϕ], Sin[-ϕ], 0 };
 { bms1 = 0.35 Mega Joule /meter^3 , bms2 = 0.7 Mega Joule /meter^3 } ;
(*magnetostriction tensor fixed for YIG*)
```

```
 bmstensor = Table[bms1 KroneckerDelta[α, β] KroneckerDelta[α,γ]
KroneckerDelta[α, ζ] + bms2 Abs[KroneckerDelta[α, γ]
KroneckerDelta[β, ζ] - KroneckerDelta[α, ζ] KroneckerDelta[β, γ] ],
{ α, { 1, 2, 3}} , { β, { 1, 2, 3}} , { γ, {1, 2, 3}} ,
{ ζ, { 1, 2, 3}} ];
 NormSW = i 1750 G /( 2 Pi 28 (Giga Hertz/Tesla) ) 10^3/(4 Pi)
Tesla/(1 G) NIntegrate[ Dot[Conjugate[ { SWvector[[1]][z],
SWvector[[2]][z], SWvector[[3]][z] } ], Cross[m0, { SWvector[[1]][z],
SWvector[[2]][z], SWvector[[3]][z] } ]], { z, 0, L} ];
 NormSAW = 2 ωSAW ρ NIntegrate[ Dot[Conjugate[ SAWvector[z, k, Y =
Ymat]], SAWvector[z, k, Y = Ymat] ], { z, 0, 𝕃] } ];
 2 /Sqrt[NormSW NormSAW] ∑_{ζ=1}^{3} ∑_{γ=1}^{3} ∑_{β=1}^{3} ∑_{α=1}^{3} NIntegrate[
bmstensor[[ α, β, γ, ζ]] m0[[γ]] (
D[ SAWvector[z, k, Y = Ymat][[α]], rVector[x, y, z][[β]] ] + i
kvector[[β]] SAWvector[z, k, Y = Ymat][[α]] )
Conjugate[SWvector[[ζ][z]], { z,  0,  L} , MinRecursion →  0,
AccuracyGoal → 10] )


 CoupledDAMPEDPlotProgram[klow_, khigh_, φ_, θ_, mat_, L_, heff_,
npts_, SWmodes_, ρ_, 𝕃_, λ_, μ_, Ymat_, η_] := (
 krange = Range[klow, khigh, (khigh - klow)/npts];
 SAWfreq[k_] := 1/(2 Pi) Sqrt[Ymat(λ+2μ)/ρ] k;
 SWfreq = codySW[# , φ, θ, mat, L , heff, SWmodes] & /@ krange];
 transposedSWfreq = Transpose[ SWfreq[[All, 1]] ];
```

```
 SWmodeFunctionList = Table[ Interpolation[ Transpose[{ krange,
Re[transposedSWfreq[[mode]]] } ]], { mode, 1, SWmodes} ];
 kintersectionList = Quiet[ Table[ { kintersection /.FindRoot[{
SWmodeFunctionList[[mode]][kintersection] == SAWfreq[kintersection] }
, { kintersection, klow, khigh } , WorkingPrecision -> 5], mode } ,
{mode, 1, SWmodes } ]];
 CouplingRateList = CouplingSAWtoSWmodes[ kintersectionList[[# , 1]],
ϕ, θ, mat, L, heff, npts, SWmodes, ρ, 𝕃, λ, μ, Ymat, # ] & /@
Range[1, SWmodes];
 DampAW = η;
 SWvector = Table[ rotateSpinWaveProfile[
kintersectionList[[mode, 1]], ϕ, θ, mat, L, heff, specificMode, npts,
SWmodes], { mode, 1, SWmodes} ];
 NormSW = Table[i 1750 G/(2 Pi 28 (Giga Hertz)/Tesla ) 10^3/(4 Pi)
Tesla/(1 G) NIntegrate[Dot[Conjugate[{ SWvector[[mode, 1]][z],
SWvector[[mode, 2]][z], SWvector[[mode, 3]][z] } ], Cross[ { Cos[ϕ]],
Sin[-ϕ]], 0 } , { SWvector[[mode, 1]][z], SWvector[[mode, 2]][z],
SWvector[[mode, 3]][z] } ]], {z, 0, L} ], { mode, 1, SWmodes} ];
 DampSW = Table[( (*Gilbert Damping factor →*) 9 10^-5 (*ωn term in
matrixfunction calculation*) ) / NormSW[[mode]] 1750 G/ (2 Pi 28 (Giga
Hertz)/Tesla ) 10^3/(4 Pi) Tesla/(1 G) NIntegrate[
Abs[SWvector[[mode, 1]][z]]^2 + Abs[SWvector[[mode, 2]][z]]^2 +
Abs[SWvector[[mode, 3]][z]]^2, { z, 0, L} ], {mode, 1, SWmodes} ];
 matrixfunction[k_] := Quiet[Table[(2 Pi SWmodeFunctionList[[mode]][k]
(1 -(*impurity factor→*) 10 i DampSW[[mode]])) (KroneckerDelta[mode,
col] - KroneckerDelta[mode, col] KroneckerDelta[mode,SWmodes + 1]) +
```

```
(2 Pi SAWfreq[k] - i DampAW) (KroneckerDelta[mode, SWmodes + 1]
KroneckerDelta[mode, col]) + ( Conjugate[ CouplingRateList[[col]] ]
KroneckerDelta[mode, SWmodes + 1] + CouplingRateList[[mode]]
KroneckerDelta[SWmodes + 1, col] - CouplingRateList[[col]]
KroneckerDelta[SWmodes + 1, col] KroneckerDelta[mode, SWmodes + 1] -
Conjugate[CouplingRateList[[col]]] KroneckerDelta[SWmodes + 1, col]
KroneckerDelta[mode, SWmodes + 1]), { mode, 1, SWmodes + 1} ,
{ col, 1, SWmodes + 1} ]];
 ωCoupledSpectrum[k_] := Table[
Eigenvalues[matrixfunction[k]][[mode]], { mode, 1, SWmodes + 1} ];
 ωPlotValues = With[{ k = krange[[# ]] }, ωCoupledSpectrum[k]] & /@
Range[1, npts + 1];
 Table[{ krange[[n]], ωPlotValues[[aa]]} , { n, 1, npts + 1} ] )


 BVSWgroupVelocity[k_, klow_, khigh_, npts_, ϕ_, θ_, mat_, L_, heff_,
SWmodes_] := (
 krange = Range[klow, khigh, (khigh - klow)/npts];
 SWfreq = codySW[# , ϕ , θ, mat, L, heff, SWmodes] & /@ krange];
 transposeSWfreq = Re[ Transpose[ SWfreq[[All, 1]] ] ];
 BVSWdispersionRelation = Interpolation[ Transpose[{ krange,
transposeSWfreq[[1]] } ]];
 (2 Pi)* BVSWdispersionRelation'[k] )
```

```
 WaveConversionSimulation[XleftBound_, XrightBound_, TimeRange_, AWP_,
SWP_, DelHx_, ExcitedFreq_, SAWspeed_, ko_, CR_, BVSWspeed_,
GammaEff_, heff_, AccuracyPoints_] := (
 PDE1 = D[S[t, x], t] == -BVSWspeed D[S[t, x], x] - i (
(ExcitedFreq - ko SAWspeed) + GammaEff ( 10^3 /(4 Pi Oe) DelHx ) )
S[t, x] - i CR A[t, x];
 PDE2 = D[A[t, x], t] == -SAWspeed D[A[t, x], x] - i CR S[t, x];
 BoundaryConditions = A[t, XleftBound] == 0, S[t, XrightBound] == 0;
 InitialConditions = { A[0, x] == AWP[0, x], S[0, x] == SWP[0, x]} ;
 ppR = AccuracyPoints;(*for better result, increase this number.
Beware, more RAM and CPU time*);
 NDSolveValue[{ PDE1, PDE2, BoundaryConditions, InitialConditions} ,
{ S, A} , { t, 0, TimeRange} , { x, XleftBound, XrightBound },
MaxSteps → 10^6, Method → { "PDEDiscretization" → { "MethodOfLines",
"SpatialDiscretization" → { "TensorProductGrid", "MinPoints" → ppR,
"MaxPoints" → ppR } } } ] )


 ContinuousPULSESimulation4DAMPING[XleftBound_, XrightBound_,
SpaceStepSize_, ω_, DelHx_, kfilm_, ϕ_, θ_, mat_, L_, heff_,
SWmodes_, SAWspeed_, BVSWspeed_, CR_, DampSW_, DampAW_] := (
 DelWx[x_] := SAWspeed/(SAWspeed - BVSWfilmvel) GammaEff
10^3 /(4 Pi Oe) DelHx[x] ;
 ContinuousMatrixM[x_] := ( { { i/SAWspeed (ω - ko SAWspeed) +
DampAW/SAWspeed, -i CR/SAWspeed} , { -i CR/BVSWspeed, i/BVSWspeed (
(ω - ko SAWspeed) - DelWx[x] ) + DampSW/BVSWspeed } } );
```

```
 InfiniteMatrix = ( { { i/SAWspeed (ω - ko SAWspeed) + DampAW/
SAWspeed, (-i CR)/SAWspeed} , { (-i CR)/BVSWspeed, i/BVSWspeed
(ω - ko SAWspeed) + DampSW/BVSWspeed } } );
 PHIofMagnusMatrix = Reverse[ codyMagnus [ContinuousMatrixM, {
XleftBound, XrightBound, SpaceStepSize } , Method → "Magnus6"] // N];
(*Transforming System*)
 AcousticVectors = Eigenvectors[InfiniteMatrix][[2]];
 SpinVectors = Eigenvectors[InfiniteMatrix][[1]];
 NormPowerAcoustic = SAWspeed Abs[AcousticVectors[[1]]]^2 + BVSWspeed
Abs[AcousticVectors[[2]]]^2;
 NormPowerSpinWave = SAWspeed Abs[SpinVectors[[1]]]^2 + BVSWspeed
Abs[SpinVectors[[2]]]^2;
 NormPowerAcoustic = 1/Sqrt[NormPowerAcoustic];
 NormPowerSpin = 1/Sqrt[-NormPowerSpinWave];
 AcousticEigenValues = NormPowerAcoustic AcousticVectors;
 SpinEigenValues = NormPowerSpin SpinVectors;
 TransformedMatrixQ = Transpose[{ AcousticEigenValues,
SpinEigenValues} ];
 TransformedInverseQ = Inverse[TransformedMatrixQ];
 NewNormPHIsystem = Table[TransformededInverseQ .
PHIofMagnusMatrix[[n]] .  TransformededMatrixQ, { n, 1,
Length[PHIofMagnusMatrix]} ];
 (*Finding the travel distance of waves and the points of Reflection,
Power of SAW initially, and final Power of BVSW *)
 SpaceRegion = Range[XleftBound, XrightBound, SpaceStepSize];
```

```
 SWpower = Table[Abs[( NewNormPHIsystem[[power]].{1, 0} )[[2]] ]^2,
{ power, 1, Length[SpaceRegion] } ];
 ReflectionPoint = TakeLargest[SWpower → "Index", 1] [[1]];
 travelingDistance = Abs[SpaceRegion[[1]] ] -
Abs[SpaceRegion[[ReflectionPoint]] ];
 EffDampAW = Eigenvalues[InfiniteMatrix] [[2]];
 EffDampSW = Eigenvalues[InfiniteMatrix] [[1]];
 If[Re[EffDampAW] > 0,
(*If True then this entry happens*)
{EffDampAW = Eigenvalues[InfiniteMatrix ][[2]],
EffDampSW = Eigenvalues[InfiniteMatrix ][[1]] } ,
(*If False then this entry happens*)
{ EffDampAW = Eigenvalues[InfiniteMatrix ][[1]],
EffDampSW = Eigenvalues[InfiniteMatrix ][[2]]} ];
 StartPower = Log[(Abs[NewNormPHIsystem[[1]] .  {1, 0} ]^2)[[1]]
Exp[-2 Re[EffAWdamp] travelingDistance ]];
 AWendPower = Log[( Abs[ NewNormPHIsystem[[Length[SpaceRegion]]] .
{1, 0} ]^2)[[1]] Exp[2 Re[EffDampAW] ( XrightBound -
SpaceRegion[[ReflectionPoint]] ) ]];
 SWendPower = Log[ (Abs[NewNormPHIsystem[[1]] .  {1, 0} ]^2)[[2]]
Exp[-2 Re[EffDampSW] travelingDistance ]];
 (*Reflection Coefficient=*) {SWendPower/StartPower,
(*Transmission Coefficient=*) AWendPower/StartPower} )
```

REFERENCES

[1] W. Bae, "Today's computing challenges: Opportunities for computer hardware design," *PeerJ Computer Science*, vol. 7, 2021. DOI: `10.7717/peerj-cs.420`.

[2] D. D'Agostino, I. Merelli, M. Aldinucci, and D. Cesini, "Hardware and software solutions for energy-efficient computing in scientific programming," *Scientific Programming*, vol. 2021, 2021. DOI: `https://doi.org/10.1155/2021/5514284`.

[3] S. S. Kim, S. K. Yong, W. Kim, *et al.*, "Review of semiconductor flash memory devices for material and process issues," *Advanced Materials*, vol. 35, 2023. DOI: `https://doi.org/10.1002/adma.202200659`.

[4] R. K. Cavin, P. Lugli, and V. V. Zhirnov, "Science and engineering beyond moore's law," *Proceedings of the IEEE*, vol. 100, pp. 1720–1749, 2012. DOI: `10.1109/JPROC.2012.2190155`.

[5] J. Yuan, Y. Zhang, F. Chen, and Z. Gu, "An overview of joule heating in energy storage materials and applications," *Journal of Materials Chemistry C*, 2024.

[6] A. Hirohata, K. Yamada, Y. Nakatani, *et al.*, "Review on spintronics: Principles and device applications," *Journal of Magnetism and Magnetic Materials*, vol. 509, 2020.

[7] P. J. Rajput, S. U. Bhandari, and G. Wadhwa, "A review on—spintronics an emerging technology," *Silicon*, vol. 14, no. 15, pp. 9195–9210, 2022.

[8] A. Hoffmann and S. D. Bader, "Opportunities at the frontiers of spintronics," *Phys. Rev. Appl.*, vol. 4, p. 047 001, 4 2015. DOI: `10.1103/PhysRevApplied.4.047001`.

[9] Z. Guo, J. Yin, Y. Bai, *et al.*, "Spintronics for energy- efficient computing: An overview and outlook," *Proceedings of the IEEE*, vol. 109, pp. 1398–1417, 2021. DOI: `10.1109/JPROC.2021.3084997`.

[10] S. M. Yakout, "Spintronics: Future technology for new data storage and communication devices," *Journal of superconductivity and novel magnetism*, vol. 33, no. 9, pp. 2557–2580, 2020.

[11] A. Chumak, V. Vasyuchka, A. Serga, and B. Hillebrands, "Magnon spintronics," *Nature Physics*, vol. 11, pp. 453–461, 6 2015. DOI: `10.1038/nphys3347`.

[12] T. Endoh and H. Honjo, "A recent progress of spintronics devices for integrated circuit applications," *Journal of Low Power Electronics and Applications*, vol. 8, 2018. DOI: `10.3390/jlpea8040044`.

[13] W. Kang, Y. Zhang, Z. Wang, *et al.*, "Spintronics: Emerging ultra-low-power circuits and systems beyond mos technology," *Association for Computing Machinery*, vol. 12, 2015. DOI: 10.1145/2663351.

[14] J. Lu, E. Chen, M. Kabir, M. Stan, and S. Wolf, "Spintronics technology: Past, present and future," *International Materials Reviews*, vol. 61, pp. 456–472, 2016. DOI: 10.1080/09506608.2016.1204097.

[15] H. Bradley, S. Louis, A. Slavin, and V. Tyberkevych, "Pattern recognition using spiking antiferromagnetic neurons," *Scientific Reports*, vol. 14, no. 1, 2024. DOI: 10.1038/s41598-024-69480-7.

[16] J. Grollier, D. Querlioz, K. Camsari, K. Everschor-Sitte, S. Fukami, and M. Stiles, "Neuromorphic spintronics," *nature electronics*, vol. 3, 7 2020. DOI: 10.1038/s41928-019-0360-9.

[17] S. Louis, H. Bradley, C. Trevillian, A. Slavin, and V. Tyberkevych, *Spintronic neuron using a magnetic tunnel junction for low-power neuromorphic computing*, 2025. DOI: 10.48550/arXiv.2409.09268.

[18] S. Louis, I. Lisenkov, S. Nikitov, V. Tyberkevych, and A. Slavin, "Reconfigurable magnonic metamaterial for microwave signal processing," *2016 10th International Congress on Advanced Electromagnetic Materials in Microwaves and Optics (METAMATERIALS)*, 2016. DOI: 10.1109/MetaMaterials.2016.7746492.

[19] C. Trevillian and V. Tyberkevych, "Universal set of magnon-mediated quantum gates," in *2023 IEEE International Magnetic Conference - Short Papers (INTERMAG Short Papers)*, 2023. DOI: 10.1109/INTERMAGShortPapers58606.2023.10228694.

[20] D. D. Awschalom, C. R. Du, R. He, *et al.*, "Quantum engineering with hybrid magnonic systems and materials," *IEEE Transactions on Quantum Engineering*, vol. 2, 2021. DOI: 10.1109/TQE.2021.3057799.

[21] D. Lachance-Quirion, Y. Tabuchi, A. Gloppe, K. Usami, and Y. Nakamura, "Hybrid quantum systems based on magnonics," *Applied Physics Express*, vol. 12, 2019. DOI: 10.7567/1882-0786/ab248d.

[22] E. T. Papaioannou and R. Beigang, "Thz spintronic emitters: A review on achievements and future challenges," *Nanophotonics*, vol. 10, pp. 1243–1257, 2021. DOI: 10.1515/nanoph-2020-0563.

[23] T. Kampfrath, A. Kirilyuk, S. Mangin, S. Sharma, and M. Weinelt, "Ultrafast and terahertz spintronics: Guest editorial," *Applied Physics Letters*, vol. 123, 2023. DOI: 10.1063/5.0167151.

[24] W. Wu, C. Yaw Ameyaw, M. F. Doty, and M. B. Jungfleisch, "Principles of spintronic thz emitters," *Journal of Applied Physics*, vol. 130, 2021. DOI: 10.1063/5.0057536.

[25] K. O. Levchenko, K. Davídková, J. Mikkelsen, and A. V. Chumak, "Review on spin-wave rf applications," *IEEE Transactions on Magnetics*, 2026. DOI: 10.1109/TMAG.2026.3657608.

[26] A. Mahmoud, F. Ciubotaru, F. Vanderveken, *et al.*, "Introduction to spin wave computing," *Journal of Applied Physics*, vol. 128, no. 16, 2020. DOI: 10.1063/5.0019328.

[27] S. Biryukov, Y. Gulyaev, V. Krylov, and V. Plessky, *Surface Acoustic Waves in Inhomogeneous Media* (Springer Series on Wave Phenomena). Springer, 1995, ISBN: 9783540584605.

[28] D. Mandal and S. Banerjee, "Surface acoustic wave (saw) sensors: Physics, materials, and applications," *Sensors*, vol. 22, 3 2022. DOI: 10.3390/s22030820.

[29] R. Hays and C. Hartmann, "Surface-acoustic-wave devices for communications," *Proceedings of the IEEE*, vol. 64, pp. 652–671, 1976. DOI: 10.1109/PROC.1976.10190.

[30] D. P. Morgan, "Surface acoustic wave devices," in *Wiley Encyclopedia of Electrical and Electronics Engineering*. John Wiley and Sons, Ltd, 1999, ISBN: 9780471346081. DOI: 10.1002/047134608X.W7423.pub2.

[31] R. Weigel, D. P. Morgan, J. M. Owens, *et al.*, "Microwave acoustic materials, devices, and applications," *IEEE Transactions on Microwave Theory and Techniques*, vol. 50, pp. 738–749, 3 2002. DOI: 10.1109/22.989958.

[32] N. Babu, A. Trzaskowska, P. Graczyk, *et al.*, "The interaction between surface acoustic waves and spin waves: The role of anisotropy and spatial profiles of the modes," *Nano Letters*, vol. 21, pp. 946–951, 2 2021. DOI: 10.1021/acs.nanolett.0c03692.

[33] R. Q. Scott and D. L. Mills, "Propagation of surface magnetoelastic waves on ferromagnetic crystal substrates," *Physical Review B*, vol. 15, pp. 3545–3557, 7 1977. DOI: 10.1103/PhysRevB.15.3545.

[34] R. E. Camley and R. Q. Scott, "Surface magnetoelastic waves in the presence of exchange interactions and pinning of surface spins," *Physical Review B*, vol. 17, pp. 4327–4334, 11 1978. DOI: 10.1103/PhysRevB.17.4327.

[35] Y. Gulyaev, I. Dikshtein, and V. Shavrov, "Magnetoacoustic surface waves in magnetic crystals near spin-reorientation phase transitions," *Physics*, vol. 40, pp. 701–716, 7 1997. DOI: 10.1070/pu1997v040n07abeh000252.

[36] Y. Li, W. Zhang, V. Tyberkevych, W.-K. Kwok, A. Hoffmann, and V. Novosad, "Hybrid magnonics: Physics, circuits, and applications for coherent information processing," *Journal of Applied Physics*, vol. 128, 13 2020. DOI: 10.1063/5.0020277.

[37] N. Homrocky, C. Trevillian, and V. Tyberkevych, "Magneto-elastic coupling of surface spin and surface acoustic waves," *IEEE Magnetics Letters*, vol. 16, pp. 1–5, 2025. DOI: 10.1109/LMAG.2025.3536936.

[38] S. Hanna, F. Friedlaender, R. Gunshor, and H. Sato, "Propagation of surface acoustic waves in magnetic bubble garnet films," *IEEE Transactions on Magnetics*, vol. 19, pp. 1802–1804, 5 1983. DOI: 10.1109/TMAG.1983.1062656.

[39] B. D. Zaitxev, A. V. Ermolenko, and V. A. Fedorenko, "Magnetoacoustic saw interaction in yig films," *IEEE Transactions on Ultrasonics, Ferroelectrics and Frequency Control*, vol. 45, 2 1998. DOI: 10.1109/58.660146.

[40] R. G. Kryshtal and A. V. Medved, "Nonreciprocity of spin waves in magnonic crystals created by surface acoustic waves in structures with yttrium iron garnet," *Journal of Magnetism and Magnetic Materials*, vol. 395, pp. 180–184, 2015. DOI: 10.1016/j.jmmm.2015.07.086.

[41] S. M. Hanna and G. P. Murphy, "Interactions between magnetostatic and surface acoustic waves in garnet films," *IEEE Transactions on Magnetics*, vol. 24, pp. 2814–2816, 6 1998. DOI: 10.1109/20.92254.

[42] D. Kobayashi, T. Yoshikawa, M. Matsuo, *et al.*, "Spin current generation using a surface acoustic wave generated via spin-rotation coupling," *Physical Review Letters*, vol. 119, 7 2017. DOI: 10.1103/PhysRevLett.119.077202.

[43] H. Meer, O. Gomonay, C. Schmitt, *et al.*, "Strain-induced shape anisotropy in antiferromagnetic structures," *Physical Review B*, vol. 106, 9 2022. DOI: 10.1103/PhysRevB.106.094430.

[44] T. Yu, "Nonreciprocal surface magnetoelastic dynmaics," *Physical Review B*, vol. 102, 13 2020. DOI: 10.1103/physrevb.102.134417.

[45] H. Arisawa, H. Shim, S. Daimon, *et al.*, "Observation of spin-current striction in a magnet," *Nature Communications*, vol. 13, no. 1, 2022. DOI: 10.1038/s41467-022-30115-y.

[46] D. Sander, "The correlation between mechanical stress and magnetic anisotropy in ultrathin films," *Reports on Progress in Physics*, vol. 62, pp. 809–858, 5 1999. DOI: 10.1088/0034-4885/62/5/204.

[47] S. Zhuang, Y. Zhu, C. Zhong, L. Jiang, X. Zhang, and J.-M. Hu, "Dynamical phase-field model of cavity electromangnetic systems," *npj Computational Materials*, vol. 10, 1 2024. DOI: 10.1038/s41524-024-01380-w.

[48] J. D. Adam, "Analog signal processing with microwave magnetics," *Proceedings of the IEEE*, vol. 76, pp. 159–170, 2 1998. DOI: 10.1109/5.4392.

[49] J. Owens, C. Smith, S. Lee, and J. Collins, "Magnetostatic wave propagation through periodic metallic gratings," *IEEE Transactions on Magnetics*, vol. 14, no. 5, pp. 820–825, 1978. DOI: 10.1109/TMAG.1978.1059970.

[50] J. Puebla, Y. Hwang, S. Maekawa, and Y. Otani, "Perspectives on spintronics with surface acoustic waves," *Applied Physics Letters*, vol. 120, 22 2022. DOI: 10.1063/5.0093654.

[51] D. Stancil and A. Prabhakar, *Spin Waves: Theory and Applications*. Springer, 2008, ISBN: 9780387778648.

[52] J. Coey, *Magnetism and Magnetic Materials*, 1st ed. Cambridge University Press, 2001, ISBN: 978-0-521-81614-4.

[53] M. Küß, M. Heigl, L. Flacke, *et al.*, "Symmetry of the magnetoelastic interaction of rayleigh and shear horizontal magnetoacoustic waves in nickel thin films on litao3," *Physical Review Applied*, vol. 15, 3 2021. DOI: 10.1103/physrevapplied.15.034046.

[54] R. Sano, Y. Ominato, and M. Matsuo, "Acoustomagnonic spin hall effect in honeycomb antiferromagnets," *Physical Review Letters*, vol. 132, 23 2024. DOI: 10.1103/PhysRevLett.132.236302.

[55] X. Zuo, Z.-Y. Fan, H. Qian, *et al.*, "Cavity magnomechanics: From classical to quantum," *New Journal of Physics*, vol. 26, 3 2024. DOI: 10.1088/1367-2630/ad327c.

[56] D. Bozhko, P. Clausen, G. Melkov, *et al.*, "Bottleneck accumulation of hybrid magnetoelastic bosons," *Physical Review Letters*, vol. 118, 23 2017. DOI: 10.1103/PhysRevLett.118.237201.

[57] A. Scherbakov, A. Carr, T. Linnik, *et al.*, "Hybrid coherent control of magnons in a ferromagnetic phononic resonator excited by laser pulses," *Physical Review Research*, vol. 6, 1 2024. DOI: 10.1103/PhysRevResearch.6.L012019.

[58] Y. Li, C. Zhao, W. Zhang, A. Hoffmann, and V. Novosad, "Advances in coherent coupling between magnons and acoustic phonons," *APL Materials*, 2021. DOI: 10.1063/5.0047054.

[59] A. Kovalev, B. Li, and E. Schwartz, "Nonreciprocal superfluidlike topological spin transport," *Physical Review B*, vol. 110, 4 2024. DOI: 10.1103/PhysRevB.110.045122.

[60] A. Koujok, A. Riveros, D. R. Rodrigues, *et al.*, "Resonant excitation of vortex gyrotropic mode via surface acoustic waves," *Applied Physics Letters*, vol. 123, 13 2023. DOI: 10.1063/5.0168968.

[61] B. A. Kalinikos and A. N. Slavin, "Theory of dipole-exhcange spin wave spectrum for ferromangetic films with mixed exchange boundary condtions," *Journal of Physics C: Solid State Physics*, vol. 19, pp. 7013–7033, 35 1986. DOI: 10.1088/0022-3719/19/35/014.

[62] K. Yamamoto, W. Yu, T. Yu, *et al.*, "Non-reciprocal pumping of surface acoustic waves by spin wave resonance," *Journal of the Physical Society of Japan*, vol. 89, 11 2020. DOI: 10.7566/JPSJ.89.113702.

[63] F. Ryburn, K. Künstle, Y. Zhang, *et al.*, "Generation of gigahertz frequency surface acoustic waves in yig/zno heterostructures," 2024. DOI: 10.48550/arXiv.2403.03006.

[64] X. Li, D. Labanowski, S. Salahuddin, and C. Lynch, "Spin wave generation by surface acoustic waves," *Journal of Applied Physics*, vol. 122, 4 2017. DOI: 10.1063/1.4996102.

[65] R. G. Kryshtal and A. V. Medved, "Nonlinear spin waves in dynamic magnonic crystals created by surface acoustic waves in yttrium iron garnet films," *Journal of Physics D: Applied Physics*, vol. 50, p. 495 004, 2017. DOI: 10.1088/1361-6463/aa93ba.

[66] T. Rossing, *Springer handbook of acoustics*, 2nd ed. Springer, 2014, ISBN: 978-1-4939-0755-7.

[67] H. v. Helmholtz, "On the sensations of tone," *Annalen der Physik*, vol. 175, no. 12, pp. 497–540, 1856.

[68] J. W. S. B. Rayleigh, *The theory of sound*. Macmillan, 1896, vol. 2.

[69] J. Greenslade Thomas B., "The acoustical apparatus of rudolph koenig," *The Physics Teacher*, vol. 30, no. 9, pp. 518–524, 1992. DOI: 10.1119/1.2343629.

[70] R. Boyle, "New experiments physico-mechanicall, touching the spring of the air, and its effects," *European Libraries, Oxford*, 1660.

[71] G. Stokes, "On the theories of the internal friction of fluids in motion and of the equilibrium and motion of elastic solids," *Cambridge Philosphoical Society*, pp. 287–319, 1845.

[72] S. Katzir, "The discovery of the piezoelectric effect," *Archive for History of Exact Sciences*, vol. 57, 1 2003. DOI: 10.1007/s00407-002-0059-5.

[73] B. A. Auld, *Acoustic fields and waves in solids*. Wiley, 1973, ISBN: 0471037028.

[74] L. E. Kinsler, *Fundamentals of acoustics*, 4th ed. Wiley, 1962, ISBN: 978-0-471-84789-2.

[75] M. Bruneau, T. Scelo, and S. F. d'Acoustique, *Fundamentals of Acoustics* (ISTE). Wiley, 2013, ISBN: 9781118613931.

[76] G. Cloutier, F. Destrempes, F. Yu, and A. Tang, "Quantitative ultrasound imaging of soft biological tissues: A primer for radiologists and medical physicists," *Insights into Imaging*, vol. 12, 2021. DOI: 10.1186/s13244-021-01071-w.

[77] G. Arfken, H.-J. WEber, and F. Harris, *Mathematical Methods for Physicists*, 7th ed. Elsevier, 2013, pp. 1089–1124, ISBN: 9780123846549.

[78] *Lamé constants – eric weisstein's world of physics*, https://scienceworld.wolfram.com/physics/LameConstants.html, 1997.

[79] T. Sato, W. Yu, S. Streib, and G. Bauer, "Dynamic magnetoelastic boundary conditions and the pumping of phonons," *Physical Review B*, vol. 104, 1 2021. DOI: 10.1103/PhysRevB.104.014403.

[80] *Surface waves*, https://www.mtu.edu/geo/community/seismology/learn/seismology-study/surface-wave/.

[81] E. Ippen, "Diffraction of light by surface acoustic waves," *Proceedings of the IEEE*, vol. 55, no. 2, pp. 248–249, 1967.

[82] M. Epstein, "Surface microacoustics," Defense Technical Information Center, Tech. Rep., 1970.

[83] A. Alippi, A. Palma, L. Palmieri, G. Socino, and E. Verona, "Acousto-optics with surface acoustic waves devices and applications," *Optica Acta: International Journal of Optics*, vol. 27, no. 8, pp. 1061–1076, 1980. DOI: 10.1080/713820375.

[84] F. Hickernell, "Surface acoustic wave devices: A rewarding past, a significant present, and a promising future," in *12th International Conference on Microwaves and Radar*, vol. 4, 1998, pp. 159–168. DOI: 10.1109/MIKON.1998.738468.

[85] K. Lange, B. E. Rapp, and M. Rapp, "Surface acoustic wave biosensors: A review," *Analytical and bioanalytical chemistry*, vol. 391, no. 5, pp. 1509–1519, 2008.

[86] J. Zhou, D. Zhang, Y. Liu, *et al.*, "Record-breaking frequency of 44 ghz based on the higher order mode of surface acoustic waves with $LiNbO_3/SiO_2/SiC$ heterostructures," *Engineering*, vol. 20, pp. 112–119, 2023. DOI: 10.1016/j.eng.2022.05.003.

[87] M. Redwood and R. Milsom, "Piezoelectric coupling coefficient of interdigital rayleigh-wave transducers," *Electronics Letters*, vol. 6, pp. 437–437, 14 1970. DOI: 10.1049/el:19700306.

[88] K.-Y. Hashimoto, *Surface acoustic wave devices in telecommunications*. Springer, 2000, vol. 116. DOI: 10.1007/978-3-662-04223-6.

[89] C. Brown, R. Kell, R. Taylor, and L. Thomas, "Piezoelectric materials, a review of progress," *IRE Transactions on component parts*, vol. 9, no. 4, pp. 193–211, 1962.

[90] M. Habib, I. Lantgios, and K. Hornbostel, "A review of ceramic, polymer and composite piezoelectric materials," *Journal of Physics D: Applied Physics*, vol. 55, no. 42, 2022.

[91] Y. Zhang, J. Luo, A. J. Flewitt, Z. Cai, and X. Zhao, "Film bulk acoustic resonators as biosensors: A review," *Biosensors and Bioelectronics*, vol. 116, pp. 1–15, 2018. DOI: 10.1016/j.bios.2018.05.028.

[92] R. M. White and F. W. Voltmer, "Direct piezoelectric coupling to surface elastic waves," *Applied Physics Letters*, vol. 7, no. 12, pp. 314–316, 1965. DOI: 10.1063/1.1754276.

[93] Jakirschner, *Surface acoustic wave sensor interdigitated transducer diagram*, https://commons.wikimedia.org/wiki/File:Surface_Acoustic_Wave_Sensor_Interdigitated_Transducer_Diagram.png, 2010.

[94] K.-Y. Hashimoto, *Interdigital Transducers*. Berlin, Heidelberg: Springer Berlin Heidelberg, 2000, pp. 47–85, ISBN: 978-3-662-04223-6. DOI: 10.1007/978-3-662-04223-6_3.

[95] W. Ziping, X. Xiqiang, Q. Lei, W. Jiatao, F. Yue, and T. Maoyuan, "Research on the progress of interdigital transducer (idt) for structural damage monitoring," *Journal of Sensors*, vol. 2021, 2021. DOI: 10.1155/2021/6630658.

[96] M. B. Mazalan, A. M. Noor, Y. Wahab, S. Yahud, and W. S. W. K. Zaman, "Current development in interdigital transducer (idt) surface acoustic wave devices for live cell in vitro studies: A review," *Micromachines*, vol. 13, 2022. DOI: 10.3390/mi13010030.

[97] A. Mujahid and F. L. Dickert, "Surface acoustic wave (saw) for chemical sensing applications of recognition layers," *Sensors*, vol. 17, 2017. DOI: 10.3390/s17122716.

[98] F. Crystal, *Surface acoustic wave devices explained: Principles, history and sensing applications*, https://www.fujicrystal.com/news_details/surface-acoustic-wave-device-intro.html, 2025.

[99] Y. Yang, C. Dejous, and H. Hallil, "Trends and applications of surface and bulk acoustic wave devices: A review," *Micromachines*, vol. 14, 2023. DOI: 10.3390/mi14010043.

[100] L. Kelly, P. Berini, and X. Bao, "Measuring velocity, attenuation, and reflection in surface acoustic wave cavities through acoustic fabry–pérot spectra," *IEEE Transactions on Ultrasonics, Ferroelectrics, and Frequency Control*, vol. 69, no. 4, pp. 1542–1548, 2022. DOI: 10.1109/TUFFC.2022.3146822.

[101] D. Lee, Y. Jiang, X. Zhang, *et al.*, "Klein tunneling of gigahertz elastic waves in nanoelectromechanical metamaterials," *Device*, vol. 2, no. 10, 2024. DOI: 10.1016/j.device.2024.100474.

[102] B. Friedrich and D. Herschbach, "Stern and gerlach: How a bad cigar helped reorient atomic physics," *Physics Today*, vol. 56, pp. 53–59, 12 2003. DOI: 10.1063/1.1650229.

[103] D. J. Griffiths and D. F. Schroeter, *Introduction to Quantum Mechanics*, 3rd ed. Cambridge University Press, 2018, ISBN: 9781316995433.

[104] J. D. Jackson, *Classical Electrodynamics*. Wiley, 2009, ISBN: 9780471309321.

[105] L. E. Reichl, *A Modern course in Statistical Physics*, 4th ed. Wiley, 2016, ISBN: 9783527413492.

[106] P. Geerlings, F. DeProft, and W. Langenaeker, "Conceptual density functional theory," *Chemical Reviews*, vol. 103, pp. 1793–1874, 5 2003. DOI: 10.1021/cr990029p.

[107] E. S. Kryachko and E. V. Ludeña, "Density functional theory: Foundations reviewed," *Physics Reports*, vol. 544, no. 2, pp. 123–239, 2014. DOI: 10.1016/j.physrep.2014.06.002.

[108] Á. Nagy, "Density functional. theory and application to atoms and molecules," *Physics Reports*, vol. 298, no. 1, pp. 1–79, 1998. DOI: 10.1016/S0370-1573(97)00083-5.

[109] R. Skomski, *Magnetic Exchange Interactions*, M. Coey and S. Parkin, Eds. Springer International Publishing, 2020, pp. 1–50, ISBN: 978-3-030-63101-7. DOI: 10.1007/978-3-030-63101-7_2-1.

[110] W. Heisenberg, "Zur theorie des ferromagnetismus," *Springer Nature Link*, 1928. DOI: 10.1007/BF01328601.

[111] L. Pauling and E. B. Wilson, *Introduction to quantum mechanics with applications to chemistry*. Courier Corporation, 2012, ISBN: 978-0486648712.

[112] R. Skomski, *Simple models of magnetism*. Oxford university press, 2008, ISBN: 978-0199655397.

[113] E. C. Stoner, "Collective electron ferromagnetism," *Proceedings of the Royal Society of London. A. Mathematical and Physical Sciences*, vol. 165, pp. 372–414, 1938. DOI: 10.1098/rspa.1938.0066.

[114] V. Tyberkevych, A. Slavin, P. Artemchuk, and G. Rowlands, "Vector hamiltonian formalism for nonlinear magnetization dynamics," 2020. DOI: 10.48550/arXiv.2011.13562.

[115] U. Atxitia, D. Hinzke, and U. Nowak, "Fundamentals and applications of the landau–lifshitz–bloch equation," *Journal of Physics D: Applied Physics*, vol. 50, no. 3, 2016. DOI: 10.1088/1361-6463/50/3/033003.

[116] S. M. Rezende, *Fundamentals of Magnonics*. Springer, 2020, ISBN: 9783030413170.

[117] N. Singh and A. M. Jayannavar, *A brief history of mangnetism*, 2019. arXiv: 1903.07031.

[118] C. Trevillian and V. Tyberkevych, "Formation of chirality in propagating spin waves," 2023. DOI: 10.21203/rs.3.rs-3212207/v1.

[119] R.-P. T. U. K.-L. (RPTU), *Spin waves*, https://mandmems.eu/impressum/, 2023.

[120] D. P. Hollis and P. W. Selwood, “Effect of chemisorbed hydrogen on the ferromagnetic resonance of finely divided nickel,” *The Journal of Chemical Physics*, vol. 35, 1961. DOI: 10.1063/1.1731927.

[121] V. Kambersky, “On ferromagnetic resonance in metals,” *Journal of Physics B*, vol. 26, 12 1976. DOI: 10.1007/BF01587621.

[122] G. T. Rado, “Theory of ferromagnetic resonance and static magnetization in ultrathin crystals,” *Physical Review B*, vol. 26, 1982. DOI: 10.1103/PhysRevB.26.295.

[123] R. Arias and D. Mills, “Extrinsic contributions to the ferromagnetic resonance response of ultrathin films,” *Physical review B*, vol. 60, no. 10, p. 7395, 1999.

[124] Y. Wang, R. Ramaswamy, and H. Yang, “Fmr-related phenomena in spintronic devices,” *Journal of Physics D: Applied Physics*, vol. 51, 2018. DOI: 10.1088/1361-6463/aac7b5.

[125] H. Li, J. Wang, J. Xue, *et al.*, “Systematic investigation of surface acoustic wave-driven ferromagnetic resonance: Model and simulation,” *Research Gate*, 2025. DOI: 10.15302/frontphys.2026.024204.

[126] D. Labanowski, “Acoustically driven ferromagnetic resonance for device applications,” Ph.D. dissertation, University of California, Berkeley, 2017.

[127] J. R. Eshbach and R. W. Damon, “Surface magnetostatic modes and surface spin waves,” *Phys. Rev.*, vol. 118, 5 1960. DOI: 10.1103/PhysRev.118.1208.

[128] S. Jun, S. Nikitov, R. Marcelli, and P. De Gasperis, “Parametric and modulation instabilities of magnetostatic surface spin waves in ferromagnetic films,” *Journal of applied physics*, vol. 81, no. 3, pp. 1341–1347, 1997. DOI: 10.1063/1.363869.

[129] B. Lüthi, D. Mills, and R. Camley, “Surface spin waves in antiferromagnets,” *Physical Review B*, vol. 28, 1983. DOI: 10.1103/PhysRevB.28.1475.

[130] A. Y. Annenkov, V. Vasil’ev, S. Gerus, *et al.*, “Magnetostatic surface wave modes in a channel created by a nonuniform magnetic field,” *Zh. Tekh. Fiz*, 1995.

[131] T. Yukawa, J.-i. Yamada, K. Abe, and J.-i. Ikenoue, “Effects of metal on the dispersion relation of magnetostatic surface waves,” *Japanese Journal of Applied Physics*, vol. 16, 1977. DOI: 10.1143/JJAP.16.2187.

[132] R. De Wames and T. Wolfram, “Dipole-exchange spin waves in ferromagnetic films,” *Journal of Applied Physics*, vol. 41, no. 3, pp. 987–993, 1970. DOI: 10.1063/1.1659049.

[133] A. Temiryazev, “Conversion of the frequency of a surface magnetostatic wave under three-magnon decay conditions,” *Sov Phys Solid State*, vol. 21, 1987.

[134] T. Wolfram and R. De Wames, “Macroscopic and microscopic theories of dipole-exchange spin waves in thin films: Case of the missing surface states,” *Physical Review Letters*, vol. 24, 1970. DOI: 10.1103/PhysRevLett.24.1489.

[135] J. Yu, R. Turk, and P. Wigen, "Exchange-dominated surface spin waves in thin yttrium-iron-garent films," *Physical Review B*, vol. 11, 1975. DOI: 10.1103/PhysRevB.11.420.

[136] J. Merry and J. Sethares, "Low loss magnetostatic surface waves at frequencies up to 15 ghz," *IEEE Transactions on Magnetics*, vol. 9, 1973. DOI: 10.1109/TMAG.1973.1067597.

[137] A. Sharaevskaya, D. Kalyabin, E. Beginin, Y. Fetisov, and S. Nikitov, "Surface spin waves in coupled easy-axis antiferromagnetic films," *Journal of Magnetism and Magnetic Materials*, 2019. DOI: 10.1016/j.jmmm.2018.11.130.

[138] X. Du, "Magnetostatic surface wave and surface acoustic wave devices for tunable and energy efficient radio frequency filters," https://www.proquest.com/dissertations-theses/magnetostatic-surface-wave-acoustic-devices/docview/3298666530/se-2?accountid=12924, Ph.D. dissertation, University of Pennsylvania, 2025.

[139] R. Damon and J. Eshbach, "Magnetostatic modes of a ferromagnet slab," *Journal of Physics and Chemistry of Solids*, vol. 19, 1961. DOI: 10.1016/0022-3697(61)90041-5.

[140] J. Parekh and H. Tuan, "Excitation of magnetostatic backward volume waves," *IEEE Transactions on Magnetics*, vol. 16, pp. 1165–1167, 5 1980. DOI: 10.1109/TMAG.1980.1060800.

[141] J. P. Parekh and H. S. Tuan, "Beams steering and diffraction of magnetostatic backward volume waves," *Journal of Applied Physics*, vol. 52, pp. 2279–2281, 3 1981. DOI: 10.1063/1.328905.

[142] G. A. Vugalter and A. G. Korovin, "Total internal reflection of backward volume magnetostatic waves and its applications for waveguides in ferrite films," *Journal of Physics D: Applied Physics*, vol. 31, pp. 1309–1319, 11 1998. DOI: 10.1088/0022-3727/31/11/004.

[143] A. S. Laurenson, J. Bertolotti, and V. V. Kruglyak, "Bloch oscillations of backward volume magnetostatic spin waves," *Physical Review B*, vol. 102, 5 2020. DOI: 10.1103/PhysRevB.102.054416.

[144] A. V. Vashkovskii and E. G. Lokk, "The physical properties of a backward magnetostatic wave described on the basis of the maxwell equations," *Journal of Communications Technology and Electronics*, vol. 57, pp. 490–497, 5 2012. DOI: 10.1134/S1064226912050105.

[145] W. Zhang and G.-Q. Liu, "Excitation and propagation characteristics of magnetostatic backward volume wave in a double-layered film structure with magnetic damping," *Journal of Applied Physics*, vol. 93, pp. 5720–5726, 9 2003. DOI: 10.1063/1.1565825.

[146] J. D. Adam and J. H. Collins, “Microwave magnetostatic delay devices based on epitaxial yttrium iron garnet,” *Proceedings of the IEEE*, vol. 64, pp. 794–800, 5 1976. DOI: 10.1109/PROC.1976.10214.

[147] J. Parekh and H. Tuan, “Beams steering and diffraction of magnetostatic backward volume waves,” *Journal of Applied Physics*, vol. 52, no. 3, pp. 2279–2281, 1981. DOI: 10.1063/1.328905.

[148] V. Takhtamyshyan and R. Babichev, “Backward volume and surface magnetostatic modes identification by distributions of radio frequency magnetic field,” in *2018 XIV International Scientific-Technical Conference on Actual Problems of Electronics Instrument Engineering (APEIE)*, IEEE, 2018, pp. 147–150, ISBN: 978-1-5386-7054-5. DOI: 10.1109/APEIE.2018.8545120.

[149] Y. Pu, C. L. Wang, and C. S. Tsai, “Magnetostaic backward volume wave-based-guided-wave mangetooptic bragg cells and application to wide-band light beam scanning,” *IEEE Photonics Technology Letters*, vol. 3, pp. 462–465, 5 1991. DOI: 10.1109/68.93879.

[150] M. Chen, M. Tsankob, J. Nash, and C. Patton, “Backward-volume-wave microwave-envelope solitons in yttrium iron garnet films,” *Physical Review B*, vol. 49, 18 1994. DOI: 10.1103/PhysRevB.49.12773.

[151] C. S. Tsai, “Wideband tunable microwave devices using ferromagnetic film–gallium arsenide material structures,” *Journal of Magnetism and Magnetic Materials*, vol. 209, pp. 10–14, 1–3 2000. DOI: 10.1016/S0304-8853(99)00634-4.

[152] A. V. Chumak, A. A. Serga, B. Hillebrands, and M. P. Kostylev, “Scattering of backward spin waves in a one-dimensional magnonic crystal,” *Applied Physics Letters*, vol. 93, 2 2008. DOI: 10.1063/1.2963027.

[153] P. Wessels, A. Vogel, J.-N. Tödt, M. Wieland, G. Meier, and M. Drescher, “Direct observation of isolated damon-eshbach and backward volume spin-wave packets in ferromagnetic microstripes,” *Scientific Reports*, vol. 6, 1 2016. DOI: 10.1038/srep22117.

[154] B. A. Kalinkos and N. G. Kovshikov, “Decay free microwave magnetic envelope soliton pulse trains in yttrium iron garnet thin films,” *Physical Review Letters*, vol. 78, pp. 2827–2830, 14 1997. DOI: 10.1103/PhysRevLett.78.2827.

[155] A. V. Chumak, A. A. Serga, B. Hillebrands, and M. P. Kostylev, “Scattering of backward spin waves in a one-dimensional magnonic crystal,” *Applied Physics Letters*, vol. 93, no. 2, p. 022 508, 2008. DOI: 10.1063/1.2963027.

[156] H. J. J. Liu, G. Riley, and K. Buchanan, “Directly excited backward volume spin waves in permally microstrips,” *IEEE Magnetics Letters*, vol. 6, 2015. DOI: 10.1109/LMAG.2015.2495162.

[157] N. Sato, N. Ishida, T. Kawakami, and K. Sekiguchi, “Propagating spectroscopy of backward volume spin waves in a metallic feni film,” *Applied Physics Letters*, vol. 104, 2014. DOI: 10.1063/1.4863215.

[158] J. P. Park, P. Eames, D. M. Engebretson, J. Berezovsky, and P. A. Crowell, “Spatially resolved dynamics of localized spin-wave modes in ferromagnetic wires,” *Phys. Rev. Lett.*, vol. 89, 27 2002. DOI: 10.1103/PhysRevLett.89.277201.

[159] T. Brächer, P. Pirro, A. A. Serga, and B. Hillebrands, “Localized parametric generation of spin waves in a longitudinally magnetized $Ni_{81}Fe_{19}$ waveguide,” *Applied Physics Letters*, vol. 103, 2013. DOI: 10.1063/1.4824304.

[160] V. E. Demidov and S. O. Demokritov, “Magnonic waveguides studied by microfocus brillouin light scattering,” *IEEE Transactions on Magnetics*, vol. 51, 2015. DOI: 10.1109/TMAG.2014.2388196.

[161] Y. Hwang, J. Puebla, K. Kondou, *et al.*, “Strongly coupled spin waves and surface acoustic waves at room temperature,” *Phys. Rev. Lett.*, 2024. DOI: 10.1103/PhysRevLett.132.056704.

[162] W. Campbell, “Electrical measurement of mechanical quantities,” *Students' Quarterly Journal*, vol. 10, 1940. DOI: 10.1049/sqj.1940.0020.

[163] C. Zener, “Internal friction in solids,” *Proceedings of the Physical Society*, vol. 52, 1940. DOI: 10.1088/0959-5309/52/1/322.

[164] J. Shur and A. Khokhlov, “The dependence of the magnetostriction of nickel upon initial magnetic texture and sequence of applying magnetic field and unidirectional elastic tension,” *Journal of Physics*, vol. 11, 1947.

[165] E. G. Spencer and R. LeCraw, “Magnetoacoustic resonance in yttrium iron garnet,” *Physical Review Letters*, vol. 1, 1958. DOI: 10.1103/PhysRevLett.1.241.

[166] A. B. Pippard, “Theory of ultrasonic attenuation in metals and magneto-acoustic oscillations,” *Proceedings of the Royal Society of London. A. Mathematical and Physical Sciences*, vol. 257, 1960. DOI: 10.1098/rspa.1960.0143.

[167] T. F. Rogers and S. J. Johnson, “Some magneto-acoustic effects in nickel,” *Journal of Applied Physics*, vol. 21, pp. 1067–1068, 1950. DOI: 10.1063/1.1699532.

[168] N. Mikoshiba, “On magneto-acoustic resonance in metals,” *Journal of the Physical Society of Japan*, vol. 13, 1958. DOI: 10.1143/JPSJ.13.759.

[169] E. W. Lee, “Magnetostriction and magnetomechanical effects,” *Reports on progress in physics*, vol. 18, 1955. DOI: 10.1088/0034-4885/18/1/305.

[170] A. Akhiezer, V. Bar'Iakhtar, and S. Peletminskii, “Coupled magnetoelastic waves in ferromagnetic media and ferroacoustic resonance,” *Sov. Phys. JETP*, vol. 35, 1959.

[171] C. Kittel and J. Van Vleck, "Theory of the temperature dependence of the magnetoelastic constants of cubic crystals," *Physical Review*, vol. 118, 1960. DOI: 10.1103/PhysRev.118.1231.

[172] S. Peletminskii, "Coupled magnetoelastic oscillations in antiferromagnetics," *Soviet Physics JETP*, vol. 37, 1960.

[173] J. Slonczewski, "Origin of magnetoelastic effects in cobalt-iron ferrite," *Journal of Physics and Chemistry of Solids*, vol. 15, 1960. DOI: https://doi.org/10.1016/0022-3697(60)90256-0.

[174] E. R. Callen and H. B. Callen, "Static magnetoelastic coupling in cubic crystals," *Phys. Rev.*, vol. 129, pp. 578–593, 2 1963. DOI: 10.1103/PhysRev.129.578.

[175] W. F. Brown, *Magnetoelastic interactions*. Springer, 1966, vol. 9, ISBN: 978-3-642-87398-0.

[176] T. Moran and B. Lüthi, "Elastic and magnetoelastic effects in magnetite," *Physical Review*, vol. 187, 1969. DOI: 10.1103/PhysRev.187.710.

[177] S. Hanna, "Rf and microwave applications to saw propagation in magnetic films," in *Proceedings., IEEE Ultrasonics Symposium*, IEEE, 1989. DOI: 10.1109/ULTSYM.1989.66970.

[178] E. Schlömann and R. Joseph, "Generation of spin waves in nonuniform magnetic fields. iii. magnetoelastic interaction," *Journal of Applied Physics*, vol. 35, 1964. DOI: 10.1063/1.1702867.

[179] S. Rezende and F. Morgenthaler, "Magnetoelastic waves in time-varying magnetic fields. i. theory," *Journal of Applied Physics*, vol. 40, 1969. DOI: 10.1063/1.1657433.

[180] J. Eshbach, "Spin-wave propagation and the magnetoelastic interaction in yttrium iron garnet," *Journal of Applied Physics*, vol. 34, 1963. DOI: 10.1063/1.1729481.

[181] H. Matthews and H. van de Vaart, "Magnetoelastic love waves," *Applied Physics Letters*, vol. 15, 1969. DOI: 10.1063/1.1652865.

[182] K. An, A. N. Litvinenko, R. Kohno, *et al.*, "Coherent long-range transfer of angular momentum between magnon kittel modes by phonons," *Phys. Rev. B*, 2020. DOI: 10.1103/PhysRevB.101.060407.

[183] V. Vlasov, A. Golov, L. Kotov, V. Shcheglov, A. Lomonosov, and V. Temnov, "The modern problems of ultrafast magnetoacoustics (review)," *Acoustical Physics*, vol. 68, 2022. DOI: 10.1134/S1063771022010079.

[184] Y. Zhou, G. Chen, X. Zhao, T. Tat, Z. Duan, and J. Chen, "Theory of giant magnetoelastic effect in soft systems," *Science Advances*, vol. 11, 2025. DOI: 10.1126/sciadv.ads0071.

[185] L. Dorfmann and R. W. Ogden, “The nonlinear theory of magnetoelasticity and the role of the maxwell stress: A review,” *Proceedings of the Royal Society A: Mathematical, Physical and Engineering Sciences*, vol. 479, 2023. DOI: 10.1098/rspa.2023.0592.

[186] A. S. Tatarenko and M. I. Bichurin, “Microwave magnetoelectric devices,” *Advances in Condensed Matter Physics*, 2012. DOI: https://doi.org/10.1155/2012/286562.

[187] X. Z. Lu, X. Wu, and H. J. Xiang, “General microscopic model of magnetoelastic coupling from first principles,” *Physical Review B*, 2015. DOI: 10.1103/physrevb.91.100405.

[188] S. Finizio, M. Foerster, M. Buzzi, *et al.*, “Magnetic anisotropy engineering in thin film Ni nanostructures by magnetoelastic coupling,” *Phys. Rev. Appl.*, 2014. DOI: 10.1103/PhysRevApplied.1.021001.

[189] R. O’Handley, “Surface magnetoelastic coupling,” *Physical Review Letters*, 1991. DOI: 10.1103/PhysRevLett.66.2798.

[190] R. Kryshtal and A. Medved, “Surface acoustic wave in yttrium iron garnet as tunable magnonic crystals for sensors and signal processing applications,” *Applied Physics Letters*, vol. 100, 19 2012. DOI: 10.1063/1.4714507.

[191] A. Clark, J. Restorff, M. Wun-Fogle, and J. Lindbarg, “Magnetoelastic coupling and ΔE effect in Tb_xDy_{1-x} single crystals,” *Journal of Applied Physics*, 1993. DOI: 10.1063/1.352732.

[192] G. Bochi, O. Song, and R. O’Handley, “Surface magnetoelastic coupling coefficients of single-crystal fcc co thin films,” *Physical Review B*, 1994. DOI: 10.1103/PhysRevB.50.2043.

[193] T. Gutjahr-Löser, D. Sander, and J. Kirschner, “Magnetoelastic coupling in co thin films on w(0 0 1),” *Journal of Magnetism and Magnetic Materials*, 2000. DOI: 10.1016/S0304-8853(00)00449-2.

[194] N. Aliouane, D. N. Argyriou, J. Strempfer, I. Zegkinoglou, S. Landsgesell, and M. v. Zimmermann, “Field-induced linear magnetoelastic coupling in multiferroic $TbMnO_3$,” *Phys. Rev. B*, 2006. DOI: 10.1103/PhysRevB.73.020102.

[195] A. E. Clark, J. B. Restorff, M. Wun–Fogle, D. Wu, and T. A. Lograsso, “Temperature dependence of the magnetostriction and magnetoelastic coupling in $Fe_{100-x}Al_x$ and $Fe_{50}Co_{50}$,” *Journal of Applied Physics*, 2008. DOI: 10.1063/1.2831360.

[196] A. Barcza, Z. Gercsi, K. S. Knight, and K. G. Sandeman, “Giant magnetoelastic coupling in a metallic helical metamagnet,” *Physical Review Letters*, 2010. DOI: 10.1103/physrevlett.104.247202.

[197] U. Adem, L. Wang, D. Fausti, *et al.*, "Magnetodielectric and magnetoelastic coupling in $TbFe_3(BO_3)_4$," *Phys. Rev. B*, 2010. DOI: 10.1103/PhysRevB.82.064406.

[198] K. Dey, S. Sauerland, J. Werner, *et al.*, "Magnetic phase diagram and magnetoelastic coupling of $NiTiO_3$," *Phys. Rev. B*, 2020. DOI: 10.1103/PhysRevB.101.195122.

[199] F. S. Barth and F. Macià Bros, "Magnetoelastic effect through coupled surface acoustic waves and spin waves in ferromagnetic cobalt thin films," *Deposit Digital*, 2022. DOI: https://hdl.handle.net/2445/188916.

[200] F. Ryburn, "Studies in magnetoelasticity," https://scholar.google.com/citations?user=IMrSPDkAAAAJ&hl=en&oi=sra, Ph.D. dissertation, University of Oxford, 2024.

[201] C. A. Marques, L. C. Rhodes, W. Osmolska, *et al.*, "Emergent exchange-driven giant magnetoelastic coupling in a correlated itinerant ferromagnet," *Nature Physics*, 2025. DOI: 10.1038/s41567-025-02893-x.

[202] A. Sohail, R. Ahmed, J.-X. Peng, *et al.*, "Controllable fano-type optical response and four-wave mixing via magnetoelastic coupling in an opto-magnomechanical system," *Journal of Applied Physics*, 2023. DOI: 10.1063/5.0133156.

[203] A. V. Azovtsev and N. A. Pertsev, "Electrically excited magnetoelastic waves and magnetoacoustic resonance in ferromagnetic films with voltage-controlled magnetic anisotropy," *Phys. Rev. B*, vol. 107, 2023. DOI: 10.1103/PhysRevB.107.054418.

[204] J. Xu, Z. Wang, H. Huang, *et al.*, "Significant zero thermal expansion via enhanced magnetoelastic coupling in kagome magnets," *Advanced Materials*, vol. 35, 2023. DOI: https://doi.org/10.1002/adma.202208635.

[205] J. Gong, Z. Zhang, H. Wang, and D. Wang, "A magnetoelastic effect-guided design for micro stress/strain detector using deep learning," *IEEE Sensors Journal*, vol. 24, 2024. DOI: 10.1109/JSEN.2023.3347853.

[206] M. Weiler, L. Dreher, C. Heeg, *et al.*, "Elastically driven ferromagnetic resonance in nickel thin films," *Phys. Rev. Lett.*, 2011. DOI: 10.1103/PhysRevLett.106.117601.

[207] T. V. Bogdanova, D. V. Kalyabin, A. R. Safin, and S. A. Nikitov, "Modelling of coupled magnetoelastic waves in structure containing thin antiferromagnetic films on an elastic substrate," *Journal of Physics D: Applied Physics*, vol. 56, 2023. DOI: 10.1088/1361-6463/acc4d3.

[208] D. J. Gillard, D. Wolverson, O. M. Hutchings, and A. I. Tartakovskii, "Spin-order-dependent magneto-elastic coupling in two dimensional antiferromagnetic $MnPSe_3$ observed through raman spectroscopy," *npj 2D Materials and Applications*, vol. 8, 2024. DOI: 10.1038/s41699-024-00441-4.

[209] K. K. Bestha, V. Kocsis, O. Janson, *et al.*, "Magnetoelastic coupling and large uniaxial pressure dependence of antiferromagnetic order in two-dimensional van der waals $Fe_2P_2S_6$ and $Ni_2P_2S_6$ single crystals," *Phys. Rev. B*, vol. 111, 2025. DOI: 10.1103/PhysRevB.111.L020409.

[210] J. M. Caron, J. R. Neilson, D. C. Miller, A. Llobet, and T. M. McQueen, "Iron displacements and magnetoelastic coupling in the antiferromagnetic spin-ladder compound $BaFe_2Se_3$," *Phys. Rev. B*, 2011. DOI: 10.1103/PhysRevB.84.180409.

[211] R. Verba, V. Tiberkevich, and A. Slavin, "Wide-band nonreciprocity of surface acoustic waves induced by magnetoelastic coupling with a synthetic antiferromagnet," *Phys. Rev. Appl.*, 2019. DOI: 10.1103/PhysRevApplied.12.054061.

[212] H. Matsumoto, T. Kawada, M. Ishibashi, M. Kawaguchi, and M. Hayashi, "Large surface acoustic wave nonreciprocity in synthetic antiferromagnets," *Applied Physics Express*, 2022. DOI: 10.35848/1882-0786/ac6da1.

[213] M. A. Dunstan, M. J. Giansiracusa, M. Vonci, *et al.*, "Direct observation of magnetoelastic coupling in a molecular spin qubit: New insights from crystal field neutron scattering data," *Chemical science*, vol. 14, pp. 3990–4001, 2023. DOI: 10.1039/D2SC05797B.

[214] S. Cui, F. Chen, L. Liao, *et al.*, "Enhancement of magnetoacoustic coupling by surface acoustic wave–driven spin current," *Physical Review Applied*, vol. 25, 2026. DOI: 10.1103/lfvn-bppq.

[215] Y. Yan and H. Zhao, "Elastodynamically induced spin current in a coupled spin-lattice system," *The European Physical Journal B*, vol. 96, 2023. DOI: 10.1140/epjb/s10051-023-00581-4.

[216] S. Mi, C. Zhao, M. Liu, J. Wang, and Q. Liu, "Detection of spin current generated by the acoustic spin–rotation coupling mechanism via acoustic voltage," *Applied Physics Letters*, vol. 125, 2024. DOI: 10.1063/5.0242879.

[217] N. Polzikova, S. Alekseev, V. Luzanov, and A. Raevskiy, "Acoustic excitation and electrical detection of spin waves and spin currents in hypersonic bulk waves resonator with YIG/Pt system," *Journal of Magnetism and Magnetic Materials*, 2019. DOI: 10.1016/j.jmmm.2019.02.007.

[218] G. Yu, S. Shi, R. Peng, *et al.*, "Strain-driven magnetic domain wall dynamics controlled by voltage in multiferroic heterostructures," *Journal of Magnetism and Magnetic Materials*, vol. 552, 2022. DOI: 10.1016/j.jmmm.2022.169229.

[219] J. Shuai, R. G. Hunt, T. A. Moore, and J. E. Cunningham, "Separation of heating and magnetoelastic coupling effects in surface-acoustic-wave-enhanced creep of magnetic domain walls," *Physical Review Applied*, vol. 20, 2023. DOI: 10.1103/PhysRevApplied.20.014002.

[220] G. Go and S. K. Kim, "Magnetoelastic coupling-driven chiral spin textures: A skyrmion-antiskyrmion-like array," *Phys. Rev. Lett.*, vol. 136, 2026. DOI: 10.1103/5csz-pw7x.

[221] R. Verba, I. Lisenkov, I. Krivorotov, V. Tyberkevych, and A. Slavin, "Nonreciprocal surface acoustic waves in multilayers with magnetoelastic and interfacial dzyaloshinskii-moriya interactions," *Physical Review Applied*, vol. 9, 6 2018. DOI: 10.1103/PhysRevApplied.9.064014.

[222] I. Lisenkov, A. Jander, and P. Dhagat, "Magnetoelastic parametric instabilities of localized spin waves induced by traveling elastic waves," *Physical Review B*, vol. 99, 18 2019. DOI: 10.1103/PhysRevB.99.184433.

[223] K. Vlasov and B. K. Ishmukhametov, "Equations of motion and state for magnetoelastic media," *Soviet Phys. JETP*, vol. 19, 1964.

[224] K. Yamamoto, M. Xu, J. Puebla, Y. Otani, and S. Maekawa, "Interaction between surface acoustic waves and spin waves in a ferromagnetic thin film," *Journal of Magnetism and Magnetic Materials*, vol. 545, 2022. DOI: 10.1016/j.jmmm.2021.168672.

[225] Ü. Özgür, Y. Alivov, and H. Morkoç, "Microwave ferrites, part 1: Fundamental properties," *Journal of Materials Science Materials in Electronics*, vol. 20, pp. 789–834, 2009. DOI: 10.1007/s10854-009-9923-2.

[226] I. Boventer, M. Pfirrmann, J. Krause, Y. Schön, M. Kläui, and M. Weides, "Complex temperature dependence of coupling and dissipation of cavity magnon polaritons from millikelvin to room temperature," *Phys. Rev. B*, vol. 97, 18 2018. DOI: 10.1103/PhysRevB.97.184420.

[227] R. Kryshtal and A. Medved, "Influence of magnetic anisotropy on dynamic magnonic crystals created by surface acoustic waves in yttrium iron garnet films," *Journal of Magnetism and Magnetic Materials*, 2017. DOI: 10.1016/j.jmmm.2016.10.148.

[228] X. Zhang, C.-L. Zou, L. Jiang, and H. X. Tang, "Strongly coupled magnons and cavity microwave photons," *Phys. Rev. Lett.*, vol. 113, 15 2014. DOI: 10.1103/PhysRevLett.113.156401.

[229] Y. H. Ren, C. Wu, Y. Gong, C. Pettiford, and N. X. Sun, "Ultrafast optical study of spin wave resonance and relaxation in a cofe/ptmn/cofe trilayer film," *Journal of Applied Physics*, vol. 105, no. 7, p. 07D304, 2009. DOI: 10.1063/1.3063675.

[230] G.-M. Yang, J. Wu, J. Lou, M. Liu, and N. X. Sun, "Low-loss magnetically tunable bandpass filters with yig films," *IEEE transactions on magnetics*, vol. 49, no. 9, pp. 5063–5068, 2013. DOI: 10.1109/TMAG.2013.2253114.

[231] G. A. Melkov, A. A. Serga, V. S. Tiberkevich, Y. V. Kobljanskij, and A. N. Slavin, "Nonadiabatic interaction of a propagating wave packet with localized parametric pumping," *Phys. Rev. E*, vol. 63, 6 2001. DOI: 10.1103/PhysRevE.63.066607.

[232] G. A. Melkov, A. A. Serga, A. N. Slavin, V. S. Tiberkevich, A. Oleinik, and A. Bagada, "Parametric interaction of magnetostatic waves with a nonstationary local pump," *Journal of Experimental and Theoretical Physics*, vol. 89, 6 1999. DOI: 10.1134/1.559071.

[233] T. Brächer, P. Pirro, and B. Hillebrands, "Parallel pumping for magnon spintronics: Amplification and manipulation of magnon spin currents on the micron-scale," *Physics Reports*, vol. 699, pp. 1–34, 2017. DOI: 10.1016/j.physrep.2017.07.003.

[234] P. Chowdhury, A. Jander, and P. Dhagat, "Nondegenerate parametric pumping of spin waves by acoustic waves," *IEEE Magnetics Letters*, 2017. DOI: 10.1109/LMAG.2017.2737962.

[235] K. Fujii, *Introduction to the rotating wave approximation (rwa) : Two coherent oscillations*, 2014. DOI: 10.48550/arXiv.1301.3585.

[236] A. Kurcz, A. Capolupo, A. Beige, E. Del Giudice, and G. Vitiello, "Rotating wave approximation and entropy," *Physics Letters A*, vol. 374, pp. 3726–3732, 2010. DOI: https://doi.org/10.1016/j.physleta.2010.07.032.

[237] C. Trevillian and V. Tyberkevych, "Formation of chirality in propagating spin waves," *npj Spintronics*, vol. 2, 1 2024. DOI: 10.1038/s44306-024-00026-3.

[238] C. Caloz and Z.-L. Deck-Léger, *Spacetime metamaterials*, 2019. arXiv: 1905.00560 [physics.optics].

[239] S. Blanes, F. Casas, J. A. Oteo, and J. Ros, "The magnus expansion and some of its applications," *Physics Reports*, vol. 470, pp. 151–238, 5–6 2009. DOI: 10.1016/j.physrep.2008.11.001.

[240] R. Hollander, "The magnus expansion," Ph.D. dissertation, Faculty of Science and Engineering, 2017.

[241] J. Jorzick, S. Demokritov, B. Hillebrands, *et al.*, "Spin wave wells in nonellipsoidal micrometer size magnetic elements," *Physical Review Letters*, 2002. DOI: 10.1103/PhysRevLett.88.047204.

[242] B. Rana, S. Saha, P. Gruszecki, and J. Puebla, "Focus on coupling phenomena in magnonics and magnonic metamaterials," *Journal of Physics: Condensed Matter*, vol. 37, 43 2025. DOI: 10.1088/1361-648X/ae1398.

[243] L. Zhang, X. Q. Chen, S. Liu, *et al.*, "Space-time-coding digital metasurfaces," *Nature Communications*, 2018. DOI: 10.1038/s41467-018-06802-0.

[244] A. Rogov and E. Narimanov, "Space–time metamaterials," *ACS Photonics*, 2018. DOI: 10.1021/acsphotonics.8b00233.